Alexander G. Grankov
Alexander A. Milshin

Microwave Radiation of the Ocean-Atmosphere

Boundary Heat and Dynamic Interaction

Second Edition

Springer

Microwave Radiation of the Ocean-Atmosphere

Alexander G. Grankov · Alexander A. Milshin

Microwave Radiation of the Ocean-Atmosphere

Boundary Heat and Dynamic Interaction

Second Edition

Alexander G. Grankov
Russian Academy of Sciences
Fryazino, The Moscow Area
Russia

Alexander A. Milshin
Russian Academy of Sciences
Fryazino, The Moscow Area
Russia

We dedicate this book of blessed memory of Prof. Anatoly Shutko

Preface

This monograph is dedicated to the elaboration of passive microwave (MCW) radiometric methods for the study of ocean-atmosphere interactions: it is a sequel to the monograph *Relation Between Natural Microwave Radiation of the Ocean-Atmosphere System with the Boundary Heat and Dynamic Interaction* by A.G. Grankov and A.A. Milshin published by Nauka (Moscow, Russia, 2004) with the support of the Russian Foundation for Basic Research. Later, in 2010, the Springer issued an expanded and revised edition of this book in English, titled *Microwave Radiation of the Ocean-Atmosphere: Boundary Heat and Dynamic Interaction*.

After publication of the book *Radioemission of the Earth as a Planet* by A.Je. Basharinov, A.S. Gurvich, and E.T. Egorov (Moscow, Russia, 1974), MCW radiometric methods based on the natural radiation of the earth and atmosphere achieved recognition and wide use. Ten years earlier, the monograph *Radiothermal Location (Passive Radiolocation)* by A.G. Nikolaev and S.V. Pertshev was published by Sovetskoe Radio; however, this monograph differed greatly because it could not display the results of the unique radiophysical experiment carried out from the satellite Cosmos-243 in 1968.

In this monograph, we discuss some possibilities for using the potential of satellite passive MCW radiometric methods in the analysis of variations of heat and dynamic processes in the ocean–atmosphere interface for a wide range of time scales—from *mesometeorogical* (of an hour), *synoptic* (of a week), and *seasonal* (of a month), to *interannual*. The methods for analysis of the processes of ocean–atmosphere interaction as a factor of seasonal and interannual variability is a very important component of international scientific programs, such as the Global Change Research Program and Earth Observing System (EOS). The need for high-resolution, accurate surface fluxes of heat, water vapor, and momentum over the global ocean has been articulated by numerous groups within the global climate community, including the World Climate Research Programme (WCRP) Working Group on Air–Sea Fluxes (WGASF), the WCRP Global Energy and Water Cycle Experiment (GEWEX) Radiation Panel, and the Climate Variations (CLIVAR)

Science Steering Group. The GEWEX Radiation Panel and the U.S. CLIVAR Committee have established a goal of 1° spatial resolution, 3- to 6-h time resolution, and accuracy of 5 Wm^{-2} for individual components of the surface heat budget. The actuality of these subjects has also been emphasized in special issues of Russian programs on ocean research and the development of systems for its studies.

As a result of the steady reduction of field measurements in the World Ocean, satellites have become the most important tools in its investigation. Measurements from vessels and buoys do not provide the required spatial resolution and time regularity for observations, whereas conventional estimates of global fields of the fluxes between ocean and atmosphere suffer from inadequate spatial and time sampling. Only a few exceptions exist, such as the network of meteorological stations in the equatorial belt of the ocean (TAO/TRITON) and the system of buoy stations in the Gulf of Mexico designed for the regular monitoring of ocean surface parameters and the near-surface atmosphere in active areas of the tropical cyclogenesis.

The parameters measured from satellites, such as vertical turbulent fluxes of sensible and latent heat and the impulse (momentum), are considered to be the so-called climatic-forming factors. The main problem in retrieving these parameters from satellites is as follows: an intensity of natural MCW radiation in the ocean–atmosphere system (SOA) results in information not only on near-surface atmospheric layers (which are most active in forming the processes of energy exchanges with the oceanic surface) but also on the higher layers. Therefore, satellite passive MCW radiometric analysis of climatic-forming parameters was recognized as an effective tool in the 1980s and 1990s (mainly in the United States, Russia, and Germany). Prior to this, in the 1960s and 1970s, some encouraging results were reported for the use of remotely sensed data in laboratory studies; in addition, measurements were obtained from aircrafts and floating platforms using microwaves and infrareds for the analysis of the heat and water exchange at the air–sea boundary.

In the twenty-first century, strong efforts have been made toward developing methods to determine geophysical parameters, such as water vapor content in the atmosphere and radiation fluxes, from geostationary and polar orbiting satellites. Retrievals developed for radiometers on the National Oceanic and Atmospheric Administration (NOAA) polar orbiting satellites, such as the Advanced Very High Resolution Radiometer (AVHRR), the Special Sensor Microwave/Imager (SSM/I) on the DMSP program, and the instruments onboard the Tropical Rainfall Measuring Mission (TRMM) satellite are distinguished by an accuracy that is comparable to or better than in situ measurements.

Various methods for estimation of the monthly mean latent heat fluxes at the SOA boundary and their seasonal variability have been proposed and approved. These methods are based on the direct (*physical*) or indirect (*correlative*) relationships between the SOA brightness temperatures measured from satellites and the most important components of heat and moisture exchange, such as the ocean (sea) surface temperature and the temperature, moisture, and wind speed of the near-surface atmosphere.

We examined the potential of the SSM/I radiometer for retrieval of the synoptic latent fluxes, but the results of these studies were not encouraging. Some research gaps should be addressed on the real and potential possibilities of satellite passive MCW radiometric methods in relation to an analysis of the heat and dynamic ocean-atmosphere interaction:

- The methods used are based on formulas of heat and water exchange between the ocean and atmosphere (*bulk formulas*), accounting for calculations of the near-surface air temperature and humidity, which are *indirectly* connected to the SOA brightness temperature.
- Usually, only the atmospheric characteristic of humidity, as measured from satellites in the spectral MCW band of water vapor absorption, is taken into consideration as the intermediate characteristic between the SOA brightness temperature and the surface heat fluxes.
- Relationships between the SOA's brightness temperature and the surface heat fluxes have a static characteristic, as they are based on *general* (climatic) regressions between the air integral and near-surface humidity, which do not reflect their effects on various mechanisms of heat and water transfer in the atmosphere (e.g., vertical diffusive, horizontal advective) in short timeframes.
- More importantly, specialists in the field of remote sensing of oceanological and climatic processes have not considered the possibility of using satellite MCW radiometric methods in *frontal* oceanic zones, where the effectiveness of bulk formulas is not yet clear.
- The potential of satellite passive MCW radiometric methods for the analysis of energy, circulation characteristics of the boundary layer of the atmosphere, and their influence on heat and water exchange at the boundary of the SOA have not been fully researched.
- Finally, for remote sensing of the World Ocean by means of passive radiometric MCW, infrared (IR), and other methods, researchers have lost sight of the urgent problem concerning the study of the initial role of the ocean and atmosphere in their heat and dynamic interactions at various spatial and time scales.

All of these circumstances were noted in our previous monograph (Grankov and Milshin 2004), which summarized the results of our work for the 20 years prior to its publication.

During 2008−2011, the scope of our interest was extended. We studied the ocean–atmosphere heat and dynamic interaction with MCW radiometric methods in midlatitude cyclones and the oceanic areas subjected to the impacts of tropical cyclones (hurricanes). In this period, several studies were conducted:

- Clarification of the role of *horizontal* (advective) heat transfer in forming the relationship between the intensity of the SOA's natural MCW radiation and the intensity of heat and moisture exchange at the ocean–atmosphere boundary.
- Study of the behavior of the SOA's oceanographical, meteorological, aerologic, and MCW radiation characteristics in areas of tropical cyclone activity, with a comparison to midlatitude North Atlantic cyclones.

- Analysis of the atmospheric dynamics and energy in oceanic (sea) waters for cyclonic (prestorm) conditions with data of simultaneous satellite MCW radiometric and station (buoy) meteorological measurements.
- Elaboration of the methods for determining heat and moisture content in the near-surface, boundary, and troposphere layers of the atmosphere with satellite and station (buoy) measurements.

A special aspect of these studies is the investigation of mechanisms of the SOA's natural MCW radiation reaction to heat property variations in the near-surface and boundary layers of the atmosphere, as well as the search for spectral intervals and suitable scales of space and time. Data from satellite measurements was averaged to provide an immediate (*direct*) connection between the SOA's brightness temperature measured from satellites and the intensity of heat and moisture exchange at the boundary of the system.

The atmosphere boundary layer plays a special role in our studies for the following reasons:

(a) Because of the processes of turbulent mixing, the atmosphere boundary layer's parameters are closely associated with the parameters of the near-surface layer $(0-10\ m)$, which affect the intensity of its heat and moisture exchange with the ocean surface.

(b) Within this layer, natural MCW radiation of the SOA is formed in a line of radiowave absorption in atmospheric water vapor (at a wavelength of 1.35 cm) and its vicinity.

At meetings and seminars, we are often asked why such a strong correlation is observed between the SOA's brightness temperature and heat processes in the atmospheric boundary and near-surface layers, and why the ocean surface temperature so weakly influences the near-surface heat fluxes at the synoptic range of time intervals. Answers to these questions will be given in this book.

The results of our studies on the role of horizontal advective heat transfer in the atmosphere boundary layer in forming relations between its enthalpy and the SOA's brightness temperature in the synoptic range of time scales were included in the 1998 and 2012 annual reports of the Russian Academy of Sciences (RAS).

An important factor in these studies was our collaboration with Moscow scientific organizations, including P.P. Shirshov's Institute of Oceanology RAS (A.I. Ginzburg, S.V. Pereslegin, V.N. Pelevin), Russian Hydrometcenter (Ju.D. Resnyaskii), Rosaviacosmos (I.V. Cherny), Institute of Space Research RAS (Yu.A. Kravtzov, Je.A. Sharkov), Institute of Water Problems RAS (G.N. Panin), Institute of Numerical Mathematics (A.I. Chavro), and Moscow Physical and Technical Institute (P.P. Usov).

An invaluable contribution to the studies was made by the unique data of vessel experiments NEWFOUEX-88 and ATLANTEX-90, which were received from the P.P. Shirshov's Institute of Oceanology RAS (S.K. Gulev), and the archive data of satellite MCW radiometric long-term (10-year) measurements derived from the U.S meteorological satellite DMSP, which were given to us by the Marshall Space Flight Center. The oceanographic, meteorological, and satellite measurements accumulated at point "M" of the North Atlantic, as reported by Joerg Schulz (Germany), expanded our understanding of the dependencies of SOA's brightness temperature and boundary heat fluxes of the middle latitudes on the higher ones.

We also note that the unique and expensive (even by Soviet measures) experiments NEWFOUEX-88 and ATLANTEX-90 will let us—as specialists in the remote sensing of the ocean from space—rest upon the data of these experiments again and again.

Moscow-Fryazino, Russia   Alexander G. Grankov
                                                     Alexander A. Milshin

Acknowledgments

Contents

Chapter 1
Accessible Parameters for Satellite MCW Radiometers and Their Relationship with Ocean–Atmosphere Interactions

1.1 Methods for Surface Heat Flux Analysis Using Radiometric Measurements

1.1.1 Traditional Approach

In remote sensing of heat exchange processes at the ocean–atmosphere system (SOA) interface, the characteristics of natural microwave (MCW) and infrared (IR) radiation of the SOA are formed not only in the near-surface atmosphere layer (10–20 m thick) but also in higher layers (2–5 km), depending on the spectral bands used in satellite measurements. There are different approaches to using MCW and IR radiometric measurements for estimating heat fluxes in the SOA interface. For example, one method retrieves the vertical temperature profiles (gradients) of the oceanic surface layer; Khundzhua and Andreev (1973) used the magnitude and the sign to judge the intensity of the vertical turbulent flux of sensible heat. The effectiveness of an infrared approach has been confirmed by the results of numerous laboratory studies, stationary coast points, and floating sea platforms; these results are in good agreement with the data from aircraft measurements (Bychkova et al. 1988).

The potential for retrieving the vertical temperature profile of the sea subsurface layer was investigated theoretically by Sharkov (1978) and Mitnik (1979). These studies were continued by specialists who developed and tested the possibilities of retrieving the water surface vertical temperature profile of the ideal (flat) and natural (waved) sea surface (Gaikovich et al. 1987) in laboratory studies.

MCW and IR ranges have not yet been proven for the determination of heat fluxes based on water surface vertical temperature profiles from satellite measurements. Modern satellite MCW and IR means, which accurately retrieve ocean surface temperatures (OST) within 0.5–1 °C, do not provide sufficient estimates of OST values and their variations. This is even true of MCW and IR methods for retrieving air vertical temperature and humidity profiles in local bands of radiation

(absorption) for the most important atmospheric components—water vapor and oxygen, whose accuracy estimates are insufficient due to low spectral resolution and the sensitivity of radiometers.

More perspective is the method for determining heat fluxes based on the statistical correlation between the integral (averaged over height) atmosphere characteristics, whose variations are neatly fixed from satellites with MCW and IR measurement data, and its temperature and humidity values. This correlation results from the air near-surface and boundary layer mechanisms of turbulent heat and water mixing. These processes are most typical and intense for the atmosphere (versus the ocean) and have apparent mean variations each month (or decade), independent of more short-term perturbations. Therefore, the best results for satellite radiometric methods are obtained by retrieving *monthly* mean SOA boundary heat fluxes. These results are based, for example, on MCW and IR passive radiometric measurements from the satellite Nimbus 7, as well as from the DMSP and NOAA satellites.

The relationship between temperature and humidity in various atmospheric layers is the starting point for using satellite radiometric data to analyze the sensible (q_h) and latent (q_e) vertical turbulent heat fluxes at the SOA boundary, if we use semi-empirical formulas (bulk formulas) based on the global bulk aerodynamic method. In this method, the values q_h and q_e are given by the following formulas (Ivanov 1978; Lappo et al. 1990):

$$q_h = c_p\,\rho\,C_T(t_s - t_a)V; \tag{1.1}$$

$$q_e = L\,\rho\,(0.622/P_a)C_E(e - e_0)V, \tag{1.2}$$

From these formulas, one can see that the values of q_h and q_e depend on parameters of the SOA, such as temperature (t_a), water vapor pressure (e), and wind speed (V) in the near-surface atmosphere, as well as oceanic water surface temperature (t_s) and the maximum for this value, air humidity (e). The parameters used in bulk formulas (1.1) and (1.2) are the numbers of Schmidt (C_T), Dalton (C_E), the specific heat of evaporation (L), the specific air heat under constant pressure (c_p), and the air density (ρ).

The aerodynamic method also allows one to obtain the simple parameterization of the relationships between the intensity of a *dynamic* air–sea interaction characterized by the turbulent flux of impulse (momentum) (q_v), which can be calculated as follows (Ivanov 1978; Lappo et al. 1990):

$$q_v = \rho\,C_v V^2, \tag{1.3}$$

where C_v is the drag coefficient.

The formulas (1.1)–(1.3) enable one to determine not only "instant" heat and impulse fluxes, but also those averaged over considerable time periods. For example, it is possible to estimate the monthly mean heat and impulse fluxes using

the monthly mean parameters of t_s, t_a, e, and V as the input data (Ariel et al. 1973; Esbensen and Reynolds 1981; Larin 1984; Gulev 1991).

This peculiarity of the global bulk aerodynamic method has attracted the attention of specialists in the fields of oceanology, meteorology, and climatology who are interested in remote sensing, especially for information on the near-surface atmosphere air temperature t_a and humidity e. However, this method has limitations. For example, the horizontal spatial gradients of the parameters t_s, t_a, and e must not exceed their critical values (Lappo et al. 1990). Consequently, the possibilities of its realization are unclear in the oceanic frontal zones, which have significant geophysical and brightness temperature spatial and temporal contrasts.

Formulas (1.1)–(1.3) show that the water surface temperature t_s, the near-surface air temperature t_a, humidity e, and wind speed V are the main factors in air–sea interchanges. Estimates of the parameters t_s and t_a can be obtained directly from satellite MCW radiometric measurements. To estimate the parameters t_a and e, one should use some correlative relations between these parameters and the intensity of the SOA natural MCW and IR radiation, which manifest only in some spectral intervals.

Extensive studies have analyzed the potential of satellite MCW and IR methods for estimating the characteristics of heat and dynamic interactions between the ocean and atmosphere. For example, Dymnikov et al. (1984) obtained some proximate estimates of oceanic layer parameters that are closely related to the SOA radiation balance. Grishin and Lebedev (1990) found the maximal values of errors of the parameters t_s, t_a, V, and e, when the estimates of the fluxes q_h, q_e, and q_v were calculated with bulk formulas; these are useful for oceanologists and climatolologists with regard to the possibilities of modern satellite MCW and IR radiometric instrumentation. Taylor (1984) studied satellite-derived monthly mean heat and latent heat fluxes, as well as their sampling frequency, during the JASIN experiment in the North Sea. The results of this study estimated the relative error of heat flux determination to be ~ 10 % for the parameter q_h and 30 % for the parameter q_e when oceanic areas were observed from satellites every 12 h.

The results of experimental measurements derived from the Nimbus 7, DMSP (microwaves), and NOAA satellites (infrared) within various physical and geographical zones of the World Ocean (Schulz et al. 1997; Grankov et al. 1999a, b; Liu 1995; Grassl et al. 2000) justify the effectiveness of this approach. For example, the square root estimate of the monthly mean latent heat fluxes averaged over $2° \times 5°$ squares for selected satellite data [September 1987, Global Ocean (Schulz et al. 1997)] is ~ 15–30 W m^{-2}. Similar results were obtained by Grankov et al. (1999a, b; in some energy-active zones of the North Atlantic in February 1994) and Liu (1995; in tropical zones of the Pacific Ocean).

An important step in remote sensing for the processes of heat and dynamic ocean–atmosphere interaction characteristics should be considered. An atlas of the monthly mean sensible and latent heat fluxes, as well as some other parameters of the SOA that are typical for the global ocean, were collected during the period from July 1987 to December 1998 (Grassl et al. 2000). These results are based on satellite MCW and IR measurements. An analysis of the potential of satellite MCW

radiometric methods for studies of the SOA's heat interaction in tropical oceanic zones was introduced by E. Sharkov from the Institute of Space Research, Russian Academy of Sciences (Sharkov 1998, 2012).

However, there are problems with using a bulk-aerodynamic method for retrieving *synoptic* variations of heat and moisture vapor exchanges, which can change with *seasonal* variations. This can be explained using our own experience:

1. When moving from the seasonal to synoptic time scales, the relationship between air temperature and humidity in different atmospheric layers weakens; hence, we may conclude that the accuracy of the parameters t_a and e in formulas (1.1) and (1.2) will decreased due to the shortening of the time scale.
2. The role of factors such as wind speed in the near-surface atmosphere, atmospheric cloudiness, and rainfall (which have limited satellite estimates of the OST in principle) has become clearly apparent in the range of the *synoptic* time scales.
3. The ambiguity of the coefficients C_T and C_E denoted in (1.1) and (1.2) plays a more essential role in the synoptic time scales than the seasonal ones.

Some efforts were undertaken to solve these problems by modifying formulas (1.1)–(1.2). These modifications take into account the close correlation between the near-surface air humidity e and the atmospheric total (integral) water vapor content Q in the North Atlantic and Pacific oceans (Schulz et al. 1997), the parameters t_a and t_s in the Caspian Sea (Il`yin et al. 1986; Panin 1987), and the parameters t_a, e, and Q in the Newfoundland active zone of the North Atlantic (Grankov and Novichikhin 1997).

1.1.2   Alternative Approach

Another approach is based on using satellite MCW and IR radiometric measurements as the *direct* characteristics of the heat dynamic interactions between the ocean and atmosphere. This idea was first presented in Dymnikov et al. (1984), in which the requirements for satellite means were discussed from the point of view of the "RAZREZY" program in studies of the ocean–atmosphere heat balance, as well as in Eyre and Lorence (1989) with regard to weather forecasts. Also, Lapshin and Ragulin (1989) showed that the intensity of the SOA's natural MCW radiation (the brightness temperature) in the centimeter range of wavelengths can be considered as a *direct* characteristic of the intensity (rate) of exchanges between the ocean and atmosphere through the CO_2 component.

We think that it is appropriate to discuss the two concepts of using satellite MCW radiometric means and methods. In the first case, we consider the traditional approach to retrieve information on near-surface air humidity and temperature characteristics, as well as the OST and near-surface wind speed, which determine the ocean–atmosphere heat and dynamic interaction. This concept is more convenient and clear for oceanologists.

In another case, our method corresponds to that proposed by A.M Shutko and E.A. Reutov (Reutov and Shutko 1987; Reutov 1989), in which remote sensing data was used for geophysics parameters such as the near-surface air humidity, temperature, and wind speed, which are significant factors used in the bulk formulas. Following this principle, we can ignore the other factors in detail—the vertical distribution of these parameters, for example.

When solving this problem, we can determine the typical problems of the extraction (retrieving) some *partial* characteristics of the media state accepted by science and practice (e.g., near-surface air temperature, humidity, wind speed), as well as for the direct use of radiation characteristics such as intensity, scattering, and polarization electromagnetic properties of natural objects (oceans, basins, lands) for determining their state as a *whole*. The realization of these ideas was demonstrated in Reutov and Shutko (1987) and Reutov (1989), where it was shown that the SOA brightness temperature at centimeters and decimeters is closely attached to the so-called *radiation index of dryness* of the land. It is also possible to associate the brightness temperature measured from satellites with the intensity of large-scale ocean–atmosphere heat interactions in energy-active zones (EAZOs) (Grankov and Shutko 1992a; Grankov and Usov 1994) for the estimation of temporal and spatial variations of the total (sensible + latent) heat fluxes in the *synoptic* range of time scales (Grankov and Resnjanskii 1998; Grankov and Milshin 1999; Grankov et al. 1999a, b; Grankov et al. 2000, 2002), as well as for an analysis of the *multiyear* changeability of their monthly mean values in the middle and high latitudes of the North Atlantic (Grankov and Milshin 2001).

In our opinion, satellite MCW radiometric methods for the direct analysis of heat and moisture exchanges in the SOA interface should be based on the following principles:

1. The methods used must be based on the models of interrelationships between the radiation characteristics of the SOA and the boundary heat processes using a clear physical interpretation, which includes a minimal number of transit parameters; in other words, the simplest parameterizations of these relationships are preferable.
2. In a desirable and effective approach, the models will include oceanic and atmospheric parameters that are accessible for satellite's SOA remote sensing methods. It is very important that these parameters provide a strong response for the SOA's natural MCW and IR radiation in contrast to other parameters of the system.
3. The parameterizations used must be universal enough to accommodate different parts of the World Ocean for various seasons. Also, these approaches must be suitable for cyclonic and frontal zones. When the classic insight on ocean–atmosphere heat and moisture interchanges are effective, we use the *climatic* data, which are collected from satellite and vessel measurements.

Some studies have met these listed requirements. For example, Grankov and Usov (1994) illustrated the close relationship between seasonal variations of the monthly mean values of the SOA brightness temperature at the specific pieces (intervals) at microwaves and the air–sea temperature differences $\Delta t = t_s - t_a$, which is considered to be a key characteristic of heat and moisture interchange in the ocean–atmosphere interface (at least, in the middle and high latitudes of the World Ocean) (Shuleikin 1968; Nikolaev 1981). The results of regressions between the values of Δt (taken from the atlas of the climatic-mean hydrometeorological parameters for the Gulf Stream active zone) with their calculated MCW estimates show us that the value of the correlation coefficient r is about 0.92; the value of the root-mean-square (rms) discrepancy σ is about 0.6 °C. This approach demonstrates an evident advantage in comparison with the methods of the single determination of t_s and t_a and the calculation of their difference. Let us note that the accuracy of a single estimation of the monthly mean values of the OST (the parameter t_s) *only* is about 1 °C (see details in Chap. 3).

More possibilities for the direct use of satellite data measurements at microwaves demonstrates a method (Grankov and Shutko 1992a) for the analysis of the integral (averaged per year) vertical turbulent heat fluxes and their year-to-year variability. This approach is based on a method for the calculation of heat fluxes (Lappo et al. 1990), taking into account not only the monthly mean values of the parameters t_s and t_a (and their annual amplitudes) but also the estimations of the time shift between them. The method is more presentable if we draw the line (phase) trajectories in the form of the $t_s - t_a$ loops. The geometric characteristics of these loops such as the square, orientation, and their distinctions from the ideal (rectangular) form allow us to estimate annual heat fluxes in different regions of the World Ocean and to evaluate their interannual variability. The advantage of this procedure is its resistance to all kinds of measurement noises; the final estimates of the heat fluxes include not only some separate data of satellite measurements but also take into account the general (seasonal) tendencies. A similar approach is used in radio-engineering and radiolocation, when we operate at a low level in contrast with noise signals; in this case, besides the amplitude (intensity) of the signals measured, other properties (e.g., spectrum form, energy, and time delay) are actively used (Kharkevich 1962; Frenks 1969).

The effectiveness of the direct use of satellite MCW radiometric measurements for the analysis of heat and water exchanges in the SOA interface is also endorsed in the *synoptic* range of time scales. In this case, the satellite methods should be quite efficient in the cyclonic zones as well as in the hydrological and atmospheric frontal areas, where oceanologists cannot effectively use traditional methods and instrumentations. This approach was also examined for an analysis of the climatic variability of the monthly mean values of the parameters q_h, q_e, and q_{he} in the Gulf Stream, Newfoundland, and Norwegian EAZOs of the North Atlantic.

1.2 Parameters of Heat Interchange in the SOA, Which are Directly Determined by Satellite MCW Radiometry

1.2.1 History of Satellite MCW Radiometry Development

One can select only a row of SOA parameters that are directly accessible for satellite passive MCW radiometry. Here, we must emphasize the oceanic (sea) surface temperature and the near-surface wind speed, which play a significant role in forming the heat and dynamic processes in the SOA interface. We consider the task of retrieving these parameters from satellite MCW radiometric data to be important from both theoretical and practical points of view in studies of the ocean–atmosphere interaction.

This problem has been the focus of scientific specialists at leading research centers in Russia, such as the Moscow and Fryazino departments of the IRE RAS, the Research Institute of Radiophysics (Nizhnij Novgorod), the Institute of Atmospheric Physics RAS (Moscow), the Sevastopol Sea Hydrophysical Institute (Ukraine Academy of Sciences), the Institute of the Space Research RAS (Moscow), Voejkov`s Main Geophysical Observatory (St.-Petersburg, Hydrometeorological Service of the Russia), Shirshov`s Institute of Oceanology RAS (Moscow), and the Scientific Research Center for Exploration of Natural Research (Moscow, Russian Hydrometeorological Service).

The interest in these themes stimulated many monographs based on theoretical and experimental studies in Russia and abroad (Nikolaev and Pertshev 1964; Basharinov et al. 1974; Bogorodskii et al. 1977; Twomey 1977; Kondrat`ev and Timofeev 1978, 1979; Ulaby et al. 1981, 1982, 1986; Tsang et al. 1985; Nelepo et al. 1985; Shutko 1986; Kochergin and Timchenko 1987; Bychkova et al. 1988; Chavro 1990; Kondrat`ev et al. 1992; Raizer and Cherny 1994; Cherny and Raizer 1998; Sharkov 2007; Grankov and Milshin 2010; Armand and Polyakov 1985, 2005). An important contribution to the theory and practice of using satellite passive MCW radiometric methods was made by Sergey V. Pereslegin in his pioneer work (Pereslegin 1967), which was devoted to an analysis of the relationship of the oceanic surface temperature and the brightness temperature contrasts observed from satellites.

Here, we briefly review of some relationships between the ocean surface brightness temperature and its thermodynamic (kinetic) temperature, as well as near-surface wind speed.

1.2.2 Relationship Between Natural MCW Radiation and the Ocean Surface Temperature

The effectiveness of satellite passive MCW radiometric methods for determining the OST (except for the influence of the noise temperature [sensitivity] of radiometers, attenuations in feeders, directional patterns, etc.) depends on the sensitivity (q^t) of natural MCW radiation intensity (brightness temperature T^b) to variations of OST ($q^t = \Delta T^b / \Delta t_s$), as well as its resistance to variations of near-surface wind speed and atmospheric meteorological parameters. The main problem is the extraction of a component of the SOA brightness temperature related to the OST variations against a background of its variations caused by the water surface roughness and its foam cover, as well as the influence of the atmosphere's cloudiness and rainfall intensity (Basharinov et al. 1974; Shutko 1986; Grankov and Shutko 1992b).

The value of the parameter q^t reaches a maximum in the centimeter range of wavelengths (see Fig. 1.1). At the wavelength 8.5 cm, a close linear correlation between the SOA brightness temperature (measured from the Russian satellite Cosmos-243) and in situ OST estimates is observed (see Figs. 1.1 and 1.2).

Satellite estimates of OST are especially critical (sensible) to a water state excitable by the wind at the SOA boundary. There are two possible reasons:

(1) The roughness of the water surface causes the appreciable brightness temperature contrasts, which are comparable with those induced by the OST variations.
(2) The spectral distinctions between the OST and near-surface wind speed effects on the SOA brightness temperature at the centimeter range of wavelengths are quiet slight; their resolution will be possible by expanding the wavelength range from centimeters to millimeters—that is, by increasing the number of radiometric channels and losing the simplicity of the radiation model (Grankov and Shutko 1992b). Even in the first remote experiments conducted of the ocean from the satellites Cosmos-243 (1968), Cosmos-1076 (1979), Cosmos-1151 (1980), and Nimbus 5 (1979), four spectral channels operating in the centimeter and millimeter ranges of wavelengths were used.

Fig. 1.1 Sensitivity of the brightness temperature to OST variations calculated for values of the parameter t_s: 0, 10, 20, and 30 °C as function of wavelength (Grankov and Shutko 1980)
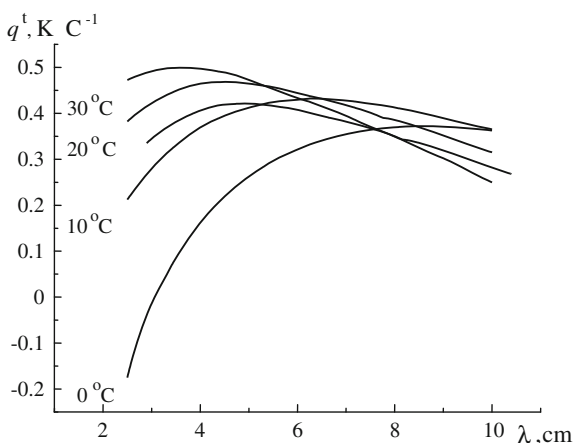
Fig. 1.2 Brightness
temperature variations
obtained from the satellite
Cosmos-243 at the
wavelength 8.5 cm, plotted as
a function of OST (Shutko
1986)
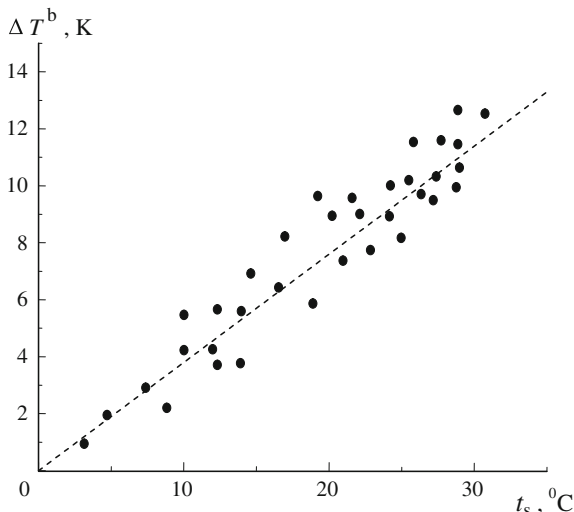
Even the early research on remote sensing displayed a close correlation between
the MCW radiation characteristics of the ocean surface and near-surface wind
speed. Some results of the systematization of experimental data obtained are
demonstrated in Figs. 1.3, 1.4, 1.5 and 1.6. Figure 1.3 shows the dispersion of the
sensitivity of the brightness temperature to near-surface wind speed variations
($q^v = \Delta T^b/\Delta V$) in the centimeter range of wavelengths, with an account of roughness
and the foam characteristics observed in different experiments.

Figure 1.4 shows the dispersion of the sensitivity of the coefficient of polar-
ization p to variations of parameter V in two subranges: $0 < V < 8$ m s^{-1} (without a
foam cover) and $8 < V < 25$ m s^{-1} (in the presence of foam). Let us note that the
polarization characteristics of MCW radiation give us additional information about
the ocean surface state. It follows from Fig. 1.4 that an account of such information
—at least at the wavelength of 3 cm for the angle of observation of 55°—gives 4–5
gradations of wind speed. Data obtained in this way may be used as some of the
basic values for the parameter V (similarly to averaged climatic data of the OST).

Figures 1.5 and 1.6 compare the brightness temperature contrasts ΔT^b measured
from satellite Cosmos-243 and their scattering with the wind speed V. These (or
similar) data are very important for determining the brightness temperature com-
ponent caused by OST variations of a rough water surface.

Fig. 1.3 Sensitivity of
brightness temperature to
wind speed variations as a
function of wavelength
(Grankov and Shutko 1980)

q^{v}, m/s

$$q^{\mathrm{v}} = \Delta T^{\mathrm{b}}/\Delta V$$

λ, cm
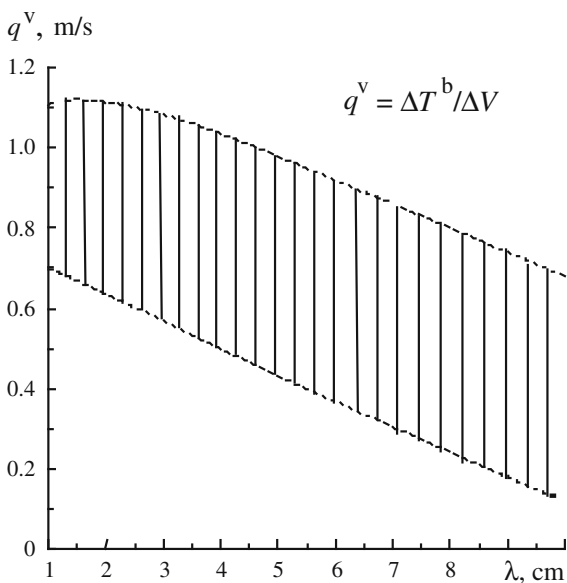
Fig. 1.4 Coefficient of
polarization at the
wavelengths 3.2–3.6 cm
under the angle of observation
of 55° as a function of wind
speed (Shutko 1986)

p

V, m s^{-1}
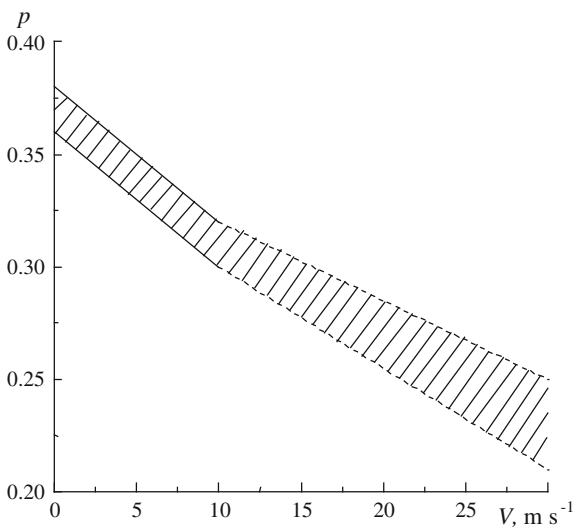
Fig. 1.5 Brightness temperature contrasts of the ocean surface at the wavelength of 8.5 cm observed in nadir from satellite Cosmos-243 as a function of wind speed (histogram in plan) (Shutko 1986)
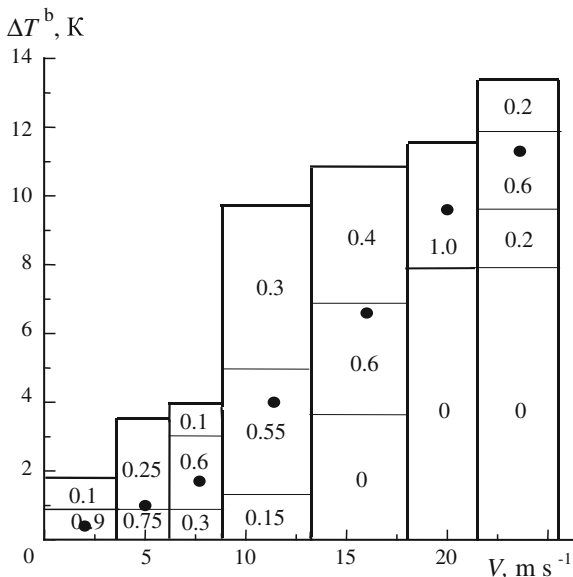
Fig. 1.6 Brightness temperature contrasts of the ocean surface observed from satellite Cosmos-243 at wavelengths of 0.8, 1.55, 3.4, and 8.5 cm as a function of wind speed (Matveev 1971)
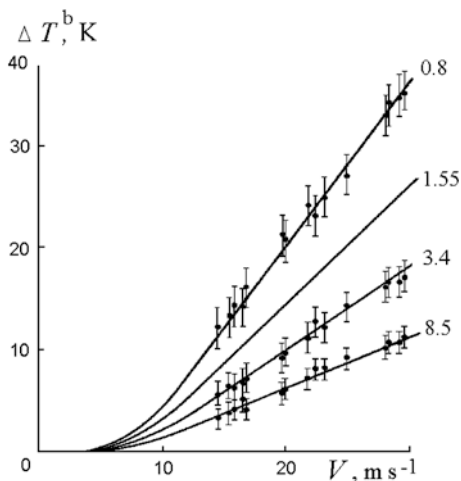
1.2.3 Estimating the Accuracy of Ocean Surface Temperature Determinations

In the 1960s and 1970s, a large number of investigations were devoted to the theoretical analysis of the accuracy of estimates of the OST derived from the data of satellite MCW radiometric measurements; one can find some results of these investigations in Basharinov et al. (1974), Wilheit (1978), Kondrat`ev and

Table 1.1 Root-mean-square errors of OST estimates under various weather conditions, °C

W, kg m^{-2}	V, m s^{-1}		
	$0 < V < 8$	$8 < V < 15$	$V > 15$
$0 < W < 0.2$	0.6 (0.5)	1 (0.1)	
$0.2 < W < 1$	0.8 (0.1)	1.2 °C (0.15)	
$W > 1$			1.2–2 (0.15)

Frequency is indicated in parentheses (Shutko 1986; Grankov and Shutko 1992b)

Timofeev (1979), Shutko and Grankov (1982), Nelepo et al. (1985), Shutko (1985), Robinson (1985), Bychkova et al. (1988).

Table 1.1 shows some estimates of potential accuracy of the OST determination with minimum *rms* error σ_T, which is accessible for satellite passive MCW radiometric methods in the centimeter wavelength range. Here, we take into account interfering factors such as the near-surface wind speed V and the integral liquid water content in the clouds W. The table shows that if the wind speed does not exceed the value 8 m s^{-1} (when the sea surface is free from foam) and water content in the clouds is less than 0.2 kg m^{-2} (a week cloudiness), the *rms* error of the OST determination reaches its margin, which is specified by the natural sensitivity of the SOA brightness temperature to OST variations. Only in this case can the satellite means provide a determination of OST with an accuracy that is acceptable to oceanologists.

The accuracy of the OST determination for more complicated weather conditions ($V > 8$ m s^{-1} and $W > 0.2$ kg m^{-2}) may increased 1.5–2 times in comparison with the data shown in Table 1.1 with the appropriate selection and averaging the results of *long-term* satellite MCW radiometric measurements. This conclusion is confirmed by results of calculations (see Fig. 1.7).

These results are in a good agreement with the data of spacious studies fulfilled at the Jet Propulsion Laboratory with the radiometers AVHRR, HIRS/MSU, and SMMR from the satellites NOAA, Seasat, and Nimbus 7 (Hofer and Njoku 1981;

Fig. 1.7 Estimates of OST errors σ_T for various time scales: mesometeorological (**I**), synoptic (**II**), and seasonal (**III**) (Grankov and Shutko 1992b)

Time scales of observations from satellite
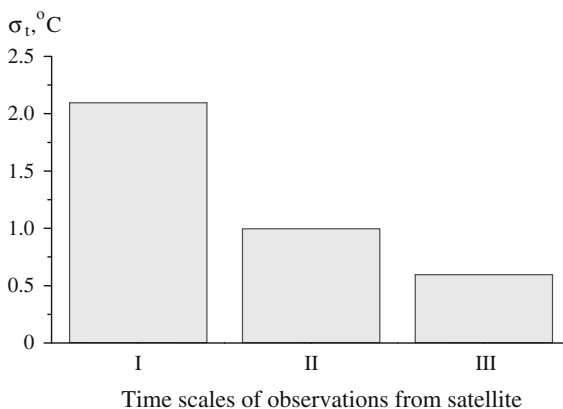
Table 1.2 Results of the comparison of satellite and vessel monthly OST averages in $2° \times 2°$ bins and the *rms* values of their differences (Bernstein and Chelton 1985), °C

Satellite sensor	November 1979	December 1981	March 1982	July 1982
AVHRR				
Mean value	0.19	−0.30	−0.36	−0.48
rms	0.61	0.58	0.62	0.92
Number of measurements	723	729	795	644
HIRS				
Mean value	−0.04	0.13	0.30	−0.07
rms	1.01	0.89	0.97	0.69
Number of measurements	735	729	795	662
SMMR				
Mean value	0.52	0.72	−0.21	−0.43
rms	1.37	1.37	1.13	1.06
Number of measurements	395	677	690	522

Njoku et al. 1985; Susskind and Reuter 1985; Bernstein and Chelton 1985; Hilland et al. 1985). We reproduced the results of these studies 30 years later because they manifested for oceanologists the completion of a whole era in understanding the potential of satellite MCW radiometry for ocean surface thermometry.

The effectiveness of satellite passive radiometric methods for OST determination with the radiometer SSMR (microwaves), AVHRR (infrared), and HIRS/MSU (microwaves and infrared) in climatologic studies of the ocean is summarized in Table 1.2. Bernstein and Chelton (1985) presented some important and edifying results related to the choice of the time intervals in a comparison of remotely sensed and in situ data obtained from different physical and geographical oceanic zones, as characterized by considerable variability and changeability of their meteorological and oceanographic parameters.

1.3 Potential of Satellite MCW Radiometric Methods for Determining Meteorological Parameters of the Near-Surface Atmosphere

1.3.1 Climatic and Seasonal Scales

As previously mentioned, the relationship between temperature and humidity characteristics in various atmosphere layers is the starting point for using the data of satellite passive radiometric methods for determining surface heat fluxes. From this point of view, the analysis of correlations between total water vapor content of the atmosphere Q and its near-surface parameters t_a and e in the ranges of seasonal, synoptic, and mesometeorological time scales is a required component of studies of

heat and moisture interchanges at the SOA interface from satellites. Some examples of such an analysis are based on the results of systematization of long-term oceanological, meteorological, and aerologic measurements (Snopkov 1977; Liu 1986; Hsu and Blanchard 1989; Grankov and Milshin 1994, 1995). In addition, recent results of satellite MCW and IR passive radiometric measurements can essentially supplement the data of direct meteorological and aerologic measurements when analyzing relationships between the atmosphere's total and near-surface humidity and temperature (Liu 1988; Schulz et al. 1993; Shibata and Konda 1996; Liu et al. 2003; Curry et al. 2004).

At least two circumstances denote the specific role of total water vapor of the atmosphere using parameter Q:

1. Parameter Q is closely related to the intensity of water vapor radiation in the resonant line 1.35 cm, whose variations are reliably measured from satellites.
2. A significant fraction of the total quantity of the heat of the SOA is concentrated in water vapor.

The premise for the joint analysis of the parameters e, t_a, and Q are the correlations between them, which are conditioned by the processes of *vertical* turbulent as well as *horizontal* (advective) heat and moisture transfer in the near-surface and boundary layers of the atmosphere.

The results of numerous experimental investigations (shipborne, satellite), which were performed in different regions of the ocean in limited time intervals (hours, days), show that the relationships between Q and e and between Q and t_a are not single-valued under these conditions. The reason is that the parameter Q is not determined only by e and t_a; rather, it is a sum of many factors, including wind speed, vertical stratification of the air temperature, and humidity.

More definite estimates of the relationships between water vapor content of the atmosphere and its near-surface temperature and humidity should be expected when they are significantly averaged in space and time, as indicated in Fig. 1.8.
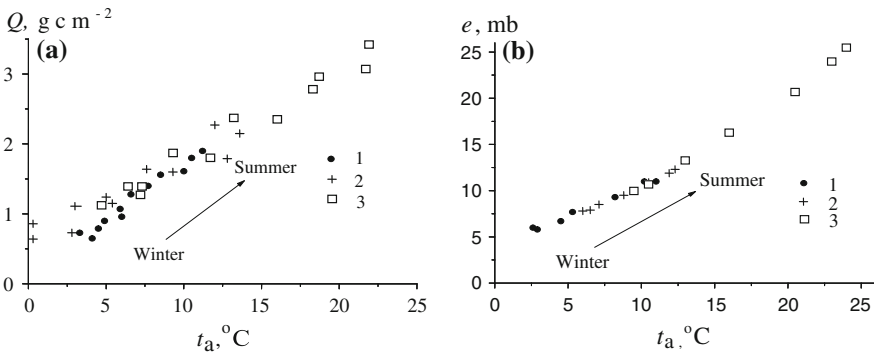
Fig. 1.8 Correlations between monthly mean parameters Q and t_a during the period of January–December (**a**) and the parameters e and t_a during the period of February–August (**b**) in the Norwegian (*1*), Newfoundland (*2*), and Gulf Stream (*3*) EAZOs

We analyzed the results of comparisons of monthly mean parameters e, Q, and t_a for their $5° \times 5°$ spatial averaging in some fragments of Norwegian, Newfoundland, and Gulf Stream EAZOs of the North Atlantic based on various climatic archives. The estimates of t_a were taken from Handbook (1977), Q estimates are from Tuller (1968), and e estimates are from Handbook (1979), Snopkov (1981), Timofeev (1979), Drozdov and Grigor`eva (1963).

We also examined to what extent the relationships between monthly means of the atmospheric water vapor and near-surface values of the air temperature and humidity could be stable (universal) if he different archival data on the parameters Q, e, and t_a are used. The result of this study confirmed our idea and experience that one can reduce the dispersion of the dependencies of $Q(t_a)$ and $Q(e)$ by operating not with the *absolute* but with *relative* values (variations) of these parameters (Grankov and Milshin 1994, 1995). Using the data accumulated in the Newfoundland EAZO for confirmation, we see that this approach is quite effective (Fig. 1.9).

Figure 1.9 shows that strong correlations between seasonal variations of the monthly mean parameters Q and t_a are obvious under these conditions, despite the diversity of initial archival data, the distinctions of observational means used, and the time and spatial scales of averaging the data.

In selected EAZOs, the relationships between the variations of the monthly mean values Q and t_a in the entire range of their variations are very strong. Changes of the $5°$ oceanic areas by 1–$2°$ in the chosen EAZOs has virtually no effect on the results of the comparison. It is remarkable that the slope of the regression dependence of ΔQ (Δt_a) is slightly varied in the middle latitudes of the North Atlantic from the value 0.1 in the Norwegian EAZO to 0.13 g cm^{-1} K^{-1} in the EAZO Gulf Stream.
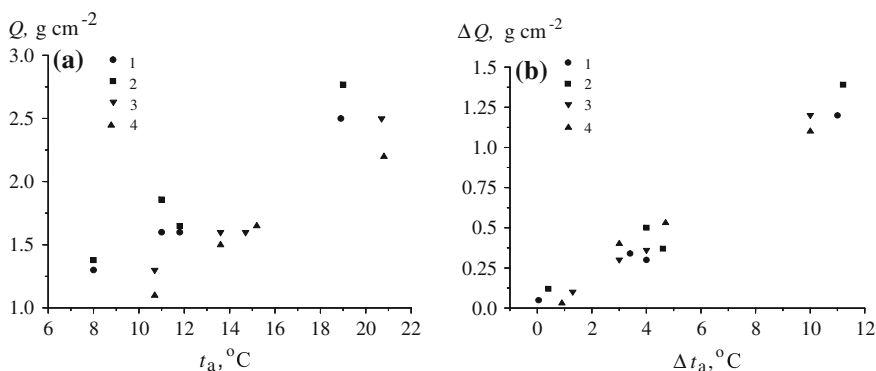
Fig. 1.9 Estimates of the relationship between monthly mean (*climatic*) values of the parameters Q and t_a (**a**) and their variations (**b**) during February, May, August, and November in the Newfoundland EAZO. Values were taken from the following sources: $1 - t_a$ and Q (Handbook 1977); $2 - t_a$ (Handbook 1977) and Q—(Snopkov 1981); $3 - t_a$ (Handbook 1977) and Q (Timofeev 1979); $4 - t_a$ (Handbook 1977) and Q (Drozdov and Grigor`eva 1963)
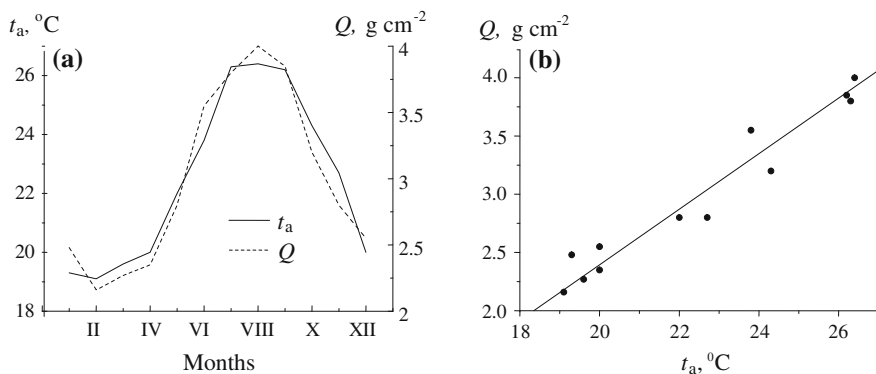
Fig. 1.10 Annual values of monthly mean water vapor of the atmosphere Q and its near-surface temperature t_a (**a**) in the island Midway in the Pacific ocean (28.2°N, 177.4°W); linear regression between them (**b**): Q—results of interpretation of the Nimbus 7 SMMR radiometer data (Liu 1988) averaged during the period 1980–1983 years, t_a—climatic data (Handbook 1977)

In the equatorial zones of the Pacific Ocean, this characteristic is more considerable (Fig. 1.10).

We analyzed the interannual variability of the regressions between the monthly mean values of the atmospheric water vapor and its near-surface temperature and humidity using meteorological and aerologic measurements from the Pacific island station St. Paul (52.7°N, 170.2°W) during the period 1964–1974 (Liu 1988). The results of analyzing these data demonstrate a steadiness of the dependences $\Delta Q/\Delta e$ and $\Delta Q/\Delta t_a$ (see Table 1.3), where the variation coefficients are 9.4 and 13.6 %, respectively.

In general, results from the analysis and systematization of long-term data show that the correlation of monthly mean values Q, e, and t_a is stable in the wide range of their variations ($0.5 < Q < 4.5$ g cm^{-2}, $5 < e < 30$ mb, $0 < t_a < 30$ °C). The results obtained illustrate clearly the general regularities of seasonal variations of the monthly mean parameters Q, e, and t_a. At the same time, they demonstrate some individual features of the dependencies $Q(e)$, and $Q(t_a)$, as well as the dependence e (t_a) in different physical and geographical zones of the North Atlantic and the Pacific Ocean.

Table 1.3 Interannual variability of the slope of regressional relationships $\Delta Q/\Delta e$ and $\Delta Q/\Delta t_a$ observed by the island meteorological station St. Paul in the Pacific Ocean

Years	1964	1965	1966	1967	1968	1969	1970	1971	1972	1973	1974
$\Delta Q/\Delta e$	0.16	0.19	0.14	0.18	0.15	0.17	0.16	0.17	0.20	0.15	0.15
$\Delta Q/\Delta t_a$	0.17	0.13	0.13	0.15	0.13	0.18	0.13	0.14	0.18	0.13	0.13

1.3.2 Synoptic Scales

Results of the experiments NEWFOUEX-88 (November 1987–April 1988) and
ATLANTEX-90 (November 1989–June 1990) on the observation of the ocean–
atmosphere interaction in the Newfoundland EAZO give us much information that
is useful for studies of the relationships between synoptic variations of the
parameters Q, e, and t_a in the middle latitudes.

   We extracted from these archives the data obtained from the research vessels
(R/Vs) *Victor Bugaev*, *Musson*, and *Volna* in the stationary phases of these
experiments (March 1988 and April 1990), when the vessels were immovable. The
initial data in each case included the following:

 (a) More than 2000 meteorological measurements in the near-surface atmosphere
     with a 1-h time resolution.
 (b) More than 400 aerologic measurements in the interval of heights 10–16,000 m
     (at 20 levels) with a 6-h time resolution.
 (c) More than 2000 measurements of the water vapor content with 15- to 20-min
     resolution obtained from the ship-boarding MCW radiometers at the 1.35 and
     0.8 cm wavelengths (R/V *Volna*) in the experiment ATLANTEX-90.

   These measurements show that the correlation between synoptic variations of the
atmospheric total water vapor obtained from aerologic measurements and the
variations of the near-surface air determined directly from meteorological mea-
surements is very strong (see Fig. 1.11 as an example).

   The analysis of relationships between the atmosphere water vapor and its
near-surface temperature and humidity within the mesometeorological time scales
(hours, days) is very important in two aspects:

1. An understanding and interpretation of these processes at the synoptic and
   seasonal time scales.

Fig. 1.11 Correlations of the daily parameters e, t_a, and Q observed at the stationary phase of the experiment NEWFOUEX-88 (R/V *Musson*)
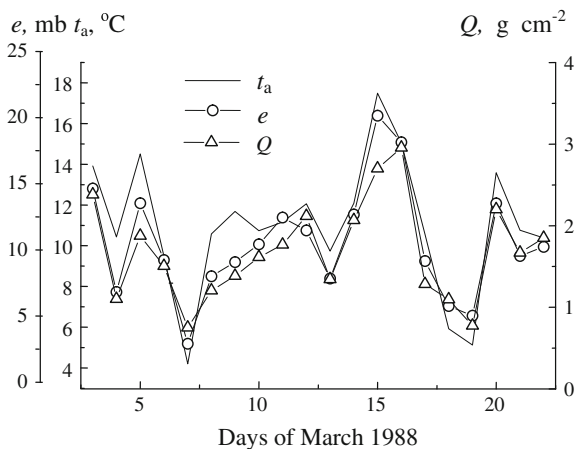
2. Estimating the possibilities of using the parameter Q, which is easily accessible for satellite MCW radiometric means, as the reliable criterion for estimating not only seasonal but also more dynamic (short-period) values of the parameters e and t_a.

Based on these ideas, we used the data accumulated in the stationary phases of the experiments ATLANTEX-90 and NEWFOUEX-88 for an analysis of the relationships between the mesometeorological variations of the parameters Q, e, and t_a, which vary intensively in the ocean (especiall, during the passage of the cyclones). Some results of this analysis are presented in Fig. 1.12, where the results of the comparison of the $1-h$ readings of the parameters e, t_a, and $6-h$ indications of the parameter Q are illustrated.

Results of the analysis show that the relationships between the atmosphere's water vapor and its near-surface temperature and humidity are developed on a daily interval. One can see the following peculiarities. First, a close correlation exists between the parameters e and t_a in the atmosphere's near-surface layer. These regularities conform to the rules of an ideal gas. Also, under the influence of energetic (cyclonic) processes of tuning the atmosphere, variations of the parameter Q often follow variations of the parameters e, t_a with a time lag of a few hours (Grankov and Milshin 1995, Grankov and Novichikhin 1997).

The atmosphere's horizontal circulation plays an important role in forming the vertical distribution of the air temperature and humidity, which strongly influences the temperature and humidity characteristics of its near-surface and boundary layers. This rule becomes apparent for the middle latitudes of the North Atlantic, especially in the periods of cyclonic activity in the atmosphere. This reason is confirmed in Fig. 1.13, which shows the data from the aerologic sounding of the atmosphere from the R/V *Victor Bugaev* during the experiment ATLANTEX-90.

Table 1.4 demonstrates some results of the correlation analysis of the aerologic measurement data.
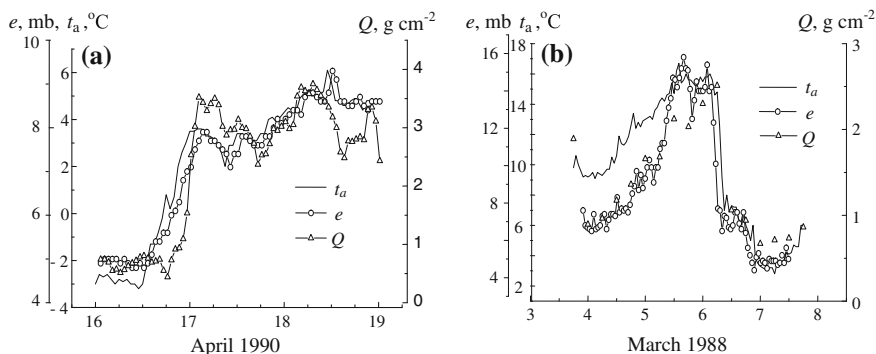
Fig. 1.12 Comparison between daily variations of the parameters e, t_a, and Q: (**a**) ATLANTEX-90 (R/V *Volna*, April 16–19, 1990); (**b**) NEWFOUEX-88 (R/V *Musson*, March 3–8, 1988)
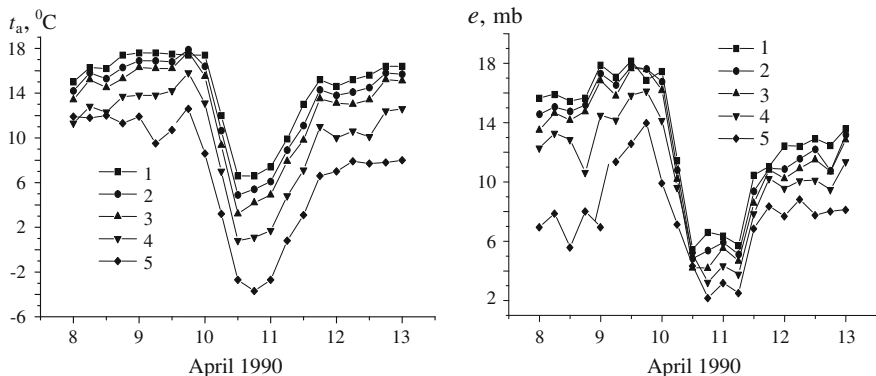
Fig. 1.13 Variations of the temperature t_a and humidity e in the atmosphere's boundary layer during the passage of a powerful cyclone for the point of the location of the R/V *Victor Bugaev* at the following horizons: 1–10, 2–100, 3–200, 4–500, 5–1000 m

Table 1.4 Correlation of the air temperature t_a and humidity e for various horizons of the atmosphere boundary layer

h, m	10	100	200	500	1000
10	1	0.993	0.988	0.968	0.788
100	0.995	1	0.998	0.979	0.812
200	0.990	0.999	1	0.982	0.827
500	0.988	0.996	0.996	1	0.857
1000	0.948	0.954	0.953	0.962	1
Near-surface air temperature			Near-surface air humidity		

However, such cooperativeness in the variations of the air temperature and humidity at various horizons can be disturbed due to the appearance of inversions in the vertical distribution of these parameters in the atmosphere.

Figure 1.14 illustrates variations of the humidity of the atmosphere for its different layers on April 12, 1990 with 6-h resolution.

As seen from the illustration, the lifetime of an inversion in this case in no way exceeded 12 h; more certain estimates are difficult because the periodicity of the aerologic soundings from vessels is 6 h. This phenomenon was observed for the stationary phases of the experiments ATLANTEX-90 and NEWFOUEX-88, but not frequently—some tens advents in hundreds aerologic soundings.

1.4   Conclusion

Satellite-derived data of passive MCW radiometric measurements have the potential to evaluate parameters of the ocean–atmosphere system (SOA), which are important for the analysis of heat processes in its interface. In particular, the brightness
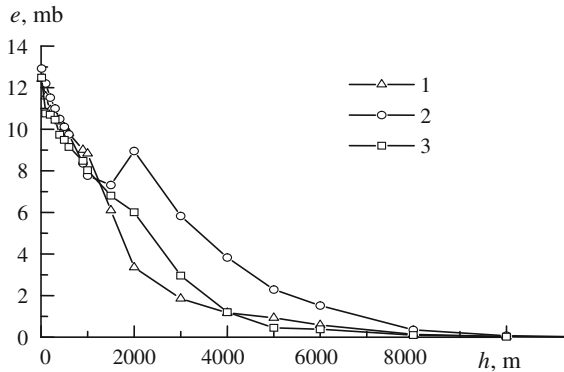
Fig. 1.14 Results of upper-air sounding of the atmospheric water vapor pressure *e* at various horizons *h* from the R/V *V. Bugaev* in the experiment ATLANTEX-90: *1*: 6 h; *2*: 12 h; *3*: 18 h

temperature of the SOA is directly connected with the water surface temperature and near-surface wind speed, which are key parameters in the formulas used for the computation of heat and water vertical turbulent fluxes at the SOA boundary (bulk formulas). Other parameters assimilated with the surface heat fluxes, such as the near-surface air temperature and humidity, only indirectly influence the characteristics of natural MCW radiation of the SOA. In areas of the North Atlantic, the total water vapor of the atmosphere, which is easily accessible for satellite MCW radiometric means, can serve as the quantitative indicator of these parameters for a wide range of time scales. Another approach is based on direct use of the SOA brightness temperature in selected spectral bands for retrieving surface heat fluxes. The possibilities of both techniques will be analyzed in the next chapters.

References

Ariel NZ et al (1973) On calculation of month mean values of heat and moisture heat over the ocean. Meterorolologiya and Gidrologiya 5:3 − 11 In Russian

Armand NA, Polyakov VM (2005) Radio propagation and remote sensing of the environment. CRC Press LLC, Roca Raton

Basharinov AE, Gurvich AS, Egorov ST (1974) Radio emission of the planet Earth. Nauka, Moscow In Russian

Bernstein RL Chelton DB (1985) Large-scale sea surface temperature variability from satellite and shipboard measurements. J Geophys Res C6:11.619 − 11.630

Bogorodskii VV, Kozlov AI, Tuchkov LT (1977) Radiothermal emission of the Earth`s covers Gidrometeoizdat, Leningrad In Russian

Bychkova IA, Victorov SV, Vinogradov VV (1988) Remote sensing of sea temperature. Gidrometeoizdat, Leningrad In Russian

Chavro AI (1990) Physical base and the methods of the sea surface determination from satellites. OVM AN USSR, Moscow In Russian

Cherny IV, Raizer VYu (1998) Passive microwave remote sensing of oceans. Wiley, UK

Curry JA, Bentamy A, Bourassa MA et al (2004) Satellite-based datasets of surface turbulent fluxes over the global oceans (SEAFLUXE Project)

Drozdov OA, Grigor`eva AS (1963) Water vapor exchanges in the atmosphere. Gidrometeoizdat, Leningrad In Russian

Dymnikov VP, Korotaev GK, Galin VYa (1984) Atmosphere, Ocean, Space -"Razrezy" Program, VINITI, Moscow In Russian

Esbensen SK, Reynolds RW (1981) Estimating monthly averaged air-sea transfers of heat and momentum using the bulk aerodynamic method. J Phys Oceanogr 11:457 − 465

Eyre JR, Lorence AC (1989) Direct use of satellite sounding radiances in numerical weather prediction. Meteorolog Magaz 118:13 − 16

Frenks LE (1969) Signal theory. Prentice-Hall, N.Y.

Gaikovich KP et al (1987) Determination of the temperature profile in the water surface layer with microwave radiometric measurements. Fizika Atmosfery i Okeana 23:761 − 768 In Russian

Grankov AG, Shutko AM (1980) Assesment of the effectiveness of estimates of parameters of the sea surface and the atmosphere. Radiotekhnika 35:38 − 41 In Russian

Grankov AG, Shutko AM (1992a) Use of remote radiophysical methods to determine the role of energy-active zones of the ocean in the development of the weather on the continents. Sov J Remote Sensing 9:926 − 941

Grankov AG, Shutko AM (1992b) Accuracy of estimates of the surface temperature and its variations using spectral techniques of satellite microwave radiometry. Sov J Remote Sensing 10:169 − 198

Grankov AG, Usov PP (1994) Intercommunication between monthly mean ai − sea temperature differences and natural microwave and infrared radiation. Meteorologiya i Gidrologiya 6:79 − 89 In Russian

Grankov AG, Milshin AA (1994) On correlation of the near-surface and total atmosphere humidity with the near-surface air temperature. Meteorologiya i Gidrologiya 10:79 − 81 In Russian

Grankov AG, Milshin AA (1995) A study of intercorrelation between thermodinamical parameters of the atmosphere for validating satellite MCW and IR-radiometric methods of determining its near-surface temperature. Institute of Radioengineering and Electronics RAS Preprint No. 3 (603), Fryazino In Russian

Grankov AG, Milshin AA (1999) Interrelation between the microwave radiation of the ocean-atmosphere system and the boundary heat and momentum fluxes. Izvestiya, Atmospheric and Oceanic Physics 35:570 − 577

Grankov AG, Novichikhin EP (1997) Formulas oh heat and moisture exchange between ocean and atmosphere used in radiometric satellite data assimilation. Russian Meteorology and Hydrology, Allerton Press 1:81 − 90

Grankov AG, Resnjanskii JuD (1998) Modeling the response of the ocean-atmosphere natural radiation system to the pertrubation of a thermal equilibrium at the interface. Russian Meteorology and Hydrology, Allerton Press 11:57 − 65

Grankov AG, Milshin AA, Petrenko BZ (1999a) Natural radiothermal radiation as a characteristic of seasonal and synoptic variation at the ocean-atmosphere heat interfaces. Doklady Earth Sciences 367A:839 − 842

Grankov AG, Gulev SK, Milshin AA, Shelobanova NK (1999b) Experimental studies of the ocean-atmosphere brightness temperature as a function of near-surface heat and impulse exchanges in the range of synoptic time scales. Issledovanie Zemli iz kosmosa 6:3 − 7 In Russian

Grankov AG, Milshin AA, Novichikhin EP (2000) Interconnection between the brightness temperature and the intensity of the thermal ocean-atmosphere interaction (Based on the data Atlantex-90 experiment). Earth Obs Rem Sens 16:457 − 467

Grankov AG, Milshin AA (2001) Evaluation of usefulness of the SSM/I data for study of climatic parameters of the ocean and atmosphere in the North Atlantic. Issledovanie Zemli iz kosmosa 5:70 − 78 In Russsian

Grankov AA, Milshin AA, Shelobanova NK (2002) Specific features of the subpolar hydrological front from microwave radiometric satellite data. Russian Meteorology and Hydrology, Allerton Press 8: 34 − 40

Grankov AG, Milshin AA (2010) Microwave radiation of the ocean-atmosphere: boundary heat and dynamic interaction. Springer Dordrecht Heidelberg London New Jork

Grassl H, Jost V, Schulz J et al (2000) The Hamburg ocean-atmosphere parameters and fluxes from satellite data (HOAPS): A climatological atlas of satellite-derived air-sea interaction parameters over the world oceans. Report No. 312. MPI, Hamburg

Grishin GA, Lebedev NE (1990) Use of IR data from satellites for monitoring the ocean and atmosphere: state of the problem. Issledovanie Zemli iz kosmosa 6:97 − 104 In Russian

Handbook (1979) Averaged month, 10 and 5-day periods values of the air water and temperature, their difference and wind speed in selected regions of the North Atlantic (1953 − 1974 years). VNII GMI, Obninsk In Russian

Gulev SK (1991) Effects of spatial and temporal averaging in estimating of energy exchange parameters between ocean and atmosphere. Fizika Atmosphery i Okeana 27:204 − 213 In Russian

Handbook (1977) Atlas of the oceans: Atlantic and Indian oceans. MO SSSR, Moscow In Russian

Hilland JE, Chelton DB, Njoku EG (1985) Production of global sea surface temperature fields for the Jet Propulsion Laboratory workshop comparisons. J Geophys Res 1985 90: 11.642 − 11.650

Hofer R, Njoku EG (1981), Waters JW. Microwave radiometric measurements of see surface temperature from the SEASAT satellite: First results. Science 212:1385 − 1387

Hsu SA, Blanchard BW (1989) The relationship between total precipitable water and surface-level humidity over the sea surface: a further evaluation. J Geophys Res 94:14539 − 14.545

Il`yin YuA., Kuznetsov AA., Malinnikov VA (1986) On the method of remote sensing of heat fluxes at the boundary of the system ocean-atmosphere, Izvestiya VUZov 6:117 − 120 In Russian

Ivanov A (1978) Introduction to Oceanography. Mir, Moscow In Russian

Kharkevich AA (1962) Spectrums and analysis. GIFML, Moscow In Russian

Khundzhua GG, Andreev EG (1973) On determination of heat and water vapor fluxes in the ocean-atmosphere system from measurements of the temperature profile in a thin water layer. Doklady Akademii Nauk SSSR 208 :841 − 843 In Russian

Kondrat`ev KYa, Timofeev YuM (1978) Meteorological probing of atmosphere from space. Gidrometeoizdat, Leningrad In Russian

Kondrat`ev KYa, Timofeev YuM (1979) Meteorological sensing of underlying surface from space. Gidrometeoizdat, Leningrad In Russian

Kochergin VP, Timchenko IE (1987) Monitoring the hydrophysical fields of the ocean. Gidrometeoizdat, Leningrad In Russian

Kondrat`ev KJa, Melent`ev VV, Nazarkin VA (1992) Remote sensing of waterareas (Microwave methods). Gidrometeoizdat, S.-Petersburg In Russian

Lappo SS, Gulev SK, Rozhdestvenskii AE (1990) Large-scale heat interaction in the ocean–atmosphere system and energy-active zones in the world ocean. Gidrometeoizdat, Leningrad In Russian

Lapshin VB, Ragulin IG (1989) The rate of air-sea gas exchange from microwave radiometric measurements, Meteorologiay i Gidrologiya 3:113 − 115 In Russian

Larin DA (1984) On calculations of heat and moisture fluxes with averaged values of meteoparameters. Trudy VNIIGMI MCD, Obninsk 110:87 − 93 In Russian

Liu WT (1986) Statistical relations between monthly mean precipitable water and surface-level humidity over global oceans. Mon Wea Rev 114:1591 − 1602

Liu WT (1988) Moisture and latent flux variabilities in the tropical Pacific derived from satellite data. J Geophys Res 93:6749 − 6760

Liu WT (1995) Satellite remote sensing of ocean surface forcing and response, COSPAR Colloq., Taipei, 15B2-1-15B2-3

Liu C-C, Liu G-R, Chen W-J, Yuang H-Y (2003) Modified Bowen ratio method in near-sea-surface air temperature estimation by using satellite data. IEEE Trans Geosci Remote Sensing 41:1025 − 1033

Matveev DT (1971) On the microwave spectrum emission of the rough sea surface. Fizika Atmosfery i Okeana 7:1070 − 1076 In Russian

Mitnik LM (1979) Possibilities of remote sensing the temperature of a thin oceanic layer. Fizika Atmosfery i Okeana 15:344 − 347 In Russian

Nelepo BA, Korotaev GK, Suetin VS, Terekhin JuV (1985) Research of the ocean from space. Naukova Dumka, Kiev In Russian

Nikolaev AG, Pertshev SV (1964) Passive radiolocation. Sovetskoe radio, Moscow In Russian

Nikolaev JuV. (1981) The role of the large-scale interaction of the ocean and the atmosphere in the development of weather anomalies. Gidrometeizdat, Leningrad In Russian

Njoku EG, Barnett TP., Laurs RM, Vastano AC (1985) Advances in satellite sea surface temperature measurement and oceanographic applications. J Geophys Res 90:11.573 − 11.586

Panin GN (1987) Evaporation and heat exchange over the Caspian Sea. Nauka, Moscow In Russian

Pereslegin SV (1967) On relations between thermal and radiobrightness contrasts of the sea surface. Fizika Atmosfery i Okeana 3:47 − 51 In Russian

Raizer VJu, Cherny IV (1994) Diagnostics of the ocean surface layer at microwaves. Gidrometeoizdat, S.-Petersburg In Russian

Reutov EA, Shutko AM (1987) On correlation of radiobrightness temperature with the radiative index of dryness. Issledovanie Zemli iz kosmosa 6:42 − 48 In Russian

Reutov EA (1989) On intercorrelation of microwave and IR radiation of natural objects with their state. Issledovanie Zemli iz kosmosa 1:70 − 76 In Russian

Robinson IS (1985) Satellite oceanography. An introduction for oceanographers and remote sensing scientists. Ellis Horwood Series Marine Science, Chichester

Schulz J, Mejwerk J, Ewald S, Schlussel P (1997) Evaluation of satellite-derived latent heat fluxes. J Climate10:2782 − 2795

Schulz J, Schluessel P., Grassl H (1993) Water vapor in the atmospheric boundary layer over oceans from SSM/I measurements. Int J Remote Sensing 14:2773 − 2789

Sharkov EA (1978) On use of thermal microwave system for investigation heat interchanges in a transient layer at the ocean-atmosphere boundary. Radiotekhnika i Elektronika 23:656 − 658 In Russian

Sharkov EA (1998) Remote sensing of tropical regions. J. Wiley & Sons/ PRAXIS, N.Y.

Sharkov EA (2012) Global Tropical Cyclogenesis The 2nd Edidtion. B., Heidelberg, L., N.Y. etc: Springer/PRAXIS

Sharkov EA (2007) Breaking Ocean Waves Springer/PRAXIS. Berlin, Heidelberg, London, N. Y.

Shibata A, Konda MN (1996) A new method to determine near-sea surface air temperature by using satellite data. J Geophys Res 101:14,349 − 14,360

Shuleikin VV (1968) Physics of the sea. Nauka, Moscow In Russian

Shutko AM, Grankov AG (1982) Some pequliarities of formulation and solution of inverse problems in microwave radiometry of the ocean surface and atmosphere. IEEE J Oceanic Eng OE-7:40 − 43

Shutko AM (1985) The status of the passive microwave sensing of the waters – lakes, seas, and oceans – under the variation of their state, temperature, and mineralization (salinity): models, experiments, examples of application. IEEE J Ocean Eng OE-10:418 − 435

Shutko AM (1986) Microwave radiometry of water surface and soils. Science, Moscow In Russian

Snopkov VG (1977) On correlation between the atmosphere water vapor and the near surface humidity seasonal variations of the water vapor content over the Atlantic. Meteorologiya i Gidrologiya 12:38 − 42 In Russian

Snopkov VG (1981) On seasonal variations of the water vapor content over the Atlantic. In: Atmosphere circulation and its interaction with the ocean in the tropical and subtropical latitudes of the Atlantic Nauka, Moscow In Russian

Susskind J, Reuter D (1985) Retrieval of sea surface temperatures from HIRS/MSU. J Geophys Res 90:11.602 − 11.608

Taylor PK (1984) The determination of surface fluxes of heat and water by satellite radiometry and in situ measurements. In: Gautier C and Fleux M (ed) Large-Scale Oceanographic Experiments and Satellites. Dordrecht, Reidel 223–246

Timofeev NA (1979) On vertical distribution of the air humidity and the atmosphere water content over the oceans. Meteorologiya and Gidrologiya 8:55 − 62 In Russian

Tsang L, Kong JA, Shin RT (1985) Theory of microwave remote sensing. Wiley-Interscience, N.Y.

Tuller ST (1968) World distribution of mean monthly and annual precipitable water. Mon Wea Rev 96:785 − 797

Twomey S (1977) Introduction to the mathematics of inversion in remote sensing and indirect measurements. Elsevier Sci. Publ., Amsterdam

Ulaby FT, Moor RK, Fung AK (1981, 1982, 1986) Microwave remote sensing. Addison-Wesley Pube, N.Y.

Wilheit TT (1978) A review of applications of microwave radiometry to oceanography. Boundary-Layer Meteorol 13: 277 − 293

Chapter 2
Modeling the SOA'S MCW and IR Radiation Characteristics and Their Relationship with Surface Heat Fluxes at Synoptic Time Scales

2.1 Modeling the SOA's Brightness Temperature with ATLANTEX-90 Vessel Experiment Data

2.1.1 Description of the Initial Data

This study used the results of the ATLANTEX-90 experiment obtained from the R/Vs *Victor Bugaev*, *Musson*, and *Volna*, which completed the final phase of the "RAZREZY" scientific project on large-scale ocean–atmosphere heat and dynamic interactions in the North Atlantic energy active zones. From this experiment, we extracted data that were obtained during the so-called stationary phase (April 4–21, 1990), which had the following features:

(a) Maximum regularity of the meteorological and, especially, aerologic measurements during this period
(b) Possibility of a fine analysis of the temporal dynamics of the oceanic and atmospheric parameters due to the fixed (stationary) positions of the R/Vs *Victor Bugaev*, *Musson*, and *Volna*

The research vessels were situated in three areas of the Gulf Stream delta: a southern periphery of the basic Gulf Stream water flow (R/V *Victor Bugaev*), its southern stream (R/V *Musson*), and an eastern branch of the Labrador Current (R/V *Volna*). This zone is characterized by strong synoptic variability in oceanic and atmospheric parameters, which is caused by an influence of the subpolar hydrological front (SHF) as a result of the interaction between the cold Labrador Current and the warm quasi-stationary anticyclon rings of the Gulf Stream. An important attribute of this zone is the intensive horizontal circulation of the atmosphere: For approximately 50 % of the time, this area of the North Atlantic feels the influence of powerful midlatitude cyclones, which excite intensive variations of the atmospheric temperature and humidity as well as boundary heat fluxes (Lappo et al. 1990).

The following parameters in each vessel experiment were selected for further analysis:

(1) Hourly values of the ocean surface temperature t_s, near-surface air temperature t_a and humidity (vapor pressure) e, and wind speed V derived from hydrological and meteorological measurements (more than 1000 measurements with 1-h resolution)
(2) Results of aerologic measurements of the total atmospheric water vapor content Q within 10–16,000 m at 20 levels with periodicity 6 h (more than 200 aerologic measurements)
(3) Hourly estimates of turbulent heat fluxes q_h and vapor q_e parameterized from hourly measurements of the parameters t_s, t_a, V and e

A fragment of the stationary phase of the ATLANTEX-90 experiment (from April 8–13, 1990) was analyzed in detail. In this period, all vessel oceanographic and meteorological sensors responded synchronously to a powerful cyclone in this area of the North Atlantic.

2.1.2　Model of the SOA's Natural Radiation with Microwaves and Infrareds

Satellite measurements of the intensity of natural MCW radiation (at millimeters and centimeters) are the result of a composition of oceanic and atmospheric vertical electromagnetic fluxes and their couplings. Therefore, we ought to consider these mediums together as the ocean−atmosphere system (SOA).

To calculate the SOA's natural radiation intensity for microwaves and infrareds using vessel measurement data, a model is required to assimilate oceanographic and meteorological parameters, as well as data on the vertical distribution of the air temperature, humidity, and pressure obtained from aerologic measurements.

Here, we use the plane-layer model of natural radiation (Basharinov et al. 1974). This model uses observations from altitude H for the intensity of radiation of the SOA I, which is the sum of three components:

$$I = I_1 + I_2 + I_3 \qquad (2.1)$$

where

$$I_1 = I_s \exp(-\tau) \qquad (2.2)$$

which is the intensity of upward radiation flux from the water (oceanic) surface I_s attenuated in the atmosphere. The quantity I_s is proportional to the emissivity of the water surface and its thermodynamic temperature T_s ($T_s = t_s + 273$).

$$I_2 = \int_0^H I_a(h) \, \exp[\tau(h) - \tau(H)] \mathrm{d}h \tag{2.3}$$

which is the intensity of the upward atmosphere radiation flux. This is computed by summing the partial fluxes $I_a(h)$, taking into account the proper attenuation values of the atmosphere layers.

$$I_3 = \exp[-\tau(H)] \, R \int_0^H I_a(h) \, \exp[-\tau(h)] \mathrm{d}h \tag{2.4}$$

which is the intensity of the atmosphere's downward radiation flux reflected by the water surface.

$$\tau(h) = \int_0^h \gamma(h') \, \mathrm{d}h' \tag{2.5}$$

is the integral attenuation of the radiation by the atmosphere, which depends on the linear absorption factor γ and the thickness h of the absorbing layer measured from the ocean surface ($h = 0$); R is the coefficient of reflection of the atmosphere's downward radiation flux from the water surface.

The intensity of natural MCW and IR radiation I_s of the water surface is proportional to the following:

At microwaves	At infrareds
$I_s = \acute{æ} \, T_s$;	$I_s = B(T_s)$,

where I_s (h) is the intensity of the water surface's upward radiation; $\acute{æ}$ is the water surface emissivity at microwaves; and $B(T_s)$ is the Plank function with the argument T_s.

The intensity of the atmosphere's MCW and IR natural radiation I at level h is determined as follows:

At microwaves	At infrareds
$I_a(h) = T_a(h) \, \gamma \, (h)$;	$I_a(h) = B[T_a(h)] \, \gamma(h)$,

where $T_a(h)$ is the thermodynamic temperature of the atmosphere at the level h in Kelvins (T_a $(h) = t_a$ $(h) + 273$). $B[T_a(h)]$ is the Plank function with the argument T_a (h).

In the MCW range of wavelengths, where the Rayleigh–Jeens approximation is valid, respective values of the brightness temperature are used as a measure of the radiation intensity of different components of the SOA. To characterize the IR radiation intensity I, we use the concept of effective (radiation) temperature T^r, defining it from the equation $B(T^r)$—that is, as a thermodynamic temperature of the absolute (ideal) black body with a radiation intensity equal to I.

2.2   SOA Brightness Temperature Contrasts and Their Comparison with Heat Fluxes

2.2.1   Calculations of SOA Brightness Temperature at Microwaves

Here, we use the model (2.1)−(2.5) to analyze daily and synoptic variations of SOA brightness temperatures in the wavelength range of 0.5–5.0 cm for the stationary phases of the ATLANTEX-90 experiment in the areas of the *Victor Bugaev*, *Musson*, and *Volna* vessels. The water surface's brightness temperature T^b was calculated according to the principles stated in Basharinov et al. (1974). The numerical estimates of the linear absorption factor γ were obtained by taking into account the dominating role of the atmosphere's water vapor and molecular oxygen using the theoretical relations of the absorption factor γ with the air temperature, humidity, and pressure; the computations of the SOA's brightness temperature were made for the case of a cloudless atmosphere.

The response of the SOA's natural MCW radiation to the variability of heat fluxes at the ocean–atmosphere interface was the most distinct during April 8−13, 1990, when a powerful cyclone occurred. Over this period, variations of the total (sensible + latent) heat fluxes were more than 800 W m^{-2} for the *Victor Bugaev*, 500 W m^{-2} for the *Musson*, and about 400 W m^{-2} for the *Volna* (Gulev et al. 1994). Among the spectral ranges used to calculate the SOA brightness temperature (5.4, 5.6, 5.9 mm, 0.8, 1.0, 1.35, 1.6, 3.2, and 5.0 cm), the brightness temperature contrasts over this time interval were greatest in the wavelength range of 0.59 −1.6 cm, which corresponds to the resonant effect of the atmospheric oxygen and water vapor on the upward radiation (Fig. 2.1).

The attenuation band of natural radiation in atmospheric water vapor at a wavelength of 1.35 cm and its vicinities plays a special role in an analysis of the ocean–atmosphere heat interaction; this region of the MCW spectrum will be the focus of our interests when studying the heat processes at the ocean–atmosphere boundary.

Fig. 2.1 Spectral dependence of the SOA's brightness temperature contrast ΔT^b in the wavelength range of 5 mm–5 cm during the passage of a cyclone (April 8–13) through the location of the RV/s *V. Bugaev* (*1*), *Musson* (*2*) and *Volna* (*3*)
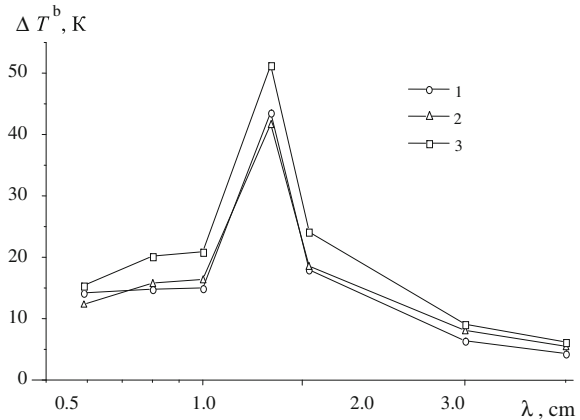
2.2.2 Relationship Between the SOA's Brightness Temperature and Heat Fluxes

The contributions of different layers to the radiation properties of the SOA and the effect on their relationship with the surface heat fluxes on the synoptic time scale were evaluated using the model (2.1)−(2.5) for various cases. In the first case, the downward-facing sensors (radiometers) were placed in free air to simulate satellite observations. In the second case, which simulates measurements aboard an aircraft, the downward sensors were placed at the boundary between free air and the atmospheric boundary layer. In the third case, the upward and downward sensors were placed 10–20 m above the water surface to simulate measurements aboard the vessels (this scheme is described in detail in Chap. 4).

A close correlation was observed between the estimated variations of the SOA brightness temperature and near-surface total heat fluxes at the *satellite*, *aircraft*, and *vessel* levels. This idea is illustrated in Figs. 2.2 and 2.3, which compare the values of $T^b_{1.35}$ (the brightness temperature at a wavelength of 1.35 cm) and $T^b_{0.59}$ (the brightness temperature at a wavelength of 5.9 mm), with total heat fluxes q_{he} obtained aboard the *V. Bugaev*, *Musson*, and *Volna*.

The satellite level of observations corresponds to the upper boundary of the troposphere. The aircraft level corresponds to the upper boundary of the atmosphere's boundary layer, whereas the vessel level corresponds to the upper boundary of the near-surface atmospheric layer.

It can be seen from the Figs. 2.2 and 2.3 that, in response to the increase in the fluxes q_{he}, the SOA's natural MCW radiation diminishes its brightness temperature T^b and vice versa: as the value of q_{he} decreases, T^b grows. Over this period, the brightness temperature variations are, on average, 15−20 K at the wavelength 5.9 mm and 30−40 K at 1.35 cm. In addition, the response of the brightness temperature lags behind the heat flux variation by 6–12 h.
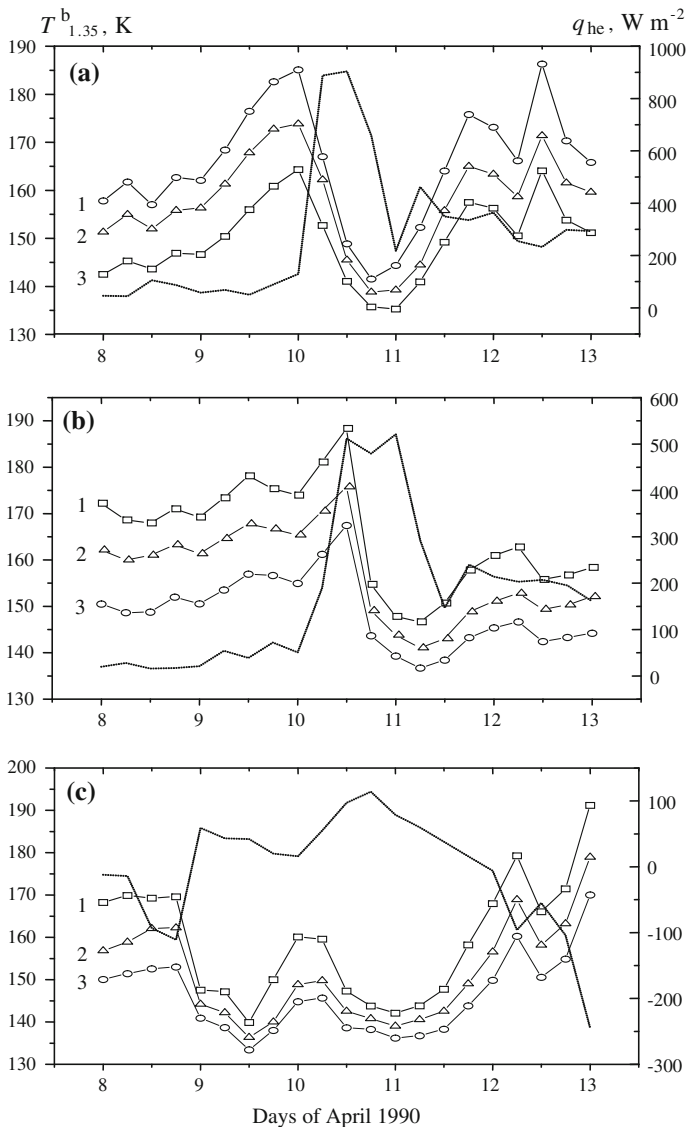
Fig. 2.2 Comparison of q_{he} (*dotted line*) with the estimates $T_{1.35}^b$ for the locations of the *V. Bugaev* (**a**), *Musson* (**b**) and *Volna* (**c**) during April 8−13, 1990 (ATLANTEX-90 experiment). Simulation of satellite (*1*), aircraft (*2*) and vessel (*3*) observations

The response of brightness temperature to surface heat fluxes depends only slightly on whether the measurements were carried out in the atmospheric surface layer, the top of the atmospheric boundary layer, or the free atmosphere. In these cases, the brightness temperature differs in magnitude but satisfies the following condition: the higher the observation height, the greater the parameter T^b.
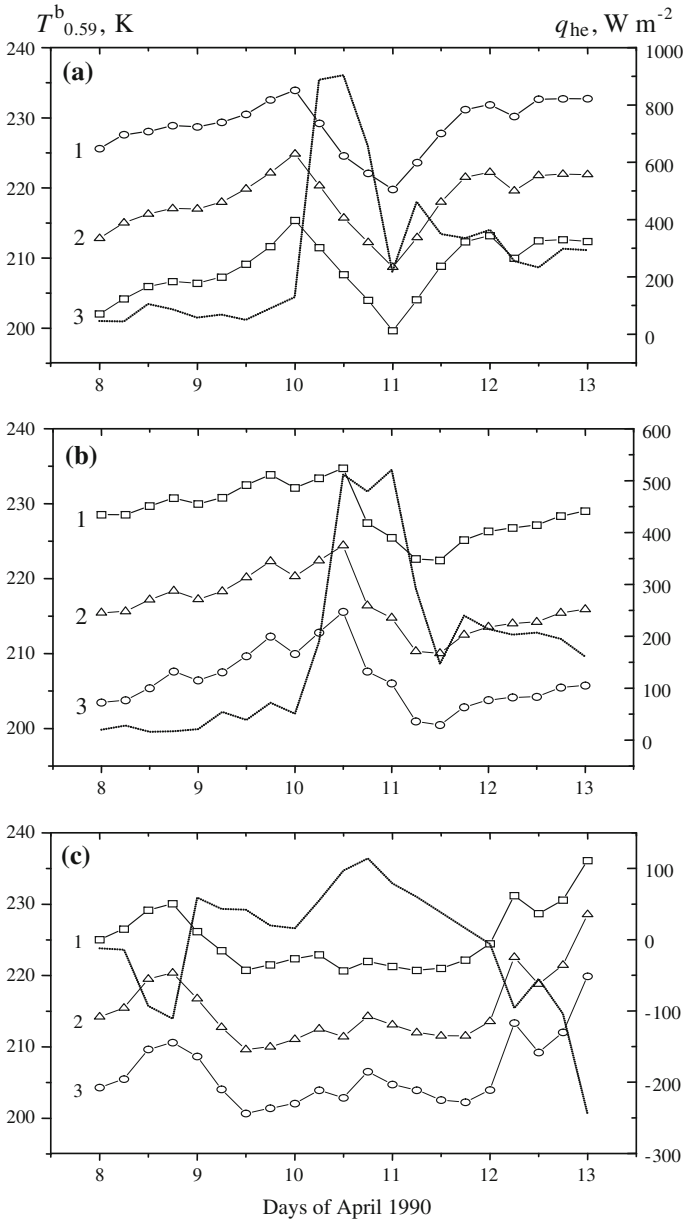
Fig. 2.3 The same data as in Fig. 2.2, but for the wavelength of 5.9 mm

We studied linear regressions between 6-h samples of the total heat flux q_{he} at the ocean–atmosphere interface recorded by the R/V *Volna* in the experiment ATLANTEX-90, as well as the SOA brightness temperatures at the wavelengths of 5.9 mm and 1.35 cm computed for the satellite-level case from the meteorological and aerologic measurements aboard this vessel in the form $q_{he} = c_1 + c_2\, T^b$ (Fig. 2.4). An intimate relationship is shown between the synoptic variations of heat fluxes and model estimates of the SOA brightness temperature. For 6-h samples of the parameters q_{he} and T^b in the resonance bands of molecular oxygen and atmospheric water vapor, the least absolute error of approximating the total heat flux q_{he} by the brightness temperature T^b is 26–28 W m^{-2} for a flux variation amplitude of 320 W m^{-2}.

The relative variations of the regression coefficients c_1 and c_2 are 13–15 %, with the regression coefficient c_2 being negative in both cases. This means that the heat flux and the brightness temperature vary in antiphase: an increase in the parameter q_{he} causes T^b to decrease and vice versa. It is remarkable that the intensity variations of the SOA's natural MCW radiation correlates well with variations of the heat fluxes in this case, although the accuracy of finding the brightness temperature, and

Fig. 2.4 Six-hour samples of total heat fluxes q_{he}, as the linear combinations of SOA brightness temperatures at the wavelengths 0.59 cm and 1.35 cm. Stationary phase of the experiment ATLANTEX-90 (R/V *Volna*)
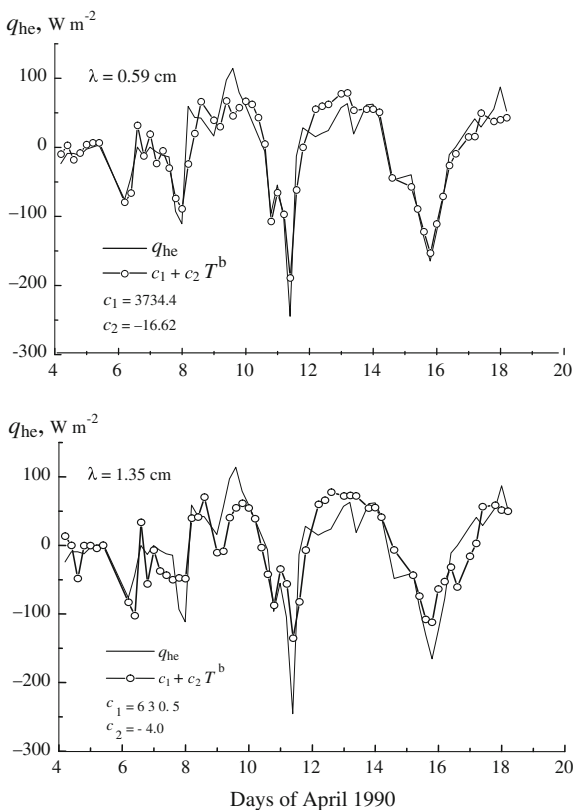
especially the heat fluxes, is not very high. The relative error involved in the model brightness temperature values found under the hydrometeorological conditions of the ATLANTEX-90 experiment is estimated to be 5–10 %, while that of the heat fluxes determined by the bulk parameterizations given in Chap. 1 may be as great as several tens of percent (Gulev et al. 1994). This factor substantiates the idea of using passive MCW radiometric data as *natural* characteristics of the ocean–atmosphere heat interaction.

2.2.3   Computation of the Brightness Temperature Response to the Heat Fluxes Variations

We analyzed Grankov et al. (2010) more rigorously with regard to the phenomenon of a time delay of the SOA brightness temperature response in the resonant spectral domains of 0.59 cm and 1.35 cm, compared with the variations of surface heat fluxes resting upon the results adjusted above (Fig. 2.5).

Fig. 2.5 Sensitivity of the SOA brightness temperature at the wavelengths of 0.59 and 1.35 cm to heat flux variations in areas observed by the R/Vs *V. Bugaev* (**a**) and *Volna* (**b**)
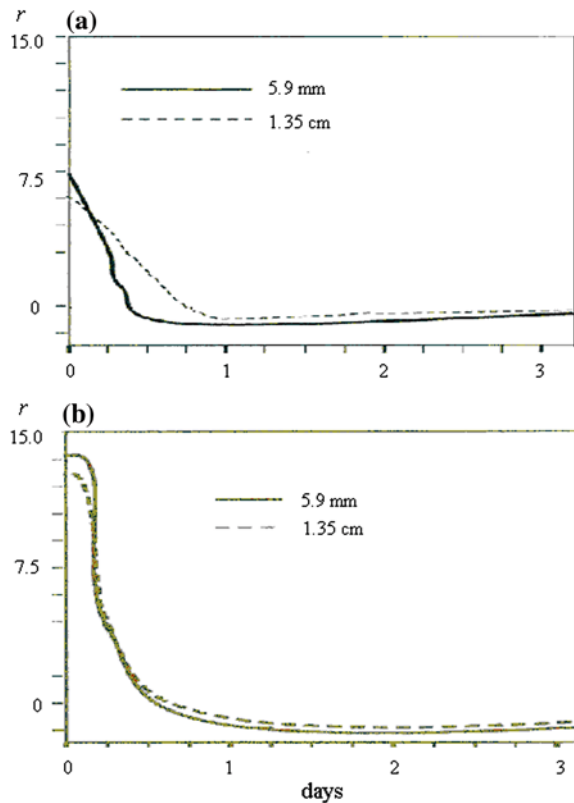
Duamel's integral equation let us calculate the function $r(t)$ of the brightness temperature T^b response (sensitivity) to the total heat flux q_{he} variations:

$$T^b(t) = \cdot \int_0^t q(\tau) \cdot r(t - \tau) \cdot d\tau \qquad (2.6)$$

Formula (2.6) can be considered as a modification of the classic Volterra`s equations of the first kind inherent to the class of equations of the convolution type. We proposed an iterative procedure to determine the function $r(t)$ as a linear superposition of the exponential functions:

$$r(t) = \sum_{i=1}^{N} a_i \exp(-b_i t) \qquad (2.7)$$

where coefficients a_i and b_i are calculated from the condition of minimal discrepancy between the SOA brightness temperature values and their approximations, characterized by values of the root-mean square (rms) error. The calculations show that the value $N = 6$ in Formula (2.7) is acceptable for this task; a mean value of the rms error in this case does not exceed 5–7 %.

The results shown in Fig. 2.5b for the vessel *Volna* are especially useful for the fuzziness of variations of the parameters T^b and q_{he} (see Figs. 2.2c and 2.3c). This case is distinguished from the cases illustrated in Figs. 2.2a, b and 2.3a, b, where the time shift between these parameters is noticeably obvious without any mathematical analysis.

Table 2.1 illustrates the results of an analysis of the role of a time delay of the SOA response on the synoptic surface heat fluxes. Here, we present the data from a regression analysis [the coefficient of correlation R and discrepancy d (rms)] between simulated estimates of the SOA brightness temperatures at the wavelengths of 0.59 and 1.35 cm and the heat flux data collected from the vessel *Musson* during the stationary phase of the ATLANTEX-90 experiment. It follows from Table 2.1 that maximal values of the coefficient of correlation ($R = 0.84$–0.86) and minimal values of the discrepancy ($d = 85$−93) take place when Δt is 12 h.

Table 2.1 Influence of the time shift Δt between the time samples of the SOA brightness temperature at the wavelengths 0.59 cm (*1*) and 1.35 cm (*2*) and heat fluxes on their correlation R and rms d (R/V *Musson*)

Time shift Δt	0 h	6 h	12 h	18 h
Correlation R (1)	0.25	0.67	0.86	0.84
Correlation R (2)	0.34	0.74	0.85	0.71
Discrepancy d, W m^{-2} (1)	160	124	85	98.7
Discrepancy d, W m^{-2} (2)	157	113	93	127.3

The peak of heat flux variations is 900 W m^{-2}

Thus, while carrying out a comparison of these data, we have to take into account the factor of a time shift between the surface heat fluxes and the brightness temperature variations in the synoptic range of time scales.

2.3   Analysis of the Factors Forming the Relationship Between Natural MCW Radiation and Heat Characteristics of the SOA

2.3.1   Parameters and Mechanisms that Form Relationships Between the Brightness Temperature and Surface Heat Fluxes

A problem that has been repeatedly discussed by teams at the Institute of Radioengineering and Electronics, the Institute of Space Research; and the Institute of Oceanology, Russian Academy of Sciences is how the SOA brightness temperature (simulated or satellite measured), for which an effectively radiating 2- to 5-km-thick stratum is responsible, can be related to the temperature and humidity properties of a much thinner (roughly 10-m-thick) near-water atmospheric layer.

Here, we examine the importance (priority) of ocean surface parameters and some parameters of different atmospheric layers—that is, their effect on the correlation between heat and humidity exchange characteristics and the MCW radiation of the SOA on the *synoptic* time scales. To this end, a regression analysis of relationships between variations of simulated brightness temperatures ΔT^b and total heat fluxes Δq_{he} was made based on the data accumulated from the R/V *Volna* in the ATLANTEX-90 experiment stationary phase with the following formulas:

$$\Delta q_{he} = k_1 \Delta T_{i1} + k_2 \Delta T_{i2}; \quad i = 1, \ldots, 4, \tag{2.8}$$

Here, the indices 1 and 2 are attached to the SOA brightness temperature of natural radiation in certain pieces of the MCW spectrum characterized by the wavelengths λ_1 and λ_2. Due to the index i, we can divide the influence of parameters forming the ocean–atmosphere heat interaction, such as the ocean surface temperature t_s ($i = 1$), the near-surface wind speed V ($i = 2$) and temperature t_a ($i = 3$), as well as the total water vapor content Q ($i = 4$). ΔT_{i1} and ΔT_{i2} are the brightness temperature variations at these wavelengths caused by variations of these parameters.

Then, we used an ordered elimination method to reveal the contribution of one or another parameter simultaneously to the heat exchange process and the SOA natural radiation in different parts of the MCW range of wavelengths. Table 2.2 lists the errors due to the approximation of the total heat fluxes q_{he} by the brightness temperatures of the SOA radiation in the wavelength range of 0.56–3.2 cm.

Table 2.2 Root-mean-square errors of approximation of the total heat fluxes by the SOA brightness temperatures simulated with various radiation models (the generalized model is shown in column d, with the simplified model shown in the other columns)

Wavelength, cm	Approximation error, W m^{-2}				
	d	d_t_s	d_V	d_t_a	d_Q
0.56	27.8	27.8	28.2	48.5	27.8
0.8	26.6	26.8	27.3	27.0	37.8
1.35	27.0	27.2	28.4	27.5	35.9
1.6	26.1	26.3	27.8	26.5	35.9
3.2	34.2	34.2	30.2	34.3	39.4

In Table 2.2, column d shows the discrepancy (rms) between the parameter q_{he} and the linear combinations of the parameters ΔT_{i1} and ΔT_{i2}, whose values were computed by a least-squares method taking into account variations of all basic parameters of the SOA (t_s, t_a, V, and Q). In columns d_t_s, d_V, d_t_a, and d_Q, the effects of the ocean surface temperature t_s, the near-surface wind speed V and temperature t_a, and the total water vapor content Q, respectively, are excluded (neutralized). The table shows that the influence of the ocean surface temperature is easier compared with the atmospheric parameters t_a and Q. This is a consequence of heat inertia in the ocean upper layer: it is seen from the ATLANTEX-90 experimental data that synoptic variations of the OST are less by an order of the temperature and humidity variations in the near-surface atmosphere.

We also analyzed the relationship between synoptic variations of the parameter q_{he} and variations of the SOA brightness temperature derived as a result of the imitation of satellite and aircraft measurements with the downward MCW sensors, as well as ship measurements with upward (1) and downward (2) sensors (antennas): these results are presented in Table 2.3. Computations of the SOA brightness temperatures were performed using the radiation model (2.1)−(2.5) for the six-hourly samples taken from measurements of the parameters t_s, V, t_a, and Q observed aboard the vessel *Volna* at the stationary phase of the ATLANTEX-90 experiment.

The results given in Tables 2.2 and 2.3 point to the primary role of the parameters t_a and Q in forming relationships between the SOA brightness temperatures in the atmospheric water vapor resonance line at 1.35 cm and in the regions (5.4–5.9 mm) of oxygen attenuation (radiation) with the surface heat fluxes.

Table 2.3 Correlation between simulated values of the SOA brightness temperature from various levels of observations at the millimeter and centimeter level and the parameter q_{he} recorded from the vessel *Volna* in April 1990

Wavelength, cm	0.54	0.56	0.59	0.80	1.0	1.35	1.6	3.2	5.0
Satellite	0.48	0.69	**0.92**	**0.87**	**0.87**	**0.83**	**0.88**	0.77	0.74
Aircraft	0.77	**0.90**	**0.89**	**0.84**	**0.85**	**0.86**	**0.88**	0.75	0.73
Vessel (1)	**0.86**	**0.87**	**0.85**	**0.80**	**0.81**	**0.84**	**0.86**	0.74	0.72
Vessel (2)	**0.81**	0.73	0.71	**0.80**	**0.82**	0.78	**0.82**	**0.80**	0.70

The cells marked in bold characterize a correlation equal or greater than 0.8

This analysis also shows that independently from the methods of observations used (*satellite, aircraft, or vessel*), the influence of the ocean surface temperature on the SOA brightness temperature is the *passive* factor in comparison with the influence of the atmospheric parameters t_a and Q in the *synoptic* range of time scales.

Figure 2.6 illustrates the important role of the air temperature parameter t_{1500} measured at a height of 1500 m and the atmospheric total water vapor content Q as the transient factor forming the relationship between the SOA brightness temperatures and the near-surface heat fluxes.

We estimated the parameters t_{1500} and Q from aerologic measurements taken aboard vessels during April 8−13, 1990. A close correlation between the vertical turbulent flux of momentum q_v and near-surface wind speed V can be observed. Figure 2.7 demonstrates this effect with data from the ATLANTEX-90 experiment derived from the R/V *Volna*.

This regularity predetermines a clear *direct* correlation between the SOA brightness temperature and the momentum fluxes. For example, we revealed a close
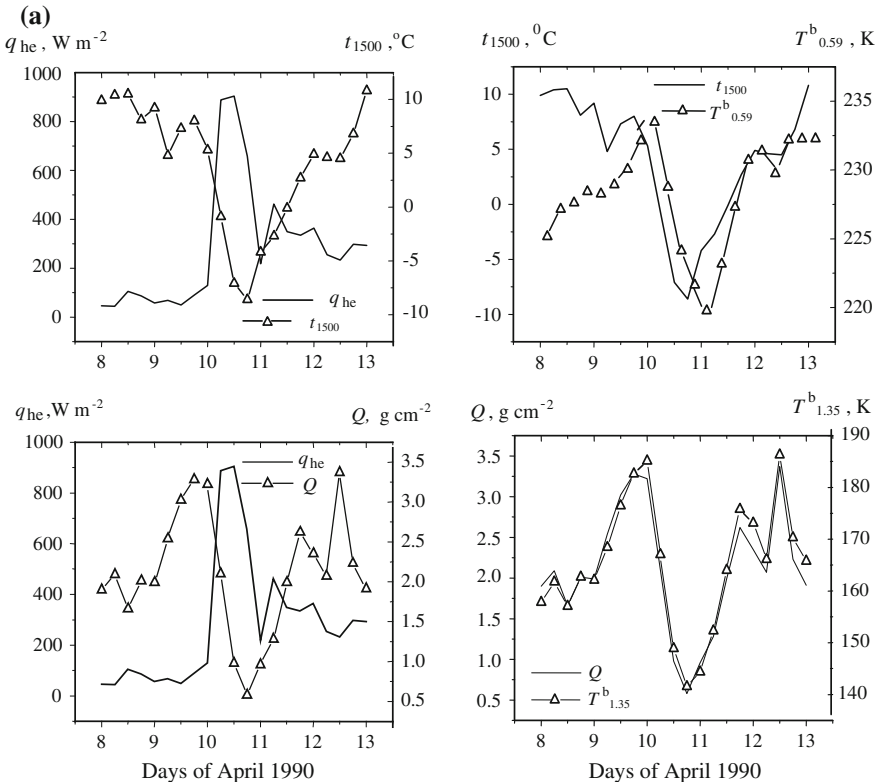
Fig. 2.6   a Results of the comparison of heat fluxes q_{he}, atmosphere temperature t_{1500}, total water vapor content of the atmosphere Q, and SOA brightness temperature at the wavelengths of 5.9 mm and 1.35 cm at the point of location of the R/V *Victor Bugaev* during 8−13 April, 1990. **b** The same as (**a**), but for the vessel *Volna*

(b)
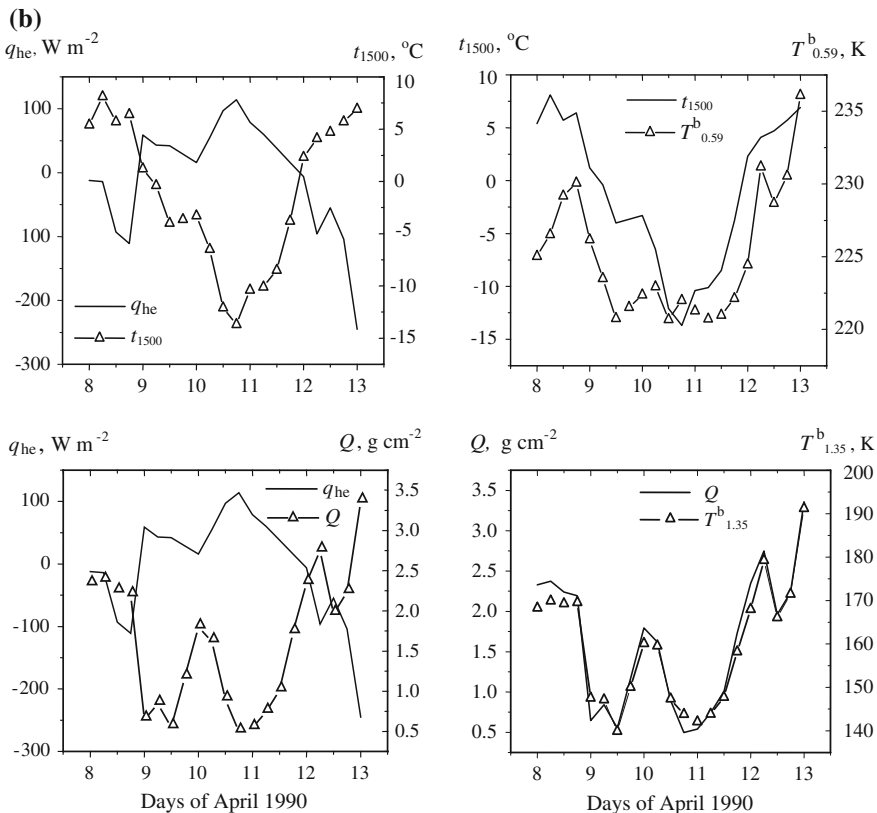
Fig. 2.6 (continued)

interrelationship between momentum fluxes at the ocean–atmosphere interface evaluated from aboard vessels in the ATLANTEX-90 experiment and the model estimates (corresponding to the satellite level of observations) of the SOA brightness temperature in the wavelength range between 3 and 5 cm, which is not affected by the atmosphere; the brightness temperature variations are governed mainly by variations in the intensity of wind stress of the water surface. These results are expected, because, by definition, the momentum flux is connected with wind speed through the air density ρ and drag coefficient C_v (see Formula (1.3) in Chap. 1).

During April 8−13, 1990 the correlation coefficient of variations of the brightness temperature T^b at the wavelength 3.2 cm and the parameter q_v observed from the vessel *Victor Bugaev* was as high as $R = 0.96$ and the discrepancy (rms error) between such variations was $d = 0.043$ for the values of parameter q_v varying from 0.044 to 0.9 N m^{-2} (in Newtons per square meter). For the R/V *Musson*, the corresponding parameters were $R = 0.95$ and $d = 0.05$ in the range of variations of q_v 0.013−0.57 N m^{-2}. Finally, for the vessel *Volna*, the values of its corresponding parameters were $R = 0.89$ and $d = 0.06$ for q_v varying from 0.014 to 0.42 N m^{-2}.
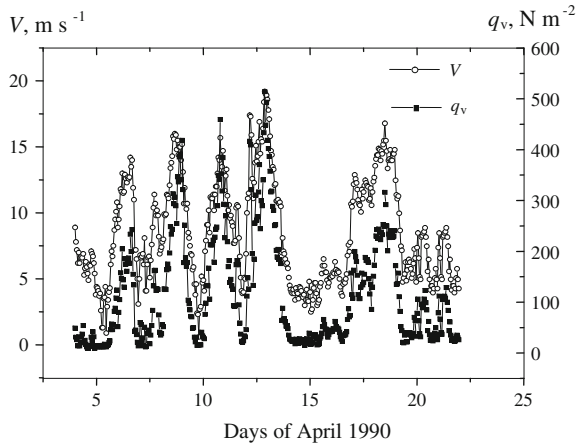
Fig. 2.7 Results of a comparison of the near-surface wind speed and momentum fluxes observed during the stationary phase of the ATLANTEX-90 experiment with a 1-h time resolution for these parameters

2.3.2 Response of the SOA Heat and MCW Radiation Characteristics on Midlatitude Cyclone Passage

Figures 2.2 and 2.3 show that the SOA brightness temperature contrasts in oceanic areas are most pronounced during the passage of cyclones, which result in deep changes of the near-surface air temperature, humidity, and heat fluxes as well as the brightness temperature of the SOA. Evidently, atmospheric enthalpy, which is a direct indicator of horizontal heat and moisture transfer, influences the near-surface heat and integral (averaged over height) MCW radiation characteristics of the system simultaneously and possibly can serve as a transient characteristic between them.
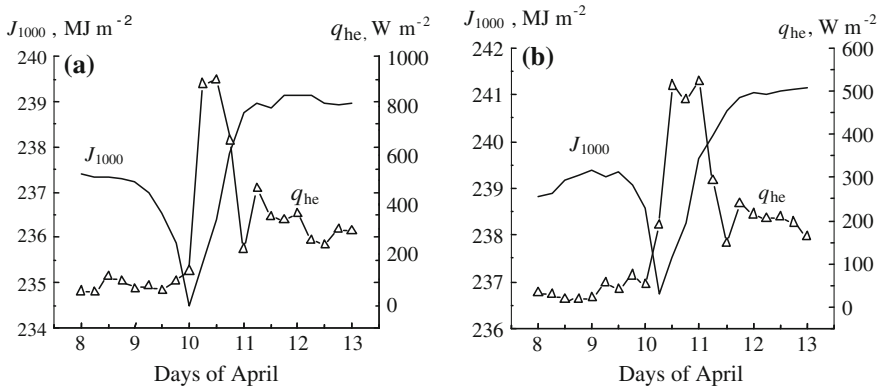
Fig. 2.8 Total heat fluxes q_{he} versus the enthalpy J_{1000} of the ABL during the passage of a cyclone (April 8−13, 1990) through the locations of the (**a**) *Victor Bugaev* and (**b**) *Musson*

Figure 2.8 compares the values of the atmosphere boundary layer (ABL) enthalpy (computed from aerologic sounding data for horizons at altitudes of 10, 100, 200, 300, 400, 500, 900, and 1000 m gathered aboard the *V. Bugaev* and *Musson* vessels. These values were estimated using the methods stated in Pinus (1982) and Perevedentsev (1984)), with the total heat fluxes excited by the powerful cyclone that originated during the stationary phase of the ATLANTEX-90 experiment on April 8−13, 1990.

Similar results were observed during periods of activity of other midlatitude cyclones in the locations of the R/Vs *V. Bugaev, Musson*, and *Volna* during the stationary phase of the ATLANTEX-90 experiment. Therefore, it is possible to consider large-scale horizontal (advective) heat and moisture transfer as a factor that provokes the vertical turbulent fluxes arising for regulating the heat balance between the ocean and atmosphere. A similar effect was marked, for example, by
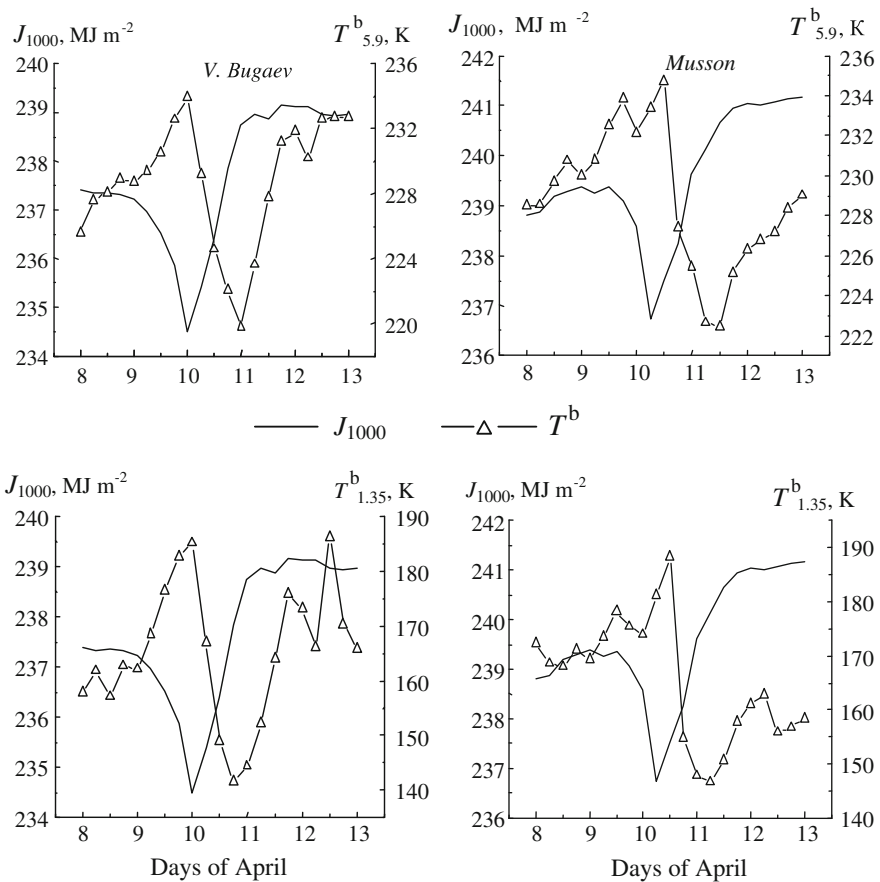
Fig. 2.9 Modeling of the response of the SOA brightness temperature at the wavelengths 5.9 mm and 1.35 cm to variations of the ABL enthalpy J_{1000} during the passage of a cyclone (April 8−13, 1990) through the locations of the R/Vs *V. Bugaev* and *Musson*

Abyzyarov et al. (1988), who noted the influence of the so-called zonal circulation index on the boundary heat fluxes in the island region.

Figure 2.9 illustrates the relationships between the ABL enthalpy J_{1000} with SOA brightness temperature variations at the wavelengths 5.9 mm and 1.35 cm over this period.

Figure 2.9 shows that synoptic variations of the enthalpy of the ABL stimulate an appreciable reaction of the SOA brightness temperature in the ranges of the effects of atmospheric oxygen (5−6 mm) and water vapor (1.35 cm), which vary from 12 to 45 K, respectively. Moreover, the response of the brightness temperature lags behind the enthalpy variation by 18−24 h. This property becomes especially apparent during periods of cyclonic activity in the atmosphere, when the ABL temperature and humidity are sharply and strongly varied.

2.4   Conclusions

1. The obtained data show a close correlation between the synoptic variations of the atmospheric temperature and humidity characteristics, as well as the intensity of the ocean–atmosphere heat interaction. The influence of the oceanic surface temperature on the relationships between the SOA brightness temperature and surface heat fluxes is a passive factor in comparison with the near-surface air temperature and humidity.
2. Based on results of the analysis derived in the ATLANTEX-90 experiment, we concluded that variations of the temperature and humidity characteristics in the ABL caused by a large-scale horizontal heat and moisture transfer in the atmosphere *rule* over the vertical turbulent heat and moisture fluxes at the SOA interface, as well as the intensity of natural MCW radiation of the system.
3. The correlation between the SOA brightness temperature and surface heat fluxes is most pronounced for intensive variations in the characteristics of horizontal heat transfer in the atmosphere, particularly for oceanic areas with high cyclonic activity. The brightness temperature of the ocean–atmosphere system in the bands of resonant attenuation of natural MCW radiation in atmospheric water vapor and molecular oxygen appears to serve as the quantitative characteristic of not only the surface sensible and latent fluxes, but also of the atmospheric boundary layer enthalpy in the synoptic range of time scales.

References

Abuzyarov ZK, Kudryavtseva KI, Seryakov EI, Skriptunova LI (1988) Marine forcasting. Gidrometeoizdat, Leningrad In Russian.

Basharinov AE, Gurvich AS, Egorov ST (1974) Radio emission of the planet Earth. Nauka, Moscow In Russian.

Grankov AG, Milshin AA, Soldatov VJu (2010) Computing the response of the ocean-atmosphere system to the heat flux variations. Issledovanie Zemli iz kosmosa 1:55−71 In Russian.

Gulev SK, Kolinko AV, Lappo SS (1994) Synoptic interaction between the ocean and atmosphere in middle latitudes. Gidrometeoizdat, St. Petersburg In Russian.

Lappo SS, Gulev SK, Rozhdestvenskii AE (1990) Large-scale heat interaction in the ocean–atmosphere system and energy-active zones in the world ocean. Gidrometeoizdat, Leningrad In Russian.

Perevedentsev JuP (1984) Circulation and energy processes in the atmosphere. Kazan University, Kazan In Russian.

Pinus NZ (1982) Available potential energy in the atmosphere and it transformation in the kinetic energy. Meteorologiya i Gidrologija 4:106-116 In Russian.

Chapter 3
Search for the Direct Relationship Between Heat Fluxes and the Parameters Associated with the SOA Brightness Temperature

3.1 Analysis of the Relationships Between Total Water Vapor Content in the Atmosphere and Heat Fluxes (ATLANTEX-90 Experiment)

3.1.1 Problem Statement

The integral (total) water vapor content of the atmosphere can provide information about near-surface air humidity e and temperature t_a, which play a key role in the atmosphere–ocean heat interaction (Snopkov 1977; Liu 1986; Grankov 1992; Grankov and Milshin 1994, 1995). The correlation between the parameters Q, e, and t_a is most pronounced for their seasonal values. Therefore, the idea of using the total water vapor content of the atmosphere as the characteristic for its near-surface temperature and humidity has been recognized as valid for analyzing the seasonal and interannual changeability of the ocean–atmosphere heat interaction characteristics from satellites (Liu 1988; Grankov 1992).

A study of the relationship between the atmosphere's total water vapor and intensity of the ocean–atmosphere heat interchanges on synoptic time scales (where most of the interchange energy is concentrated) is a more complicated task because the synoptic ocean–atmosphere interaction is especially changeable and regional (Gulev et al. 1994). The works in this field are limited, and their results are mostly qualitative. For example, based on an analysis of the ATLANTEX-90 experimental data, Lebedeva (1991) concluded that "the total water vapor content of the atmosphere is determined by the value of sensible and latent heat fluxes and influences, in turn, on the value of latent heat (p. 44)."

The following questions may clarify the effectiveness of using satellite MCW radiometric means for studying both the seasonal and the synoptic components of the ocean-atmosphere heat interaction:

1. Is it possible to use the total content of water vapor in the atmosphere as the quantitative indicator of the near-surface temperature t_a and humidity e in the synoptic range of time scales?
2. If so, is it possible to use atmospheric water vapor instead of the parameters t_a and e in the semi-empiric relationships of the *global bulk aerodynamic method* to estimate the synoptic variability of sensible and latent heat fluxes at the ocean–atmosphere interface?

Answers to these questions may be found in data from meteorological and aerologic measurements conducted on the R/V *Volna* in April 1990 in the Newfoundland EAZO (Grankov and Novichikhin 1997).

3.1.2 Analysis of Meteorological and Aerologic Data from the ATLANTEX-90 Experiment

The research vessel *Volna* was located in the eastern branch of the cold Labrador Current, 40 miles from a hydrological front formed by the Labrador Current and a warm quasi-stationary Gulf Stream anticyclonic vortex. The vortex leads to the regeneration of cyclones and determines the strong synoptic variability of oceanic and atmospheric parameters in this region (Gulev et al. 1994). Thus, the amplitudes of the near-surface temperature, humidity, and total water vapor content of the atmosphere during the passage of a cyclone typical for this region and season (April 15–19) are 9.9 °C, 4.7 mb, and 3.5 g cm^{-2}, respectively, which exceed by 3–5 times their *rms* deviations from the mean April norms.

From current (hourly) measurements, the daily values of the near-surface temperature, humidity, and total water vapor of the atmosphere were computed. Their variations during April 4–20, 1990 are presented in Fig. 3.1. This figure shows that the correlation between synoptic variations of the parameters t_a, e, and Q is very strong. The coefficients of correlation r between these parameters are $r(t_a, e) = 0.96$,

Fig. 3.1 Correlations of the daily parameters t_a, e, and Q observed from the vessel *Volna* for the stationary phases of the ATLANTEX-90 experiment
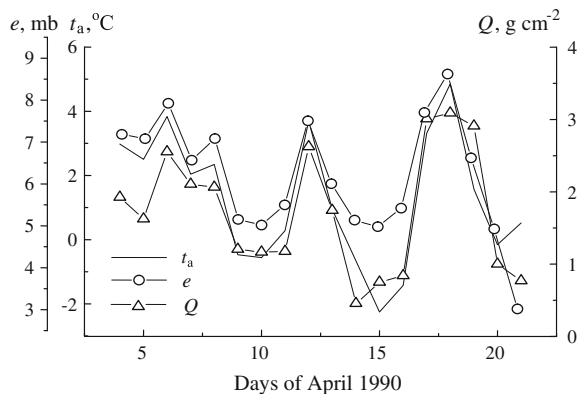
$r(t_a, Q) = 0.88$, and $r(e, Q) = 0.89$. Similar results were observed for the R/Vs *Victor Bugaev* and *Musson*.

Table 3.1 shows the data from a regression analysis presented in the form of linear relationships (of the kind $y = A + B\,x$) between current daily values of the parameters Q, e, and t_a measured during periods of time in April 1990, which characterize the history of evolution of the atmosphere's temperature and humidity characteristics for the stationary phase of the ATLANTEX-90 experiment derived from the R/V *Volna*.

Strong correlations between these parameters and their stability can be observed, despite the intensive variability caused by the typical effects for cyclones in these areas. As evident from Table 3.1, the current samples of mean daily values of the parameters t_a and e, t_a and Q have the most stable regressions: the coefficients of variation of the parameter B for these combinations is half the respective coefficients for the combination of e and Q values (the coefficient of variation of the parameter A is an order of magnitude less).

These results indicate a close correlation between the total water vapor content of the atmosphere Q and the near-surface air temperature t_a and humidity e in the synoptic range of time scales. It allows us to see the problem of using parameter Q as the quantitative characteristic of heat exchanges at the ocean–atmosphere interface—in particular, to consider the possibility of substituting parameters t_a and e, which are hardly accessible for satellite MCW radiometric means, by parameter Q in the formulas for the computation of heat fluxes.

Table 3.1 Regression parameters between daily t_a, e, and Q for the stationary phase of the ATLANTEX-90 experiment (R/V *Volna*) (Grankov and Novichikhin 1997)

Data	Regression parameters								
April 1990	t_a and e			e and Q			t_a and Q		
Coefficients	A	B	r	A	B	r	A	B	r
4–8	5.33	0.67	0.96	−0.86	0.41	0.59	1.24	0.30	0.62
4–10	5.40	0.64	0.99	−0.93	0.42	0.90	1.31	0.27	0.90
4–12	5.39	0.63	0.99	−1.34	0.48	0.91	1.25	0.31	0.92
4–14	5.42	0.62	0.99	−1.83	0.55	0.89	1.15	0.35	0.91
4–16	5.67	0.51	0.96	−2.08	0.59	0.91	1.23	0.32	0.92
4–18	5.67	0.55	0.97	−2.33	0.63	0.93	1.24	0.35	0.93
4–20	5.62	0.56	0.96	−2.24	0.63	0.89	1.29	0.36	0.88

3.1.3 Reconstruction of the Bulk Formulas

To answer the question of whether total atmospheric water vapor can be used instead of parameters t_a and e for the analysis of synoptic variability of sensible and latent heat fluxes, the original (taken from archival materials in the stationary phase of the experiment) values of q_h and q_e were calculated by standard methods (Guidelines 1981) from the R/V *Volna* hydrological and meteorological measurements with the results of independent aerologic measurements of parameter Q:

$$q_h^* = c_0 + c_1 t_s V + c_2 t_a V; \tag{3.1}$$

$$q_h^* = c_0 + c_1 t_s V + c_2 Q V, \tag{3.2}$$

where t_s, t_a, V, and Q are data of standard measurements of the ocean surface temperature, near-surface air temperature and wind speed, and the total water vapor content in the atmosphere averaged over every 24 and 6 h, respectively, during 18 days (April 4–21); the coefficients c_0, c_1, and c_2 were determined using the least-squares method by minimizing the discrepancy (residual) d between the original values of fluxes q_h and their estimates q_h^* for 24-h and 6-h averages.

A similar parameterization was examined for the fluxes of latent heat q_e

$$q_e^* = c_0 + c_1 t_s V + c_2 e V; \tag{3.3}$$

$$q_e^* = c_0 + c_1 t_s V + c_2 Q V. \tag{3.4}$$

As an example, Figs. 3.2 and 3.3 shows the average values of the original sensible q_h and q_e heat fluxes for every 24 h and also their approximate estimates q_h^* and q_e^*.

Parameterizations (3.1) and (3.3) include the same components that are used in traditional bulk formulas for the calculations of sensible and latent heat fluxes in a wide range of space and time scales and have a similar form. However, c_0, c_1, and c_2 are invariable, while the coefficients in the bulk parameterizations generally depend on the near-surface wind speed. Parameterizations (3.2) and (3.4) follow from parameterizations (3.1) and (3.3) after the near-surface temperature t_a and vapor pressure e are replaced by Q; therefore, they contain only those components of the SOA that are reliable recorded by methods of satellite MCW and IR radiometry.

As seen from Figs. 3.2 and 3.3, parameterizations (3.2) and (3.4) provide a rather accurate approximation of the mean daily sensible and latent fluxes in the ATLANTEX-90 stationary phase. However, the main result seen in Figs. 3.2 and 3.3 is that q_h and q_e are closely connected with q_h^* and q_e^*, calculated from (3.2) and (3.4), which use total vapor content of the atmosphere as a characteristic of sensible and latent heat fluxes. This result is the quantitative substantiation of the relationships between atmospheric total water vapor content and the intensity of the
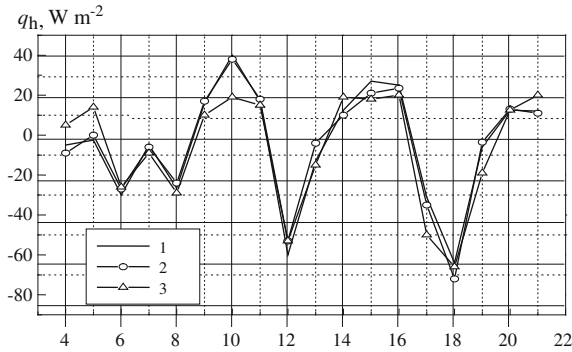
Fig. 3.2 Original values of sensible heat fluxes (*1*) and their approximations (*2, 3*) calculated from parameterizations (3.1) and (3.2), respectively, in April 1990
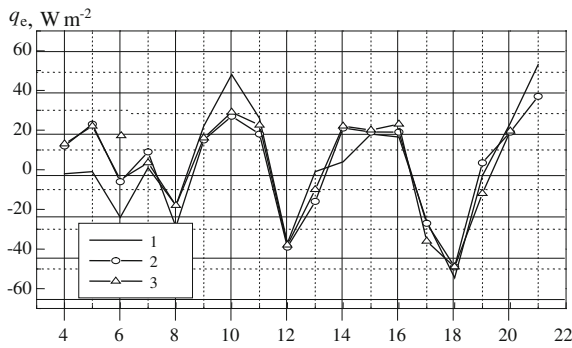
Fig. 3.3 Original values of latent heat fluxes (*1*) and their approximations (*2, 3*) calculated from parameterizations (3.3) and (3.4), respectively, in April 1990

ocean–atmosphere heat exchange in the synoptic range of time scales, as studied in Lebedeva (1991), for example.

More comprehensive results of the analysis of the efficiency of the previously mentioned and other parameterizations of synoptic fluxes of sensible and latent heat in the ATLANTEX-90 stationary phase are given in Table 3.2, which contains the values of the residual d and correlation coefficient r between q_h and q_h^*, q_e and q_e^*, as well as the coefficients c_0, c_1, and c_2 for various time averages of standard measurement data. The calculation results confirm the efficiency of parameterizations (3.2) and (3.4), which have the largest r and smallest d values.

Table 3.2 shows that the temperature and humidity of the near-surface atmosphere in bulk parameterizations can be replaced by total atmospheric vapor content. Thus, the residual in the approximations of sensible heat fluxes q_h by formula (3.2) is 10–13 W m^{-2}, while the amplitude of q_h variations (Δq_h) attains 100 W m^{-2} with 24-h averaging and 160 W m^{-2} with 6-h averaging. The approximation of

Table 3.2 Sensible (q_h) and latent (q_e) heat flux approximations with 6-h (numerator) and 24-h (denominator) averaging for different parameterizations of heat and moisture exchange between the ocean and atmosphere

Parameterizations	c_0	c_1	c_2	r	d
$q_h^* = c_0 + c_1 t_s + c_2 t_a V$	1.61/−0.84	1.53/1.64	−1.36/−1.36	0.99/0.99	4.16/4.09
$q_h^* = c_0 + c_1(t_s - t_a)V$	3.24/1.99	1.35/1.34	–	0.99/0.99	4.23/4.21
$q_h^* = c_0 + c_1 t_s V + c_2 QV$	22.7/17.9	0.61/1.45	−0.02/−0.02	0.91/0.93	13.0/10.4
$q_h^* = c_0 + c_1 t_s V + c_2 eV$	27.0/27.4	1.99/1.98	−0.93/−0.94	0.89/0.91	14.0/11.6
$q_h^* = c_0 + c_1 t_s + c_2 Q$	24.2/25.6	8.30/12.3	−0.23/−0.27	0.76/0.85	20.0/14.6
$q_h^* = c_0 + c_1 t_a$	12.3/12.0	−13.0/−12.8	–	0.88/0.90	14.6/12.4
$q_h^* = c_0 + c_1 Q$	36.4/43.8	−0.24/-0.28	–	0.76/0.84	20.3/15.3
$q_h^* = c_0 + c_1 t_s$	−30.6/−39.1	20.2/26.9	–	0.29/0.37	29.8/26.0
$q_e^* = c_0 + c_1 t_s V + c_2 eV$	25.7/27.1	2.70/2.64	−0.91/−0.93	0.86/0.89	15.4/1.3
$q_e^* = c_0 + c_1 t_s V + c_2 t_a V$	1.36/0.31	2.17/2.14	−1.29/−1.28	0.94/0.93	10.4/9.73
$q_e^* = c_0 + c_1 t_s V + c_2 QV$	21.6/17.8	1.35/2.04	−0.02/−0.02	0.87/0.89	14.7/12.2
$q_e^* = c_0 + c_1 t_s + c_2 Q$	31.2/32.0	8.71/12.2	−0.23/−0.26	0.79/0.85	18.6/14.1
$q_e^* = c_0 + c_1 t_s$	17.6/1.7	−11.2/−11.3	–	0.78/0.82	18.7/15.7
$q_e^* = c_0 + c_1 Q$	43.9/49.9	−0.24/0.27	–	0.78/0.84	18.9/14.8
$q_e^* = c_0 + c_1 e$	122.0/118.0	−19.2/−18.6	–	0.92/0.94	11.9/9.5

latent heat flux by Formula (3.4) yields the following values: $d = 12$ W m^{-2} (at $\Delta q_e = 105$ W m^{-2}) with 24-h averaging and $d = 15$ W m^{-2} (at $\Delta q_h = 205$ W m^{-2}) with 6-h averaging. The quantity $\Delta q/d$—a valid signal/noise ratio—does not decline upon transition from 24-h to 6-h averaging, which may be explained by the stability of the relationship, not only between mean daily variations of Q and t_a but also between their more dynamic (diurnal) variations.

Table 3.2 also shows that the total atmospheric vapor content can be used most effectively as a characteristic of heat and moisture exchange between the ocean and atmosphere when it is combined with ocean surface temperature t_s and, especially, with the near-surface wind speed V.

Thus, the analysis of data from hydrological, meteorological, and aerologic measurements made aboard the R/V *Volna* in the Newfoundland EAZO in the ATLANTEX-90 experiment suggests that bulk parameterizations for calculating the vertical turbulent fluxes of sensible and latent heat over the ocean can be reconstructed in the form of combinations of only those parameters of the SOA that are directly associated with satellite-derived characteristics of MCW and IR natural radiation of the SOA in the synoptic range of time scales. This reconstruction is based on a close correlation between the near-surface air temperature and humidity with the total water vapor content in the atmosphere.

3.2   The Role of Near-Surface Wind in Heat Flux Determinations

3.2.1   Specific Objective

In this section, we continue the theme of bulk formula modification with satellite MCW radiometric data, analyzing the endowment of the near-surface wind in the processes of heat exchange in the ocean–atmosphere interface at the synoptic time scales (Grankov 2011). Studying the role of the surface wind speed V against the air–sea temperature differences appearing in bulk formulas is a main objective here.

The results of measurements from R/Vs *Victor Bugaev*, *Musson*, and *Volna* obtained in the ATLANTEX-90 experiment in April 1990 in the Newfoundland EAZO are used as the initial data and include the following:

1. Hourly values of the ocean surface temperature t_s, near-surface air temperature t_a, humidity e, and wind speed V.
2. Hourly estimates of turbulent sensible q_h and latent q_e heat fluxes, parameterized from hourly measurements of the parameters t_s, t_a, V, and e.

The processes of heat and moisture exchange in the ocean–atmosphere interface in this area of the North Atlantic differ *qualitatively*. For example, at the location of R/Vs *V. Bugaev* and *Musson* in warm waters of the Gulf Stream, a heat transfer from the ocean to atmosphere is observed; however, at the point of location of R/V *Volna* (in cold waters of the Labrador Current), the atmosphere transfers heat to the ocean. Also, the *quantitative* characteristics of the ocean–atmosphere heat interaction strongly differ at the locations of R/Vs *V. Bugaev*, *Musson*, and *Volna* where, for example, the amplitudes of variations of the total heat flux attain 800, 500, and 350 W m^{-2}, respectively (Gulev et al. 1994).

3.2.2   Results of the Analysis on the Influence of the Wind Factor

We compared the total heat fluxes at the points of location of R/Vs *Victor Bugaev*, *Musson*, and *Volna* in April 1990 with the difference (Δt) between the ocean surface temperature t_s and atmosphere near-surface temperature t_a. The compound parameter $\Delta t = (t_s - t_a) V$ considers not only the heat characteristics of the ocean–atmosphere interface but also its dynamic properties determined by the near-surface wind speed. Results of the comparative analysis are presented in Fig. 3.4.

From Fig. 3.4, it follows that taking into account the factor V results in a stricter correlation between the total heat fluxes and temperature difference. For example, the coefficient of correlation r between total heat flux, parameter $\Delta t = t_s - t_a$ (see left group of figures), and compound parameter $\Delta t V$ (right group) increases from 0.82 to 0.94 (R/V *V. Bugaev*), from 0.82 to 0.93 (R/V *Musson*), and from 0.89 to 0.97
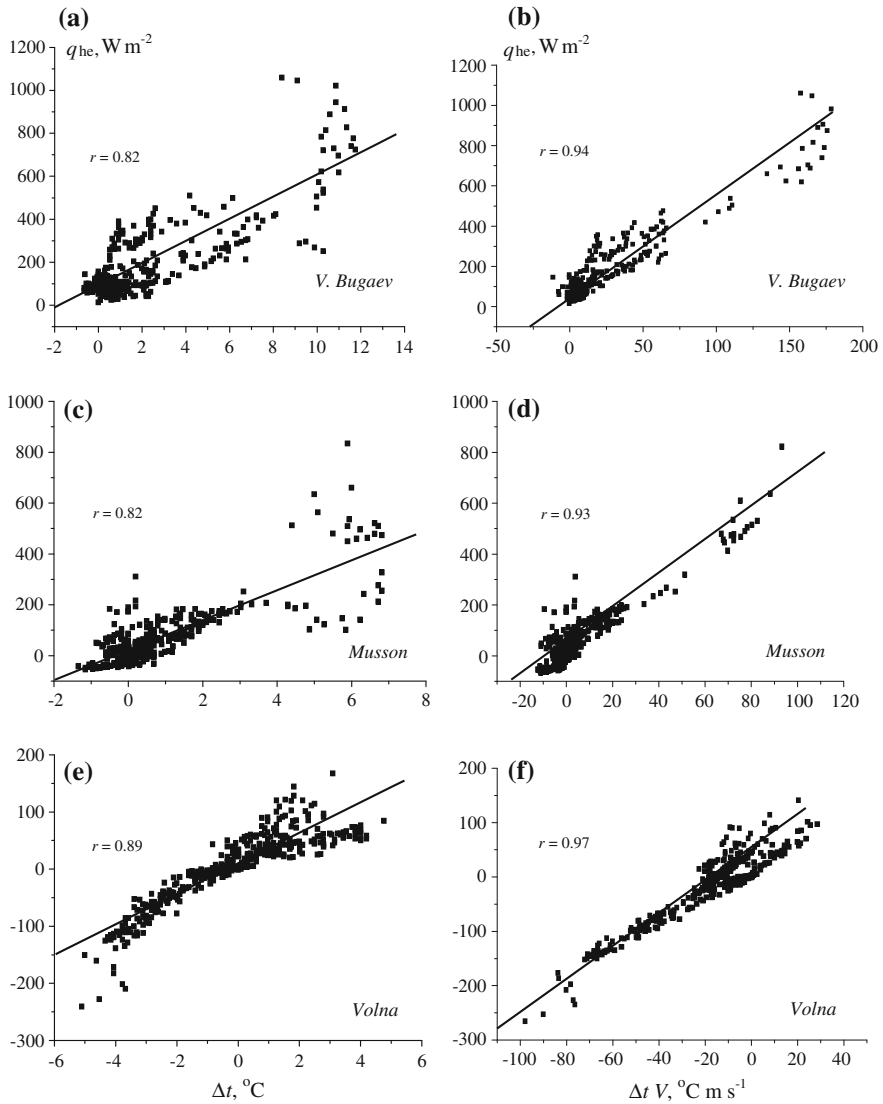
Fig. 3.4 **a** Comparison of the total heat fluxes with parameters Δt (a) and $\Delta t\,V$ (b) for the vessel *Victor Bugaev*. **b** The same as (**a**), but for the vessel *Musson*. **c** The same as (**a**) and (**b**), but for the vessel *Volna*

(R/V *Volna*). This conclusion agrees with the results of analysis for various alternate versions of the reconstruction of the bulk formulas (see Table 3.2).

Thus, it is important to consider the wind factor when analyzing the ocean–atmosphere heat and moisture exchange in the synoptic range of time scales. Due to the results of analysis of the ATLANTEX-90 experimental data, accounting for this

factor allows one to reduce appreciably a discrepancy between heat fluxes parameterized from bulk formulas as well as from their "truncated" modifications, which are more convenient for analysis of the ocean–atmosphere heat interaction with satellite MCW radiometric methods.

3.3 Relationships Between Monthly Mean Ocean–Atmosphere Temperature Differences and MCW and IR Radiation Intensity of the SOA

3.3.1 Statement of the Problem

As previously ascertained, direct relationships between SOA brightness temperature and surface heat fluxes are available for synoptic time scales. These relationships become more apparent in areas of short-term and intensive impacts, such as middle latitude cyclones, which cause quick disturbances of meteorological and SOA natural radiation characteristics against slow seasonal changeability of the processes of heat and dynamic interaction of the ocean and atmosphere. Hence, the following question arises: Is the relationship between the SOA brightness temperature and heat fluxes maintained for their monthly mean values at the seasonal time scales, when periods of cyclonic activity alternate with dominating "quiet" periods (i.e., a lack of intensive storms, cloudiness, precipitation)?

The background for the joint analysis of characteristics of the ocean–atmosphere system radiation and heat exchange in its interface at the seasonal time scales is a close correlation between the monthly mean temperature and humidity of the near-surface and upper atmosphere layers (see Chap. 1).

The main objective of this study is modeling the seasonal dynamics of monthly mean characteristics of the SOA's natural MCW and IR radiation and analyzing their correlations with seasonal dynamics of monthly mean differences between the surface temperature of the ocean t_s and the near-surface atmosphere temperature t_a. (Grankov and Usov 1994). As is known, the parameter $\Delta t = t_s - t_a$ directly determines the vertical turbulent fluxes of sensible and latent heat in the case of large-scale interactions of the ocean and atmosphere. In addition, the average multiyear (climatic) values of Δt in the North Atlantic agree well with the average multiyear values of heat exchange between the ocean and atmosphere. In the center of the study is the Gulf Stream energy active zone, which is characterized by the availability of spacious oceanographic, meteorological and other archives.

The following tasks are under consideration:

1. Calculation of the MCW and IR temperatures of the SOA and their seasonal dynamics (simulation of MCW and IR passive radiometric measurements from satellites with archival data of oceanographic and hydrometeorological measurements) in the Gulf Stream EAZO.

2. Analysis of the influence of the SOA parameters (emphasizing the parameters t_s and t_a) on MCW and IR radiation intensity for centimeters, millimeters, and infrareds in this area.
3. Analysis of the steadiness of relationships between MCW and IR radiation intensity in various pieces of the spectrum and the parameter Δt.
4. Exposure of spectral pieces at centimeters, millimeters, and infrareds, which provides a steadiness for the dependence of MCW radiation versus parameter Δt and its seasonal dynamics.

In the analysis, we used long-term data of oceanographic and meteorological measurements gathered in the fragment of Gulf Stream EAZO, which is a 5-degree square centered about the point (vessel station) with coordinates 38°N, 71°W—so-called point H (HOTEL).

To compute the SOA radiation characteristics and their temporal dynamics for microwaves and infrareds, the model described by relationships (2.1)–(2.5) is used (see Chap. 2).

3.3.2 Approximations and Limitations Used

The analysis of SOA radiation characteristics was made with the assumption that the ocean surface is calm (flat) and the atmosphere is cloudless. The relative frequency of these situations in SOA is around 50 % (Shutko 1986). In addition, the results of a special study show that the monthly mean values of the brightness temperature of the SOA as well as the estimates of monthly mean parameters retrieved from satellite sensors (at microwaves) are practically inert to wind speed, cloudiness, and precipitation intensity.

The intensity of the ocean surface's natural radiation was computed within a wide range of its temperature variations in accordance with the well-known methods cited in Handbook (1977) and Basharinov et al. (1974). Numerical estimates of the atmosphere's attenuation γ were obtained by taking into account the water vapor content (at microwaves and infrareds), molecular oxygen (at microwaves), and aerosol (at infrareds) on the basis of theoretical (Zhevakin and Naumov 1964, 1965) and empirical (Arefjev 1991; Paramonova 1985) relationships.

In accordance with Arefjev (1991), Paramonova (1985), Zhevakin and Naumov (1964, 1965), the attenuation of natural radiation in the atmosphere in the MCW and IR ranges of wavelengths is caused mainly by its parameters as the air temperature t_a, humidity ρ, and pressure P, as well as their vertical distributions. As the *monthly mean* parameters t_a, ρ, and P are considered in our study, the model of the standard atmosphere (Xrgian 1978) is appropriate:

$$T_a(h) = T_a(0)\exp[-0.02h], T = t + 273; \qquad (3.5a)$$

$$P(h) = P(0) \exp[-0.125h]; \tag{3.5b}$$

$$\rho(h) = \rho(0) \exp[-ah]. \tag{3.5c}$$

Monthly mean values of the parameter a in Formula (3.5c) can be determined from the monthly mean values of near-surface water vapor pressure $e(0)$ and total water vapor content $Q = \int_0^H \rho(h)\mathrm{d}h$ in the atmosphere, with an account of the next relationship between $e(0)$ (in mb) and $\rho(0)$ (in kg m^{-3}):

$$\rho(0) = 0.22e(0)/t_a(0). \tag{3.6}$$

From Formulas (3.5c) and (3.6), it follows that:

$$a = 0.22e(0)/Qt_a(0), \ \mathrm{km}^{-1}. \tag{3.7}$$

The near-surface atmospheric pressure is taken as equal to its standard value $P(0) = 1013$ mb for all seasons, because the seasonal variations of $P(0)$ are of 10–15 mb for the main active zones of the North Atlantic, including its Gulf Stream zone (Handbook 1979). These variations are the cause of negligible variations of the line absorption of natural electromagnetic radiation, which does not exceed 0.5–0.7 % of the average per-year (climatic) absorption at the wavelength 1.35 cm and 1–1.5 % in the IR band 8–12 mcm, respectively.

Let us note that variations of the near-surface air humidity yield the effect of tens of percents in seasonal variations of absorption at microwaves and infrareds.

3.3.3 Relationships Between the SOA's Natural Radiation and the Near-Surface Atmosphere Characteristics

We computed the monthly mean values of brightness temperature at wavelengths 3 mm–8.5 cm and radiation temperature at the window of 8.5–14 mcm, corresponding to monthly mean values of parameters t_s, $t_a(0)$, a, $\rho(0)$, and Q (Table 3.3).

The monthly mean parameters t_s, $t_a(0)$, $e(0)$, a, Q, and $\rho(0)$ shown in Table 3.3 are used as the initial data for calculations of natural MCW and IR radiation in the

Table 3.3 Monthly mean (climatic) temperature and humidity characteristics in the Gulf Stream active zone of the North Atlantic

Months	February	May	August	November
t_s, K	286	291	298	293.5
$t_a(0)$, K	282.5	289	297	289.5
$e(0)$, mb	11	7	26	15
Q, g cm^{-2}	1.0	2.3	3.5	1.5
$\rho(0)$	8.6	12.9	19.2	11.4
a, km^{-1}	0.86	0.56	0.55	0.76

Gulf Steam active zone for various seasons. It follows from calculations that the SOA's natural IR and MCW radiation is most sensible to seasonal variations of the near-surface atmospheric temperature and humidity variations in the window of 9–10 mcm of relative transparency of IR radiation, at the vicinity of the 5 mm-line of resonant absorption of MCW radiation by molecular oxygen, and in the 1.35 cm-line of resonant absorption of MCW radiation by a water vapor, as well as in the nonresonant spectral interval of 3–8 cm (Fig. 3.5 illustrates these features for microwaves).

Figure 3.5 also shows the results of the linear regression analysis between the monthly mean values of the SOA brightness temperatures and parameters t_s, $t_a(0)$, and Q in the form of diagrams illustrating the relative contribution of the variations of these parameters into variations of the parameter T^b at the wavelengths 5.7 mm, 1.35 cm, and 5 cm during the winter-summer period.

Let us note that parameter Q is a more reliable factor governing the brightness temperature at wavelength 1.35 cm in comparison with the parameter $\rho(0)$, as the parameter T^b depends not only on the near-surface air humidity but also on its vertical distribution. That is why the total water vapor content Q appears in Fig. 3.5 along with parameters t_s and $t_a(0)$. The results of a regression analysis clarify some important peculiarities of relationships between MCW and IR radiation and the SOA parameters. For example, the seasonal variations of the intensity of natural radiation in spectral intervals 10 mcm and 5 cm are well-correlated with seasonal variations of the ocean surface temperature t_s. Parameter t_a shows its worth at the wavelengths 5.7 mm, and the parameter Q is in the line 1.35 cm of water vapor absorption; at these wavelengths, the values of T^b and T^τ are increasing linearly with increasing parameters t_s, t_a, and Q. The coefficient of regression $\Delta T^b / \Delta t_s$ for the dependence of brightness temperature versus water surface temperature is about 0.4–0.45 K/°C at the wavelength 5 cm; the coefficient of regression $\Delta T^b / \Delta Q$ for the
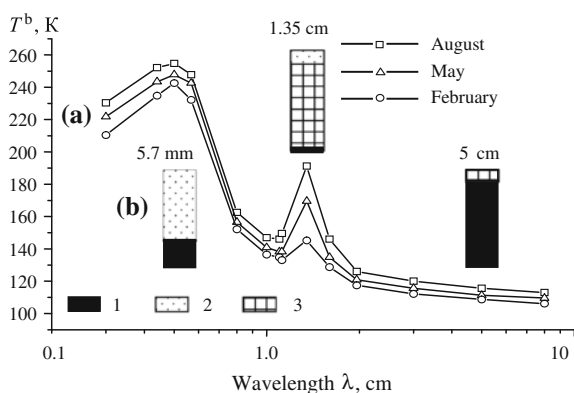
Fig. 3.5 Seasonal dynamics of the monthly mean values of the brightness temperature in the Gulf Stream active zone (**a**) and the relative contribution of the parameters (*1*) t_s, (*2*) $t_a(0)$, and (*3*) Q in the T^b variations (**b**)

dependence brightness temperature versus total vapor content of the atmosphere at the wavelength 1.35 cm varied from 14.4 K g^{-1} cm^{-2} between May and August to 17.3 K g^{-1} cm^{-2} between February and May. These results are in agreement with well-known estimates obtained for shorter periods (hours, weeks) (Basharinov et al. 1974; Shutko 1986).

3.3.4 Relationships Between Monthly Mean Differences of the Ocean Surface and Atmosphere Near-Surface Temperatures and the Intensity of SOA's Natural Radiation

The natural radiation of the SOA provides information on the ocean surface temperature and the near-surface air temperature in appropriate spectral intervals. This suggests the idea of their use for determining the difference between parameters t_s and t_a, which is the key factor of heat and water exchange at the ocean–atmosphere interface. In fact, the parameter t_s can be determined *directly* with the data of measurements of the SOA brightness temperature at the wavelength 5 cm or radiation temperature at the wavelength 10 mcm; estimates of the parameter t_a can be derived *directly* from the SOA brightness temperature at the vicinity of the resonance line 5 mm or *indirectly* from the SOA brightness temperature at the wavelength 1.35 cm (if one is to take into account a close correlation between parameters t_a and Q in a wide range of time scales, as discussed in Chap. 1).

We examined the possibility of using the SOA intensity radiation for microwaves and infrareds in an analysis of seasonal dynamics of the monthly mean difference $\Delta t = t_s - t_a$. We studied the relationships between this parameter and various pairs of monthly mean values of $I(\lambda_1)$, $I(\lambda_2)$ for different combinations of λ_1 and λ_2 and the parameter Δt for the Gulf Stream EAZO. The initial values of Δt and estimates of seasonal variations of monthly mean brightness (radiation) temperatures were computed by taking the monthly mean values of parameters t_s, t_a, a, and $\rho(0)$ into account (Table 3.4).

Table 3.4 Seasonal variations of monthly mean values for the parameter Δt and brightness (radiative) temperatures in the active zone of the Gulf Stream

Variations of initial characteristics	Time periods (seasons)			
	February–May	May–August	August–November	November–February
$\Delta(\Delta t)$, °C	−1.5	−1	3	−0.5
ΔT^r(10 mcm), K	4.1	6.2	−3.2	−7.1
ΔT^b(5.7 mm), K	5.6	6.8	−6.4	−6
ΔT^b(1.35 cm), K	24	21.1	−34.9	−10.2
ΔT^b(5 cm), K	2.5	3.6	−2.5	−3.6

On the basis of the data shown in Table 3.4, we analyzed the following regressions:

$$\Delta_i(\Delta t) = k_1 \Delta T_{i1} + k_2 \Delta T_{i2}; \; i = 1, \ldots, 4, \tag{3.8}$$

where the indices i_1, i_2 applied to brightness (radiation) contrasts mean one or another wavelength, and the index i applied to the parameter Δt means one or another season of a year. It is supposed that the coefficients k_1, k_2 remain the same for all seasons.

To evaluate the effectiveness of the procedure (3.8) for estimating the seasonal variations of Δt, the following criteria are used:

1. The index k, which displays the steadiness of estimates of $\Delta_i(\Delta t)$ to errors of the values ΔT_{i1}, ΔT_{i2}:

$$k = (k_1 + k_2)^{1/2};$$

2.

   The discrepancy δt between the left-hand and right-hand members of (3.8)—that is, between real values of $\Delta_i(\Delta t)$ and their estimates:

$$\delta T = [1/4 \sum \Delta_i - (k_1 \Delta_{i1} + k_2 \Delta_{i2})]^{1/2}; \; i = 1, \ldots, 4$$

The results of computations for the criteria δt and k for several pairs of λ_1 and λ_2 are listed in Table 3.5.

As shown in Table 3.5, the parameters δt and, especially, k greatly increase if the spectral intervals λ_1 and λ_2 duplicate one another. For example, this is true for case 3 because both wavelengths (10 mcm and 5 cm) provide similar information, mainly on the ocean surface temperature t_s and its seasonal variations.

An increase of the number of spectral intervals from 2 to 3 results in a decrease of the value δt by approximately 3 times; at the same time, the coefficient k increases by 2–3 times. The minimum values of criteria k are ensured if only one wavelength is used; however, the value of δt becomes unacceptable in this case. For example, for $\lambda = 10$ mcm, $\delta t = 3.1$ °C and $k = 0.16$, whereas for $\lambda = 1.35$ cm, $\delta t = 1.4$ °C and $k = 0.067$.

The best results (minimum values of k and δt) ensure the pairs of λ_1 and λ_2, which include the wavelengths 1.35 cm: 10 mcm and 1.35 cm (case 2), 5.7 mm and 1.35 cm (case 4), and 1.35 cm and 5 cm (case 6). Here, as is typical for modern

Table 3.5 Values of the criteria k and δt for different combinations of wavelengths

Case	λ_1 and λ_2	δT, °C	k, °C K^{-1}
1	10 mcm and 5.7 mm	0.1	1.18
2	10 mcm and 1.35 cm	0.9	0.24
3	10 mcm and 5 cm	0.33	4.2
4	5.7 mm and 1.35 cm	0.22	0.35
5	5.7 mm and 5 cm	0.39	2.86
6	1.35 cm and 5 cm	0.25	0.46

radiometric values of errors ΔT_{i1}, ΔT_{i2}, it is possible to determine the accuracy of the parameter δt estimates to 0.25–0.3 °C and, therefore, to derive reliable estimates of seasonal variations of the monthly mean differences Δt, which vary from 0.5 to 3 °C in the EAZO Gulf Stream.

The results of our study show that it is sufficient to merely use a pair of wavelengths to estimate the parameter Δt and its seasonal variations for the accuracy required by oceanologists and climatologists, despite the fact that the SOA's radiation characteristics depend not only on the parameters t_s and t_a, but also on the air humidity. This fact, which is substantial for understanding the remote diagnostic capabilities of the SOA heat interface for microwaves and infrareds, can be justified solely by the close correlation between monthly mean temperature and humidity characteristics of the atmosphere appearing in this zone and in the middle and high latitudes.

3.4   Brightness Temperature as a Characteristic of Seasonal and Interannual Dynamics of Ocean–Atmosphere Heat Interaction

3.4.1 t_s, t_a Loops as Characteristics of Heat Exchange Between the Ocean and Atmosphere

Here, we examine one approach for data utilization of long-term MCW radiometric measurements resting upon the method (Lappo et al. 1990) for determining integral (averaged per year) sensible and latent fluxes at the SOA interface, which prevail in climatic studies. The method is based on the fact discovered by authors that the magnitude of integral heat flux depends not only on the values of monthly mean ocean surface temperature (t_s) and air near-surface atmosphere temperature (t_a), but on forestalling (lag) one of these with respect to another during a year cycle. One ought to keep in mind the fact that parameters t_s and t_a adapt one to another over a year or longer periods; their average values during these periods are practically equal. In *seasonal* time scales, when intending to estimate the intensity of the ocean–atmosphere heat exchange and the characteristics of this process in various situations (either a heat influx is directed from the ocean to atmosphere or from the atmosphere to ocean), it is necessary to take into account the degree of match (mismatch) of these parameters (Lappo et al. 1990). The interannual variations of monthly mean parameters t_s and t_a can be visually presented in the form of specific trajectories—(t_s, t_a) loops in the two-dimensional system of coordinates (see Fig. 3.6). Namely, the availability of the time shift between the evolutions of the parameters t_s and t_a predetermines their visual presentation. It can be shown that geometric characteristics (e.g., the loop squares and their orientations, the degree of distinctions of their forms from the rectangular ones) can serve as quantitative characteristics of the intensity of heat processes at the SOA interface.
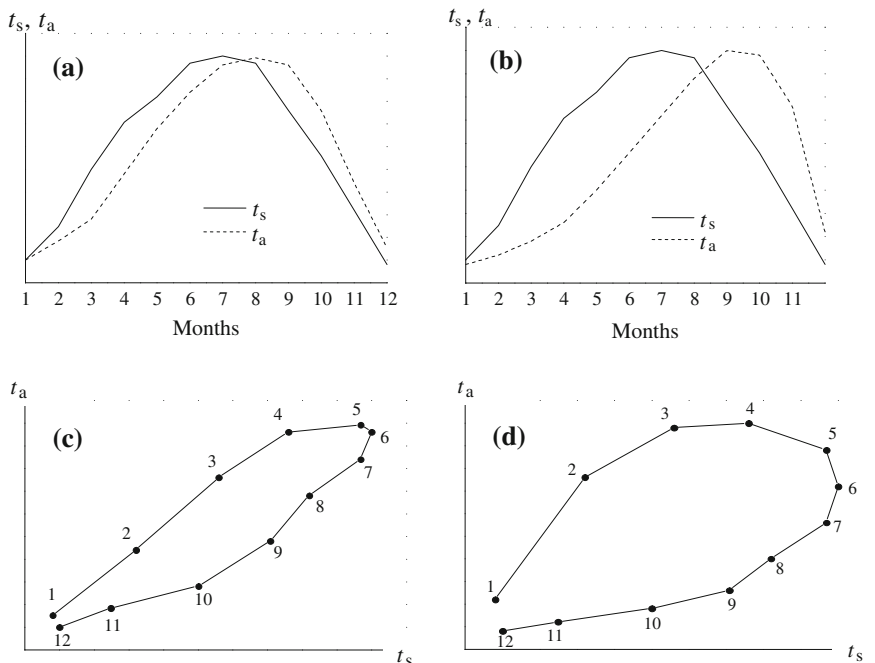
Fig. 3.6 Annual evolutions of monthly mean parameters t_s and t_a (**a**, **b**) and corresponding phase trajectories (**c**, **d**): the figures denote the months of the year

Taking into account the close correlation between the SOA's own characteristics (oceanographic, meteorological, and aerologic characteristics) and its MCW and IR radiation characteristics, we can expect that this method is effective if we use in place of parameters t_s and t_a suitable values of brightness (radiation) temperatures of the SOA for estimating the intensity of heat interchanges between the ocean and atmosphere in different areas of the World Ocean and estimate the annual heat fluxes and their interannual variability (Grankov 1992).

3.4.2 Using Brightness Temperature Loops to Estimate Annual Heat Fluxes

Because of the sensitivity of the SOA natural MCW and IR radiation to variations of the oceanic surface and atmospheric near-surface temperature, we can construct some analog of the processes existing at the SOA interface. That is, we can build radiation images of the annual t_s, t_a cycles using, for example, the brightness temperature in the spectral interval 3–8 cm as initial data, where the highest possible values of sensitivity of the parameter T^b to variations of the parameter t_s is

observed, and the brightness temperature at the wavelength 1.35 cm, which is a considerable source of information on the atmospheric temperature and humidity characteristics.

In comparison with traditional methods of estimating annual heat fluxes based on the separated determination of the parameters t_s, t_a as the input values used in the bulk formulas, the peculiarity of this approach consists of a higher stability of the estimates sought under the effect of accidental errors. In this case, the final estimates of heat fluxes are based not only on the selected (monthly mean) samples, but they assimilate their seasonal dynamics as a whole—that is, the possibility of accumulation of these data is used. If the measurements of the SOA brightness temperature are compared to the values of heat fluxes gathered a few times in a year in reference zones of the World Ocean, we can successfully estimate annual heat fluxes and their interannual variability.

We studied the possibilities of MCW radiometric methods for determining annual sensible heat fluxes by way of comparing the characteristics of the brightness temperature annual loops with the climatic values of the OST and the atmospheric near-surface and integral humidity in Norwegian, Newfoundland, and Gulf Stream active zones of the North Atlantic (taken from Handbook 1977; see Fig. 3.7 for the Newfoundland and Gulf Stream EAZO examples).

The calculations were made using the technique described in Sect. 3.3 for the wavelengths 1.35 and 3.4 cm, which are traditionally exploited in meteorological and oceanographic satellites. From these results, it is seen that the ratio between the loop squares for these EAZOs is 1: 1.25: 2.33. The results of the analysis of climatic (archival) data shows the following:

1. The ratio between the annual fluxes of sensible heat in the Newfoundland and Norwegian active zones was calculated as 1.08 (estimations of the State
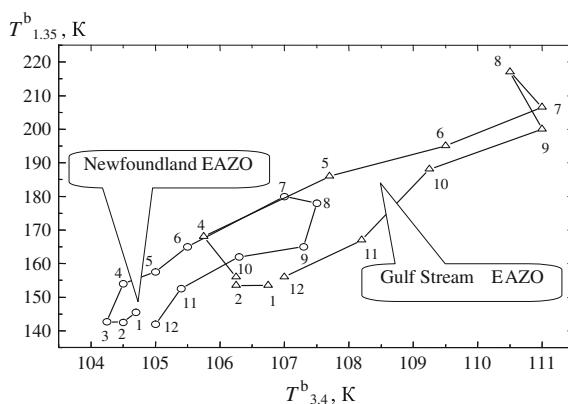
Fig. 3.7 Seasonal evolutions of the SOA monthly mean brightness temperatures at the wavelengths 1.35 and 3.4 cm in the Newfoundland and Gulf Stream active zones of the North Atlantic. Figures show the months of the yearly cycle, counted from the January

Oceanographic Institute [SOI]), 1.16 (the Main Geophysical Observatory), and 1.41 (the Institute of the Water Problems [IWP]).

2. The ratio between the annual fluxes of sensible heat between the Gulf Stream and Norwegian active zones varies from 1.24 (SOI) to 1.59 (IWP).

Excessive values of the annual sensible heat flux (a square of the $T_{1.35}^b - T_{3.4}^b$ loop) in the Gulf Stream EAZO can be explained by the specifics of this oceanic area—namely, by dominating the component of latent heat in comparison with sensible heat as a result of intensive evaporations from the ocean surface.

The estimates of annual heat fluxes made by oceanologists strongly differ from one to another versions (see Table 3.6). This gives rise to some problems in the validation of results of MCW radiometric sensing of heat processes in the SOA interface. Also, considerable scatter of zonal averaged surface latent heat fluxes is discovered when comparing various sources, such as Comprehensive Ocean–Atmosphere Data Set (COADS), National Centers for Environmental Prediction (NCEP), European Centre for Medium Weather Forecasts (ECMWF), Goddard Satellite-Based Surface Turbulent Fluxes (GSSTF), and Japanese Ocean Flux Data Sets with Use of Remote Sensing Observations (J-OFURO). It follows from the data cited in Curry et al. (2004) and Kubota et al. (2002) that variations of the estimates of climatic monthly mean latent heat fluxes are of 50–60 W m^{-2} for their mean values of 140–150 W m^{-2} (for tropical north and south belts) and 15–20 W m^{-2} versus 70–90 W m^{-2} (for high latitudes in northern hemisphere). The latent flux scatter for high latitudes in the southern hemisphere is even more.

Table 3.6 Estimates of the annual heat fluxes in active zones of the North Atlantic

Author, year	Heat fluxes, W m^{-2}			
	Norwegian EAZO	Newfoundland EAZO	Gulf Stream EAZO	Tropical EAZO
Budyko (1962)	140	230	285	170
Bunker (1976)	150	240	380	165
Mintz (1979)	110	235	220	180
Lappo et al. (1990)	200	245	385	185
Birman et al. (1983)	70	120	185	155
Strokina (1989)	90	235	240	170
Grassl et al. (2000)	120	120	200	150

3.5 Conclusion

1. We presented a possible modification of bulk formulas used for calculating the synoptic surface fluxes of sensible and latent heat using combinations of ocean-atmosphere system parameters that are directly related to satellite-derived characteristics of the MCW and IR natural radiation of the system.

2. **The MCW brightness (IR radiation) temperature of the** ocean–atmosphere **system in the spectral bands of resonant absorption of its natural radiation in** atmospheric water vapor and **molecular oxygen can be used as a** direct **characteristic of** seasonal **and** interannual **variability of the processes of heat interaction at the ocean–atmosphere interface.**

References

Arefjev VN (1991) Molecular absorption of emission in the window of relative transparency of the atmosphere 8-13 mcm (review). Fizika Atmosfery i Okeana 27:1187 − 1225 In Russian.

Basharinov AE, Gurvich AS, Egorov ST (1974) Radio emission of the planet Earth. Nauka, Moscow In Russian.

Birman BA, Larin DA, Pozdnyakova TG (1983) Some questions of climatology of heat exchanges in energy active zones of the World ocean. Meteorologiya I Gidrologiya 5:79 − 86 In Russian.

Budyko MI (1962) The Earth heat balance atlas. AN SSSR, Moscow In Russian.

Bunker AF (1976) Computations of surface energy flux and annual sea-air interaction cycles of the North Atlantic ocean. Mon Wea Rev 96:1122 − 1140.

Curry JA, Bentamy A, Bourassa A (2004) Satellite-based datasets of surface turbulent fluxes over the global oceans are being evaluated and improved Americ Meteorol Soc 3:409 − 424.

Grankov AG (1992) Microwave-radiometric diagnostics of integral fluxes of sensible heat at the ocean-atmosphere boundary. Izvestija, Atmosph Oceanic Phys. 28:883 − 889.

Grankov AG, Milshin AA (1994) On correlation of the near-surface and total atmosphere humidity with the near-surface air temperature. Meteorologiya i Gidrologiya 10:79 − 81 In Russian.

Grankov AG, Milshin AA (1995) A study of intercorrelation between thermodinamical parameters of the atmosphere for validating satellite MCW and IR-radiometric methods of determining its near-surface temperature. Institute of Radioengineering and Electronics RAS (Preprint No. 3 (603), Fryazino In Russian.

Grankov AG, Novichikhin EP (1997) Formulas oh heat and moisture exchange between ocean and atmosphere used in radiometric satellite data assimilation. Russian Meteorology and Hydrology Allerton Press 1:81 − 90.

Grankov AG (2011) On the role of the near-surface wind speed when calculating the surface heat fluxes in ocean with the data of experiment ATLANTEX-90. Issledovaniya Zemli iz kosmosa, 5:11 − 14 In Russian.

Grankov AG, Usov PP (1994) Intercommunication between monthly mean air-sea temperature differences and natural microwave and infrared radiation. Meteorologiya i Gidrologiya 6:79 − 89 In Russian.

Grassl H, Jost V, Schulz J et al (2000) The Hamburg ocean-atmosphere parameters and fluxes from satellite data (HOAPS): A climatological atlas of satellite-derived air-sea interaction parameters over the world oceans. Report No. 312. MPI, Hamburg.

Guidelines (1981) Calculation of turbulent fluxes of heat, moisture, and the momentum fluxes over the ocean. GGO, Leningrad In Russian.

Gulev SK, Kolinko AV, Lappo SS (1994) Synoptic interaction between the ocean and atmosphere in middle latitudes. Gidrometeoizdat, St. Petersburg In Russian.

Handbook (1977) Atlas of the oceans: Atlantic and Indian oceans. MO SSSR, Moscow In Russian.

Handbook (1979) Averaged month, 10 and 5-day periods values of the air water and temperature, their difference and wind speed in selected regions of the North Atlantic (1953-1974 years). VNIIGMI-MZD, Obninsk In Russian.

Kubota M., Iwasaka N, Kizu S, Knoda M (2002) Japanese ocean flux data sets with use of remote sensing observations (J-OFURO). J Oceanography 58: 213–215.

Lappo SS, Gulev SK, Rozhdestvenskii AE (1990) Large-scale heat interaction in the ocean–atmosphere system and energy-active zones in the world ocean. Gidrometeoizdat, Leningrad In Russian.

Lebedeva EL (1991) Integral water vapor content of the atmosphere as the characteristic of air-sea interaction in the Newfoundland energy active zone Trudy GGO, Leningrad 535:32-45 In Russian.

Liu WT (1986) Statistical relations between monthly mean precipitable water and surface-level humidity over global oceans. Mon Wea Rev 114:1591 − 1602.

Liu WT (1988) Moisture and latent flux variabilities in the tropical Pacific derived from satellite data. J Geophys Res 93:6749 − 6760.

Mintz Y (1979) Simulation of the oceanic general circulation GARP Publ. Ser. 2:607 − 687.

Paramonova NN (1985) Comparison of results of new laboratory measurements of emission absorption in water vapor in the window 8 − 12 mcm with data of natural experiments. Trudy GGO, Leningrad 496:79 − 84 In Russian.

Shutko AM (1986) Microwave radiometry of water surface and soils. Nauka, Moscow In Russian.

Snopkov VG (1977) On correlation between the atmosphere water vapor and the near surface humidity seasonal variations of the water vapor content over the Atlantic. Meteorologiya i Gidrologiya 12:38 − 42 In Russian.

Strokina LA (1989) Heat balance of the oceans surface (handbook) Gidrometeoizdat, Leningrad In Russian.

Xrgian AX (1978) Physics of the atmosphere. vol.1, Gidrometeoizdat, Leningrad In Russian.

Zhevakin SA, Naumov AP (1964) Absorption of centimeter and millimeter radiowaves in water vapor of the atmosphere. Radiotekhnika i Elektronika 9:1327 − 1337 In Russian.

Zhevakin SA, Naumov AP (1965) On determining the coefficient of absorption of centimeter radiowaves in atmospheric oxygen. Radiotekhnika i Elektronika 10:987 − 996 In Russian.

Chapter 4
Influence of Vertical Heat Transfer on the Relationships Between the SOA MCW and IR Radiation Intensity and Surface Heat Fluxes: Modeling

4.1 Model of Heat Interaction Between the Oceanic and Atmospheric Boundary Layers

To study the thermal response of the atmospheric and oceanic boundary layers (hereafter ABL and OBL, respectively) to heat perturbation at their interface, the following model is used:

$$
\begin{aligned}
dT_1/dt &= (q_{ha} - q_{hs})/(\rho_a c_a h_1), \\
dT_2/dt &= (q_{hs} - q_{hw} - Le_s + R)/(\rho_w c_w h_2), \\
dq/dt &= (e_a - e_s)/(\rho_a h_1),
\end{aligned}
\tag{4.1}
$$

$$
T_1 = T_{10}, \; T_2 = T_{20}, \; q = q_o (t = 0)
\tag{4.2}
$$

Here, the values T_1 and T_2 are denoted as the temperatures of the atmospheric and oceanic boundary layers, respectively; q is the specific humidity in the ABL; h_1 and h_2 are the thickness of the ABL and OBL, respectively; ρ_a and ρ_w are the air and water densities, respectively; c_a and c_w are the air and water specific capacities, respectively; q_{ha} and q_{hw} are the latent heat fluxes at the air–water interface; e_s is the moisture flux (rate of evaporation/condensation) at the water surface; e_a is the moisture flux at the upper boundary of the ABL; L is the specific heat of evaporation; and R is the sun's shortwave radiation flux heating the ocean surface.

The temperature-moisture regime of the SOA is parameterized under the following assumptions:

- The simulated system is laterally homogeneous.
- The boundary layers of the atmosphere and ocean are well mixed, such that the T_1, T_2, and q values are independent of the height (depth) within the ABL and OBL.
- The boundary-layer thickness h_1 and h_2 remain unchanged with time.

- The ABL heat budget is controlled only by sensible heat fluxes q_{ha} and q_{hs}.
- The OBL heat budget is controlled only by sensible heat q_{hw} and q_{hs} and also by the latent heat Le_s, resulting from water surface evaporation (condensation), and by the solar radiation flux R, which is entirely absorbed within the OBL.
- The ABL moisture budget is determined by the surface evaporation e_s and the moisture exchange e_a with the overlying air layer; phase conversions of water do not occur in the ABL.
- The ABL and OBL temperature regimes are independent of the electromagnetic radiation intensity in the ocean–atmosphere system.

The problem is formulated analogously to Grankov and Resnjanskii (1998), with the only difference being that in the evolution of the ABL moisture regime, the respective component of the OBL heat budget is taken into account.

To solve the problem, it is necessary to express the fluxes q_{hs}, q_{ha}, q_{hw}, e_s, and e_a in terms of the sought variables and q as well as the external conditions. The radiation flux R is assumed to be specified. It serves as a thermal perturbation. The simulation of the response to this perturbation is the essence of the given problem. To determine the fluxes, the following expressions are used:

$$
\begin{aligned}
q_{hs} &= c_1 \rho_a c_a V_a (T_1 - T_2), \\
e_s &= c_2 \rho_a V_a (q - q_s), \\
q_{ha} &= c_3 \rho_a c_a V_a (T_a - T_1) \\
e_a &= c_4 \rho_a V_a (q_a - q), \\
q_{hw} &= c_5 \rho_w c_w u_w (T_2 - T_w),
\end{aligned}
\tag{4.3}
$$

The first two expressions are conventional bulk formulas, and the last three are based on the assumption that the fluxes q_{ha}, q_{hw}, and e_a at the outer boundaries of the ABL and OBL, to first approximation, can be expressed similarly through the values of the q_{hs} and e_s with a proper choice of the transfer coefficients c_3, c_4, and c_5.

In Formula (4.3), T_a is the air temperature just above the ABL; T_w is the water beneath the OBL; q_w is the saturation-specific humidity at the water temperature T_2; V_a is the mean near-surface wind speed; and u_s is the mean oceanic current; and c_1, c_2, …, c_5 are some nondimensional transfer coefficients.

Using one more assumption of the linearized dependence of saturation humidity q_w versus the temperature T_2,

$$
q_w = q_r + a(T_2 - T_r),
\tag{4.4}
$$

where q_r and T_r are the reference humidity and temperature; the set of Eq. (4.1) taking into account (3.3) and (4.4) can be rewritten in a vector form as follows:

$$
dy/dt = Ay + f,
\tag{4.5}
$$

where $y = (T_1, T_2, q)$ is the vector of the sought variables. $f = (f_1, f_2, f_3)$ is the vector of three terms:

$$
\begin{aligned}
f_1 &= (c_3 u_a / h_1) T_a, \\
f_2 &= [R + c_5 \rho_w c_s u_s T_s - c_2 \rho_a u_a L(q_r - aT_r))]; \\
f_3 &= (u_a / h_1)[c_4 q + c_2 (q_r - aT_r)];
\end{aligned}
\tag{4.6}
$$

$A = |a_{ik}|$, $i, k = 1, 2, 3$, is the matrix of coefficients. Unlike f, the expressions for a_{ik} comprise only the model parameters h_1, h_2, a, c_1, c_2, …, but not R, T_a, T_w, and q_a, which characterize the external conditions of forcing with respect to the ABL (OBL).

The solution of (4.5) is written as follows:

$$
\begin{aligned}
T_1 &= C_1 e^{r_1 t} + C_2 e^{r_2 t} + C_3 e^{r_3 t} + T_1^*, \\
T_2 &= C_1 p_1 e^{r_1 t} + C_2 p_2 e^{r_2 t} + C_3 p_3 e^{r_3 t} + T_2^*, \\
q &= C_1 s_1 e^{r_1 t} + C_2 s_2 e^{r_2 t} + s_3 C_3 e^{r_3 t} + q^*,
\end{aligned}
\tag{4.7}
$$

Here, r_i, $(i = 1, 2, 3)$ are the roots of a characteristic equation of the homogeneous system (4.5) as shown in Table (4.1).

The values T_1^*, T_2^*, and q are the partial solutions of the inhomogeneous system (4.7), sought by the method of variation of constants and expressed in terms of a_{ik}, f_i, and r_i; p_i, s_i, and C_i are some combinations of coefficients and initial values T_{10}, T_{20}, q_o from condition (4.2).

Numerical estimates show that, for typical values of the model parameters, the determinant of the characteristics of the Eq. (4.5) is negative; all of its roots r_j, $(i = 1, 2, 3)$ are real, different, and negative. Hence, the solution (4.7) describes the adaptation of the ABL-OBL system to the external conditions (factors) R, T_a, (t_a), T_w, (t_s) q_a, which tend with time to a stable state (T_1^*, T_2^*, q^*). The characteristic adaptation time $[\min(|r_i|)]^{-1}$ is about 18 h for typical values of the parameters: $\rho_a = 1.25$ kg m^{-3}; $\rho_w = 10^3$ kg m^{-3}; $c_a = 10^3$ J kg deg^{-1}; $c_w = 4100$ J kg deg^{-1}; $h_1 = 1500$ m; $h_2 = 30$ m; $L = 2.4 \times 10^6$ J kg^{-1}; $R = 200$ W/m^2; $V_a = 10$ m s^{-1}; $u_w = 0.1$ m s^{-1}; $c_i = 1.3 \times 10^{-3}$ $(i = 1, 2, …, 5)$; $T_r = 10$ °C; $q_r = 7.5 \times 10^{-2}$ kg kg^{-1}; and $a = 5 \times 10^{-4}$ deg^{-1}.

Table 4.1 Matrix of the coefficients a_{ij} characterizing the equation of the system (4.7)

$a_{11} - r$	a_{12}	a_{13}
a_{21}	$a_{22} - r$	a_{23}
a_{31}	a_{32}	$a_{33} - r$

4.2 Parameterized Radiation Model of the SOA for Microwaves and Infrareds

In the framework of a plane-layered model of thermal radiation (absorption) in the ocean–atmosphere system (Fig. 2.1), it is possible to analyze the processes of electromagnetic energy transfer in various layers, as well as to estimate the intensity of these radiation components, which can be registered with satellite (A), airplane (B), and shipboard (C) equipment. The model (2.1)–(2.5) (see Chap. 2) cannot be used immediately in this case because the initial meteorological and thermal characteristics of the air are assigned not in the form of their vertical distributions, but are parameterized for separate atmospheric layer forms (Fig. 4.1).

Satellite Equipment (A)

In satellite observations, the ocean–atmosphere natural MCW radiation I_{sat} is composed of the intensity of the free-atmosphere radiation I_a and intensity of the upward radiation flux $I_1^\uparrow$ at the top of the ABL attenuated in the free atmosphere (multiplier G_a):

$$I_{sat} = I_a + I_1^\uparrow G_a, \tag{4.8}$$

Here, $I_1^\uparrow = I_1 + (I_1^\downarrow R_{21} + I_2)G_1$ is the intensity of the upward radiation flux at the top of the ABL; $I_1^\downarrow = I_1 + I_a$; G_1 is the intensity of the downward radiation flux at the bottom of the ABL; I_1 is the intensity of natural radiation of the ABL; I_2 is the intensity of the OBL natural radiation; G_1 is the integral attenuation of radiation in the ABL; and R_{21} is the coefficient of reflection of the downward radiation flux $I_1^\downarrow$ from the water surface.
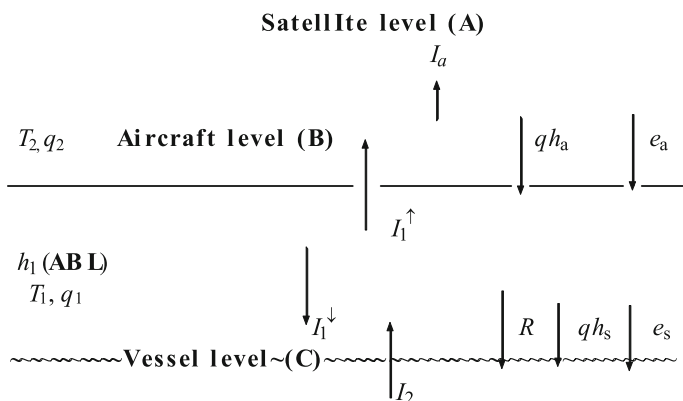
Fig. 4.1 Parameterization scheme of the main characteristics of thermal and electromagnetic energy transfer in the ocean–atmosphere system

It is assumed that the electrophysical parameters of the ABL and the free atmosphere, in spite of the difference (in a general case) between their temperature and humidity characteristics, are consistent with each other. That is, the reflectivity at their interface is absent or negligibly small compared with R_{21}.

Airplane Equipment (B)

In observations from an aircraft (at the top of the ABL), the ocean–atmosphere radiation intensity I_{air} is determined solely by the component $I_1^\uparrow$:

$$I_{air} = I_1^\uparrow \tag{4.9}$$

Shipboard Equipment (C)

In shipboard observations (at the lower boundary of the ABL), the intensity of radiation I_{ship} is computed as follows:

$$I_{ship} = I_2 + I_1^\downarrow R_{21} \tag{4.10}$$

The characteristics of natural radiation of the boundary (I_1) and free (I_a) atmosphere in expressions (4.8)–(4.10) are related to the corresponding values of temperature T_1, T_a and of the integral absorption G_1, G_a of this media:

$$I_1 = T_1(1 - G_1); I_a = T_a(1 - G_a) \tag{4.11}$$

An intensity of the thermal radiation of the ocean surface I_2 is proportional to $I_2 = \text{æ} \, T_2$ in the MCW wavelength range and $I_2 = \delta \, B(T_2)$ in the IR band. Here, T_2 is the OBL temperature; $B(T_2)$ is Planck's function with T_2 as an argument; æ is the emissivity of the ocean surface at microwaves; and δ is the IR emissivity of the ocean surface.

4.3 Numerical Analysis of the Dynamics of Thermal and Electromagnetic Fluxes and Their Correlations

Numerical estimates were obtained for the temporal evolutions of fluxes q_h and q_e at the ABL–OBL interface boundary and the radiation fluxes I_{sat}, I_{air}, and I_{ship} in terms of the corresponding values of the brightness temperature at the wavelength range (5 mm–3 cm) and infrared radiation temperatures (8–12 mcm), after the ocean–atmosphere system was forced out of thermal equilibrium. The estimates were obtained for typical values of thermal constants (air and density, heat capacity, specific heat of evaporation (condensation), heat and humidity interchange coefficients), ABL and OBL thickness, mean wind, and current velocities, as given previously.

The computations were performed in the following sequence:

(a) derivation of the system solution (4.7) as related to the tasks (4.1) and (4.2) in terms of the ocean–atmosphere interface layer variables T_1, T_2, and q_a for given values of the thermodynamic parameters T_w, T_1, and q_a at the outer boundaries of the ABL and OBL and of the solar heat flux R at the water surface;

(b) determination of heat fluxes q_h and q_e at the ocean–atmosphere interface from the defined values of T_1, T_2, and q_a;

(c) determination of electromagnetic fluxes I_{sat}, I_{air}, and I_{ship} from the calculated values of parameters T_1, T_2, and q_a and specified values of T_1, T_2, and q_a;

(d) regression analysis of the interrelation between the evolutions of the q_h and q_e parameters and the evolutions of the I_{sat}, I_{air}, and I_{ship} values in various MCW and IR spectral bands.

An analysis of the brightness temperature of the OBL-ABL system was carried out for the range of wavelengths from 5 mm to 3 cm, where the natural MCW radiation of the system is most sensitive to variations of temperature and humidity characteristics. The radiation temperature was used as a measure of natural IR radiation in the atmospheric window of 8–12 mcm. The atmospheric absorption was computed while accounting for the effect of the water vapor content (in MCW and IR bands), molecular oxygen (in the MCW bands), and the aerosol component (in the IR band) on the basis of theoretical relationships (Zhevakin and Naumov 1964, 1965). Semi-empirical relationships (Arefjev 1991; Paramonova 1985) were mainly used for infrareds.

The simulation of the dynamics of thermal and electromagnetic fluxes and an analysis of their interrelationships was performed for several variants differing in the character of the thermal energy outflow from the ocean–atmosphere interface toward the outer boundaries of the ABL and OBL and beyond their borders. This was achieved by the proper choice of parameters of the free atmosphere and of the lower quasi-homogeneous ocean in reference to the initial ABL and OBL conditions invariant in all cases ($T_{10} = T_{20} = 10$ °C, $q_0 = 6$ g kg^{-1}). The results given below illustrate the following variants:

(1) $T_w = T_a = 5$ °C; $q = 4$ g kg^{-1} (the heat propagates toward the outer boundary of the ABL and simultaneously to the outer boundary of the OBL);

(2) $T_w = 5$ °C; $T_a = 10$ °C; $q = 6$ g kg^{-1} (heat propagates only to the lower oceanic layer); and

(3) $T_w = 10$ °C; $T_a = 5$ °C; $q = 4$ g kg^{-1} (heat propagates only to the free atmosphere).

Figure 4.2 demonstrates the results of an analysis of the response of the ABL and OBL parameters T_1, T_2, and q, which determine natural MCW and IR radiation of the SOA, for the first (most general of the above-mentioned) variant. As seen from the figure, a complete adaptation of the SOA parameters to the impact of the solar radiation flux R occurs during 1–2 days; the adaptation of the ABL temperature occurs about twice as fast as that of the ABL parameters T_1 and q.
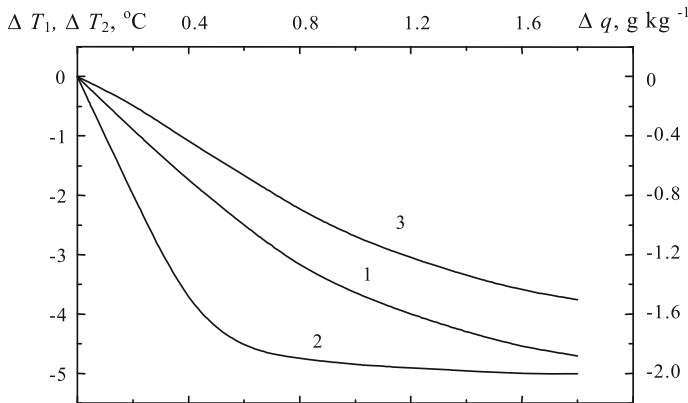
Fig. 4.2 The response of (*1*) ABL temperature T_1, (*2*) OBL temperature T_2, and (*3*) ABL humidity *q* to the thermal excitation of the SOA in the case of heat outflow from the ocean–atmosphere interface toward the outer boundaries of the ABL and OBL. The horizontal axis shows days and nights in fractions

The analysis of the corresponding variations of sensible and latent heat fluxes q_h and q_e shows that the response of heat fluxes and of the ocean–atmosphere brightness (radiation) temperature is also formed during 1–2 days. That is, it agrees with the time of adaptation of the ocean–atmosphere characteristics to the external influx *R*.

A regression analysis was performed to derive some relationship between variations of sensible and latent heat fluxes, Δq_h and Δq_e, and brightness ΔT^b (radiation ΔT^r) temperature variations at microwaves and infrareds, accordingly, for versions 1, 2, and 3 at different observation levels (from satellites, aircrafts, and vessels). In particular, the feasibility of approximation of Δq_h and Δq_e was examined for the case of the heat outflow in both directions from the ocean–atmosphere interface; the approximations were constructed as linear pair combinations of ΔT in different spectral bands (for the satellite level) and are shown in Fig. 4.3.

The solution of this problem involves the following:

(1) determination of regression coefficients between Δq_h, Δq_e, and ΔT in the initial stage of formation of the SOA response to a thermal perturbation (hatched area in Fig. 4.3);

(2) approximation of Δq_h and Δq_e using the computed regression coefficients; and

(3) extrapolation (prediction of the subsequent evolution) of Δq_h and Δq_e with the regression relationships derived in the initial stage with an account for the evolution of ΔT in the final stage of formation of the ocean–atmosphere response.

As seen from the Fig. 4.3, the variations of the intensity of the ocean–atmosphere natural radiation in the spectral windows ~ 10 mcm and ~ 5.7 mm provide the best reconstruction of the q_h and q_e fluxes in the entire time interval (two days) of the formation of the radiation and heat response.
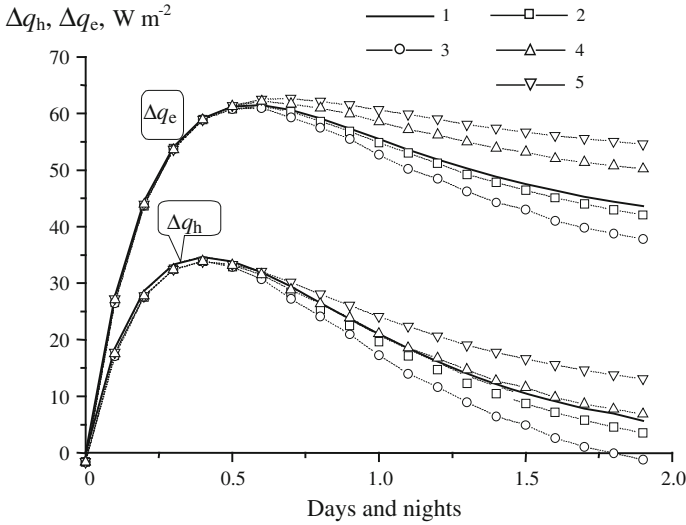
Fig. 4.3 Simulated results of approximation and extrapolation of sensible q_h and latent q_e fluxes (*1*) with the data of satellite passive radiometric measurements at the spectral intervals: 10 mcm, 5.7 mm (*2*), 10 mcm and 1.35 cm (*3*), 1.35 and 3.2 cm (*4*), 5.7 mm and 3.2 cm (*5*) (Grankov and Resnyanskii 1998)

The results of a regression analysis for different versions of heat outflow from the interface to the outer boundaries of the ABL and OBL are given more completely in Table 4.2.

It follows from these data that the lowest estimation errors $\delta(q_h)$ and $\delta(q_e)$ (a few percent of the amplitude of natural variations of these parameters) correspond in most cases to spectral intervals 10 and 5.7 mcm as well as 1.35 and 3.2 cm. The increase in the number of spectral intervals as degrees of freedom from two to three (or more) in the approximation of heat fluxes by MCW and IR radiation characteristics does not lead to any significant reduction of the errors.

The results of the regression analysis of heat fluxes at the ocean–atmosphere interface and electromagnetic fluxes at the top of the ABL (the aircraft level) are quite close to those given in Table 4.2. At the same time, the results of the regression analysis of the heat and electromagnetic fluxes at the lower boundary of the ABL (the vessel level), where the atmosphere influence is minimal, differ from the data in the table by substantially larger values of q_h and q_e, which in this case equal 5–6 W m^{-2} and are scarcely affected by the selection of the spectral intervals.

Table 4.2 Approximation errors δq_h and δq_e for fluxes q_h and q_e in different spectral bands for the overall (2-day) cycle of the SOA response as observed from satellite

Wavelength, cm (mcm)						Version 1		Version 2		Version 3	
10 mcm	0.57 cm	0.8 cm	1.35 cm	1.6 cm	3.2 cm	δq_h (Wm^{-2})	δq_e (Wm^{-2})	δq_h (Wm^{-2})	δq_e (Wm^{-2})	δq_h (Wm^{-2})	δq_e (Wm^{-2})
+	+					0.14	0.13	0.10	0.13	0.05	0.24
+		+				0.40	0.37	0.40	0.31	0.06	0.26
		+	+			0.91	1.18	0.91	1.21	0.08	0.25
	+		+		+	0.64	0.86	0.67	0.90	0.08	0.22
	+				+	0.20	0.46	0.16	0.46	0.42	0.27
			+			0.64	0.23	0.97	0.32	0.42	0.27
+	+					0.11	0.09	–	–	–	–
	+	+				0.10	0.08	–	–	–	–
+	+	+	+	+	+	0.10	0.08	–	–	–	–

The wavelengths involved into the analysis are marked by the sign "+"

4.4 Conclusion

1. The heat and moisture exchange processes in the ocean–atmosphere interface layer have a profound effect on the MCW and IR radiation characteristics—not only in the interface layer, but also in the entire atmosphere. This is evident from an analysis of the evolutions of the SOA brightness temperatures at the top of the ABL and in the free atmosphere, as well from a comparison of these data with the evolutions of heat fluxes at the ocean–atmosphere interface. One can see that the response of thermal and electromagnetic fluxes to the excitation of the system is developing during approximately the same time period (several days, typically).
2. A connection of the brightness and radiation temperatures at the top of the ABL and in the free atmosphere with sensible and latent heat fluxes at the SOA interface is most pronounced in certain spectral intervals; the main effect of the outflows from the ocean–atmosphere interface toward the outer boundaries of the ABL and OBL becomes more apparent in the regions of the atmospheric resonance absorption by molecular oxygen (~ 5 mm) and in the water vapor line 1.35 cm. Hence, the oxygen and water vapor atmospheric factors can serve as some transient parameters ("bridges") between the natural radiation of the SOA and the heat exchange intensity at its interface—not only on seasonal and synoptic scales, but also on smaller (daily, for example) time scales.
3. Because of the theoretical analysis fulfilled in the framework of the plane-layered problem, the brightness (radiation) temperature variations at the top of the ABL and in the free atmosphere caused by the vertical transfer of heat and water transfer in the interface of the system are of a few degrees of Kelvins (K). At the same time, as will be shown later (see Chap. 5), the satellite-derived estimates of SOA brightness temperature variations can reach the tens of K, as measured at the wavelength of 1.35 cm.

References

Arefjev VN (1991) Molecular absorption of emission in the window of relative transparency of the atmosphere 8−13 mcm (review). Fizika Atmosfery i Okeana 27:1187−1225 In Russian

Grankov AG, Resnjanskii JuD (1998) Modeling the response of the ocean-atmosphere natural radiation system to the pertrubation of a thermal equilibrium at the interface. Russian Meteorology and Hydrology, Allerton Press 11:57–65

Paramonova NN (1985) Comparison of results of new laboratory measurements of emission absorption in water vapor in the window 8−12 mcm with data of natural experiments. Trudy Glavnoi Geofizicheskoi Observatorii, Leningrad 496:79−84 In Russian

Zhevakin SA, Naumov AP (1964) Absorption of centimeter and millimeter radiowaves in water vapor of the atmosphere. Radiotekhnika i Elektronika 9:1327−1337 In Russian

Zhevakin SA, Naumov AP (1965) On determining the coefficient of absorption of centimeter radiowaves in atmospheric oxygen. Radiotekhnika i Elektronika 10:987−996 In Russian

Chapter 5
Influence of Horizontal Heat Transfer in the Atmosphere Boundary Layer on the Relationship Between the SOA's Brightness Temperature and Surface Heat Fluxes: Modeling

5.1 Dependence of the Atmosphere Boundary Layer's Meteorological Structure on Horizontal Heat Transfer

5.1.1 Objectives and Approach

We conducted an analysis of the role of horizontal (advective) heat transfer in the development of the vertical structure of the atmospheric boundary layer. The response of natural MCW radiation intensity (brightness temperature) of the ocean–atmosphere system at various wavelengths to variations of air temperature and humidity that are excited by horizontal heat transfer associated with atmospheric cyclones is also considered. In this study, the atmosphere boundary layer (ABL) plays a peculiar role for the following reasons:

1. Arising horizontal advective heat fluxes in the ABL result in perturbations of the vertical profiles of air temperature and humidity.
2. Changes in the vertical profiles of air temperature and humidity give rise to changes of substantial characteristics of the heat balance in the ABL–OBL (ocean boundary layer) system as vertical turbulent heat and moisture fluxes.
3. At the same time, changes in the vertical profiles of air temperature and humidity determine variations in the SOA brightness temperature.

These statements are the basis of our analysis of the relationships between variations of the horizontal advective heat fluxes, vertical turbulent heat and moisture fluxes in ABL, and the SOA brightness temperature within atmospheric cyclonic disturbances. Based on an analysis of this study, we can address the possibility of using the SOA brightness temperature as an indicator of heat and moisture fluxes at the ocean–atmosphere boundary for different types of ABL stratification and different configurations of horizontal transport.

5.1.2 *Heat and Moisture Transfer Model*

The structure of meteorological fields in the ABL determining the ocean–atmosphere energy exchange and radiance fluxes registered at the atmosphere upper boundary form primarily under the influence of vertically developing processes and can be described in the framework of one-dimensional models (Zilitinkevich 1970; Stull 1997). Yet in certain situations, particularly near frontal boundaries connected with intense cyclones or in the neighborhood of the land–sea margin, where the horizontal gradients of meteorological fields become sharper, the influence of horizontal advection may become meaningful.

Here, we use an ABL model for the description of its structure and related vertical heat fluxes. The model was formulated in the framework of traditional approximations regarding the parameterizations of vertical turbulent fluxes, but it accounts for horizontal heat and moisture advection:

$$f(v - v_g) + \frac{1}{\rho} \frac{\partial \tau_x}{\partial z} = 0, \quad -f(u - u_g) + \frac{1}{\rho} \frac{\partial \tau_y}{\partial z} = 0, \tag{5.1}$$

$$\frac{1}{\rho c_p} \frac{\partial F_T}{\partial z} + u \cdot \nabla_x T + v \cdot \nabla_y T = 0, \tag{5.2}$$

$$\frac{1}{\rho} \frac{\partial F_q}{\partial z} + u \cdot \nabla_x q + v \cdot \nabla_y q = 0, \tag{5.3}$$

$$u = u_h = u_g, \quad v = v_h = v_g, \quad T = T_h, \quad q = q_h \\ \text{at } z = h \sim 1500 \text{ m } (\sim 850 \text{ mb}), \tag{5.4}$$

$$u = 0, \quad v = 0 \quad \text{at } z = z_0, \tag{5.5}$$

$$T = T_0, \quad q = q_0 \quad \text{at } z = z_{0H} \tag{5.6}$$

Here $\tau_x = -\rho \overline{u'w'}$ and $\tau_y = -\rho \overline{v'w'}$ are the components of vertical momentum flux (tangential stress); $F_T = \rho c_p \overline{T'w'}$ and $F_q = \rho \overline{q'w'}$ are vertical turbulent heat and moisture fluxes, correspondingly; $\mathbf{u} = $ (u, v) is the horizontal vector of the average motion velocity with components u and v along Cartesian coordinates x and y; w is the vertical velocity along coordinate z; T is air temperature; q is humidity; ρ is air density; c_p is its specific heat capacity at constant pressure; $\nabla_x T$ and $\nabla_y T$ are components of horizontal temperature gradient within ABL along x and y coordinates correspondingly; $\nabla_x q$ and $\nabla_y q$ are the similar components of air humidity; $u_g = -((1/(\rho f)) \cdot \partial P/\partial y$ and $v_g = ((1/(\rho f)) \cdot \partial P/\partial x$ are the horizontal components of geostrophic wind, which are assumed to be independent of height (independence of horizontal pressure gradient on z is a usual assumption in a boundary layer theory; Monin and Yaglom 1992); f is the Coriolis parameter; P is atmospheric pressure; h is ABL height; z_0 is roughness parameter for momentum

flux, and z_{0H} is the corresponding parameter for heat and moisture fluxes. Prime symbols designate turbulent fluctuations, and an overbar is a sign of statistical averaging.

Our model is based on the numerical solution of Eqs. (5.1)–(5.3), with the first-order closure scheme for the vertical turbulent fluxes:

$$\tau_x/\rho = -\overline{u'w'} = k_m \partial u/\partial z, \quad \tau_y/\rho = -\overline{v'w'} = k_m \partial v/\partial z, \tag{5.7}$$

$$F_T/(\rho c_p) = \overline{T'w'} = -k_H(\partial T/\partial z + g/c_p), \tag{5.8}$$

$$F_q/\rho = \overline{q'w'} = -k_H \partial q/\partial z, \tag{5.9}$$

This includes nonlinear dependences of coefficients of turbulent mixing

$$k_m = l_m^2 f_m(Ri)|\partial \mathbf{u}/\partial z|, \quad k_H = l_m l_H f_H(Ri)|\partial \mathbf{u}/\partial z| \tag{5.10}$$

from a local shift of the motion velocity $|\partial \mathbf{u}/\partial z|$ and density stratification characterized by local Richardson number:

$$Ri = \frac{g[(1/T)(\partial T/\partial z + g/c_p) + 0.61\,\partial q/\partial z]}{|\partial \mathbf{u}/\partial z|^2}$$

In these formulas, g/c_p is the adiabatic temperature gradient, g is gravity acceleration, q is the air specific heat capacity at constant pressure; l_m and l_H are mixing lengths at a neutral stratification specified by the Blackadar's formulae (Blackadar 1962); and f_m and f_H are dependent from Ri stability functions determined empirically.

The turbulent fluxes at the air–water boundary are determined by a classical Monin-Obukhov similarity theory for the near-surface atmosphere. The influence of horizontal inhomogeneity on a large scale (i.e., exceeding the sizes of small-scale turbulent eddies) is accounted for by adding the corresponding terms into the ABL Eqs. (5.2)–(5.3), in which the horizontal gradients of air temperature $\nabla T = (\nabla_x T, \nabla_y T)$ and its humidity $\nabla q = (\nabla_x q, \nabla_y q)$ are assumed to be known and are specified depending on the situation to be modeled.

Based on this model, we will estimate the influence of horizontal transports on the structure of meteorological fields within the ABL and on its energy exchange with the ocean.

5.1.3 Description of the Numerical Experiment

Three series of numerical experiments have been performed to quantitatively estimate the influence of horizontal transports. In doing so, three types of density stratification within the ABL were considered as reference background

conditions: 1) near neutral, 2) unstable, and 3) stable stratification. The background conditions are understood to be the cases of horizontal homogeneity, in which horizontal advection is absent. The changes of density stratification were specified through the variations of air temperature at the upper ABL boundary in the range of $T_h = 280-310$ K , while the temperature at the ocean–atmosphere interface was fixed at $T_0 = 300$ K. The height of the upper ABL boundary is assumed to be equal to 1400 m.

According to Gulev et al. (1994), seasonal recurrence of selected types of ABL stratification occurs in the Newfoundland energy active zone of the North Atlantic. For example, neutral or stable stratification (when the ocean–atmosphere temperature drops are small or slightly negative) are typical for the summer, whereas unstable stratification (when water is warmer than air) is most common in winter. The climatic recurrence of the meridional atmosphere circulation averages 40 %, whereas the zonal one is 60 % (Gulev et al. 1994).

To more distinctly describe the effects of horizontal advection, we selected rather large values of horizontal gradients at this stage—on the order of 5×10^{-5} K m^{-1} = 5 K 100 km^{-1}. Such sharpening of horizontal gradients, as compared with the usual values that are smaller by an order of magnitude, is observed near frontal zones related to intense atmospheric cyclones or to the vicinity of marginal zones between different types of underlying surfaces, such as the land–sea boundary.

Modeling of various types of background stratification was carried out through variations of air temperature at the ABL upper boundary under a fixed value of the ocean surface $T_0 = 300$ K and specific humidity q_h = 30 %: $T_h = 290$ K for the case of neutral stratification, $T_h = 280$ K for unstable stratification, and $T_h = 310$ K for stable stratification. For all cases presented here, the geostrophic wind vector at the upper ABL boundary is $\mathbf{u}_g = (u_g, v_g) = (10, 0)$ m s^{-1}, ocean surface temperature $T_0 = 300$ K, saturation humidity $q_0 = 2.12 \times 10^{-2}$ kg/kg, and $\nabla_x q = \nabla_y q = 0$.

5.1.4 Results of the Computation of the ABL Vertical Meteorological Structure

The computation of vertical distributions of the air temperature and specific humidity for various background conditions of the density stratification and different endowments of horizontal advection are shown in Fig. 5.1. Related to these distributions, the fluxes of sensible ($F_{T0} = F_T|_{z=z_{0H}}$) and latent ($F_{L0} = L_e F_q|_{z=z_{0H}}$) heat at the ocean–atmosphere boundary (where $L_e = 2.5 \times 10^6$ J kg^{-1} is the specific heat of evaporation and F_q is the moisture flux) are presented in Table 5.1.

A comparative analysis of these characteristics allows us to solve a major problem—namely, to obtain the estimates of sensitivity of the ABL natural MCW
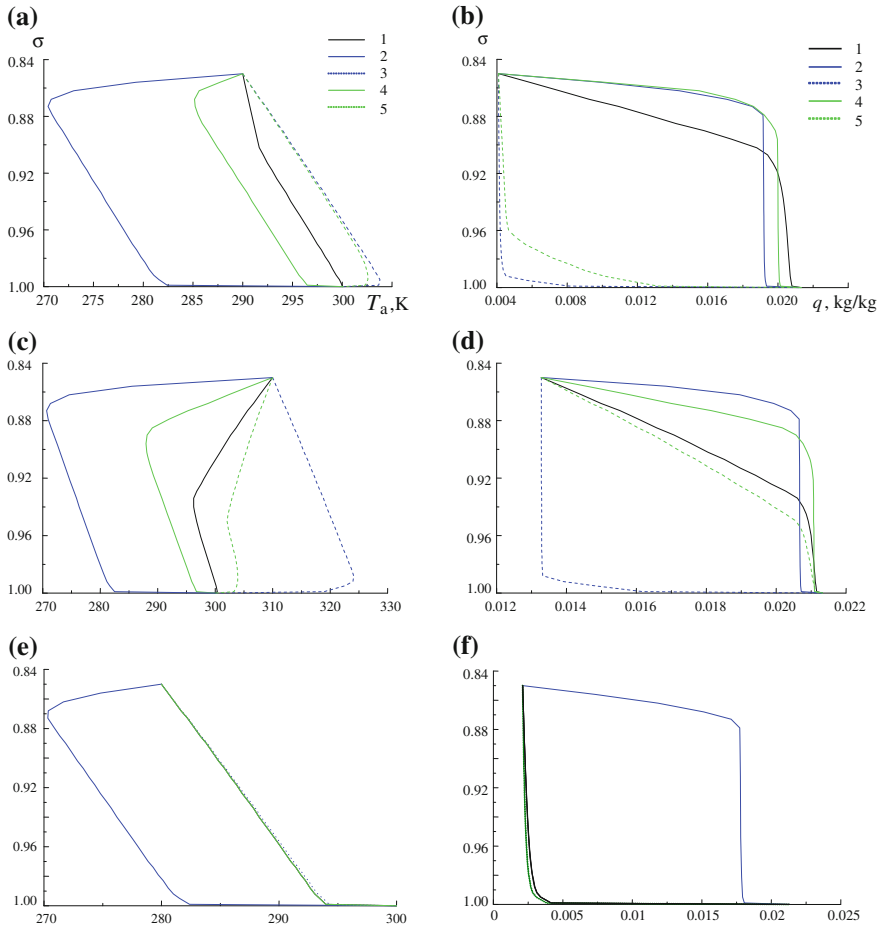
Fig. 5.1 Vertical profiles of the air temperature (**a**, **c**, **e**) and specific humidity (**b**, **d**, **f**) in the cases of neutral (**a**, **b**), stable (**c**, **d**), and unstable (**e**, **f**) background stratification and under different conditions of heat transfer within ABL. The number of curves in the legend corresponds to the sets of parameters in the lines with corresponding numbers in Table 5.1

radiation characteristics to changes of heat regime characteristics caused by the horizontal heat transfer.

In Fig. 5.1, the vertical axis is a nondimensional coordinate σ (sigma), which is a relationship of atmospheric pressure at an arbitrary height z to sea level pressure. The upper ABL boundary is placed at the $\sigma = 0.85$ level, which corresponds to atmospheric pressure $p \approx 850$ mb or geometrical height $z \approx 1,400$ m. The numbers of curves in the figure legend correspond to the sets of parameters in the lines with corresponding numbers in Table 5.1. The results for the first sets (without advection) are displayed in the subsequent figures by black curves; the sets numbered as 2 and 3 in the tables (aligning directions of vectors $\mathbf{u}_g$ and ∇T) are represented by

Table 5.1 Characteristics of heat exchange at the ocean–atmosphere boundary in the case of neutral, unstable, and stable background stratification with different orientations of horizontal temperature gradients relative to geostrophic wind vectors at the upper ABL boundary

No	$\nabla_x T$ (K m^{-1})	$\nabla_y T$ (K m^{-1})	Neutral		Unstable		Stable	
			F_{T0} (W m^{-2})	F_{L0} (W m^{-2})	F_{T0} (W m^{-2})	F_{L0} (W m^{-2})	F_{T0} (W m^{-2})	F_{L0} (W m^{-2})
1	0	0	−1.4	15.7	136.8	998.3	−5.5	4.5
2	5×10^{-5}	0	610.6	173.3	616.4	288.6	600.5	52.7
3	-5×10^{-5}	0	−39.6	345.2	131.1	1021.8	−66.8	45.1
4	0	5×10^{-5}	61.3	53.9	136.9	997.0	54.8	10.1
5	0	-5×10^{-5}	−22.0	182.4	136.6	999.6	−26.2	3.8

blue curves; whereas the sets numbered as 4 and 5 in the tables (normal to vectors $\mathbf{u}_g$ and ∇T) are represented by green curves.

The first set (1) of input parameters in Table 5.1 corresponds to the background conditions without advection; the second one (2), in which the geostrophic wind vector aligns with positive temperature gradient, corresponds to cold advection; and the third one (3), in which the air masses in a free atmosphere are transported in the direction of decreasing temperature, corresponds to warm advection. The fourth and fifth sets hold an intermediate place because the temperature gradient vector aligns in a normal to $\mathbf{u}_g$ direction. Advection transfer takes place in this case, too; within the ABL, the wind speed vector rotates with height and a horizontal gradient at roughly the same at each height within the ABL, as is the case in the real atmosphere.

In the following, we consider in detail some results of computations of the ABL structure for the cases of neutral, unstable, and stable background stratifications.

Neutral background stratification

As seen from Table 5.1 and Fig. 5.1, the influence of advection in the case of neutral background stratification manifests itself rather substantially. As expected, the temperature background within the ABL either decreases (in the course of cold advection) or increases (in the course of warm advection), during which the temperature values at the lower and upper ABL boundaries remain invariable according to the experiment outline. While these values stay invariable, heat fluxes at the ocean surface change cardinally: instead of a close-to-zero sensible heat flux F_T, as registered in the absence advection, the value of F_T can reach up to 600 W m^{-2} during cold advection. This value is close to the values of heat fluxes observed in the Newfoundland EAZO of the North Atlantic in areas of activity of mid-latitude cyclones in the experiments NEWFOUEX-88 and ATLANTEX-90 (Gulev et al. 1994), as well to heat flux values typical for tropical hurricanes (Golytsin 2008).

During warm advection, an excess of heat is transferred to the ocean: the corresponding negative values of F_T can reach −56.4 W m^{-2}. The latent heat flux intensifies independently in the direction of advective transport, although not as

much as F_T. However, the heat exchange through latent heat should depend sufficiently on moisture advection, which was assumed to be absent in the conducted experiments.

Unstable background stratification

In the case of unstable background stratification, the perturbations produced by horizontal advection, even in its most expressed manifestations (i.e., for the first and second sets of conditions in Table 5.1), have consequential changes of F_T and F_L by several times, although the sign of these fluxes remains the same in all the cases. As is characteristic for unstable ABL stratification, the ocean loses heat to the atmosphere in the form of sensible and latent heat fluxes.

The monotonic, relatively uniform decrease of temperature within the ABL that occurs in cases without advection, is replaced by a sharp decrease in the near-surface layer in cases of cold advection, which changes with increasing with height temperature in the vicinity of the upper ABL boundary (see Fig. 5.1).

Stable background stratification

The perturbations produced by horizontal advection in the surface fluxes F_T and F_L in the case of stable stratification are similar as a whole to those considered previously for the case of neutral stratification. The notable differences are seen only in the latent heat flux F_L, which turns out to be negative for all directions of horizontal transport. However, the absolute values of F_L remain relatively small.

The vertical structure of ABL fields with such stratification is characterized by the usual temperature inversion near the upper ABL boundary, which is accompanied by weakened vertical mixing (i.e., by reduced k_m and k_H values not exceeding one or two tens of $m^2\ s^{-1}$ with a maximum in the lower ABL part) and by a notable rotation of wind speed vector. These peculiarities are in accordance with published ideas on the structure of stably stratified ABL (Zilitinkevich 1970).

5.2   Response of the SOA's Brightness Temperature to ABL Temperature Changes and Humidity Characteristics

Calculations of the ABL's brightness temperature were carried out with the radiation model (2.1)–(2.5) (see Chap. 2) in the wavelength range of 0.6–1.6 cm for the case of vertical sounding from a satellite. This range partially includes the region of resonance absorption (radiation) of radiowaves in the molecular oxygen of the atmosphere (its right vicinity) and fully covers the region of resonance absorption of radiowaves in the water vapor of the atmosphere. These regions of MCW range bring information about the air temperature and humidity and play an important role in studies of the ocean and atmosphere heat interaction by satellite MCW radiometric methods (Grankov 2003; Grankov and Milshin 2010).

We analyzed the response of the ABL brightness temperature in the range of wavelengths 0.6–1.6 cm to the vertical distributions of the air temperature and humidity for different types of the ABL stratification and different orientations of horizontal temperature gradients relative to the geostrophic wind vector at the upper ABL boundary (situations 1–5 in Table 5.1). Figure 5.2 shows the results of computation of the brightness temperature contrasts ΔT^b at different wavelengths, when going from background conditions (when the horizontal advection in ABL is absent; case 1 in Table 5.1) to cold advection (case 2), and to warm advection (case 3) for the neutral, stable, and unstable density stratification of ABL.

Fig. 5.2 Brightness temperature contrasts ΔT^b at different wavelengths under the transition from background conditions (when the horizontal advection in ABL is absent) to cold advection (*blue curves*), and to warm advection (*red curves*) for the neutral (*1*), stable (*2*) and unstable (*3*) density stratification of ABL (Grankov et al. 2014)
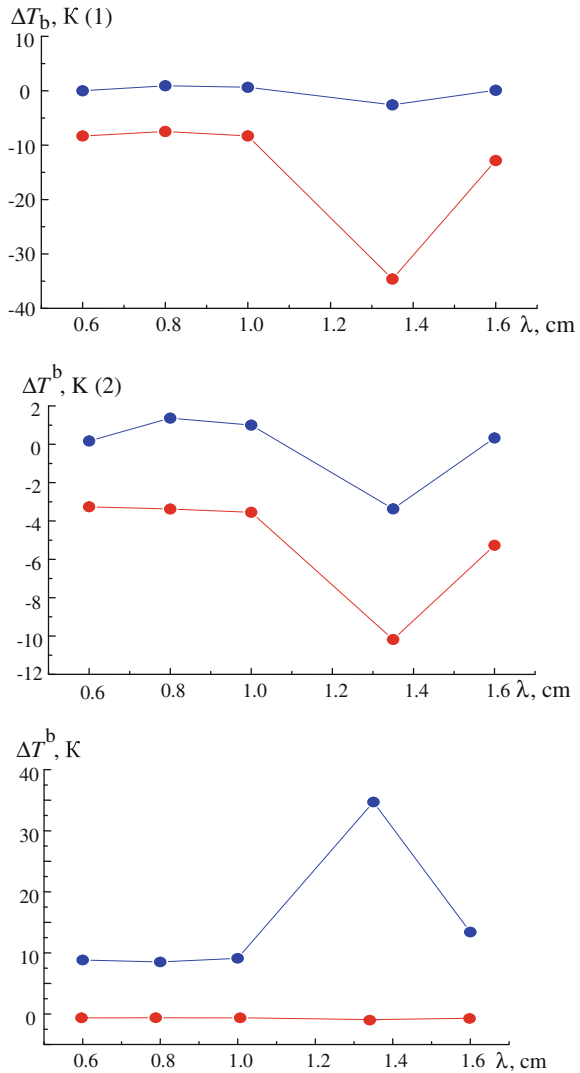
Figure 5.2 shows that, in the spectral region of absorption of radiowaves in water vapor of the atmosphere centered relatively on the 1.35 cm line, sensitivity of the ABL brightness temperature to changes of the ABL heat structure is maximized. This result confirms the importance of a given region of the MCW range for studying the processes of heat and moisture exchange between the ocean and atmosphere. Previously, our findings demonstrated the effectiveness of its use in studies of heat ocean–atmosphere interactions with passive MCW radiometric methods at the seasonal and climatic scales (Grankov 1992).

Figure 5.3 gives more specific information on dependence of the brightness temperature contrasts ΔT^b at the wavelength 1.35 cm from intermediate (current) values of the zonal gradient $\nabla_x T$. The figure illustrates the cases of cold advection/unstable stratification (blue marks) and warm advection/neutral stratification (red marks). Figure 5.3 shows that already at the values $\nabla_x T = \pm 0.00002$ k m^{-2}, the value ΔT^b is closed to their upper limits ± 40 K; a further increase of the gradient results in negligible variations of the brightness temperature.

The main result is the fact that ABL brightness temperature variations at the wavelength of 1.35 cm can amount to 35–40 K, which noticeably exceeds the value of their variations caused by the processes of the vertical transfer of heat and moisture in the ABL, which vary from 3 to 5 K (Grankov and Resnyanskii 1998; Grankov et al. 1999).

Natural MCW radiation of the SOA at the wavelength 1.35 cm is formed in a so-called effective layer, whose thickness (1.8 km) is close to the ABL thickness used in our analysis (1.4 km). Therefore, one can expect that the previously marked effect discovered for the ABL will be more pronounced, taking into account that the heat and MCW radiation characteristics of the higher atmosphere layers (1.4–10 km), which are also undergoing horizontal heat transfer, contribute to the total radiation of the SOA.

We analyzed the relationships between variations of the ABL brightness temperature at the wavelength 1.35 cm and vertical fluxes of sensible and latent heat for

Fig. 5.3 Dependence of the brightness temperature contrasts at the wavelength of 1.35 cm from the horizontal (zonal) gradient of the air temperature in ABL
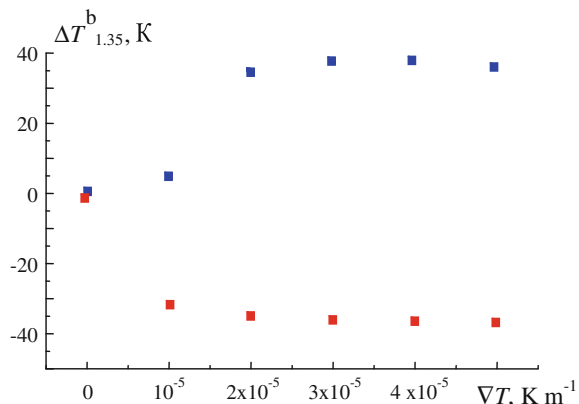
the neutral, stable, and unstable ABL stratifications and for various types of advection (cases 1, 2, and 3 from Table 5.1); the results of this analysis are presented in Fig. 5.4. Cases 2 (cold advection) and 3 (warm advection) are emphasized due to their contrast to cases 4 and 5, which are the minor ones (intermediate).

Figure 5.4 demonstrates a close correlation of the parameters ΔT^b, F_{T0}, F_{L0}. The mismatch (root mean square difference) between the parameters ΔT^b and F_{T0} is 11.2 K and between the parameters ΔT^b and F_{L0} is 6.4 K—a few percent of the magnitudes of the F_{T0} and F_{L0} variations. This result is in a good agreement with the data derived from a comparison of the results of MCW radiometric measurements of the SOA brightness temperature from the meteorological satellite DMSP F-08 and estimates of heat and moisture fluxes determined from the meteorological

Fig. 5.4 Correlation between variations in the ABL brightness temperature at the wavelength 1.35 cm, and the near-surface vertical fluxes of sensible and latent heat for neutral, stable, and unstable ABL stratification and various types of advection (Grankov et al. 2014)
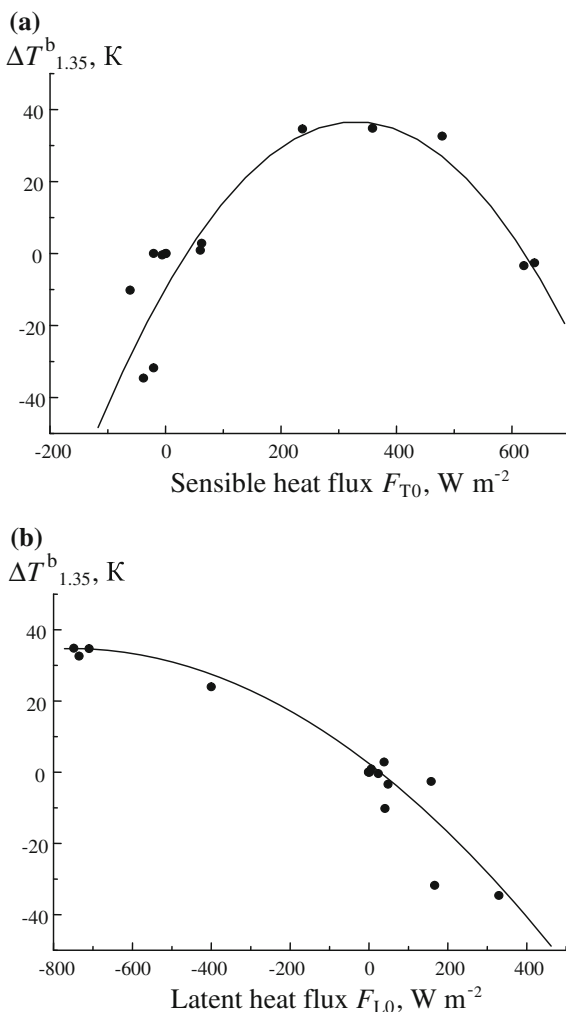
measurements fulfilled in the NEWFOUEX-88 and ATLANTEX-90 experiments (Grankov 2003, Grankov and Milshin 2010).

5.3 Conclusion

The estimates of the influence of horizontal heat transport on the structure of meteorological fields in ABL and its energy exchanges with the ocean provide evidence of their strong dependence from the horizontal advection within ABL. The magnitude and the sign of the SOA brightness temperature perturbations produced by the horizontal heat transport depend on background ABL stratification and on the orientation of the transport vector's relative temperature and humidity gradients. This dependence should be properly accounted for when retrieving the surface heat fluxes from the remotely sensed data.

The ABL brightness temperature variations at the wavelength 1.35 cm caused by horizontal heat transfer can amount to 30–40 K, which noticeably exceeds the value of their variations produced by the processes of vertical transfer of heat and moisture in ABL. This result is in agreement with the satellite-observed brightness temperature contrasts in areas of activity of midlatitude cyclones, which in no way can be explained by an account of the processes of forming the ABL vertical structure.

The close correlation between variations of the ABL brightness temperature at the wavelength 1.35 cm and vertical fluxes of sensible and latent heat for different types of ABL stratification and various types of advection were revealed in this chapter.

References

Blackadar AK (1962) The vertical distribution of wind and turbulent exchange in a neutral atmosphere. J Geophys Res 67: 3095–3102.

Golytsin GS (2008) Polar lows and tropical hurricanes: Their energy and sizes and a quantitative criterion for their generation. Fizika Atmosfery Oceana 44: 579–590 In Russian.

Grankov AG (1992) Microwave-radiometric diagnostics of integral fluxes of sensible heat at the ocean-atmosphere boundary. Izvestija, Atmosph Oceanic Phys 28:883–889.

Grankov AG, Resnyanskii YuD (1998) Modeling the response of the ocean-atmosphere natural radiation system to the perturbation of a thermal equilibrium at the interface. Russian Meteorology and Hydrology, Allerton Press 11: 57–65.

Grankov AG, Milshin AA, Resnyanskii JuD (1999) Intercommunication between heat exchange in the air-sea interface and upgoing microwave radiation in the range of synoptic time scales Proc. Intern. Symp. on Remote Sensing (IGARSS): Coll. Papers Germany Hamburg 2324–2326.

Grankov AG (2003) Thermal analysis of atmosphere-ocean interaction by means of satellite microwave radiometry in the 0.5- and 1.35-cm resonance bands. Techn Physics 7: 906–913.

Grankov AG, Milshin AA (2010) Analysis of the factors exiting the ocean-atmosphere heat interaction in the North Atlantic using satellite and vessel data. Intern J Rem Sensing 31: 913–930.

Grankov AG, Resnyanskii JuD, Milshin AA, Novichikhin EP (2014) Influence of the horizontal heat transfer within the atmosphere boundary layer on its vertical heat structure and natural up-going microwave radiation. Russian Meteorology and Hydrology, Allerton Press 2:33–44.

Gulev SK, Kolinko AV, Lappo SS (1994) Synoptic ocean-atmosphere interaction in mid-latitudes. S.-Petersburg, Gidrometeoizdat In Russian.

Monin AS, Yaglom AM (1992) Statistical hydromechanics. Theory of turbulence, v.1. S.-Petersburg Hidrometeoizdat In Russian.

Stull R (1997) An introduction to boundary layer meteorology. Kluwer Academic Publishers, Boston.

Zilitinkevich SS (1970) Dynamics of the atmosphere boundary layer. Hidrometeoizdat, Leningrad In Russian.

Chapter 6
Experimental Studies of the Relationships Between SOA Radiation and Heat Characteristics in the Synoptic Range of Time Scales

6.1 Laboratory Study of the Response of Natural MCW and IR Radiation from the Water Surface to Its Upper Layer Enthalpy

6.1.1 Matter of the Study

Studies of the relationship between the characteristics of natural MCW and IR radiation with water surface temperature characteristics, such as as vertical turbulent heat fluxes and heat content (enthalpy) of the upper layer, are important tasks in the remote sensing of the World Ocean and seas from aircrafts and satellites that are directed to interests of oceanologists and climatologists (Bychkova et al. 1988; Grankov and Milshin 1999).

The intensity of microwave radiation (characterized by its brightness temperature $T^b = æ\, T_s$) can be computed by multiplying the emission coefficient æ and the thermodynamic temperature of the water surface t_s appropriated to the thickness of its effective radiating layer l_{eff}.

In the IR range, the following is true:

1. The value of æ is close to 1 and variations of the water surface state slightly change its emissivity. As a result, the sensitivity of the natural radiation field to water surface temperature variations $\Delta T^b/\Delta t_s$ is close to 1 and the accuracy of the temperature determination is weakly dependant on its state (particularly from the sea wave intensity [roughness]).
2. The atmosphere and atmospheric formations (primarily the aerosols, cloudiness, and hydrometeors) influence the screening effect on the underlying surface radiation. For this reason, IR methods and means provide information about the water surface temperature and its heat properties only in cloud-free areas (i.e., over approximately 25–33 % of the World Ocean).
3. The value of the effective layer l_{eff} is in the millimeter range.

Peculiarities of the MCW range include the following:

1. More less in comparing the IR range sensitivity of natural radiation to variations of the water surface temperature ($\Delta T^{\mathrm{b}}/\Delta t_{\mathrm{s}} \leq 0.5$).
2. Practically, the full transparency of the atmosphere includes the cloudiness areas for the radiowaves at 3–5 cm and beyond.
3. The value of the effective radiation layer l_{eff} is in the centimeter range.

We studied experimentally (in the laboratory) the behavior of the water surface, initially at room temperature and sharply cooled with liquid nitrogen. Characteristics included variations in the intensity of natural MCW radiation at the wavelength of 2.25 cm and infrared (IR) heat radiation in the window of 10.5 mcm, as well as the value of the heat content (enthalpy) in the upper water surface layer.

The difference between these values is a key characteristic of ocean–atmosphere heat interaction. It determines the enthalpy of the upper water layer and the intensity of the vertical turbulent fluxes at the ocean–atmosphere boundary (Khundzhua and Andreev 1973).

A comparison of the evolution of the heat content computed from the difference between temperatures of the upper and lower boundaries of the subsurface layer with evolutions of MCW and IR radiation intensity was conducted accordingly.

6.1.2   Description of the Experiment and Its Results

We investigated direct measurements of the water surface temperature and its value at a depth of 1 cm with mercurial thermometers. In addition, measurements of the water surface brightness temperature at the wavelength 2.25 cm (frequency 13.33 GHz) and its radiation temperature in the spectral IR window 10.5 mcm were conducted. Radiometric measurements were carried out with MCW and IR radiometers designed by the Special Designing Bureau of the Institute of Radioengineering and Electronics Russian Academy of Sciences. Linear sizes of the dish with water exceeded the electromagnetic wavelength by dozens of times; in this manner, we avoided the influence of the edge diffraction effects on the results of MCW radiometric measurements.

The lower temperature level of our measurements ($\sim 5\,°C$) was provided by cooling the upper water layer with liquid nitrogen; the upper boundary (14–15 °C) was in accordance with the room air temperature. Accuracy of the temperature variations measured by the mercurial thermometers was about ±0.1 °C, and accuracy of the brightness (MCW) and radiation (IR) temperatures. The measurement accuracy of the MCW brightness temperature and IR radiation temperature varies with the water temperature: 0.2–0.3 K. The measurements were conducted in triplicate.

The results of direct radiometric measurements are shown in Fig. 6.1. The MCW radiometric measurements were carried out for research; later, the full program measurements with the MCW radiometer were not completed because the radiometer become inoperable. Measurement data of the brightness and radiation
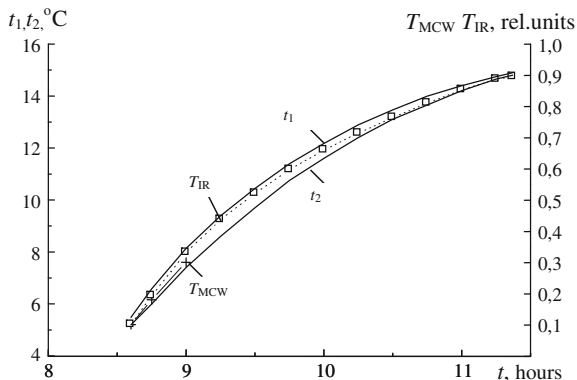
Fig. 6.1 Results of simultaneous measurements of the water temperature at its surface (t_1) and its subsurface values (t_2) with simultaneous radiometric measurements T_{MCW} and radiation T_{IR} temperatures

temperatures are shown in relative units. Figure 6.1 shows that the process of heat relaxation in the near-surface water layer in our experiment continued for approximately 3 h. During this time (from 8 h 30 min to 11 h 30 min), the difference between the values of the parameters T_1 and T_2 returned to their initial values (0.1–0.2 °C), reaching a maximum (about 1 °C) during the time from 9 to 10 h in the morning. Here, the time evolutions of the parameter T_{IR} and the brightness temperature T_{MCW} of the water surface (at the first stage of our experiment) are in good accordance with evolutions of the parameters T_1 and T_2.

Figure 6.2 shows the relationship of the difference ΔT between the brightness (MCW) and IR radiation temperatures (in Kelvins and relative units, respectively) with variations of the enthalpy of the 1-cm depth water layer Q during heat evolution. The value of parameter Q was determined with known expressions, which account for the water mass in the 1-cm layer, its heat capacity, and the difference between the upper- and lower-layer temperatures.

Fig. 6.2 Dependence of the difference ΔT between the brightness and radiation temperatures from variations of the heat content in the subsurface water layer Q
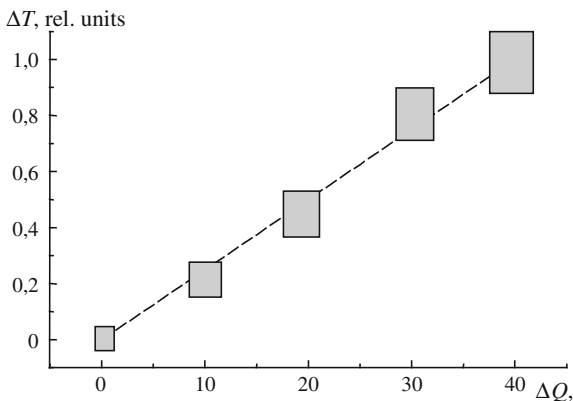
The values of $T_{2.25}$ during the time interval 9–11.5 h were obtained by extrapolating their indications at the initial stage of the experiment. The scattering denoted in Fig. 6.2 is caused by errors of the MCW and IR measurements as well as by inaccurate extrapolation of the data measurements from the MCW radiometer.

Figure 6.2 shows a clear bound between the difference of the parameters T_{MCW} and T_{IR} and the heat content of the water subsurface layer. The basis for this bound is that the brightness temperature T_{MCW}, unlike the radiation temperature T_{IR}, provides information not only on the water surface temperature but also on the temperature subsurface water layer. Therefore, this difference characterizes the value of the vertical temperature gradient, which determines the heat content of the subsurface layer and the intensity of its heat exchange with the air.

Thus, a clear relationship between the difference of the parameters T_{MCW} and T_{IR} and the heat content of the subsurface water layer can be ascertained. The brightness temperature—unlike the radiation temperature—provides information not only about the water surface but also about the temperature of the subsurface layer. That is why their difference defines the value of the vertical temperature gradient related to the heat content of the upper layer and a heat exchange with the air.

6.2 Experimental Studies of the Relationships Between the Brightness Temperature, Heat, Moisture, and Impulse Fluxes with Satellite Data and Vessel Measurements

6.2.1 SSM/I Radiometer of the DMSP Satellites

The multichannel radiometer Special Sensor Microwave/Imager (SSM/I) is one of the best satellite passive MCW radiometric systems within the framework of the Defense Meteorological Satellite Program (DMSP). It was designed for long-term monitoring of the earth to provide US Forces with global meteorological, oceanographic, and solar-geophysical information (Kramer 1994). In December 1992, the DMSP data were declassified and became available to the civil and scientific community.

The operative satellites of the DMSP series have a solar-synchronous low circular orbit close to the polar titled by 98.8, with an altitude of about 850 km and period of 102 min (14.2 circuits per day). Presently, several satellites of this series (F-10, F-11, F-12, F-13, F-14, and F-15) are actively operating in space and have been for a few years.

The radiometer SSM/I of the satellite F-08, which has been out of operation since December 1991, is of particular interest in our investigation because it was the only satellite MCW radiometer for observation of the earth from in 1988 and 1990 during the wide-scale NEWFOUEX-88 and ATLANTEX-90 experiments. This device was designed for global and synoptic sounding of the atmospheric liquid

Table 6.1 Main parameters of the SSM/I radiometer

Frequency (GHz)	19.35	22.235	37.0	85.5
Wavelength (cm)	1.55	1.35	0.81	0.35
Polarization (V/H)*	V, H	V	V, H	V, H
Symbol of channels used	19.35V(H)	22.2V	37V(H)	85.5V(H)
Spatial resolution (km)	43 × 69	40 × 60	29 × 37	13 × 15
Sensitivity (K)	0.7	0.7	0.4	0.8

*V vertical polarization; H horizontal polarization

water content in clouds (parameter W), precipitation intensity I, water vapor total content (parameter Q), near-surface wind speed (parameter V), and different land and ice cover parameters. This radiometer is a scanning seven-channel four-frequency system at a 52° angle at horizontal and vertical polarizations (see its parameters in Table 6.1). It measured the SOA brightness temperature in a view band of 1,400 km, providing global coverage of the Earth in 3 days and incomplete coverage in a day (Hollinger et al. 1990).

A description of the ship-borne and satellite-derived passive MCW radiometric measurements used in the analysis of the correlation between the SOA brightness temperature and the boundary heat fluxes at the stationary phases of the NEWFOUEX-88 and ATLANTEX-90 experiments is presented in Table 6.2. A unique archive of long-term satellite data was obtained with the help of the

Table 6.2 Description of ship-borne and satellite-derived MCW radiometric measurements used in the stationary phases of the NEWFOUEX-88 and ATLANTEX-90 experiments

Type	Sources	Makeup	Volume	Purposes
Meteorological observations	R/Vs *V. Bugaev*, *Musson*, and *Volna*	Ocean surface temperature, near-surface wind speed	More than 2000 observations with 1-h resolution	Determination of heat, moisture, and momentum fluxes; evaluation of the ocean surface MCW radiation characteristics
Aerologic observations	R/Vs *V. Bugaev*, *Musson*, and *Volna*	Air temperature, humidity, pressure within 10–16,000 m at 20 levels	More than 400 observations with an interval of 6 h	Determination of the total water vapor content of the atmosphere; evaluation of the atmospheric MCW radiation characteristics
Satellite measurements	The SSM/I radiometer of the F-08 satellite (DMSP)	Brightness temperature frequencies 19.3, 37, 22.2, and 85.5 GHz for two types of polarization	More than 120 sessions of measurements with an interval of about 24 h	Validation of the modeling results

SSM/I radiometer in NASA's Marshall Center (MSFC—specifically, in its special center, DAAC). To determine the brightness temperatures with the SSM/I device, its telemetric data (forming the SSM/I archive) were transformed for each channel into the antenna temperatures using a priori known antenna-feeder-radiometer tract parameters with a help of the absolute calibration principle. Then, the antenna temperatures measured directly by satellite radiometers were converted to SOA brightness temperatures through parameterization of the so-called equation of smoothing. Both stages were performed with the algorithms developed by Wentz (1991).

6.2.2   Results of Modeling Synoptic Variations of SOA Brightness Temperatures and Their Comparison with Satellite Measurements

We compared the simulated SOA brightness temperatures evaluated from vertical observations (toward the nadir) in oceanic areas where the R/Vs *V. Bugaev*, *Musson*, and *Volna* resided with simultaneous microwave radiometric measurement data derived from the SSM/I radiometer of the F-08 satellite during the stationary phases of the NEWFOUEX-88 and ATLANTEX-90 experiments (Grankov and Milshin 1999). For this purpose, we analyzed data from the MSFC archive and selected some of its fragments corresponding to surveys made in the areas of location these vessels during March 3–23, 1988 and April 4–21, 1990. The corresponding survey sessions occurred in the morning (between 8:00 and 9:00, Greenwich Time) and evening (between 21:00 and 22:30, Greenwich Time) and the average interval between sessions is about 24 h.

Maximal variations (contrasts) of the brightness temperature fixed during the stationary phases of the NEWFOUEX-88 and ATLANTEX-90 experiments at the locations of the vessels *V. Bugaev*, *Musson*, and *Volna* for various channels of the SSM/I radiometer (see Fig. 6.3) are in good agreement with their simulated estimates (see Chap. 2). As seen from Fig. 6.3, values of the SOA brightness contrast in the Newfoundland EAZO vary from 30 to 80 K, which is much more than the minimal values (1–3 K) determined by the SSM/I radiometer. Therefore, this device can serve as an effective tool for analysis of the processes of SOA heat interaction in the synoptic range of time scales.

Figure 6.4 compares the SOA brightness temperatures evaluated at the wavelength 1.35 cm with those obtained from satellite measurements. The temporal resolution of the evaluated estimates (four times a day) follows from the frequency of aerologic measurements, and the temporal resolution of the satellite measurements (about once a day) is governed by the frequency of satellite surveys.

Let us note that the theoretical estimates of the parameter T^b were obtained with a nadir-looking radiometer, whereas the SSM/I radiometer provides measurements of the brightness temperature measurements at an angle of 52°. Thus, essential

(a)

ΔT^b, K

(b)

Channels of the SSM/I radiometer

Channels of the SSM/I radiometer
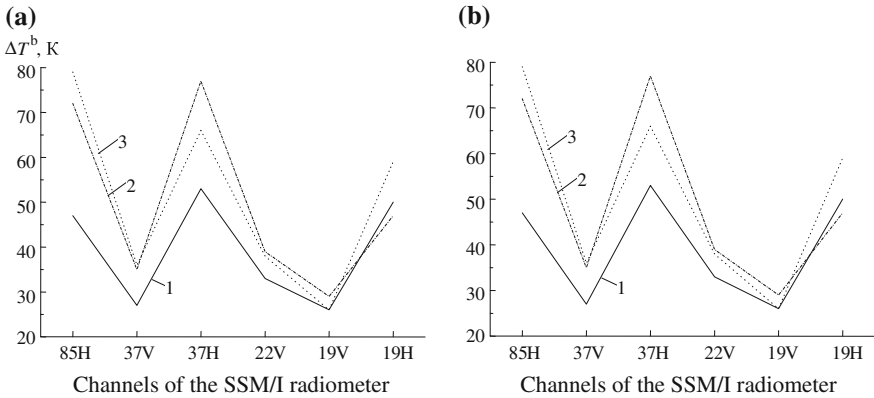
Fig. 6.3 Brightness temperature contrasts during the stationary phases of the NEWFOUEX-88 and ATLANTEX-90 experiments measured by the SSM/I radiometer. The horizontal axis indicates the SSM/I working frequencies in GHz with indication of the polarization type: *H—horizontal; V—vertical: 1—V. Bugaev, 2—Musson, 3—Volna*

differences (tens of K) can be observed between *absolute* values of evaluated and measured brightness temperature for the R/Vs *V. Bugaev*, *Musson*, and *Volna*; at the same time, the correlation coefficient *r* between their *relative* variations ranges from 0.89 to 0.91. For areas where these weather research vessels resided, the mismatch *d* (rms difference) between the evaluated and measured brightness temperatures ranges between 3 and 5 K; that is, it reaches 5–10 % of the magnitude of the parameter T^b_{135} variations. With the use of additional measurements at the wavelength 0.81 cm for vertical and horizontal polarizations (these data predominantly give information on the liquid water content in the clouds), the quantity *d* reduces to 2–3 K and the correlation coefficient *r* increases to 0.94–0.9; one can observe good similarity between simulated and measured brightness temperatures in this case.

Formally, this result follows from the fact that the evaluation of brightness temperatures is carried out from a model with three degrees of freedom instead of a model with one degree of freedom. A possible physical interpretation lies in the improvement of the signal-to-noise ratio in channel 22V of the SSM/I radiometer due to the channels 37V, 37H. Ad hoc, the signal received from the satellite is meant to be the brightness temperature variations caused by variations in the atmospheric water vapor content, and the noise is meant to be the brightness temperature variations caused by variations of the atmospheric cloudiness characteristics.

The relationships between the brightness temperature evaluated at 1.6 cm and that measured with the SSM/I radiometer at 1.55 cm are characterized by approximately the same values of the correlation coefficient and mismatch (discrepancy). Thus, there is good agreement between theoretical and experimental estimates of the brightness temperature of the SOA natural MCW radiation during the stationary phases of the NEWFOUEX-88 and ATLANTEX-90 experiments.
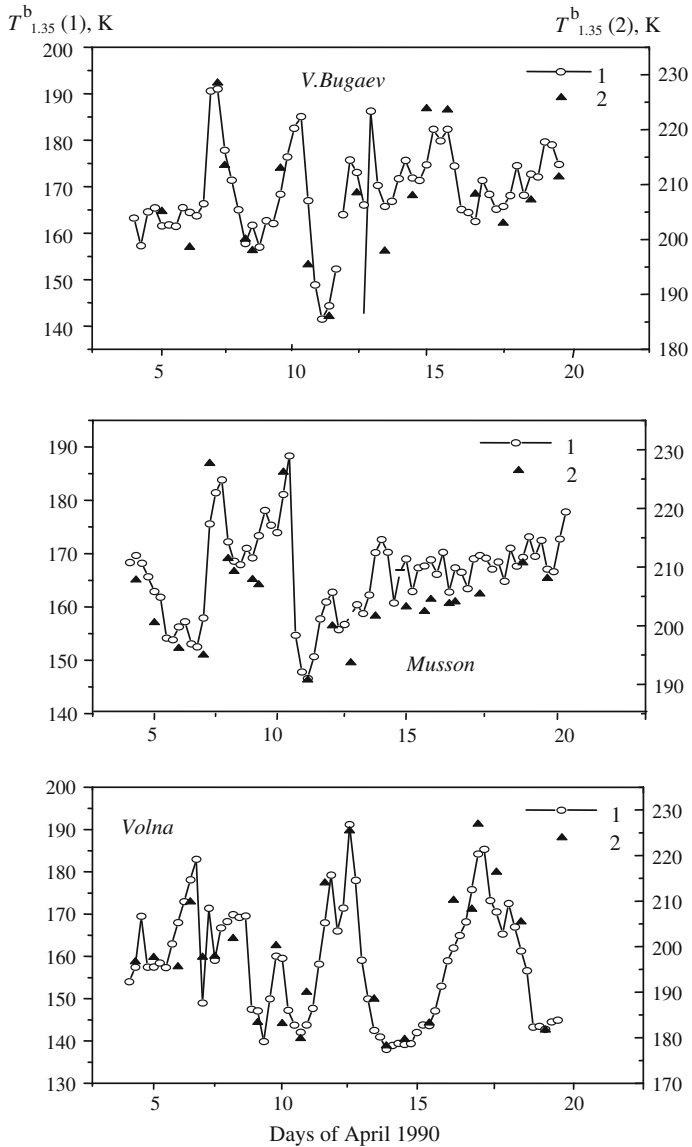
Fig. 6.4 Comparison of (*1*) the evaluated ocean–atmosphere brightness temperatures (temporal spacing 6 h) and (*2*) satellite (temporal spacing 24 h) estimates for the resonance line of the water vapor at 1.35 cm during April 4–21, 1990

6.2.3   Relationships Between the SSM/I-Derived Brightness Temperatures with the Near-Surface Fluxes of Heat and Impulse

The response of natural MCW radiation to variations of the heat fluxes at the SOA interface is most prominent during the passage of mid-latitude cyclones. We analyzed the relationships of the SSM/I-derived SOA brightness temperature measured by various channels and the near-surface heat and momentum (impulse) fluxes observed in the stationary phases of the ATLANTEX-90 and NEWFOUEX-88 experiments. For weak cloudiness, the brightness temperature in channel 22V and the brightness temperatures in channels 19V and 19H are good qualitative characteristics of heat and momentum fluxes, respectively. In general, however, it is necessary to use additional data of the measurements of channels 37V and 37H, which allow for the effect of cloudiness.

Figures 6.5 and 6.6 show some results of a comparison of the ship-borne estimates of the total fluxes of heat q_{he} and momentum q_v recorded at the stationary phase of the ATLANTEX-90 experiment with their satellite estimates obtained as linear combinations of the brightness temperature values measured at wavelengths 1.35 cm (channel 22V) and 0.81 cm (37V, and 37H). These combinations were constructed to ensure the minimum *rms* differences (mismatch) with the original values of q_{he} and q_v. Although the characteristics of ocean–atmosphere heat at the locations of the R/Vs *V. Bugaev*, *Musson*, and *Volna* are quantitatively and even qualitatively different, the estimates made afloat and aboard the satellites are in good agreement.

The correlation coefficients of heat fluxes and their estimates are as high as $r = 0.85$ for the R/V *V. Bugaev*, $r = 0.73$ for the R/V *Musson*, and $r = 0.84$ for the R/V *Volna*. The corresponding correlation coefficients for the momentum fluxes are

Fig. 6.5 Comparison of total heat fluxes q$_{he}$ parameterized from vessel measurements (*1*) and their estimates (*2*) derived from the SSM/I channels 22V (1.35 cm), 37 V, and 37H (0.81 cm) in the ATLANTEX-90 experiment
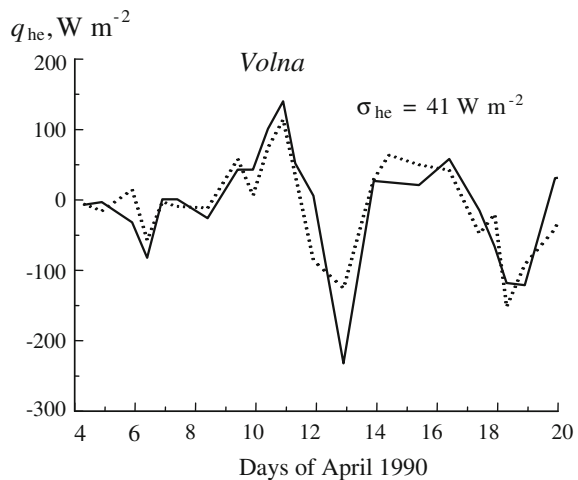
Fig. 6.6 Comparison of impulse fluxes q_v parameterized from vessel measurements (*1*) and their estimates (*2*) derived from the SSM/I channels 19V, and 19H (1.55 cm), 37V, and 37H (0.81 cm) in the ATLANTEX-90 experiment

q_v, N m^{-2}

Volna

$\sigma_v = 0.068$ N m^{-2}

Days of April 1990
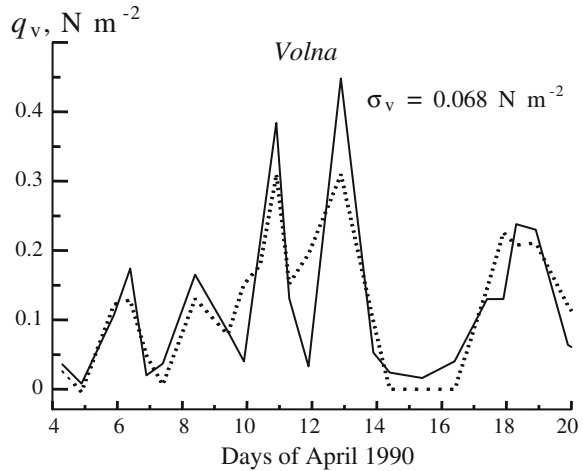
0.87, 0.81, and 0.84, respectively. The ratio of mismatch between the original fluxes and their satellite estimates to the maximum variations of fluxes varies from 12 % (R/V *Volna*) to 19 % (R/V *Musson*) for the parameter q_{he} and from 13 % (R/V *Musson*) to 18 % (R/V *V. Bugaev*) for the parameter q_v.

Figure 6.7 illustrates the results of applying this technique to the data of synchronous measurements from the satellite F-08 and weather research vessels *V. Bugaev* and *Musson* in the stationary phase of the NEWFOUEX-88 experiment. The correlation coefficients of heat fluxes and their estimates are as high as $r = 0.85$ for the R/V *V. Bugaev* and $r = 0.91$ for the R/V *Musson*.

The total heat fluxes estimated afloat at higher latitudes, at the point M (66°N, 2°E) of the Norwegian-Greenland EAZO (the data distributed by the Scientific

q_{he}, W m^{-2} *V. Bugaev*

$\sigma_{he} = 143$ W m^{-2}

Days of March 1988

q_{he}, W m^{-2} *Musson*

$\sigma_{he} = 121$ W m^{-2}

Days of March 1988
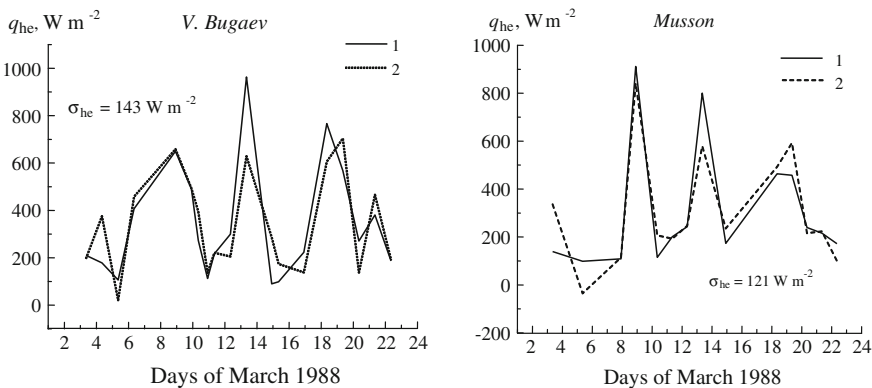
Fig. 6.7 Comparison of total heat fluxes q_{he} parameterized from vessel measurements (*1*) and their estimates (*2*) derived from the SSM/I channels 22V (1.35 cm), 1.55V, and 1.55H (19 GHz) in the NEWFOUEX-88 experiment (Grankov and Milshin 1999)

Fig. 6.8 Total heat fluxes q_{he} parameterized from measurements of the weather ship M and satellite-derived estimates q_{he}^* (**a**) and results of their comparison (**b**) in April 1988: r coefficient of correlation; σ rms of mismatch

(a)

q_{he}, q_{he}^*, W m^{-2}

(b)

q_{he}^*, W m^{-2}

$$q_{he}^* = 32.83 + 0.81\; q_{he}$$
$$r = 0.93; \quad \sigma = 24.6 \text{ W m}^{-2}$$

q_{he}, W m^{-2}
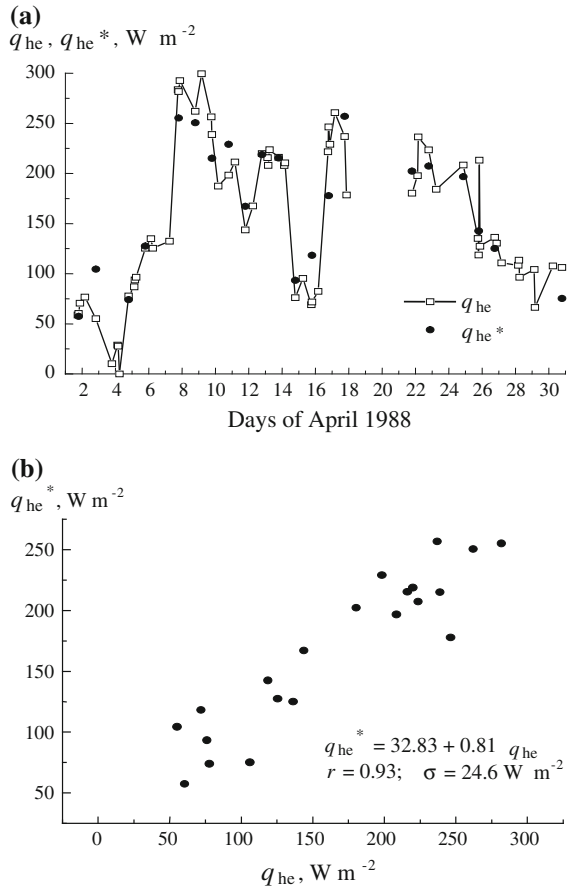
Computing Division of the National Center for Atmospheric Research [NCAR]; submitted courtesy of Joerg Schulz, Germany), also closely correlated with the satellite estimates made by linear regressions applied to the data obtained simultaneously from channels 22V, 37V, 37H, and 19V of the F-08 SSM/I radiometer in April 1988 (Fig. 6.8).

6.2.4   Stability of the Relationships Between Satellite and Vessel Estimates of Heat and Impulse Fluxes

The stability of relationships between the total heat fluxes and their satellite MCW radiometric estimates constructed by linear regressions applied to the data from the channels 22V, 37V, H, and 19V of the F-08 SSM/I radiometer is readily apparent from comparing the parameters q_{he} and q_{he}^*. These were determined with a two-year

shift in time (i.e., during the NEWFOUEX-88 and ATLANTEX-90 stationary phases) in nearly the same areas of the Newfoundland EAZO (Fig. 6.9).

In our opinion, the following reasons add to the mismatch occurring in these experiments between direct and satellite estimates of the boundary heat and

Fig. 6.9 Comparison of the direct measurements of total heat fluxes q_{he} and their satellite estimates q_{he}^* in the locations of the R/Vs *V. Bugaev*, *Musson*, and *Volna* during stationary phases of the NEWOUEX-88 and ATLANTEX-90 experiments
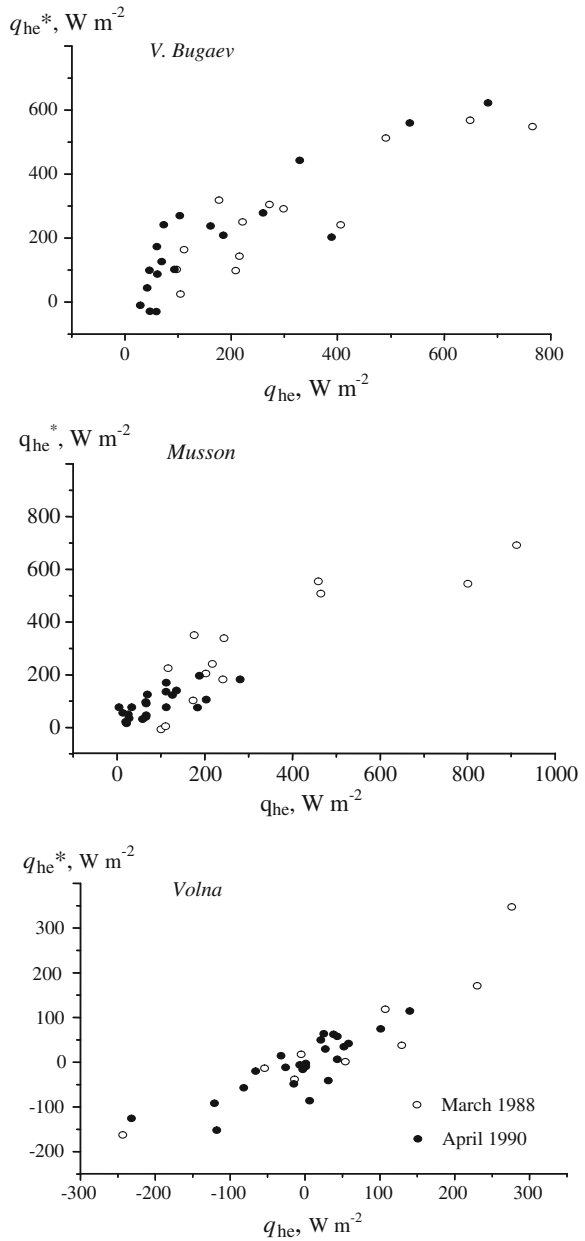
momentum fluxes and hamper the stability of interrelationships between the characteristics of the SOA natural MCW radiation and parameters q_{he} and q_v.

1. The areas where the R/Vs *V. Bugaev*, *Musson*, and *Volna* resided are characterized by significant horizontal gradients of heat and momentum fluxes. For example, judging from the data (Gulev et al. 1994), the horizontal gradient of the total heat flux was as high as 2–4 W m^{-2}/km in the area where the R/V*V. Bugaev* resided, which is closest to the subpolar hydrologic front. As a result, the ambiguity in the parameters q_{he} can be as much as 30–200 W m^{-2}, because the field of view of the radiometer's receiving antenna covers an area whose linear size can reach 15–50 km (see Fig. 6.10).
2. The ships' measurements shift in time (to 30 min) relative to satellite measurements, which can introduce an additional error into the results of comparison. By our estimates, this error can reach 20 W m^{-2} for the parameter q_{he} and 0.03 N m^{-2} for the parameter q_v. (see Fig. 6.11).
3. Typically in the Newfoundland EAZO, mid-latitude cyclones cause a time delay (of 6–12 h) of the SOA brightness temperature response to heat flux variations. Therefore, this factor is accounted for when comparing direct and satellite estimates of parameter q_{he}.

Additionally, the relative error of the bulk formulas used by oceanologists and meteorologists for calculations of the heat and momentum fluxes from direct measurements of the parameter t_s, V, and t_a measures 10–30 %.

Fig. 6.10 Comparison of direct measurements of the total heat fluxes q_{he} and their satellite estimates q_{he}^* with $0.5 \times 0.5°$ (*1*) and $1 \times 1°$ (*2*) spatial resolution in the NEWFOUEX-88 experiment from the *Volna vessel*
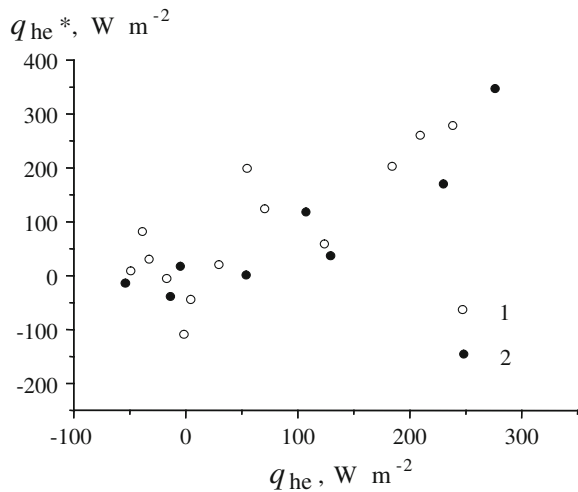
Fig. 6.11 Comparing of direct measurements of the total heat fluxes q_{he} (*1*) and those shifted by 1 h (*2*) in the NEWFOUEX-88 experiment from the *V. Bugaev* vessel
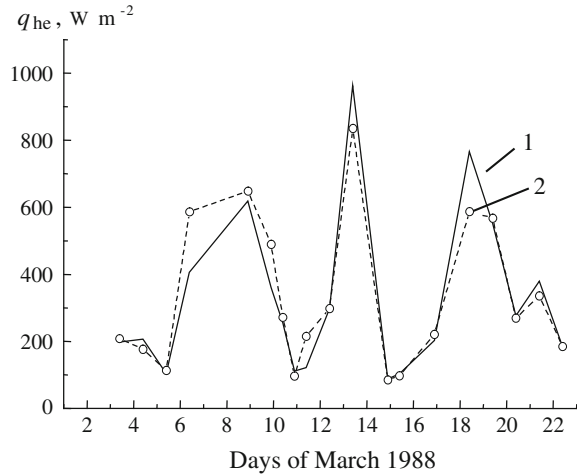
6.3 Experimental Studies of Relationships Between the Brightness Temperatures and SOA Parameters in Front Zones

6.3.1 Synoptic Variability of the SOA Parameters and Brightness Temperature in the Subpolar Hydrological Front

Studying the dynamics and energy of the subpolar hydrological front (SHF) in the North Atlantic, which separates the cold Labrador Current and the warm Gulf Stream, is of key importance in investigating the North Atlantic climate. This front is a unique source of generation (regeneration) of the mid-latitude cyclones. Thus, according to NEWFOUEX-88 data, seven frontal cyclones were generated in March–April 1988 in the SHF area, with a mean lifetime of 3–5 days. This area of the Atlantic is subjected to intensive cyclonic impacts, which are accompanied about 50 % of the time by substantial variations in the atmospheric temperature and humidity fields and in the characteristics of the energy exchange with the sea surface (Gulev et al. 1994).

We analyzed the synoptic variability of oceanographic and meteorological parameters of the SOA as well as its natural MCW radiation characteristics in the SHF region using data of observations from R/Vs *V. Bugaev*, *Musson*, and *Volna* at the stationary phases of the NEWFOUEX-88 and ATLANTEX-90 experiments (see Fig. 6.12) and data of simultaneous measurements from the SSM/I radiometer (satellite F-08).
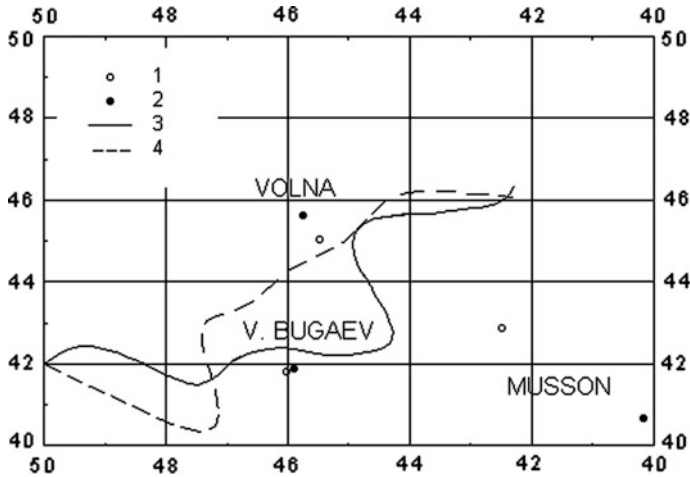
**Fig. 6.12** Locations of the vessels *V. Bugaev*, *Musson*, and *Volna* during the stationary phases of the NEWFOUEX-88 (*1*) and ATLANTEX-90 (*2*) experiments as related to the subpolar hydrological front in March 1998 (*3*) and April 1990 (*4*) (Gulev et al. 1994). The numerals along the axes are the latitude and longitude

Here, we present some results of the study of the SHF using passive MCW radiometric methods in the stationary phase of the NEWFOUEX experiment (March, 3–23, 1988). The oceanic area was remarkable in this period for the strong variability of the near-surface air temperature t_a and humidity e and wind speed V, as well as the fluxes of sensible q_h and latent q_e heat and momentum q_v. This is confirmed by the data in Table 6.3. Such strong variability of the SOA parameters in the SHF area, from where the R/Vs *V. Bugaev*, *Musson*, and *Volna* resided and which were simultaneously observed by the SSM/I radiometer from satellite F-08, initiated the appropriate brightness temperature contrasts in the areas observed (see Table 6.4).

Table 6.3 Extreme values of the SOA parameters

Parameter	Measurement unit	*V. Bugaev*		*Musson*		*Volna*	
		Min	Max	Min	Max	Min	Max
t_a	°C	6.4	17.6	2.8	17.8	−2.2	13.3
e	mb	5.8	18.1	4.4	18.2	2.9	14.6
V	m s^{-1}	0.6	25.2	0.8	26.6	0.6	27.7
q_h	W m^{-2}	−35	455	−19	601	−270	480
q_e	W m^{-2}	3	1208	42	1232	255	574
q_v	N m^{-2}	0.1	1.3	0.1	1.6	0.05	1.9

Table 6.4 Brightness temperature contrasts (in K)

SSM/I channel	85H	37 V	37H	22 V	19 V	19H
V. Bugaev	46.6	26.8	56.3	33.6	25.1	45.7
Musson	72	33.6	78.8	40.4	29.5	62.8
Volna	78.2	33.6	67.5	37.9	24.3	45.8

6.3.2 Features of Atmospheric Dynamics Observed in the SHF Region

The satellite images received by different SSM/I channels give an idea of SHF characteristics, such as the sizes and the position of a frontal area in the synoptic range of time scales. As an example, Fig. 6.13 shows the black-and-white half-tint illustrations of spatial brightness temperature distribution (scan fragments) measured with the SSM/I radiometer channels 19V, H and 37V in the SHF area during an intense cyclone on March 6, 1988 (brightness temperature increases are shown
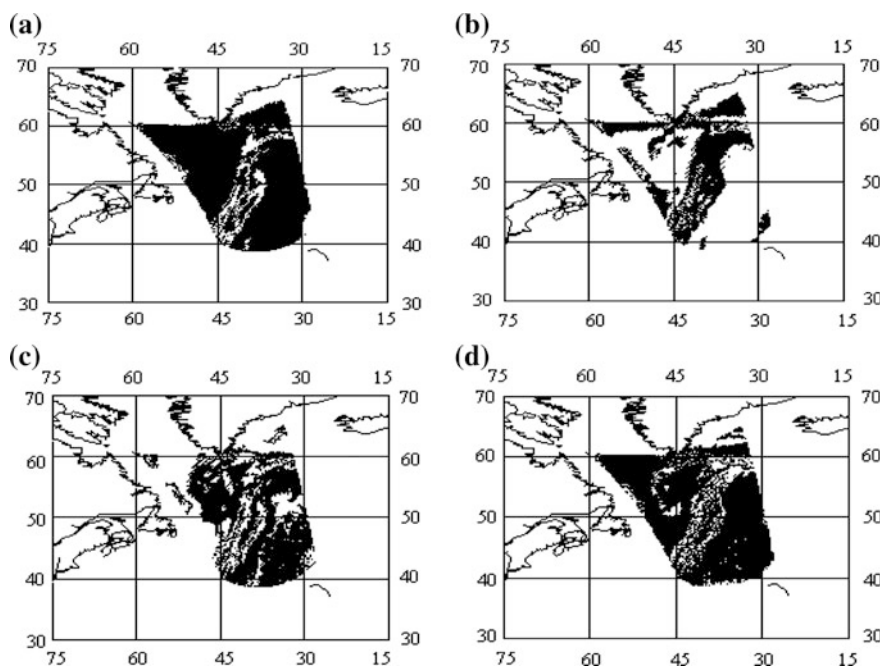
Fig. 6.13 Spatial distribution of the SOA brightness temperature in the SHF area at 08:00 local time on March 6, 1988 based on data from different SSM/I channels: **a** 19V at a range of brightness temperature variations of 175–220 K; **b** 37V at a range of 200–250 K; **c** 19H at a range of 125–190 K; and **d** 37H (150–230 K). The numbers along the axes are the degrees of latitude and longitude

from darker to lighter tones). It follows from the quantitative analysis that the spatial brightness temperature contrasts can be 45–50 K at the vertical polarization and 65–80 K at the horizontal one, depending on frequency. These contrasts are localized within the extended and narrow ocean area that is 500–700 km wide, which corresponds to the SHF position.

Synoptic variability of atmospheric parameters—namely, the near-surface wind speed V, the total water vapor content Q, and the liquid water content W (in the absence of precipitation)—makes a great contribution to brightness temperature variations in the operating SSM/I frequency (wavelengths) range. Figure 6.14 illustrates the example of recovering spatial variations in the above parameters with the SSM/I data from F-08 satellite in the SHF area (the growth of the parameters V, Q, and W is indicated by the transition from darker to lighter tones). In this case, the algorithms are based on the regression analysis of the relationship between the long-term series of SOA brightness temperatures and the direct V, Q, and W measurement data in different physical and geographical zones of the World Ocean.

It follows from the analysis that the satellite V, Q, and W estimates vary from 8 to 32 m s^{-1}, 0.6 to 2.6 g cm^{-2}, and 0 to 1 kg m^{-2}, respectively. Of note is that the pattern of the spatial V and Q distribution (unlike the W distribution) obtained from the SSM/I data corresponds to the generally accepted notions of frontal zones in the ocean and atmosphere, which suppose the availability of two contiguous areas differing substantially in their parameters and separated by a sharp boundary.

The MCW measurements from the F-08 satellite give some idea of the intensity of the horizontal circulations of the atmosphere, particularly of the dynamics of cyclone development with diurnal resolution. For example, the brightness temperature of the SOA in channel 22V of the SSM/I radiometer, which mainly characterizes the total water vapor content of the atmosphere, clearly responded to cyclone development in the SHF area in the morning hours of March 6–7, 1988 (Fig. 6.15). A comparison of Fig. 6.15a and b shows that the atmospheric front was shifting at that time towards the Azores at a rate of approximately 30 km h^{-1}.
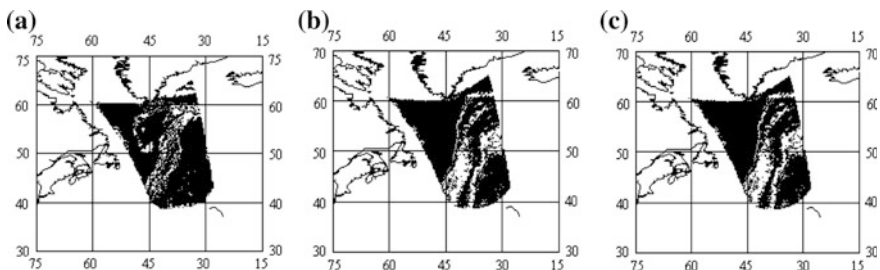
Fig. 6.14 Satellite MCW estimates of **a** near-surface wind speed V, **b** total water vapor content of the atmosphere Q, and **c** liquid water content of the clouds W in the area of the SHF at 08:00 local time on March 6, 1988. The range of V, Q, W is 8–32 m s^{-1}, 0.6–2.6 g cm^{-2}, and 0–1 kg m^{-2}. The numbers along the axes are the degrees of latitude and longitude
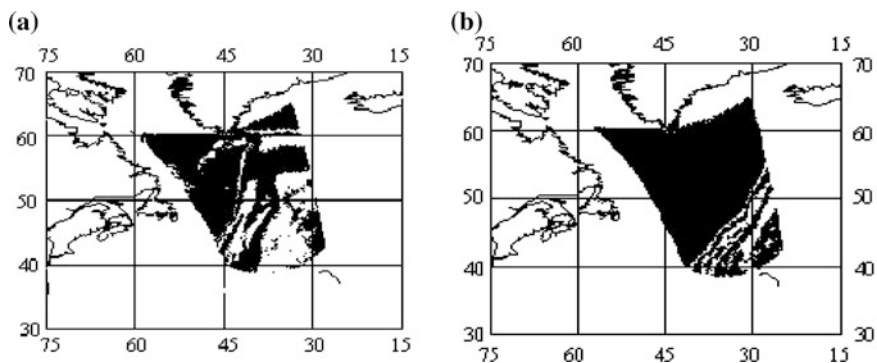
Fig. 6.15 Brightness temperature spatial distribution for SSM/I channel 22 V in the SHF area in the range of its variation from 190 to 240 K: **a** 8:00 local time on March 6, 1988 and **b** 08:00 local time on March 7, 1988. The numbers along the axes are the degrees of latitude and longitude

The potential of the assessment of spatial and temporal contrasts of vertical turbulent fluxes of total (sensible and latent) heat and impulse at the ocean–atmosphere interface in the SHF is based on the radiometric SSM/I data from the F-08 satellite and direct measurement data from R/Vs *V. Bugaev* and *Volna* participating in the NEWFOUEX-88 experiment. The technique used satellite SHF sections crossing both vessels simultaneously. The idea of sections was used previously in vessel investigations in the energy active oceanic zones under the RAZREZY program. The regression coefficients between the brightness temperature measured for different radiometric channels and the intensity of vertical turbulent fluxes of total heat q_{he} and impulse q_v at the SOA interface calculated from the weather research vessels for March 3–23 were determined. Then, the local regression ratios were used to retrieve the variations in the heat and impulse along the satellite SHF sections. Figure 6.16 shows the results of retrieving these variations for the satellite section crossing the R/Vs *V. Bugaev* and *Volna* in the morning and evening of March 6. This illustration demonstrates the effect of the q_{he} and q_v variations (related to the effect of atmosphere cyclonic activity) in the warm SHF area formed by the southern periphery of the Gulf Stream.

6.3.3 Relationship of the Brightness Temperature and Wind Direction in the SHF

A distinguishing feature of the SHF is that the SOA heat exchange characteristics here and in adjacent areas depend not only on the intensity but also on the direction of the air mass transfer relative to the front (Grankov and Milshin 2002). Table 6.5 presents data on heat fluxes at the SOA interface for different directions of the horizontal air-mass transfer counted clockwise from the north (Gulev et al. 1994).

Fig. 6.16 Scheme of **a** the section of the SHF over the subsatellite path F-08 crossing the R/Vs *Volna* and *V.Bugaev* on March 6, 1988 and variations of **b** heat fluxes q_{he} and **c** impulse q_v fluxes: (*1*) 08:00, (*2*) 22:00 this day. *Points* indicate the satellite samples, *N*, subsatellite path number
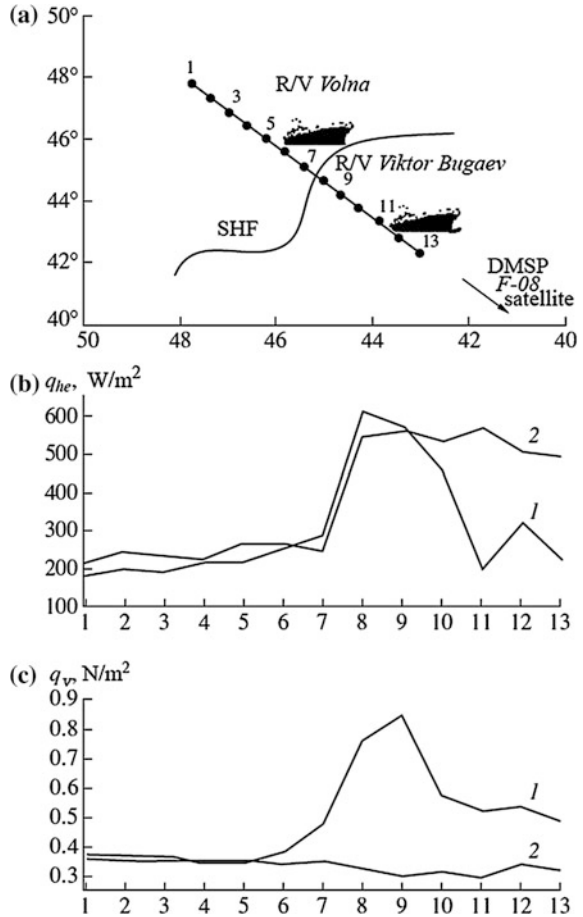
Table 6.5 Mean values of sensible q_h and latent q_e heat fluxes (in W m^{-2}) at different wind directions in the stationary phase of NEWFOUEX-88

φ (°)	V. Bugaev		Musson		Volna	
	q_h	q_e	q_h	q_e	q_h	q_e
30–90	30	104.4	42.3	90.9	10.8	4.5
90–210	39.3	213.2	69.4	256.9	−35.6	−16.5
210–270	83.3	301.1	100.2	313.5	65.3	109
270–30	131.7	319.4	141.4	271.7	92.7	111.3

The ranges selected correspond to the monthly mean directions of transfer along and across the front.

Table 6.5 shows that q_h and q_e are maximal at all points of observations at northwesterly winds. To the north of the SHF (R/V *Volna*) at southeastern winds, when the air assimilated the heat and moisture over the warm oceanic area (R/Vs *V. Bugaev and Musson*) is transferred toward the cold surface, favorable conditions for phase transitions arise in the near-surface atmospheric layer. Due to moisture condensation, the air to the north of the front is heated, and heat fluxes are directed from the atmosphere to the ocean. Therefore, atmospheric synoptic processes in this case play the role of one of the mechanisms of heat and moisture transfer across the front from the warm to the cold part of the ocean.

We also estimated the influence of the near-surface wind speed and its direction on synoptic variability of meteorological parameters, total heat (sensible and latent fluxes), and the SOA brightness temperature for the stationary phase of the ATLANTEX-90 experiment in cold oceanic waters in the area of the R/V *Volna* position, located at a distance about 200 km from the SHF. The results of the regression analysis of the relationships between these parameters demonstrate that the variability of the near-surface air temperature and humidity is determined by a combined effect of wind speed and direction, characterized quantitatively by a projection of the wind vector V_n onto the normal passing through the R/V *Volna* to the curve describing the position of the SHF. A linear regression analysis of the relationships between the near-surface t_a and V_n, e and V_n parameters in the range of the angle φ from 290 to 340° was carried out, taking into account the approximate data for the SHF position in April 1990 (Gulev et al. 1994). The largest values of the correlation coefficients in these relationships correspond to $\varphi = 330°$. Figure 6.17 illustrates a relationship between hourly samples of sheep measurements of the near-surface air temperature and humidity and V_n for the period April 4–21, 1990.

Figure 6.18 compares variations of the total heat fluxes q_{he} and the brightness temperature T^b as measured in the SSM/I channel 22V with variations of the parameter V_n at $\varphi = 330°$. A well-marked connection is found between variations of q_{he} and V_n ($r = 0.79$). As V_n increases, discrepancies between the heat characteristics of the ocean and atmosphere are growing; consequently, the total heat fluxes are increasing. The brightness temperature of the SOA natural MCW radiation measured by the SSM/I channel 22V is closely related to the intensity of heat and moisture exchange at the system interface. Its value increases with an increase in temperature and humidity of the atmosphere. The minimum brightness temperature and maximum heat flux on April 9–11 were caused by the transfer of cold dry air from the northwest, which led to the formation of positive total heat fluxes directed from the ocean to atmosphere. On the contrary, on April 13, southeasterly winds blowing from the warm Gulf Stream caused heating of the atmospheric layers in the area of the R/V *Volna*. This heating produced heat fluxes directed from the atmosphere to the ocean and simultaneously resulted in an increase of the SOA brightness temperature.
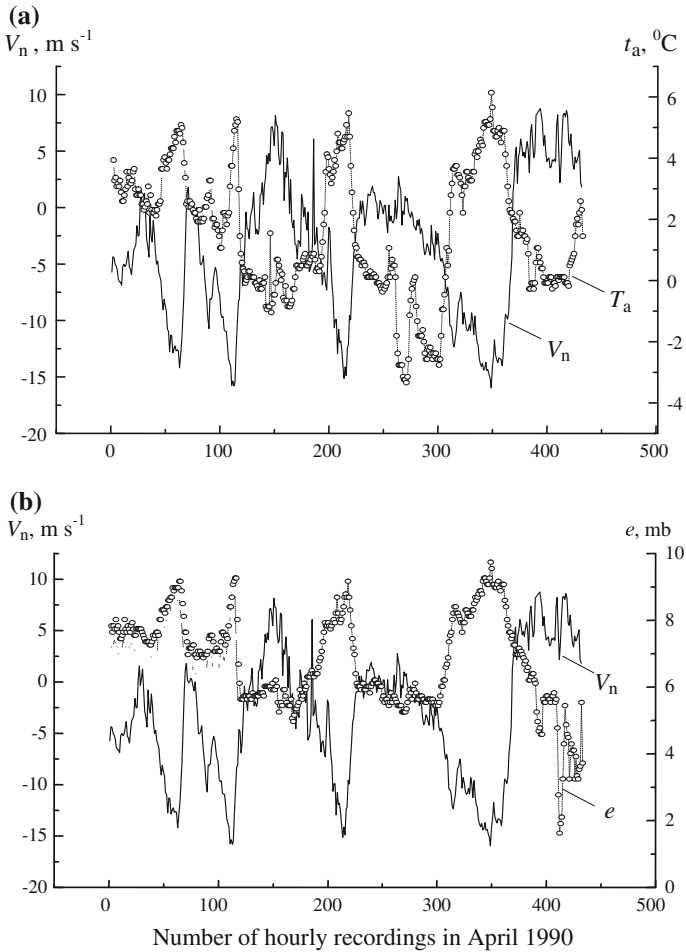
Fig. 6.17 Results of a combined analysis of hourly samples of **a** V_n and t_a; **b** V_n and e at the stationary phase of the ATLANTEX-90 experiment (R/V *Volna*, April 4–21, 1990) Correlation coefficient **a** $r = -0.7$; (b) $r = -0.81$

A close connection was also found between the mean daily values of total heat fluxes and the brightness temperature measured from F-08 approximately once per 24 h and mean daily values throughout the stationary phase of the ATLANTEX-90 experiment (Fig. 6.19). Regression analysis was made for the relationships between variations of q_{he}, T^b, and V_n. The value of the latter was determined based on the assumption that the angle of the normal to the SHF boundary passing through the R/V *Volna* was kept constant for the period from 4 to 21 April 1990 ($\varphi = 330°$). Under this condition, the variations of V_n were caused only by variations of wind speed and direction with respect to the normal. The values of correlation coefficients between q_{he} and V_n, T^b, and V_n are 0.85 and -0.73, respectively.
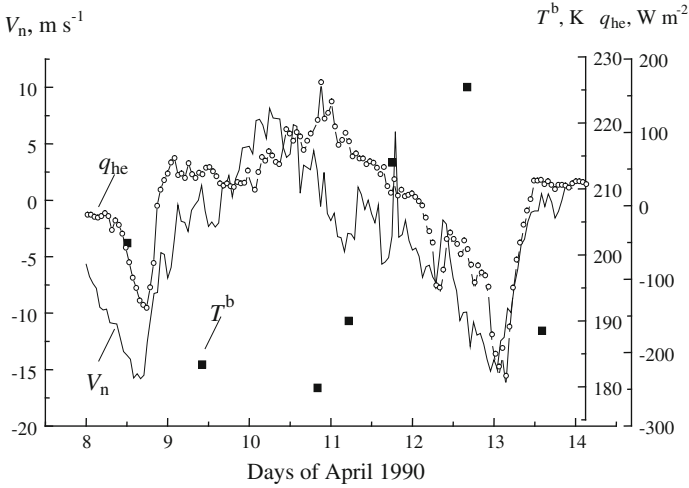
Fig. 6.18 Response of SOA brightness temperature T^b at the wavelength 1.35 cm and total heat fluxes q_{he} to variations of V_n during the passage of a cyclone for the R/V *Volna*, April 8–13, in the Newfoundland EAZO

Fig. 6.19 Variations of the daily values of the parameter q_{he} and the SSM/I-derived parameter T^b during the stationary phase of ATLANTEX-90 (R/V *Volna*)
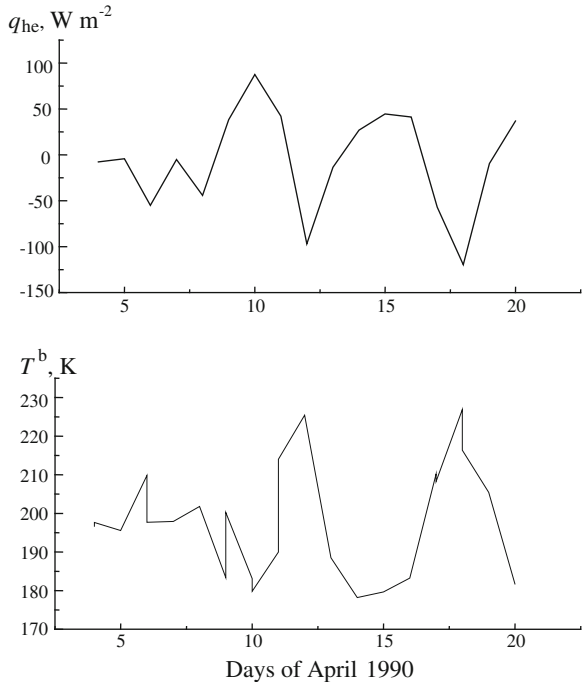
Thus, the data of the combined ship and satellite analysis of the SHF suggest that there is a close connection between the brightness temperature of the SOA in cold frontal waters and the intensity and direction of the air-mass transfer from the opposite warm oceanic areas determining the heat characteristic of the cold areas. This result points to the potential possibility of using satellite MCW radiometric measurements to estimate the influence of the heat and moisture transfer across the front on the intensity of the ocean–atmosphere heat interaction in Newfoundland and possibly other energy-active zones.

6.4   Conclusions

The relationships between the ocean–atmosphere system's natural MCW radiation with the processes of heat interchanges in the system are most prominent at the synoptic range of time scales. The following regularities were observed for this case:

1. A good agreement between theoretical and experimental (satellite) estimates of the brightness temperature of the ocean atmosphere system's natural MCW radiation and the surface heat fluxes as a result of their processing was observed in the mid- and north latitudes of the North Atlantic.
2. The direct relational influence of the near-surface wind speed and its direction on synoptic variability of meteorological parameters, the total heat (sensible and latent fluxes), and the ocean–atmosphere system's brightness temperature were observed.

References

Bychkova IA, Victorov SV, Vinogradov VV (1988) Remote sensing of sea temperature. Gidrometeoizdat, Leningrad In Russian.

Grankov AG, Milshin AA (1999) Interrelation between the microwave radiation of the ocean-atmosphere system and the boundary heat and momentum fluxes. Izvestiya, Atmospheric and Oceanic Physics 35:570–577.

Grankov AG, Mishin AA (2002) Influence of the near-surface wind speed and direction on the heat and radiative characteristics of the ocean-atmosphere system in areas of the subpolar hydrological front. Russian Meteorology and Hydrology. Allerton Press 7: 41–46.

Gulev SK, Kolinko AV, Lappo SS (1994) Synoptic interaction between the ocean and atmosphere in middle latitudes. Gidrometeoizdat, St. Petersburg In Russian.

Hollinger PH, Peirce JL, Poe GA (1990) SSM Instrument evaluation. IEEE Trans. Geosci. Rem. Sensing 28:781–790.

Khundzhua GG, Andreev EG (1973) On determination of heat and water vapor fluxes in the ocean-atmosphere system from measurements of the temperature profile in a thin water layer. Doklady Akademii Nauk SSSR 208 :841–843 In Russian.

Kramer HJ (1994) Observation of the Earth and environment. Survey of missions and sensors. Second edition. Springer-Verlag, Berlin.

Wentz FJ (1991) User's manual SSM/I Antenna temperature tapes (Revision 1). RSS Technical RSS technical report. Santa Rose.

Chapter 7
Seasonal and Interannual Changeability of Heat Fluxes in the North Atlantic as Seen from the SSM/I Radiometer

7.1 Satellite-Derived Estimates of Monthly Mean Brightness Temperature, Total Water Vapor of the Atmosphere, and Wind Speed

7.1.1 Monthly Mean Brightness Temperatures Observed with the SSM/I Radiometer over the North Atlantic

Satellite MCW radiometric methods can be used as an effective tool when investigating SOA parameters in ocean–atmosphere interaction processes, such as the near-surface wind speed (V), total water vapor content (Q), and integral liquid water content in the clouds (W), which are characterized by strong variability in their current (hourly, daily) values. Based on the results of SSM/I radiometric measurements from satellite F-08 carried out in January, February, July, and August 1994 (taken from the archive of the Remote Sensing Laboratory, California), we retrieved the monthly mean values of parameters V, Q, and W for selected points of the North Atlantic. These points coincide with the locations of the following weather stations: Alpha (A), Bravo (B), Charlie (C), Delta (D), Echo (E), Hotel (H), India (I), Juliett (J), Kilo (K), Lima (L), and Mike (M). Some of these points are related to the Norwegian, Newfoundland, and Gulf Stream energy active zones (EAZOs) characterized by intensity values of the ocean–atmosphere heat interaction (see Fig. 7.1). Most of the values are related to areas of the Gulf Stream and North Atlantic currents where appreciable values of air–sea temperature differences and their changeability are observed (see Fig. 7.2).

The number of satellite orbits suitable for the weather station locations varies from 17 to 34 per month. This frequency of spatial observations determines the monthly mean surface parameters V, Q, and W with suitable accuracy for oceanologists and meteorologists.

The SSM/I data from various EAZOs shows the appreciable monthly mean brightness temperature contrasts that were observed between February and August

Fig. 7.1 Location of vessel weather stations in the North Atlantic
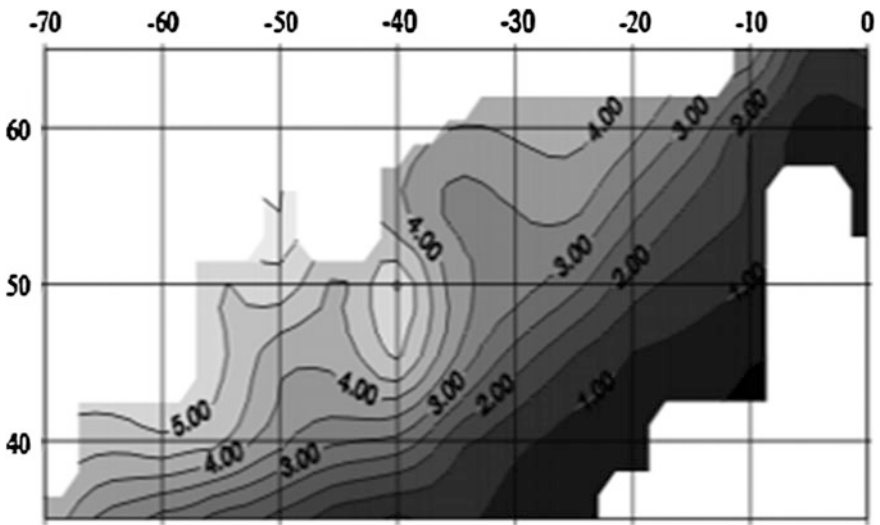
Fig. 7.2 Spatial distribution of the climatic ocean and atmosphere temperature differences in the Gulf Stream and North Atlantic currents. The numbers along the axes indicate the degrees of latitude and longitude

1994 (see Table 7.1). This work was conducted as part of the NASA and Roscosmos contract during 1996–98 and published later by Grankov and Gulev (1996).

For example, at point H within the Gulf Stream EAZO, seasonal variations of the SOA monthly mean brightness temperatures in millimeter and centimeter

Table 7.1 Monthly mean brightness temperatures of the SOA (in Kelvins) observed in active points of the North Atlantic in February and August 1994

Points	85V	85H	37V	37H	22V	19V	19H
February 1994							
A	234.5	196.5	201.4	147.8	188.2	177.0	112.1
B	232.1	192.5	200.9	147.5	184.7	175.7	110.4
C	237.3	201.1	202.2	149.3	189.9	177.1	113.0
D	242.4	213.2	207.7	160.1	198.9	183.8	123.4
E	250.3	221.1	206.2	154.1	210.6	186.6	126.0
H	239.4	198.4	201.0	144.1	193.9	178.3	111.9
I	238.0	200.5	202.8	150.6	192.3	178.7	115.3
J	240.1	206.5	204.3	153.3	196.8	180.7	118.8
K	245.0	214.9	206.3	156.3	202.5	183.2	122.6
L	238.8	204.9	203.9	153.1	194.4	179.8	117.6
M	236.9	197.7	201.7	145.7	187.8	175.9	108.8
August 1994							
A	250.2	220.6	207.5	153.4	204.6	182.4	119.3
B	249.9	222.7	211.8	163.0	210.1	186.8	128.2
C	252.3	223.3	207.9	154.0	207.7	184.0	122.0
D	259.8	235.6	214.1	163.1	225.2	195.6	137.9
E	267.0	244.9	216.0	162.0	235.0	201.1	142.8
H	264.3	242.7	216.9	165.7	234.5	201.6	145.1
I	249.2	215.2	205.0	147.7	203.1	181.5	116.5
J	251.9	223.3	208.2	155.0	209.2	185.1	123.4
K	258.4	234.2	211.7	159.1	219.1	190.7	130.6
L	249.9	217.7	205.7	150.0	205.1	182.6	118.9
M	247.3	210.9	203.6	145.3	201.9	180.4	114.8

wavelengths varied from 16 to 45 K. At point M (in the Norwegian EAZO), these contrasts were about 13 K. This level of brightness temperature contrasts with the sensitivity of the SSM/I device and its calibration errors, which forms the background of an analysis of seasonal dynamics of the ocean–atmosphere interaction.

7.1.2 Monthly Mean SOA Parameters Retrieved with the SSM/I Radiometer over the North Atlantic and Their Accuracy

Using algorithms from Alishouse et al. (1990), Alishouse et al. (1990), and Goodberlet et al. (1990), along with data from durational satellite and direct measurements in various physical and geographical areas of the World Ocean, we

obtained daily estimates of the near-surface wind speed (*V*), total water vapor content of the atmosphere (*Q*), and integral liquid water content in the clouds (*W*) for the previously listed locations in the North Atlantic. On the basis of these results, we estimated the monthly mean values for the parameters *V*, *Q*, and *W*, as well as their variability for different scales of spatial averaging for the brightness temperatures measured by the SSM/I radiometer. Tables 7.2 and 7.3 show some results from this analysis for the points A–M in the North Atlantic.

For validation of satellite MCW radiometric estimates of the monthly mean wind speed and total atmospheric water vapor content, we used data from the Comprehensive Ocean and Atmosphere Data Set (COADS) archive and the National Centers for Environmental Prediction (NCEP)/National Center for Atmospheric Research (NCAR) for seasonal time scales (between February and August months). The NCEP/NCAR archive includes the results of long-term

Tables 7.2 MCW radiometric estimates of monthly mean wind speed and their rms values using various spatial averaging of the satellite data

Points	Mean	rms	Mean	rms	Mean	rms
Without any corrections for the effects precipitation						
A	17.9	3.86	17.8	3.71	18.0	3.67
B	18.7	4.16	18.4	3.22	18.6	3.15
C	17.1	3.70	16.6	3.83	16.3	3.87
D	19.7	4.99	18.9	5.34	18.9	5.39
E	14.9	3.16	15.1	3.04	15.0	2.89
H	14.6	4.09	14.7	4.13	14.9	3.99
I	17.7	4.17	17.5	4.22	17.6	4.21
J	17.4	–	17.0	4.00	17.9	3.91
K	16.3	4.02	16.6	3.38	16.7	4.62
L	18.0	4.32	18.2	4.41	18.4	4.50
M	15.4	–	15.6	–	15.2	3.25
Accounting for the influence of precipitation						
A	17.7	3.30	17.7	3.67	17.8	3.70
B	18.9	3.60	18.2	3.22	18.5	3.50
C	16.2	3.70	16.5	3.60	16.8	3.50
D	18.9	4.40	18.7	4.00	17.7	4.30
E	14.8	2.90	14.6	2.50	14.0	2.70
H	14.5	4.30	14.0	4.20	14.6	4.00
I	17.2	3.70	17.2	4.13	17.2	4.12
J	16.9	–	16.4	4.45	17.1	3.81
K	15.8	3.57	15.8	3.87	15.8	3.92
L	17.2	3.85	17.3	3.91	17.2	3.87
M	14.9	3.21	14.9	3.22	15.0	3.11
	5° × 5°		2.5° × 2.5°		1° × 1°	

Table 7.3 MCW radiometric estimates of monthly mean total vapor content of the atmosphere and their rms values for various spatial averaging of the satellite data

Points	Mean	rms	Mean	rms	Mean	rms
Without any corrections for precipitation and cloudiness effects						
A	0.74	0.16	0.73	0.16	0.74	0.17
B	0.62	0,16	0.60	0.13	0.59	0.13
C	0.81	0.18	0.81	0.18	0.10	0.09
D	1.09	0.70	1.00	0.60	0.90	0.3
E	1.90	0.54	1.92	0.55	1.70	0.70
H	1.12	0.46	1.11	0.43	1.12	0.30
I	0.90	0.19	0.80	0.70	0.88	0.70
J	1.13	–	1.18	–	–	–
K	1.38	0.42	1.40	0.44	1.39	0.44
L	0.98	0.25	0.98	0.22	0.98	0.21
M	0.77	–	0.80	–	–	–
Accounting for cloudiness and precipitation						
A	0.72	0.16	0.73	0.16	0.74	0.17
B	0.61	0.14	0.60	0.13	0.59	0.13
C	0.80	0.17	0.81	0.18	0.81	0.19
D	1.00	0.38	1.00	0.36	0.99	0.33
E	1.88	0.53	1.90	0.54	1.96	0.57
H	1.08	0.42	1.09	0.41	1.10	0.42
I	0.87	0.16	0.87	0.15	0.87	0.15
J	1.09	–	1.16	–	1.08	0.27
K	1.31	0.38	1.31	0.40	1.31	0.41
L	0.93	0.20	0.93	0.19	0.92	0.18
M	0.74	0.16	0.74	0.16	0.75	0.14
	5° × 5°		2.5° × 2.5°		1° × 1°	

observations in areas of study such as oceanography, weather and climate, hydrology and glaciology, biogeochemistry, etc. (Kalnay et al. 1996).

We established that the discrepancy between the satellite and direct data was 0.2–0.4 g cm^{-2} for the parameter Q in the range of its variations $0.5 < Q < 4$ g cm^{-2}; 2–3 m s^{-1} for the parameter V in the range of its variations $0 < V < 10$ m s^{-1}, and 3–5 m s^{-1}, if $V > 10$ m s^{-1}. It follows from Tables 7.2 and 7.3 that (1) the SSM/I estimates of the monthly mean near-surface wind speed and total water vapor of the atmosphere slightly depend on the spatial averaging of satellite data; and (2) in the range of time and spatial resolution suitable for the SSM/I device, atmospheric cloudiness and precipitation do not influence the accuracy of the MCW radiometric estimates of the near-surface wind speed V and total water vapor content Q.

7.2   Estimates of Monthly Mean Heat Fluxes in the North Atlantic Using Data from the F-08 Satellite (DMSP)

7.2.1   Validation of the Monthly Mean Heat Fluxes Estimated from Satellites with Archival Data

The average monthly sensible and latent heat fluxes were estimated based on satellite measurements and compared with the estimated heat fluxes taken from the COADS climatic archives and 1994 data from the NCEP/NCAR archives (Grankov et al. 1999). Satellite passive MCW radiometric data were used for the determination of near-surface wind speed (V) and total water vapor content of the atmosphere (Q), whose monthly mean values Q clearly correlate with those of the-near surface air humidity (water vapor pressure) e and temperature t_a. The relationships between monthly mean values of Q and e parameters were calculated by analyzing 49 oceanic aerologic stations during 17 years (Liu 1988). We used these data as well as the results of systematization for an extensive series of atmospheric humidity observations (Matveev and Soldatov 1982) to estimate some local regressions for the determination of water vapor pressure (e) in the near-surface atmosphere in the formula (1.2). The monthly mean values of the near-surface air temperature (t_a) necessary for the calculation of sensible heat fluxes (q_h) by the formula (1.1) can be determined from monthly mean values of the near-surface air humidity (e) with the help of the regression relationships between t_a and e parameters using the archival data of VNII GMI (All-Russian Research Hydrometeorological Institute, Obninsk) averaged over the period 1957–1990 (the archives of Birman).

The monthly mean OST values (t_s) necessary for the calculations of sensible heat fluxes (q_h) were borrowed from the archives of oceanographic and hydrometeorological COADS data in the form of averaged many-year values, which can be explained by the following two circumstances:

1. The channels for the OST determination are absent as such in the SSM/I radiometer, whose data are used for approbation of this algorithm.
2. The interannual variability of monthly mean OST values is substantially lower than their seasonal variability—the analysis of which is our basic purpose.

To calculate the monthly mean heat fluxes q_h and q_e, the parameterizations (1.1) and (1.2) are used. Here, the monthly mean values of t_s, t_a, e, and V parameters serve as initial values. Such an approach yields results close to those obtained by a more rigorous method for the calculation of heat fluxes, taking into account the synoptic variability of these parameters of the SOA.

The average (monthly mean) values of sensible and latent heat fluxes were assessed in January, February, July, and August 1994 for 16 regions of the North Atlantic, for which the most representative archives of oceanological and meteorological data are available. The assessments for 11 areas of the North Atlantic (weather stations A, B, C, D, E, H, I, J, K, L, and M) for January 1994 are presented
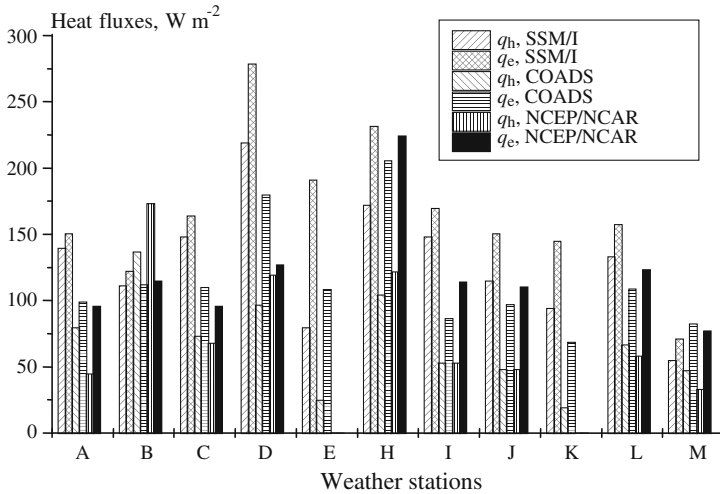
Fig. 7.3 Comparison of satellite-derived (SSM/I) and archival (COADS and NCEP/NCAR) estimates of the monthly mean sensible (q_h) and latent (q_e) heat fluxes attached to various weather stations in the North Atlantic in February 1994 with spatial averaging of $2.5 \times 2.5°$

in Fig. 7.3. Many of these stations are confined to energy-active zones, such as the Norwegian, Newfoundland, and the Gulf Stream zones, which are characterized by the highest intensity of thermal interaction between the ocean and atmosphere. The number of satellite orbits falling on these regions of the North Atlantic varies from 17 to 34 per month and ensures a quite satisfactory (according to measures accepted in toceanology) quality of heat flux estimations (Taylor 1984).

7.2.2   Disagreements Between Satellite and Archival Data

The results of the comparison of SSM/I estimations of monthly mean sensible and latent heat fluxes averaged in $2.5 \times 2.5°$ squares with COADS and NCEP/NCAR archival data are quite satisfactory. In our opinion, the main reasons for the discrepancies between satellite and direct measurement data are as follows:

1. The errors in computing heat fluxes from the monthly mean parameters V and Q, but not from its current (hourly, daily) values
2. Ignoring the spatial and seasonal variability of some parameters of the bulk parameterizations, such as the coefficients of heat (C_T) and moisture (C_V) interchange between ocean and atmosphere errors in calculations

Moreover, there exist considerable differences between various archival data that characterize the spatial and temporal variability of the monthly mean sensible and latent heat fluxes estimates in the North Atlantic, reaching 50 % and sometimes even 100 % (Lappo et al. 1990). The results of the analysis also show that the

satellite passive MCW radiometric estimates of the monthly mean heat fluxes, as well as their most dynamic components in the form of monthly mean values of wind speed and total water vapor content in the atmosphere, are weakly changed in transition from the 1° to 5° squares.

7.3 Estimates of Interannual Variability of Surface Heat Fluxes in the North Atlantic with DMSP SSM/I Radiometric Data

7.3.1 Problem Statement

The use of satellite passive MCW radiometric methods in climatic studies came into use only after launching the NIMBUS 7 satellite (1978) with the Scanning Multichannel Microwave Radiometer (SMMR) radiometer on board, which operated for about 9 years. Since 1987, the DMSP satellite series (1987) equipped with the Special Sensor Microwave/Imager (SMM/I), the Atmospheric Temperature Profiler (SSM/T-1), and the Atmospheric Water Vapor Profiler (SSM/T-2) have been operating. In addition to this, the EOS Aqua (2002) satellite with the Advanced Microwave Scanning Radiometer (AMSR-E) and the data satellites of the METEOR-3M series with the radiometer module of temperature and humidity sensing of the atmosphere (MTVZA) provide us with a unique possibility to study the *decadal* processes of ocean-atmosphere heat and dynamic interaction over periods of 30 years. These tools can be used in the frame of the program's climate variability and predictability (CLIVAR Implementation Plan 1998) and other prominent projects.

Here, we present some estimates of the usefulness of the SSM/I data collected during the DMSP satellite missions to evaluate the long-term dynamics of large-scale heat fluxes at the boundary of the SOA, as well as the most significant of its components, such as the wind speed (V), total water vapor of the atmosphere (Q), and precipitation (R). The Norwegian, Newfoundland, and Gulf Stream energy-active zones of the North Atlantic, including their local parts related to the oceanic weather stations M (66°N, 2°E), D (44°N, 41°W), and H (38°N, 71°W), were considered as the areas of our paramount interests. These zones are situated in a course of the Gulf Stream and North Atlantic current and exert appreciable influence on the weather conditions of Europe and European part of Russia (see Fig. 7.4).

For examination of the feasibility of determining the heat fluxes and their main components for efficient accuracy using DMSP SSM/I measurements, we used the data measurements from the satellites F-08 and F-10–F-13 during the period January 1988 to December 1996 (these data are available from the Goddard Distributed Active Archive Center (DAAC) of NASA Marshall Space Flight). The initial telemetry signals (more than 200-gigabyte datasets in formats SSM and
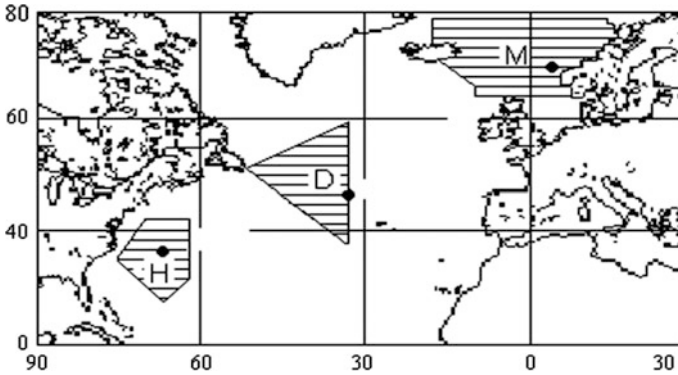
Fig. 7.4 Location of Norwegian, Newfoundland, and Gulf Stream active zones and the ocean weather stations M (MIKE), D (DELTA), H (HOTEL)

HDF) were converted into antenna, then into brightness temperatures by applying the special calibration procedure described in Wentz (1991). The next step was to evolve from the global data sets the fragments appropriate to the Norwegian, Newfoundland, and Gulf Stream active zones of the North Atlantic. Then, the sequences of current (daily) and monthly mean SSM/I brightness temperatures over the period 1988–1994 were developed for satellite orbits that passed through more local areas (squares 0.5 by 0.5°) covering the points M, D, and H.

7.3.2 Initial Satellite and Oceanic Archival Data

Figure 7.5 illustrates variations of the monthly mean parameters V, Q, and R in the point **M** in the Norwegian EAZO, which were retrieved from the SSM/I data with algorithms (Alishouse et al.; Goodberlet et al. 1990; Ferraro and Marks 1995). These algorithms are based on the regressions between the SOA brightness temperatures and the parameters V, Q, R accumulated during long-term synchronous satellite and in situ measurements in different physical and geographical zones of the earth; the discrepancies between the estimates of the parameters V, Q, and R were 2 m s^{-1}, 0.02 g cm^{-2}, and 5 mm h^{-1}, accordingly. The time interval of January 1988 to June 1988 was omitted because the initial data were inaccessible for processing in these series.

We analyzed the possibilities of using the SSM/I radiometer to study interannual variations of the parameters V, Q, and R during 1988–1998s (see Fig. 7.6). Good compliance is shown between climatic satellite-derived MCW radiometric estimates of the monthly mean wind speed at the centimeter level averaged during the 1988–1998 period and the data collected at point M by traditional means at the Obninsk Center during 1953–1974 (Handbook 1979). Their correlation varied from 0.84 to 0.88. On the basis of the archival NCEP/NCAR data, we discovered that the

Fig. 7.5 Seasonal and annual
variability of the monthly
mean parameters *V*, *Q*, and
R at point M in the North
Atlantic derived from the
SSM/I radiometer
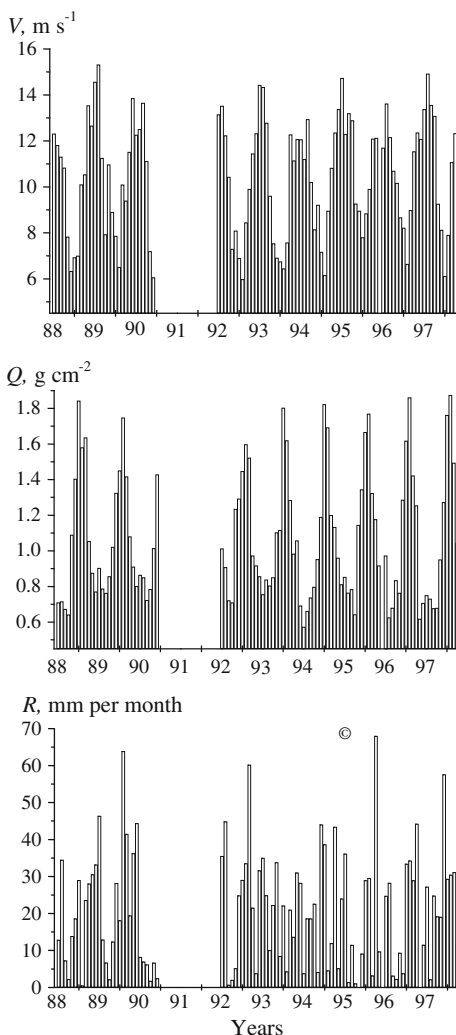
differences between the satellite and direct estimates (in terms of their absolute
values) were 3–4 m s^{-1}.

The satellite MCW radiometric estimates of the monthly mean total water vapor
content of the atmosphere slightly differed from the NCEP/NCAR estimates. In our
opinion, this fact is due to the active use of satellite MCW radiometric data in the
NCEP/NCAR archive in the later years, when satellite data (especially the SSM/I
radiometric data) naturally enlarged the arsenal of traditional (vessel, meteorolog-
ical, and aerologic) means. Figure 7.6 shows appreciable year-to-year variations of
seasonal contrasts of the monthly mean brightness temperature at points M, D, and
H; this gives us a good basis for an analysis of the interannual dynamics of

Fig. 7.6 Seasonal dynamics of monthly mean parameters *V*, *Q*, and *R* from 10-year measurements of the SSM/I radiometer in the Newfoundland EAZO: *1* SSM/I, *2* extreme values from Handbook (1979), *3* Snopkov (1981)
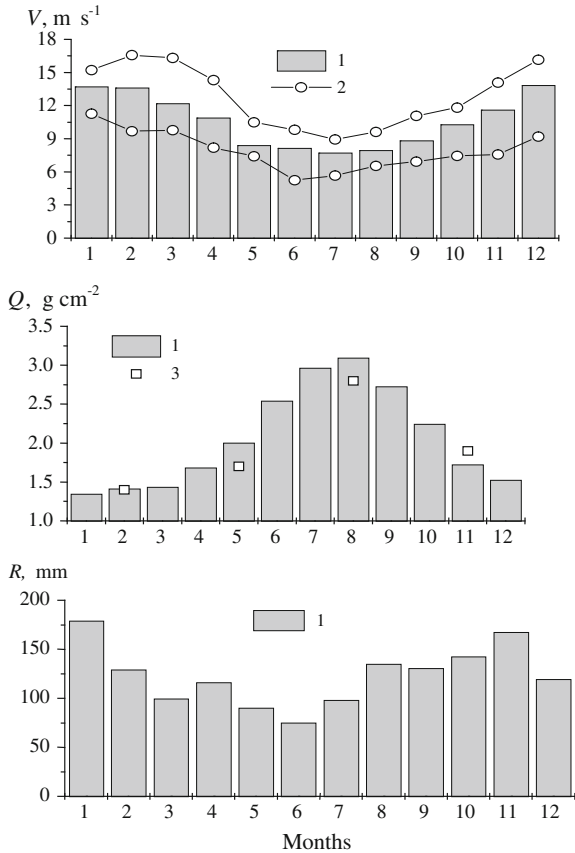
large-scale ocean–atmosphere interaction characteristics and the data of the SSM/I long-term measurements.

We compared the seasonal trends of the monthly mean SSM/I brightness temperature of the SOA in points M, D, and H averaged over the period 1988–1999 and their interannual variations during this time interval. Figure 7.7 demonstrates these results for the SSM/I channel 22 V (the wavelength 1.35 cm) which, as stated above, are the most informative for the analysis of ocean–atmosphere interaction in the synoptic range of time intervals.

Taking into account the strong correlation between brightness temperature at the wavelength 1.35 cm and the parameters of heat exchange processes in the ocean–atmosphere interface at synoptic and seasonal time scales, we can expect that the long-term measurements from the SSM/I device (or similar devices) will be useful in studies of these processes at climatic scales. Possibly, an analysis of relationships between seasonal and climatic components of the brightness temperature variability will explain the peculiarities of the SOA's behavior as a climatic system in various oceanic regions.

Fig. 7.7 Seasonal trends of the monthly mean SSM/I brightness temperature at the wavelength 1.35 cm averaged over the period 1988–1999 (*1*) and their interannual variations during this time interval (*2*) at points M, D, and H
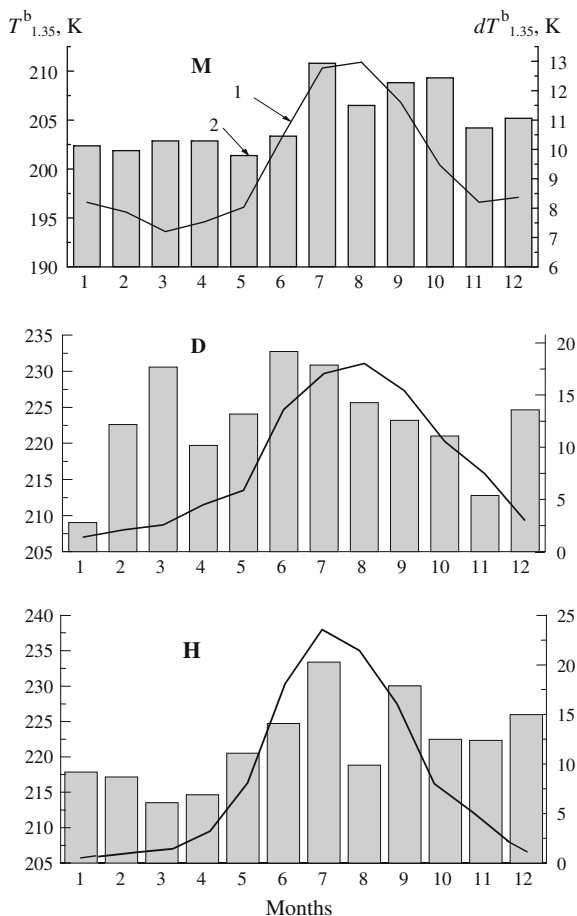
7.3.3 Brightness Temperature as the Direct Characteristic of Surface Heat Fluxes and Their Variability

We have revealed that the SSM/I-derived brightness temperatures of the SOA are responsive to intra- and interannual variations of sensible, latent, and total heat fluxes at the points M, D, H (i.e., in 0.5 by 0.5° areas covering these points and in line with the SSM/I spatial resolution). For example, Figs. 7.8 and 7.9 demonstrate a noticeable relationship between long-term variability of monthly mean total heat flux and SSM/I brightness temperature at the wavelength 1.35 cm measured in the 22 V channel of the radiometer (available gaps in the brightness temperature data are caused by trouble processing the initial SSM/I data). Figure 7.9 shows some results of comparison between the total heat fluxes and their estimates, which are

Fig. 7.8 Comparison of
monthly mean heat fluxes q_{he}
(*1*) and brightness
temperature $T_{1.35}^{b}$ (*2*) at the
points M, D, H during 1988–
1994
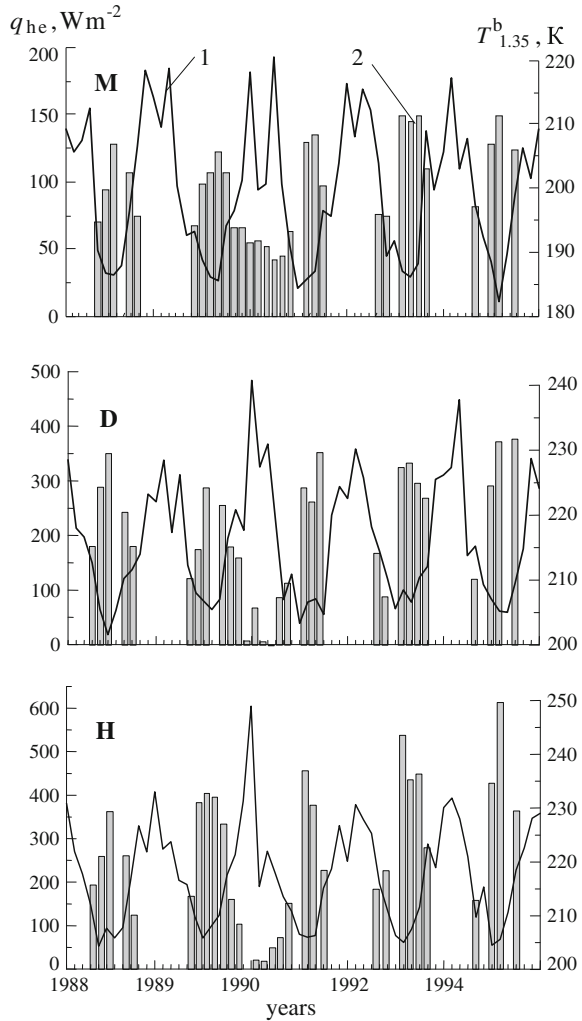
represented as a linear combination of brightness temperatures T_{22V}^{b}, T_{155V}^{b}, and T_{155V}^{b}.

Thus, it has become possible to determine the total heat flux as a linear combination of SSM/I brightness temperatures. The use of another SSM/I channel (besides the 22 V channel) is helpful for corrections of heat flux estimates subjected to an influence of the atmospheric liquid water and near-surface wind speed variations.

Our results display the feasibility of determining the climatic heat flux in the ocean–atmosphere interface based on *meteorological* sensing of the atmosphere. This question occurred to us while studying the contribution of different parameters

Fig. 7.9 Correlation of monthly mean heat fluxes q_{he} (*1*) with their SSM/I-derived estimates (*2*) at the points M, D, H during 1988–1994 (*r* coefficient of correlation)
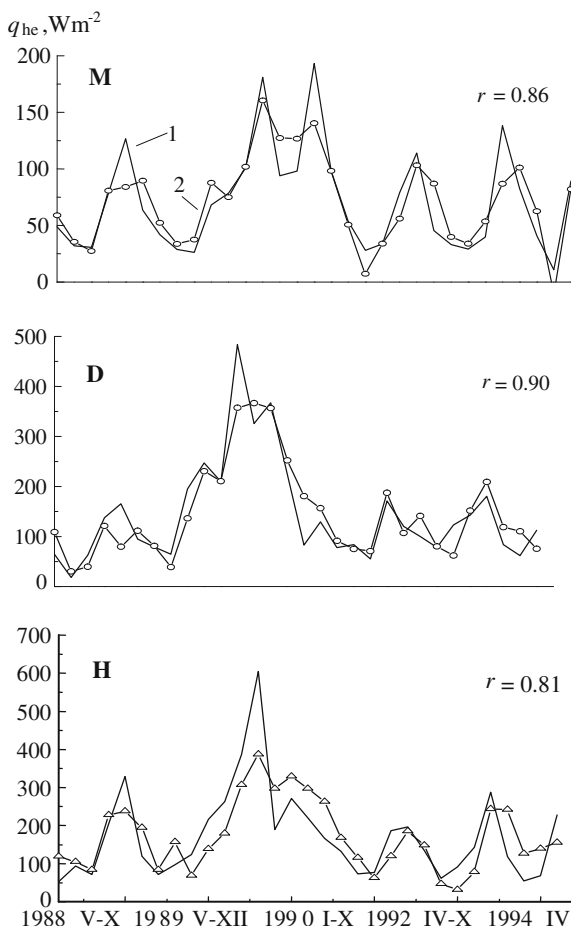
of the ocean and atmosphere on relationships between the brightness temperature and heat fluxes in the *synoptic* range of time scales (Grankov et al. 2000). We observed in this case a negligible effect of the water surface temperature on these relationships by more considerable heat inertia of the ocean against the atmosphere. However, why this peculiarity is extending over climatic scales is the urgent question. Its solution is substantial when we analyze the following problems:

(a) What are the original factors in processes of large-scale ocean–atmosphere heat interaction (from a scientific point of view)?
(b) To what extent are meteorological satellites effective in studies of these processes (as the practical aspect)?

7.4   Conclusion

Long-term measurements from the DMSP SSM/I devices allow us to estimate the monthly mean values of most changeable SOA parameters, which form the ocean-atmosphere heat interactions on seasonal and climatic time scales as the monthly mean, including its more dynamic (changeable) components: wind speed and total water vapor content in the atmosphere, and which current values cannot be evaluated with ordinary reference data. The satellite estimates of the monthly mean estimates of wind speed and atmospheric total water vapor content slightly depend on the spatial averaging (within the squares varying from $1 \times 1°$ to $5 \times 5°$); the cloudiness and precipitation do not influence the accuracy of these parameters' estimation. A strong correlation between monthly mean values of the SOA brightness temperature at the resonant line of water vapor absorption in the atmosphere (1.35 cm) and the surface vertical turbulent heat fluxes in some areas of the North Atlantic over a period of years has been justified.

References

Alishouse JC, Snyder SA, Vongsatorn J, Ferrado RR (1990) Determination of oceanic total precipitable water from the SSM/I. J Geophys Res 28:811–816 (a).

Alishouse JC, Snyder JB, Westwater ER et al. (1990) Determination of cloud liquid water content using the SSM/I. J Geophys Res 28:817–821.

Goodberlet MA, Swift CT, Wilkerson JC (1990) Ocean surface wind speed measurements of the Special Sensor Microwave/Imager (SSM/I). IEEE Trans Geosci Remote Sens 28:823–828.

Grankov AG, Gulev SK (1996) Use of the radiometric measurements from the "Priroda-Mir" (Alpha) station for estimating seasonal and synoptic vertical fluxes of heat and water over oceans, earth and basins. In: NASA/RSA Science and Technical Advisory Council research.

Grankov AG, Milshin AA, Petrenko BZ (1999) Natural microwave radiation as a characteristic of the ocean-atmosphere heat interaction on seasonal and synoptic time scales, Doklady Earth Sciences 367A:839–842.

Grankov AG, Milshin AA, Novichikhin EP (2000) Interconnection between the brightness temperature and the intensity of the thermal ocean-atmosphere interaction (Based on the data Atlantex-90 experiment). Earth Observations Remote Sensing 16:457–467.

Ferraro RR, Marks GF (1995) The development of the SSM/I rain rate retrieval algorithms using ground based radar measurements. J Atmos Oceanic Tech 12:755–770.

Handbook (1979) Averaged month, 10 and 5-day periods values of the air water and temperature, their difference and wind speed in selected regions of the North Atlantic (1953–1974 years). VNII GMI, Obninsk In Russian.

Kalnay E, Kanamitsu M, Kistler R et al. (1996) The NCEP/NCAR Reanalysis Project. Bull Amer Meteorol Soc 77:437–471.

Lappo SS, Gulev SK, Rozhdestvenskii AE (1990) Large-scale heat interaction in the ocean–atmosphere system and energy-active zones in the world ocean. Gidrometeoizdat, Leningrad In Russian.

Liu WT (1988) Moisture and latent flux variabilities in the tropical Pacific derived from satellite data. J Geoph Res 93:6749–6760.

Matveev JuL, Soldatov SA (1982) Water content of the atmosphere. Trudy VNII GMI 94:36–42 In Russian.

Snopkov VG (1981) On seasonal variations of the water vapor content over the Atlantic. In: Atmosphere circulation and its interaction with the ocean in the tropical and subtropical latitudes of the Atlantic Nauka, Moscow In Russian.

Taylor PK (1984) The determination of surface fluxes of heat and water by satellite radiometry and in situ measurements. In: Gautier C and Fleux M (ed) Large-Scale Oceanographic Experiments and Satellites. Dordrecht, Reidel 223–246.

Wentz FJ (1991) User`s manual SSM/I antenna temperature tapes (Revision 1). RSS Technical Report, Santa Rose.

Chapter 8
Fluxes of Sensible Heat, Latent Heat, Impulse, and Atmospheric Water Vapor over the North Atlantic from the EOS Aqua AMSR-E Radiometer

8.1 Spatial and Seasonal Variability of Monthly Mean Heat, Moisture, Impulse Fluxes, and Atmospheric Water Vapor in the North Atlantic from the AMSR-E Radiometer

8.1.1 Satellite Archives

Multiyear measurements from the SSM/I, TMI, AMSR-E, and MTVZA-GY radiometers with daytime resolution are used to form global archives of the SOA's brightness temperatures in the millimeter and centimeter wavelength ranges, as well as the daily mean and monthly mean values of heat fluxes. Detailed information on frequency and polarization characteristics for the channels of these radiometers are presented in Grankov et al. (2012) and Barsukov et al. (2011).

Procedure for creating the brightness temperature files

When creating the brightness temperature files, the diurnal cycle is used for the information presentation. These files provide information on the global spatial distributions of the brightness temperature. Two files are formed every 24 h for ascending and descending orbits. The spatial area is the global rectangular grid with a 0.5 by 0.5° resolution that constitutes an array with 720 × 360 elements. The grid is centered relative to the equator and Greenwich meridian. Values of the brightness temperature for every cell of the grid are equal to values of the brightness temperature averaged within all pixels relating to this cell. The initial format of files is HDF, with HDF Explorer software used for their processing. The values of the brightness temperature in various satellite channels are converted from a binary format into a text format at the preliminary stage of processing.

Archives of brightness temperatures and heat fluxes

The following is a list of the main archives accumulated during 2008–2011 (more than 52,000 files, greater than 1000 Gb capacity):

- Archive of satellite SSM/I data (1996–1999)
- Archive of satellite TMI data (1997–1999)
- Archive of satellite AMSR-E data (2002–2008)
- Archive of averaged daily and monthly heat fluxes (1996–1999)

The following is a list of the main archives accumulated during 2012–2013 (more than 9000 files, greater than 200 Gb capacity):

- Archive of satellite SSM/I data (2009–2011)
- Archive of satellite TMI data (2009–2011)
- Archive of satellite AMSR-E data (2009–2010)
- Archive of averaged daily and monthly heat fluxes (2009–2010)
- Archive of satellite MTVZA data (November 2009–May 2010)

8.1.2 Technique for Determining the Monthly Mean Fluxes of Sensible Heat, Latent Heat, and Impulse Fluxes from AMSR-E Radiometric Data

The starting point for using satellite MCW radiometric methods for determining the main quantitative characteristics of the ocean–atmosphere heat interaction—vertical turbulent fluxes of sensible and latent heat at the SOA boundary—are widely used by oceanologists and meteorologists in bulk formulas, which characterize heat and moisture interchanges between the ocean surface and near-surface atmosphere for wide range of time scales (Lappo et al. 1990). The key parameters of these formulas are the ocean surface temperature (t_a) and the near-surface wind speed (V) (see relationships (1.1) and (1.2) in Chap. 1, as well as the materials of the Grankov and Milshin 2010). The near-surface wind speed is also a quantitative characteristic of the mechanical energy interchanges in the ocean-atmosphere interface (Lappo et al. 1990).

Parameters t_a and V can be determined using regression algorithms based on the results of comparative analysis of the data from mass satellite MCW radiometric and simultaneous buoy measurements in different physical and geographical zones of the World ocean in various seasons. For example, the algorithm by Kubota and Hihara (2008) uses linear regression relationships between the temperature and specific humidity of near-surface air and brightness temperatures measured by various spectral and polarization channels of the EOS Aqua radiometer AMSR-E.

More detailed information about the methods for calculating the monthly mean values of sensible, latent heat, and impulse fluxes from the data of radiometer AMSR-E is presented in the Appendix, including calculations of the monthly mean

fluxes of heat and impulse. These have been generalized with the data of Lappo et al. (1990), Andersson et al. (2010), Repina (2007), and Panin (1987), Panin and Krivitskii (1992) on the drag coefficient C_v for calm weather, where the largest scatter of estimates of this coefficient is observed.

8.1.3   Variability of Fields of Monthly Mean Sensible Heat, Latent Heat, and Impulse Fluxes

We processed AMSR-E brightness temperatures for the ascending and descending orbits of the EOS Aqua satellite in the period of November 2009–December 2010 in areas of the North Atlantic with coordinates 67°N, 95°E–0°N, 0°E. Based on these data, estimates of the *daily* fluxes of sensible heat, latent heat, and impulse were obtained; then, the *monthly* mean fluxes were computed.

Graphically, the results are presented in Fig. 8.1 for the seasons typical for climatic atlas (February, May, August, and November periods). Spatial resolution of the data is 0.25 × 0.25°. One can see a high spatial variability of monthly mean fluxes of all types in the North Atlantic. It is typical for the fluxes of latent heat to change by more than tenfold from minimum to maximum values; the maximum values of this parameter are observed in the summer period.

A high level of latent heat flux was observed in the tropical zone near Cuba in the spring and summer seasons as well as in September–October. This zone is a usual area of tropical cyclone formation. Differences in the behavior of latent heat fluxes are minimal in the summer season; in the autumn and winter seasons, its contrasts increase. In sensible heat fluxes, one can observe a clear latitude dependence: they are most intense in the north Atlantic, with their values diminishing as they approach the equatorial latitudes.

Figure 8.1 demonstrates an important result—the observation of the Gulf Stream from space in the field of the latent heat fluxes with spatial resolution 0.25 × 0.25°, as provided by modern satellite MCW radiometric means. We marked the effect of corrections of the monthly mean impulse fluxes due to the dependence of the coefficient C_v from the wind speed in Fig. 8.2.

Figure 8.2 shows that the spatial pictures are similar in both cases; however, an essential shift in the scale of the q_v parameter can be observed. Much details are provided in Appendix 2. Figure 8.3 defines these data more exactly for their initial distinctions.

Suitable corrections have been produced for the coefficients of heat and moisture exchanges in the SOA interface, adapting these processes to satellite-derived brightness temperatures at the millimeter and centimeter wavelengths (see also Appendix 2). It follows from the results presented that satellite scanning radiometers, such as the AMSR-E device, can be used as effective tools for studying the seasonal dynamics of vertical turbulent fluxes of heat, moisture, and impulse at the boundary of the ocean and atmosphere.

(a)   **(b)**   **(c)**

Latent heat flux
Feb 2010, 0–300 W m^{-2}

Sensible heat flux
Feb 2010, 0–20 W m^{-2}

Impulse flux
Feb 2010, 0–0.4 N m^{-2}

May 2010, 0–150 W m^{-2}

May 2010, 0–15 W m^{-2}

May 2010, 0–0.25 N m^{-2}

Aug 2010, -15–115 W m^{-2}

Aug 2010, 0–5 W m^{-2}

Aug 2010, 0–0.2 N m^{-2}

Nov 2010, 0–120 W m^{-2}

Nov 2010, 0–5 W m^{-2}

Nov 2010, 0–0.3 N m^{-2}
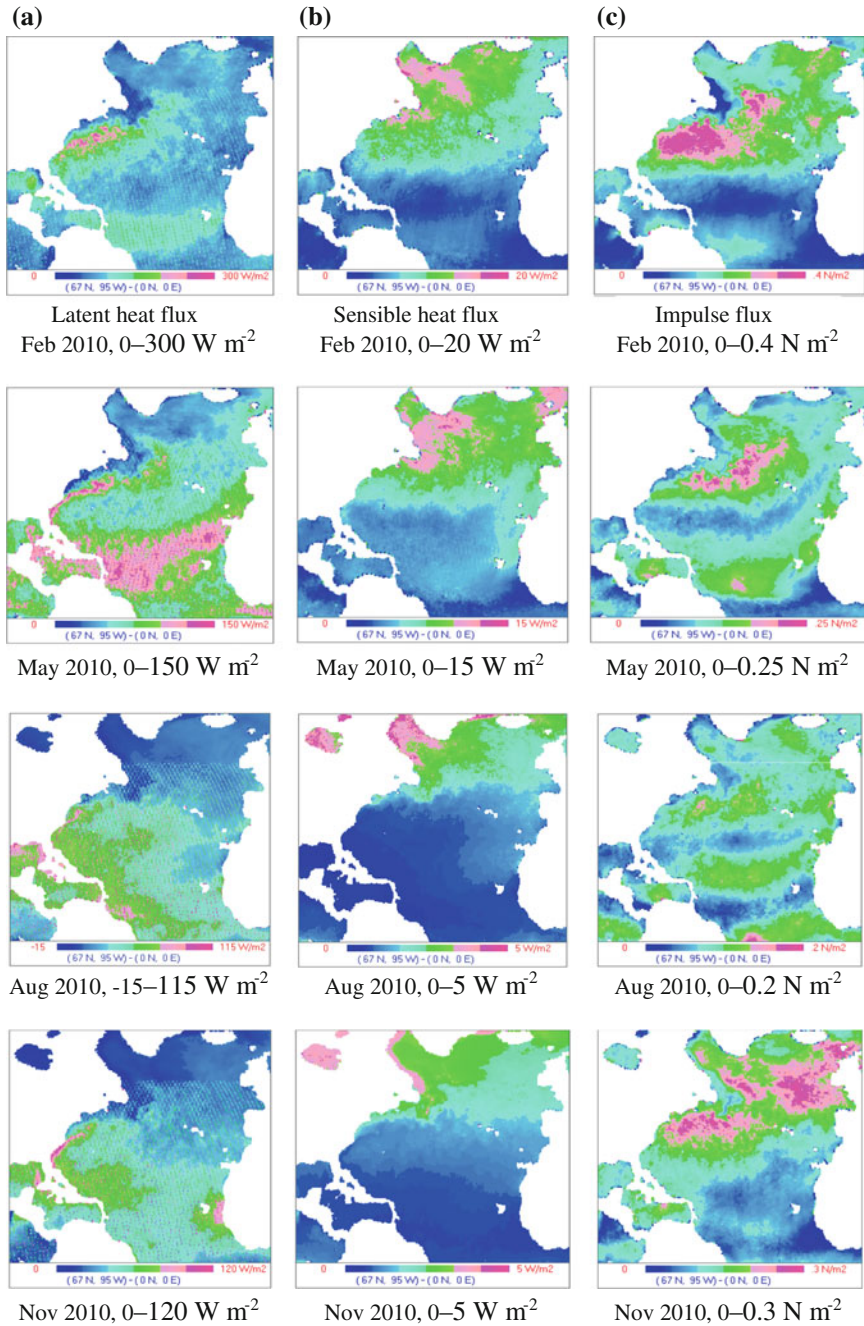
Fig. 8.1 Monthly mean fluxes in the North Atlantic in 2010: **a** latent heat, **b** sensible heat, **c** impulse
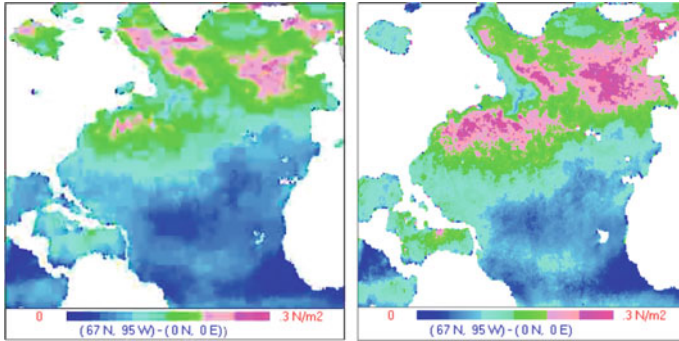
Fig. 8.2 Spatial picture of impulse fluxes: *left*—without accounting for the dependence of the coefficient C_V from the wind speed; *right*—the alternative version
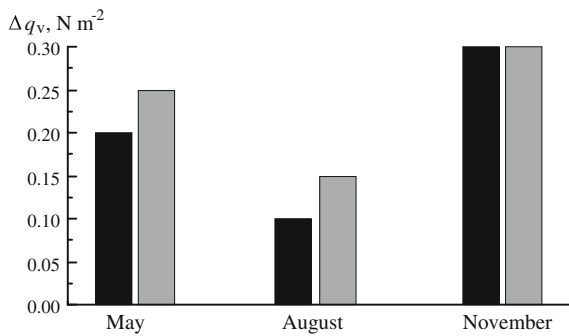
Fig. 8.3 Variations of the monthly mean impulse fluxes in the North Atlantic in 2010: *1*—without accounting for the wind factor correction; *2*—taking account of this

8.1.4 Field Variability of the Atmospheric Monthly Mean Water Vapor Content in the North Atlantic

At the Remote Sensing Systems website (http://www.ssmi.com), one can select some results for data processing of measurements from the EOS Aqua radiometer AMSR-E using the algorithms described in Wentz and Meissner (2000), including the ocean surface temperature, near-surface wind speed, and total content of the atmospheric water vapor. Figure 8.4 shows MCW radiometric estimates taken from this website after our processing for reduction of the monthly mean total content of the atmospheric water vapor in the North Atlantic in 2010. This year is notable due to a large oil spill in Gulf of Mexico and anomalously hot summer in the European part of the Russia. We transformed the website data into the *daily* data, then into the *monthly* mean heat and impulse fluxes.

Figure 8.4 demonstrates the specific striation effect for the picture of spatial distribution of the atmospheric water vapor; that is, its zonal regularity is expressed.
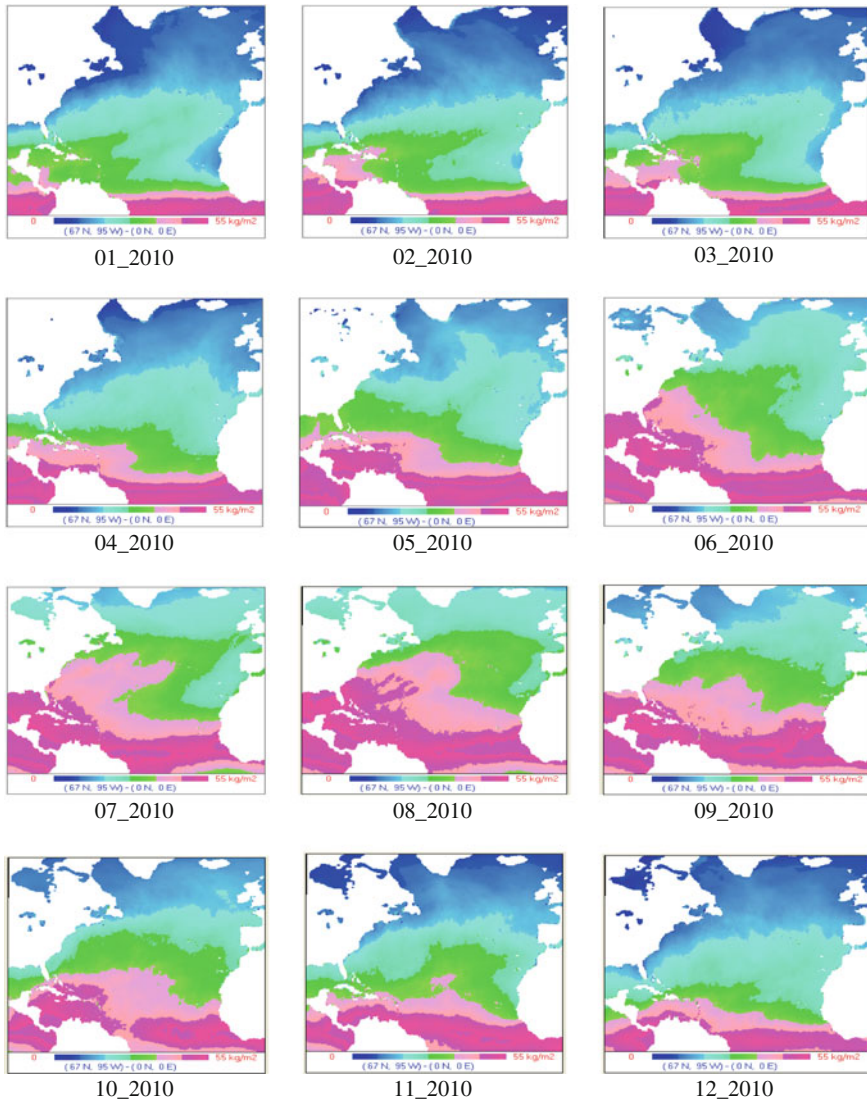
Fig. 8.4 Spatial distribution of the total content of atmospheric water vapor (monthly mean values) in the North Atlantic in 2010 from the data of EOS Aqua radiometer AMSR-E

High changeability of this parameter was noted, varying from 1.5 to 5.5 g cm^{-2} depending on the geographical latitude of the ocean and season. A similar effect was observed for fluxes of sensible and latent heat and, to a lesser extent, impulse.

Figure 8.5 illustrates the seasonal variability of monthly mean values of the atmospheric total water vapor content over local areas (squares $0.5 \times 0.5°$) centered relative to the following points: M (MIKE), D (DELTA), and H (HOTEL), which lie in the waters of Norwegian, Newfoundland, and Gulf Stream EAZOs,

Fig. 8.5 Seasonal variabilitySeasonal of atmospheric water vapor content at points H, D, and M in 2010, derived from the AMSR-E data
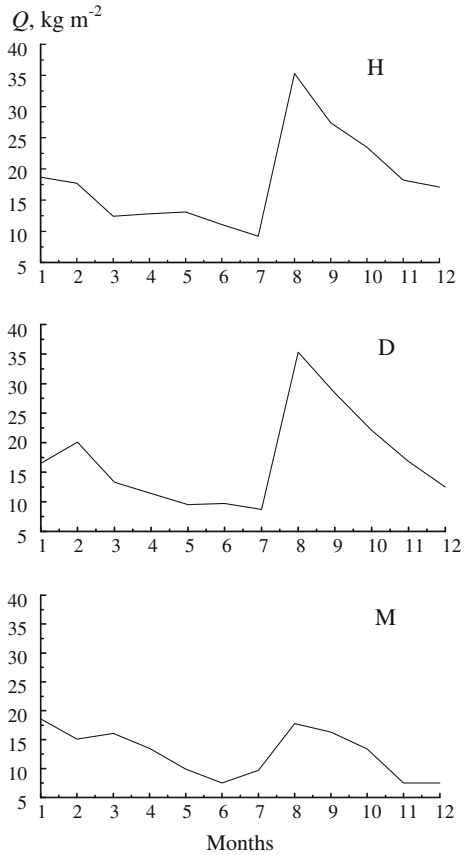
respectively. Figure 8.5 reflects the typical changes in the SOA parameters obtained with the SSM/I brightness temperature variations, measured at the wavelengths 1.35 cm and 5.9 mm.

8.2 Brightness Temperature as a Characteristic of Ocean-Atmosphere Heat Interaction in Areas of the Gulf Stream and North Atlantic Current

8.2.1 Analysis of Seasonal Variability of the Brightness Temperature in Areas H and D of the Gulf Stream

An analysis was performed of the seasonal variability of monthly mean brightness temperature measured by the AMSR-E channels in various areas of the North Atlantic located along the Gulf Stream and North Atlantic current watercourses.
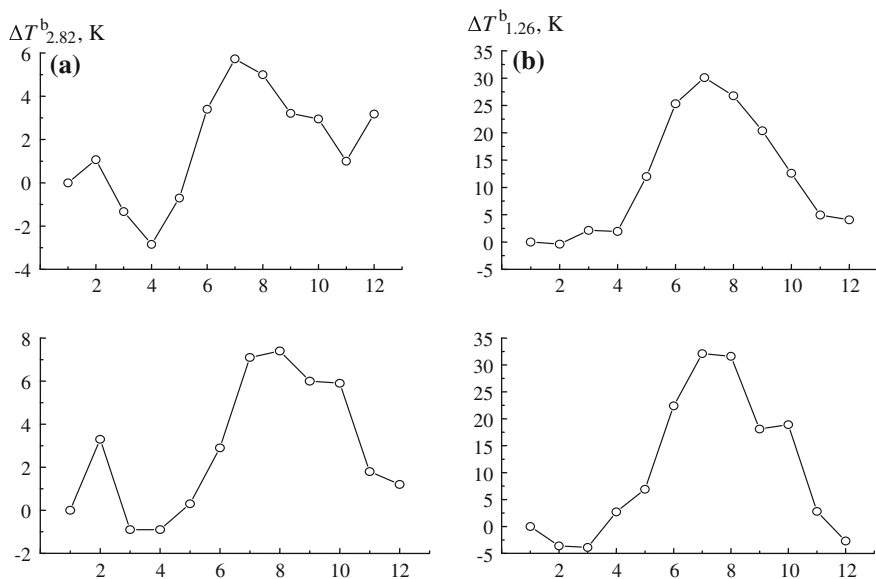
Fig. 8.6 Variations of monthly mean values of the brightness temperature at the wavelengths 2.82 and 1.26 cm in area **H** for **a** 2010 and **b** 2005. The numbers along the horizontal axes are months of the year

Figures 8.6 and 8.7 show the results of the analysis for the AMSR-E radiometer channels 10 V (the wavelength 2.82 cm, vertical polarization) and 23 V (the wavelength 1.26 cm, vertical polarization) over the Gulf Stream (H) and Newfoundland (D) EAZOs for 2010 (a) and ordinary conditions in 2005 (b), tending to climatic norms.

It follows from Figs. 8.6. and 8.7 that maximal changes of seasonal variations at the wavelength 2.82 cm vary from 7 K (in area **D**) to 9 K (in area **H**) and from 20–30 K to 30–35 K at wavelength 1.26 cm, respectively. This result is in agreement with the fact that heat and moisture exchange between the ocean and atmosphere is more intense in tropical latitudes in comparison with middle latitudes.

An analysis of the seasonal variability of the monthly mean brightness temperature measured by the AMSR-E channel 6.9 V (wavelength 4.35 cm, vertical polarization) in areas H and D in 2010 was made. In April of this year, a large oil spill occurred in the Gulf of Mexico; this event became the cause of a partial blockade of heat transport by the Gulf Stream to European shores. The brightness temperature at wavelength 4.35 cm more strictly reacts to OST variations than at a wavelength of 2.82 cm (Shutko 1986).

Figure 8.8 compares variations of monthly mean values of the brightness temperature $\Delta T^{b}_{3.45}$ and OST Δt_{s} in North Atlantic areas **H** and **D** in 2010 year. The minimal values of the parameters $T^{b}_{3.45}$ and t_{s} in area **D** (in August 2010) were taken as the reference points here. Proximate estimates of the OST were derived from the
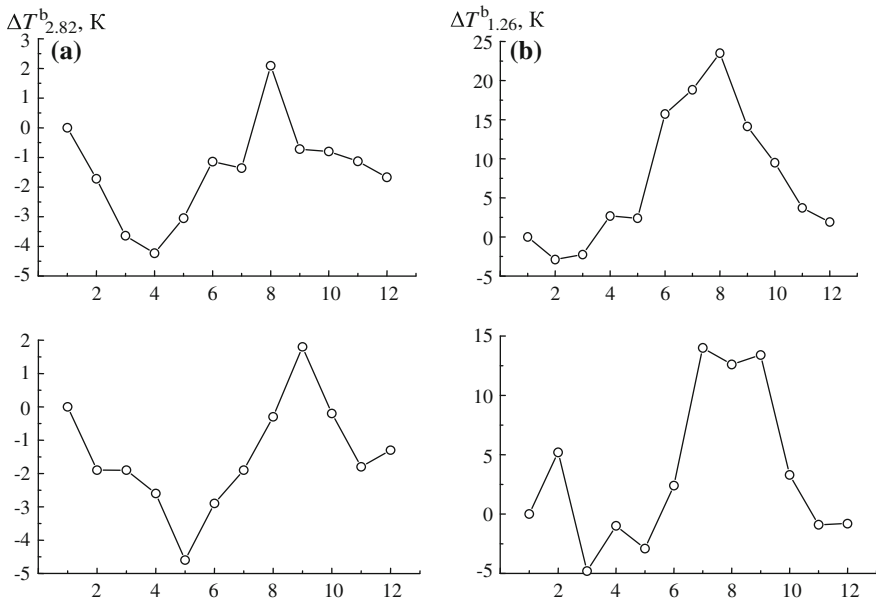
Fig. 8.7 Variations of monthly mean values of the brightness temperature at the wavelengths 2.82 and 1.26 cm in area **D** for **a** 2010 and **b** 2005. The numbers along the horizontal axes are months of the year

Fig. 8.8 Seasonal variations of monthly mean values of the brightness temperature at the wavelength 3.45 cm $T_{3.45}^b$ and OST t_s in areas **H** (*1*) and **D** (*2*) in 2010
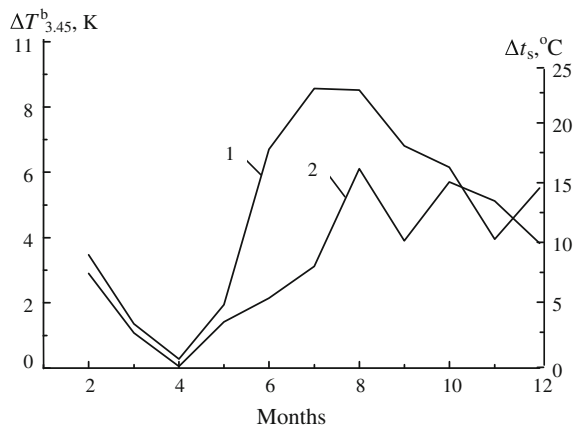
known regression relationships between parameters $T_{3.45}^b$ and t_s in the range of variations proper to the **H** and **D** areas. It follows from Fig. 8.8 that the changes of the parameters $T_{3.45}^b$ and t_s in areas **H** and **D** were similar until April–May. Later, their behavior strongly differed; a possible reason could be the oil spill in the Gulf of Mexico.
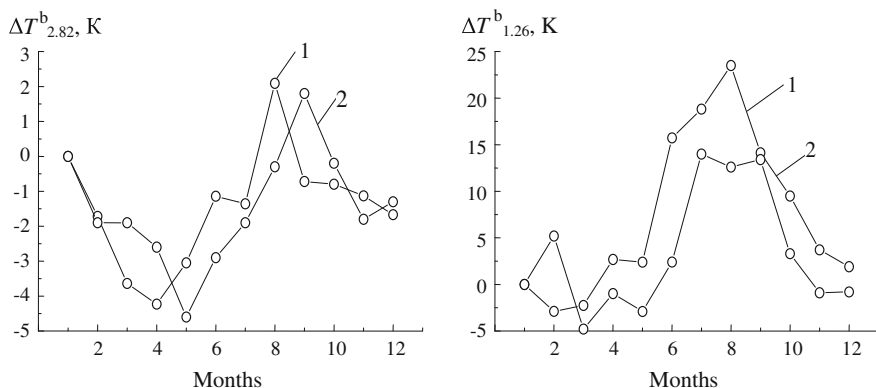
Fig. 8.9 Variations of monthly mean values of the brightness temperature at wavelength 2.82 and 1.26 cm in area **D** for 2010 (*left*) and 2005 (*right*)

Figure 8.9 shows combined in the united scale variations of the SOA monthly mean brightness temperatures in area **D**. One can clearly see the time lag (~ 1 month) of the brightness temperature response at the wavelength 2.82 cm to the OST variations in comparison with those at the wavelength 1.26 cm to variations of the atmospheric total water vapor content. This peculiarity determines the possibility of constructing MCW radiation images of the annual dynamics of heat and moisture exchange between the ocean and atmosphere in various EAZOs of the North Atlantic in the form of phase trajectories (loops) of the SOA brightness temperature.

8.2.2 Annual Brightness Temperature Cycles (Loops) in Areas H and D of the Gulf Stream

Lappo et al. (1990) developed a method of estimating the widely used integral (averaged per year) heat fluxes at the ocean–atmosphere boundary (see Chap. 2). The method is based on an important observation that the integral (annual) heat flux depends not only on values of the amplitudes of monthly mean ocean surface temperature (t_s) and near-surface atmosphere temperature (t_a) variations but also on the time shift between their intraannual (seasonal) evolutions. It is important to account for the time match (mismatch) between evolutions of the parameters t_s and t_a, when analyzing the intensity of the ocean–atmosphere heat interaction at the seasonal scale and its characteristics (either heat influx from the ocean to atmosphere or vice versa).

Due to the sensitivity of the SOA's natural MCW radiation to the ocean surface temperature and atmospheric near-surface temperature, we can construct some radiation images of the annual t_s, t_a cycles using as initial data, for example, the
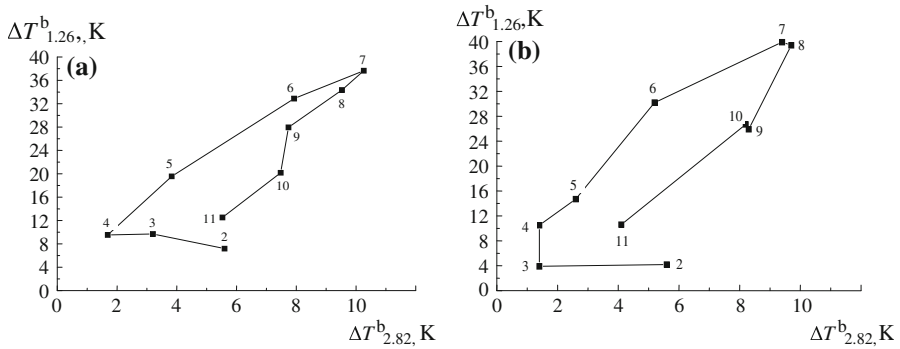
Fig. 8.10 Annual trajectories of the SOA brightness temperatures coupled at the wavelengths 1.26 and 2.8 cm in area H of the North Atlantic: 2010 (*left*) and 2005 (*right*)

brightness temperature in the spectral interval 3–8 cm, where the highest possible values of its sensitivity to variations of the parameter t_s are observed, and the brightness temperature at the wavelength 1.35 cm, which is closely connected with the atmospheric temperature and humidity characteristics. This approach was considered and stated in Grankov and Milshin (2004) monograph (see also Chap. 2), where estimates of the SOA brightness temperature were computed with archival oceanographic and meteorological parameters using known microwaves radiation models of the system. We may investigate these problems experimentally because the global archive of satellite MCW radiometric measurements accumulated during last 25 years is at our disposal.

Figure 8.10 compares this scheme of the trajectories of the AMSR-E brightness temperatures averaged monthly in 2010 and 2005 over the Gulf Stream EAZO of the North Atlantic. One can see real distinctions of the MCW radiometric characteristics expressed by their geometrical figures in these years.

Some distinctions in the form of the annual brightness temperature loops and their squares can be observed, which define the changes in intensity of the ocean-atmosphere heat and dynamic interaction in these years. Also, the peculiarities of the annual brightness temperature cycle of the Gulf Stream in area **D** with regard to its heat transport are shown (see Fig. 8.11).

The square of the brightness temperature loops in this zone of the North Atlantic (which is equivalent to the annual heat flux in the SOA in our minds) decreased in 2010 by 1.7 in comparison with those in 2005. A possible explanation for such a contrast of heat and MCW radiation characteristics is the oil spill in the Gulf of Mexico in April 2010. This year differed from the ordinary year of 2005 with higher values for these contrasts.
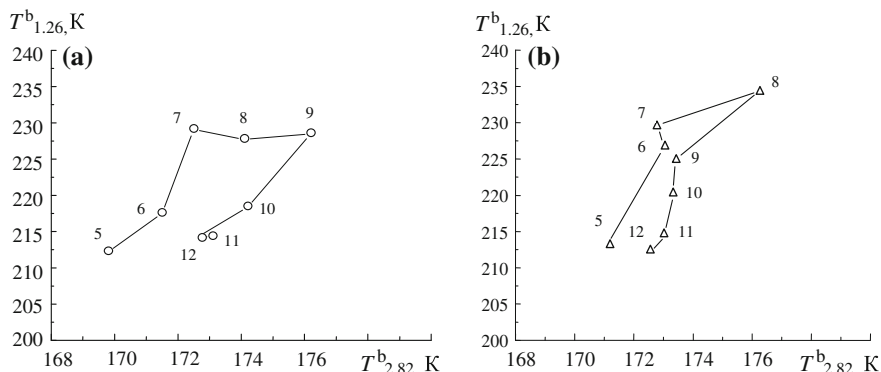
Fig. 8.11 Annual trajectories of the SOA brightness temperatures coupled at the wavelengths 1.26 and 2.8 cm in area **D** of the North Atlantic: 2010 (*left*) and 2005 (*right*)

8.3 Conclusion

The global estimates of seasonal dynamics of the monthly mean vertical turbulent fluxes of sensible and latent heat and impulse over the North Atlantic in the period from November 2009 to December 2010 were derived using the data of measurements from the EOS Aqua scanning radiometer AMSR-E. The Gulf Stream and its annual changeability were observed from space in the field of the latent heat fluxes with spatial resolution $0.25 \times 0.25°$, which was provided by modern satellite MCW radiometers.

The capability of the radiometer AMSR-E to estimate the integral (annual) heat fluxes at various energy active zones of Gulf Stream and to carry out a comparative analysis of the seasonal and spatial variability of these characteristics were shown. These are important when studying climatic trends in the North Atlantic and their influence on weather conditions in Europe and the European territory of Russia.

It seems realistic to use the data of long-term MCW radiometric measurements from the AMSR-E radiometer to study the influence of the oil spill in the Gulf of Mexico on the heat regime of Gulf Stream and its components, such as the surface fluxes of sensible and latent heat, total water vapor content in the atmosphere, etc.

Method for Computing the Monthly Mean Fluxes of Heat, Moisture, and Impulse from the Radiometer AMSR-E

Initial relationships and approximations. At present, a more realistic scenario for estimating the surface fluxes of sensible heat, latent heat, and impulse at the ocean–atmosphere boundary are the bulk formulas cited in Chap. 1. The important points in this analysis of ocean surface temperature (OST), near-surface air temperature,

humidity, and wind speed can be determined from the EOS Aqua AMSR-E radiometer.

To estimate the relative near-surface air humidity q_a, we used the following relationships, where the data of measurements of the SOA brightness temperature in all twelve AMSR-E radiometric channels were used:

$$
\begin{aligned}
q_a = a_0 &+ a_1 T_{6V} + a_2 T_{6H} + a_3 T_{10V} + a_4 T_{10H} + a_5 T_{18V} + a_6 T_{18H} \\
&+ a_7 T_{22V} + a_8 T_{22H} + a_9 T_{36V} + a_{10} T_{36H} + a_{11} T_{89V} + a_{12} T_{89H}
\end{aligned}
\tag{8.1}
$$

Here, the digital indexes of T denote the frequency of the radiometric channel (in GHz); the symbols V and H indicate vertical and horizontal polarization, respectively.

To estimate the near-surface air temperature, the parameterization is used (Algorithm, HOAPS 2011; Andersson et al. 2010):

$$
T_a = 1.03 T_S - 1.32
\tag{8.2}
$$

Computation of the saturated relative humidity e_0 was performed using Magnus' formula:

$$
e_0 = 6.1078 \cdot \exp\left[\frac{17.2693882 \cdot (T_S - 273.16)}{T_S - 35.86}\right]
\tag{8.3}
$$

The following relationships were used to determine the saturated near-surface air humidity over a salty water surface proper for the ocean (q_s), proper for the ocean surface:

$$
e_{0S} = 0.98 e_0
\tag{8.4}
$$

$q_S = 0.622 \dfrac{e_{S0}}{p - 0.378 e_{S0}}$, at the standard near-surface atmospheric pressure.

The main problem of the Global Aerodynamic Method is the alternatives for determining the coefficients in these formulas. As a rule, the values of the heat and moisture exchange in the SOA interface vary essentially from $C_H = (1-2) \times 10^{-3}$, $C_E = (1.0-1.7) \times 10^{-3}$ (Lappo et al. 1990).

Figure 8.12 illustrates the dependence of the number of Schmidt (C_T) from the near-surface wind speed on the coefficient C_H for the two parameterizations, which denote go-no-go scattering of this parameter in many other known variants (cited in Lappo et al. 1990, resting upon the works of Garrat 1977 and Kondo 1975).

Figure 8.12 shows that maximal distinctions between various parameterizations of heat and moisture exchanges in the SOA interface are apparent in a weak weather force under wind speed to 3 m s^{-1}. Panin (1987), Panin and Krivitskii (1992) provided useful relationships for sensible and latent fluxes in these conditions:
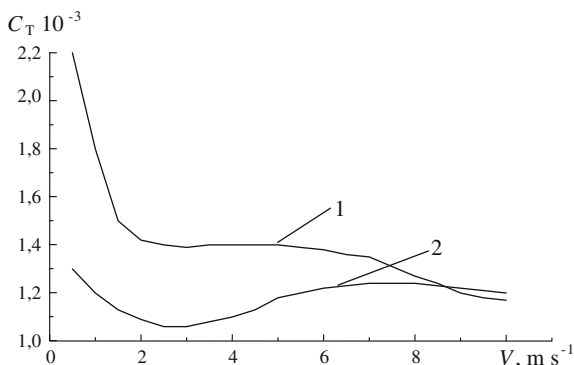
$$H = A\rho_a c_p (T_S - T_a)^{4/3} \left[\alpha g k_T^2 v^{-1} (1 + b/\mathrm{Bo})\right]^{1/3}; \qquad (8.5)$$

$$L_E = A\rho_a L_S (q_S - q_a)^{4/3} \left[\beta g k_q^2 v^{-1} (1 + \mathrm{Bo}/b)\right]^{1/3}. \qquad (8.6)$$

Here, $A = 0.15$, $\beta = 0.61$, $L_S = 25.04 \times 10^5$ J kg^{-1} is the specific evaporation heat, $g = 9.81$ m s^{-2}, α is the coefficient of the air heat expanding ($b \approx 0.073$), v is the air kinematic viscosity (thickness); $\mathrm{Bo} = \frac{H}{L_E}$ is the Bowen number; and k_T, k_q are the kinematical coefficients of the molecular diffusion of heat and water vapor exchanges.

For wind speed exceeding 3 m s^{-1}, the values of the heat exchange coefficients were taken as $C_H = 0.0012$ and $C_E = 0.0011$. For evaluation of the resistance coefficient, we summarized the data of Panin (1987), Panin and Krivitskii (1992) and Repina (2007) in the form of piecewise linear dependence $C_D = a + b\,(V - c)$ in the following conditions:

> For $V < 3$ m^{-1}, $C_D = 0.001$ does not depend on V
>
> For $V = 3 - 12.5$ m s^{-1}, $a = 1$, $b = 0.0706$, and $c = 3$
>
> For $V > 12.5$ m s^{-1}, $a = 1.6$, $b = 0.02286$, and $c = 12.5$

References

Andersson A, Fennig K, Klepp C et al (2010) The Hamburg Ocean Atmosphere Parameters and Fluxes from Satellite Data – HOAPS-3. Earth Syst Sci Data 2: 215–234.

Barsukov ID, Nikitin OV, Streltsov AM et al (2011) Preprocessing the data of Meteor-M No. 1 MCW radiometer MTVZA GY. Modern problems of remote sensing the Earth from space: 257–263 In Russian.

Grankov AG, Milshin AA (2010) Microwave radiation of the ocean-atmosphere: Boundary heat and dynamic interaction. Springer Dordrecht Heidelberg London New Jork.

Grankov AG, Milshin AA, Soldatov VJu, Shelobanova NK (2012) Archives of microwave, oceanographic, and meteorological data in zones of appearance of the tropical hurricanes. Problemy Okruzhayushchei Sredy i Prirodnykh Resursov 12: 17–34 In Russian.

http://www.ssmi.com/.

Kubota M, Hihara T (2008) Retrieval of surface air specific humidity over the ocean using AMSR-E measurements. Sensors 8: 8016–8026.

Lappo SS, Gulev SK, Rozhdestvenskii AE (1990) Large-scale heat interaction in the ocean–atmosphere system and energy-active zones in the world ocean. Gidrometeoizdat, Leningrad In Russian.

Panin GN (1987) Evaporation and heat exchange in Caspian Sea. Nauka, Moscow In Russian.

Panin GN, Krivitskii SV (1992) Aerodynamic roughness of the water body. Nauka, Moscow In Russian.

Repina IA (2007) Methods of determination of the turbulent fluxes over sea surface. Institute of Space Researches RAS (Preprint), Moscow In Russian.

Shutko AM (1986) Microwave radiometry of water surface and soils. Nauka, Moscow In Russian.

Wentz FJ and Meissner T (2000) Algorithm Theoretical Basis Document (ATBD). Version 2. AMSR Ocean Algorithm // RSS Tech. Proposal 121599A-1. Remote Sensing Systems, Santa Rosa.

Appendix References

Algorithm Theoretical Basis Document HOAPS (2011) release 3.2 Ref Number: SAF/CM/DWD/ATBD/HOAPS. Issue/Revision Index: 1.1. 25.03.2011

Garrat JR (1977) Review of drag coefficients over oceans and continents. Monthly Weath Rev. 105:17–28

Kondo J (1975) Air-sea bulk transfer coefficient in diabatic conditions. Bound Layer Meteor 9:91–112

Chapter 9
Analysis of the Dynamics of SOA Parameters in Areas of Tropical Cyclone Activity

9.1 Dynamics of Parameters of the Ocean Surface and Near-Surface Atmosphere in the Gulf of Mexico During Tropical Cyclones Katrina and Humberto

9.1.1 Matter and Tasks of the Study

We analyzed the reaction of the ocean–atmosphere system when the powerful tropical hurricane (TC) Katrina passed through in the Florida Strait in area of the buoy station SMKF1 (Sombrero Key) in August 2005. We also examined the behavior of the system in the period of time preceding the formation, development, and extinction of TC Humberto in September 2007 in the Gulf of Mexico at the point of the buoy station 42019. (The code names and numbers of buoy stations are taken from the existing NOAA classification.)

An analysis of the synoptic variations of the following ocean and atmosphere characteristics in these time periods was conducted:

1. Temperature of the ocean surface, air temperature, humidity, pressure, and wind speed in the near-surface atmosphere layer (thickness: 10–20 m) at the stations SMKF1 and 42019
2. Vertical turbulent heat flux of the sensible and latent heat, as well as impulse at the ocean-atmosphere boundary, computed with measurement data from the stations SMKF1 and 42019
3. Total (integral) atmospheric water vapor content and enthalpy computed by integration of the air humidity and temperature within the height range 10–10,000 m

The source of information for the Earth-based data was the NOAA's National Data Buoy Center (NDBC). Measurements from the microwave radiometers SSM/I (Special Sensor Microwave/Imager) of the meteorological satellite F15 DMSP and AMSR-E (Advanced Microwave Scanning Radiometer) of the satellite EOS Aqua

were used as the source of satellite data. The technical characteristics of these radiometers are given in Hollinger et al. (1990) and Kawanishi et al. (2003), respectively.

9.1.2   Dynamics of Meteorological Parameters Measured from Stations SMKF1 and 42019

Station SMKF1 (TC Katrina)

The station SMKF1 from the NDBC data arsenal was used as the reference point in the Florida Strait (24.38°N, 81.07°W) when analyzing the influence of TC Katrina on atmospheric parameters. The nearest distance between the trajectory of TC Katrina and this station was ~ 120 km at noon of August 25, 2005; at this moment, the cyclone had passed about 800 km from the place of its formation near the Bahamas.

The NDBC data was analyzed in the area of the station SMKF1 between 21 and 31 August 2005. Significant contrasts of the near-surface air parameters appeared with respect to their undisturbed (background) values before the arrival of TC Katrina and after it moved away. Variations of the air temperature, humidity, and pressure were about −6 °C, −15 mb, and −13 mb, respectively.

Figure 9.1 illustrates the variations in the air temperature t_a and pressure P in the atmosphere's near-surface layer between 21st and 31st August 2005, as recorded by sensors of the SMKF1 station as well as computed values of the near-surface air humidity (water vapor pressure) e. These results were obtained using the data from previous studies for the relationship of parameter e with the difference of water and air temperatures in various zones of the World Ocean, as derived by Snopkov (1977); the NOAA buoy stations do not include direct measurements of the air humidity.

Figure 9.1 presents the smoothed results of station measurements for the parameters t_a, P, and calculated estimates of the parameter e. The smoothing was compiled with the standard means of the ORIGIN Adjacent Averaging program using a 3-h interval for averaging the hourly samples. The initial data from the SMKF1 sensors included 240 hourly samples for each of the parameters t_a, e, and P, characterizing the time points preceding the appearance of TC Katrina in the area of the SMKF1 station (21–24 August), passing through this area (25–29 August), and SOA relaxation (30–31 August). These results suggest the need to consider the explosive effects in the atmosphere during TC activity.

Results of the linear regression analysis show close interrelations between variations of the near-surface air temperature and humidity, with the coefficient of correlation of the parameters t_a and e being 0.94. Based on buoy meteorological measurements and using the technique cited in Xrgian (1978), we computed the values of internal energy (enthalpy) of the near-surface atmosphere in the period from 21 to 31 August 2005. When passing the point SMKF1, TC Katrina collected

Fig. 9.1 Variations of the near-surface air temperature t_a, humidity e, and pressure P in the area of location of the station SMKF1 in the Florida Strait during the passage of TC Katrina in August 2005
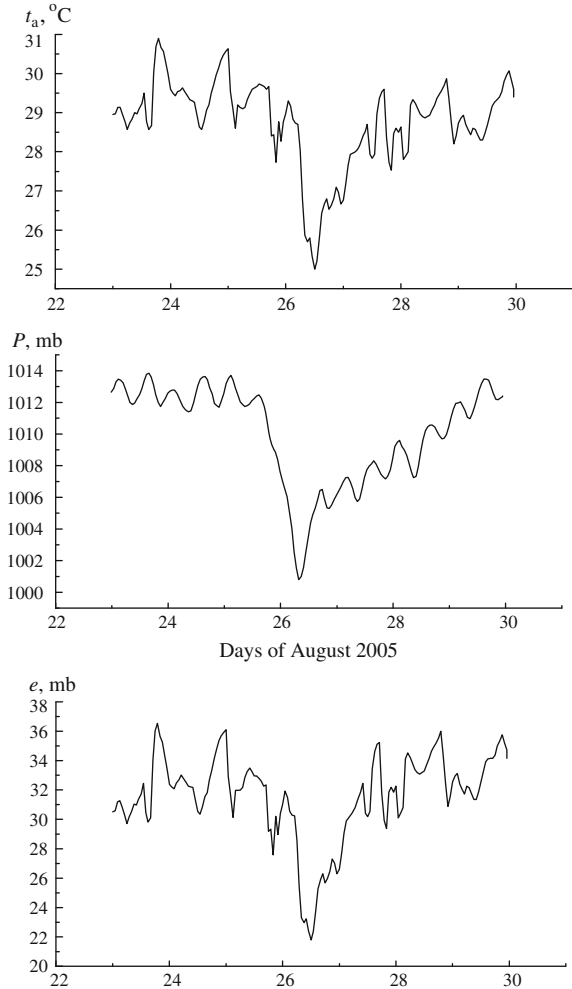
heat energy from the atmosphere's near-surface layer; according to our estimates, it reduced to approximately 32,500 J m^{-2} in this period.

Station 42019 (TC Humberto)

TC Humberto formed in mid-September 2007 in the Gulf of Mexico. It was not as intense as TC Katrina, but it is important in these studies because its source area coincided with the location of buoy station 42019 (situated at coordinates 27.91°N, 95.35°W). This location allowed the monitoring of atmospheric near-surface layer parameters (as well as parameters of overlying layers when using data from simultaneous MCW radiometric measurements) over various stages of this cyclone's formation. According to data measurements from station 42019, this
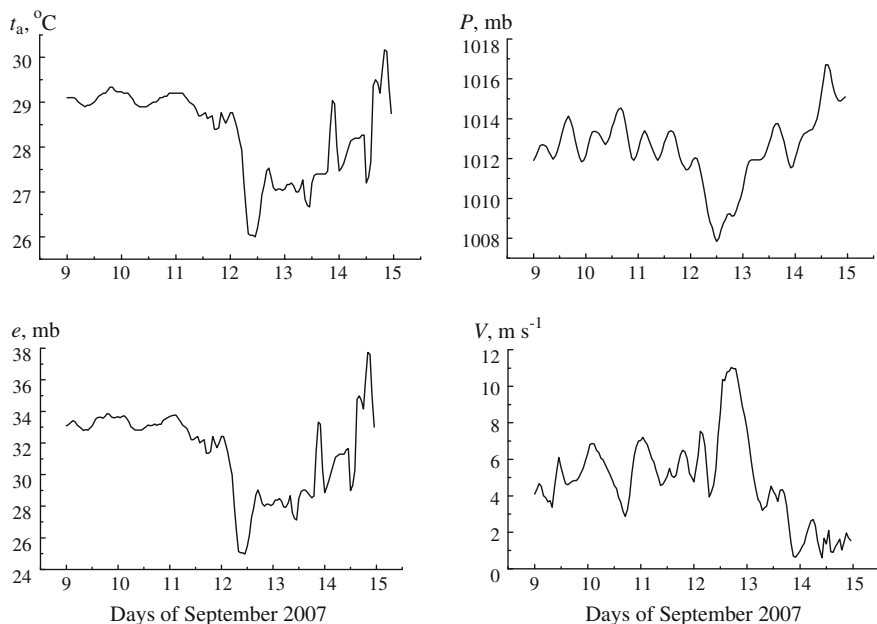
Fig. 9.2 Variations of the near-surface temperature t_a, humidity e, pressure P, and wind speed V from the measurement data of the station 42019 in the Gulf of Mexico during TC Humberto's formation in September 2007

point was characterized by a strong changeability of parameters of the atmospheric near-surface layer in the period TC Humberto's formation. Variations in the air temperature, humidity, pressure, and wind speed amounted to 3 °C, 8 mb, 5 mb, and 8 m s^{-1}, respectively (see Fig. 9.2).

Variations of the near-surface air humidity in the period September 9–14 are practically identical to the variations of the near-surface air temperature: the coefficient of their correlation was 0.97. The near-surface air pressure sharply declined at the stage of this cyclone's development (12 September). The enthalpy of the atmospheric near-surface layer was computed between 9th and 14th September 2007 in the location of station 42019. It follows from the results of computation that the enthalpy reduced by 12,500 J m^{-2} during the development of TC Humberto.

9.1.3 Dynamics of the Ocean Surface Temperature, Heat, Moisture, and Impulse Fluxes in Areas of Activity of TCs Katrina and Humberto

An analysis of ocean surface temperature variations during TC Katrina's passage through station SMKF1 (August 22–31, 2005) and during the period of formation
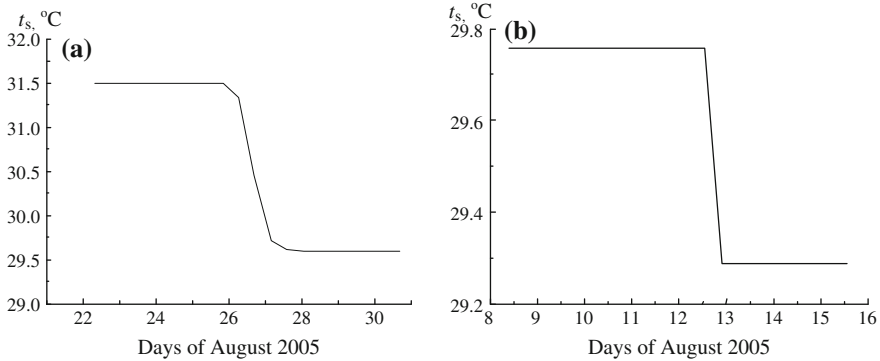
Fig. 9.3 Characteristics of changes in the ocean surface temperature t_s: **a** an area of station SMKF1 during the passage of TC Katrina; **b** an area of station 42019 during the formation of TC Humberto

and development of TC Humberto (September 8–16, 2007) was conducted, with the results shown in Fig. 9.3. To demonstrate the behavioral characteristics of the ocean surface temperature, buoy measurements were approximated with standard means using the computer technique ORIGIN (the sigmoidal function), which produced the stick-slip motion of original dependencies. Figure 9.3 shows that a "jump" in the ocean surface temperature values in area of station SMKF1 caused by the passage of TC Katrina is a few times when compared with the values observed during the formation of TC Humberto.

Based on buoy measurements of the ocean surface temperature, the near-surface air humidity estimates, and wind speed, we computed the values of sensible q_h and latent q_e heat at the ocean–atmosphere boundary using the well-known dynamic meteorology formulas of the global aerodynamic method (so-called bulk formulas) were justified in Lappo et al. (1990; see Chap. 1). In the following sections, some results from the calculation of heat fluxes with reference to stations SMKF1 and 42019 based on buoy measurements in these areas of the Gulf of Mexico are presented.

Station SMKF1 (TC Katrina)

Figure 9.4 shows some results from the calculation of heat fluxes (with 3-h averaging). One can observe the influence of TC Katrina's passage through the station SMKF1, which is seen in the appreciable reduction of heat fluxes—about 20 W m^{-2} (from 30 to 10 W m^{-2}) for the fluxes of sensible heat and about 150 W m^{-2} (from 350 to 200 W m^{-2}) for the fluxes of latent heat. This result demonstrates the effect of smoothing the heat contrasts between the ocean surface and near-surface atmosphere due to the effects of the cyclone's passage.

The moment that the cyclone passed over the SMKF1 station (noon on 26 August) was accompanied by a positive increase in the parameters q_h and q_e, which amount to 80 and 500 W m^{-2}, respectively.
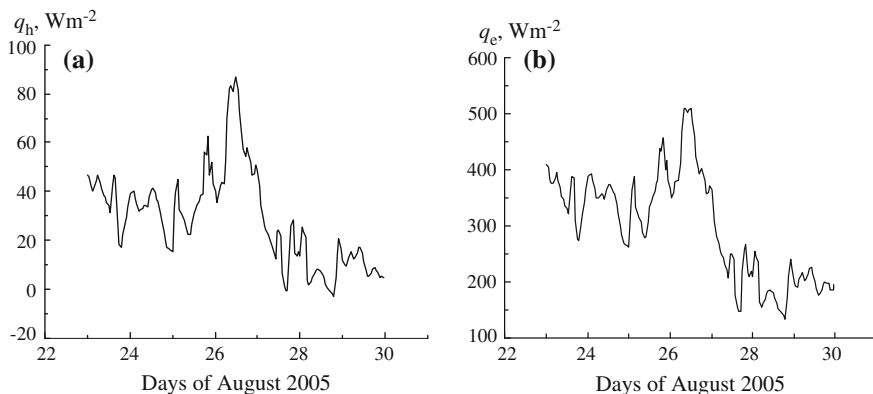
Fig. 9.4 Variations of **a** sensible and **b** latent heat fluxes at the ocean surface in the area of SMKF1 station during the passage of TC Katrina in August 2005

Station 42019 (TC Humberto)

Figure 9.5 shows the results of calculating the fluxes of sensible and latent heat, as well as impulse (with the 3-h smoothing). One can observe a sharp maximum peak of the values q_h and q_e simultaneously, which occurred at noon on September 12, 2007; this coincides with the data for ground observations of TC Humberto's development.

The average values of heat and moisture fluxes at the stage preceding TC Humberto's appearance (9–12 September) were 5 W m^{-2}, 150 W m^{-2}, and 0.05 N m^{-2}, respectively. Their maximal values at the stage of its development at noon on 12 September reached 75 W m^{-2}, 530 W m^{-2}, and 0.2 N m^{-2}. Notably, the maximal value of the total (sensible + latent) heat fluxes in area of station 42019 ($\sim$600 W m^{-2}) is close to the estimate cited by Golitsyn for tropical latitudes (Golitsyn 2008). In addition, this value is comparable with the total heat flux values in the Newfoundland energy active zone of the North Atlantic, which is regularly subjected to the influence of powerful mid-latitude cyclones. In line with data from the NEWFOUEX-88 and ATLANTEX-90 experiments, they reached values of 800 W m^{-2} in March 1988 and April 1990 (Grankov and Milshin 2010).

Figure 9.6 demonstrates variations in heat and moisture fluxes in the period September 17–20 at the stage of relaxation of the SOA parameters in area of station 42019 after the development of TC Humberto and its departure from the area. It can be seen from the illustration that the average values of the parameters q_h and q_e are a few times under their limit values, as observed at noon on 12 September. One interesting situation occurred: the oscillatory characteristics of variations in heat and moisture fluxes in this time corresponded with an oscillation period close to 24 h—that is, to a *diurnal cycle*. In addition, the *sensible heat* fluxes alternated; that is, the

Fig. 9.5 Variations of sensible heat (**a**), latent heat (**b**), and impulse (**c**) fluxes at the ocean surface in the area of station 42019 at the formation of TC Humberto in September 2007
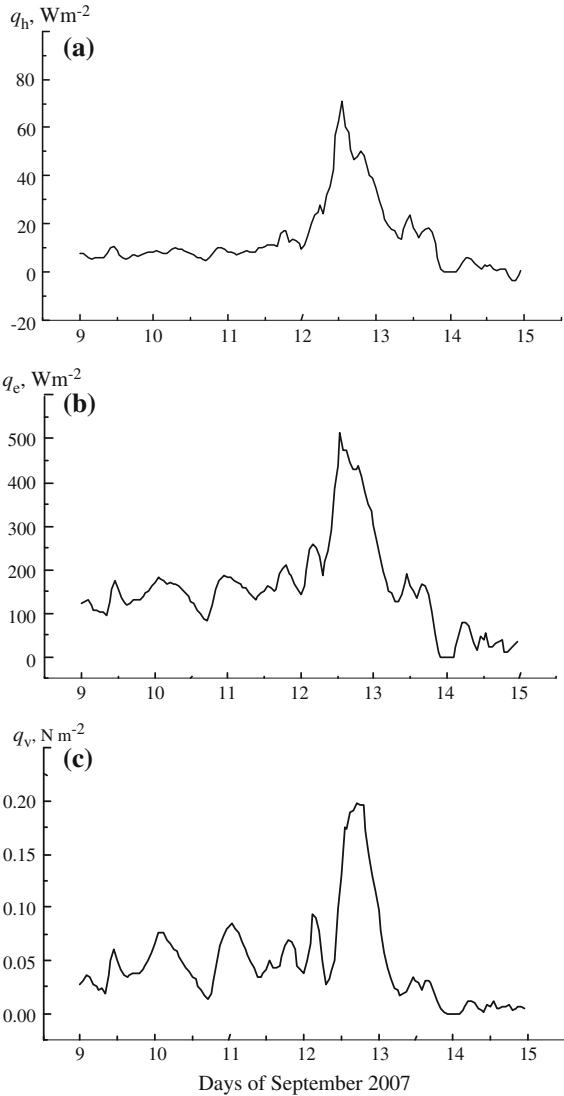
processes of heat transfer from the ocean surface to the atmosphere alternated with the processes of heat transfer from the atmosphere to the ocean surface. This phenomenon was not observed in the period of September 9–12, preceding the appearance of TC Humberto (see Fig. 9.2). This effect is similar to the excitation effect of oscillations in high-Q resonant systems, as in the ringing circuits in radioengineering described by Kharkevich (2007), for example.
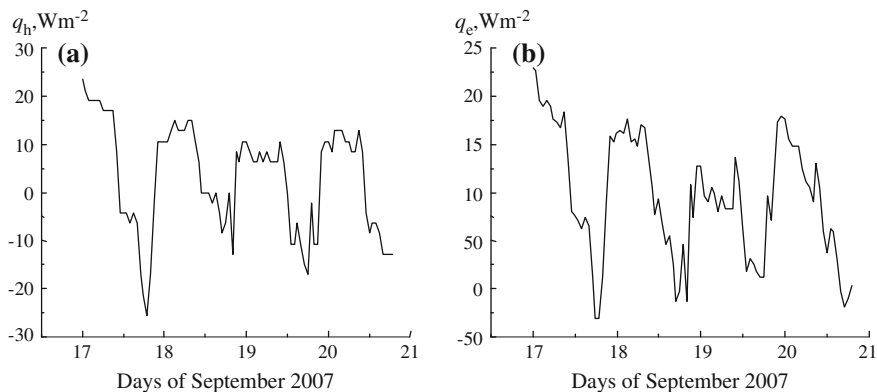
Fig. 9.6 Behavior of the sensible (**a**) and latent (**b**) heat fluxes at the ocean surface in area of the station 42019 after TC Humberto's appearance

9.1.4 Spatial and Temporal Dynamics of the SOA Brightness Temperature Along the Trajectory of TC Katrina

TC Katrina

We studied the temporal and spatial variability of the SOA brightness temperature in the Gulf of Mexico from the region of the TC Katrina's formation (the Bahamas) to the south shore of the United States (Louisiana state) for August 24–30, 2005. An analysis was performed of the temporal changeability of the brightness temperatures measured by the AMSR-E radiometer channels in the Gulf of Mexico along the trace of the EOS Aqua satellite at the range of the wavelengths (0.82–1.6 cm) at the horizontal and vertical polarizations in fixed points of the trace of the satellite movement during TC Katrina's activity.

Figure 9.7 shows results of measurements of the SOA brightness temperature at wavelength 1.26 cm at horizontal polarization in August 2005 for these points of TC Katrina's spreading. It follows from the illustration that appearance of TC Katrina in the Gulf of Mexico is accompanied by sharp peaks of the SOA brightness temperature at the wavelength 1.26 cm. The nature of this effect is explained by the resonant character of the radiowave attenuation in the water vapor of the atmosphere. In each case, a gradual increase (over the course of 5–6 days) of the SOA brightness temperature precedes the current peak of its values, which is explained by the accumulation of atmospheric water vapor before the cyclone's arrival. It was ascertained that water vapor content in the atmosphere increased from 40–45 to 55–60 kg m^{-2} in this period.

An analogical effect was observed during the NEWFOUEX-88 and ATLANTEX-90 experiments in the Newfoundland energy active zone of the North Atlantic, where a positive increase of this atmospheric parameter fixed from vessels

Fig. 9.7 Variations of the SOA brightness temperature at the wavelength measured by the AMSR-E radiometer for horizontal polarization at the various points for TC Katrina spreading from its source to the U.S. southern shore: **a** 26°N, 78°W; **b** 25°N, 83°W; **c** 27°N, 89°W
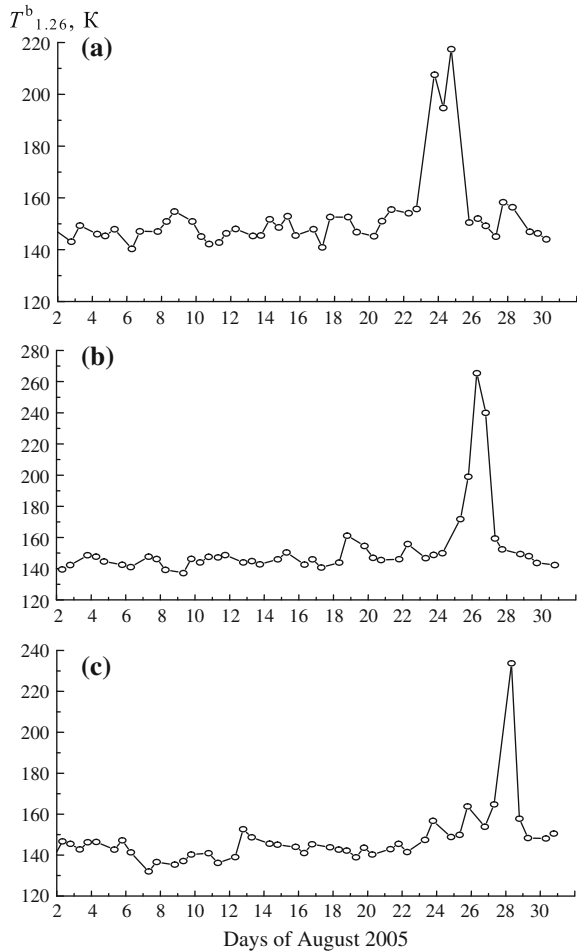
V. Bugaev and *Musson* before the powerful midlatitude North Atlantic cyclones were 10–15 kg m^{-2} (Grankov and Milshin 2010). This phenomenon may be useful for forecasting the rate and data of approaching tropical cyclones in selected oceanic area where their appearance is regular and quite expected.

TC Humberto

We analyzed the response of the SOA brightness temperature in the range 0.8–1.6 cm of resonant absorption of radiowaves in atmospheric water vapor, which was used by the EOS Aqua AMSR-E radiometer in the beginning of TC Umberto (12–13 September, 2007). By way of example, Fig. 9.8 shows the measurement data from the AMSR-E radiometer at the wavelength 1.26 cm (23.81 GHz). In the beginning of TC Umberto at station 42019, there was a strong decrease in the surface values of air temperature, humidity, and pressure (see Fig. 9.2). This caused

Fig. 9.8 The SOA brightness temperature T^b measured by AMSR-E radiometer at the wavelength 1.26 cm for the vertical (*1*) and horizontal (*2*) polarizations in the beginning TC Umberto

$T^b_{1.26}$, K

Days of September 2007
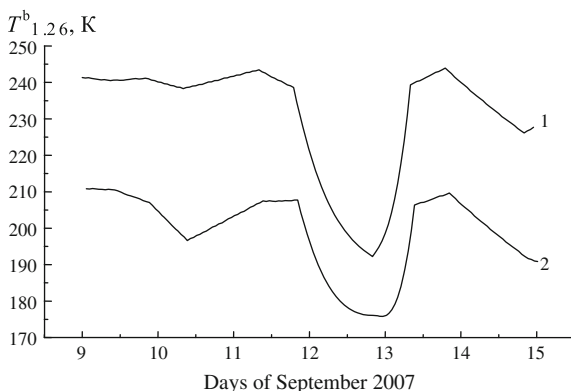
a significant decrease in the absorption of radiowaves in the atmosphere and a "gap" of the SOA brightness temperature in the millimeter and centimeter wavelength range, which is illustrated in Fig. 9.8. A negative jump of the MCW radiation temperature occurred on the ocean surface, which indicates the extraction of thermal energy into the atmosphere from the ocean surface.

9.2 Dynamics of the Atmospheric Meteorological Characteristics at the Beginning of Tropical Cyclones

9.2.1 Technique for Retrieval of the Atmospheric Temperature and Humidity from Satellites and Buoys

The large network of NOAA meteorological stations—particularly the stations situated in the Gulf of Mexico and the equatorial zone of the Pacific Ocean—provide measurements of the parameters of the ocean surface and near-surface atmosphere. Meteorological observations from these stations are not able to provide information on the vertical distribution of temperature and humidity in the atmosphere. This problem can be solved by using measurement data from the multi-channel MCW radiometer SSMIS (Special Sensor Microwave Imager/Sounder) from satellites DMSP F16 and F17 (Kunkee et al. 2006). In addition to this function, the device is able to determine the atmospheric temperature and humidity at various heights. However, periodic remote sensing of these atmospheric characteristics (once per day) is not enough for studying fast processes that have noticeably varying characteristics over several hours, such as tropical cyclone formation.

The method for combining the data from buoy measurements of the atmospheric near-surface layer and the ocean surface parameters with data obtained from satellite MCW measurements has been developed. This provides information on the

air temperature and humidity, not only in the near-surface atmosphere but also in overlying atmospheric layers. This technique allows the determination of values of the atmosphere temperature $t_a(h)$ and humidity $\rho(h)$ at its various horizons (by satellite MCW radiometric measurements) and hourly (by buoy meteorological measurements) (Grankov et al. 2012a, b).

The sought dependences $t_a(h)$ and $\rho(h)$ are found in the form of exponential functions $t_a(h) = t_a(0) \exp(-\kappa_t\ h)$; $\rho(h) = \rho(0) \exp(-\kappa_\rho\ h)$ providing a minimal root-mean-square error (discrepancy) between data measured by the MCW radiometers SSM/I and AMSR-E for SOA brightness temperatures and their simulated (model) estimates. With the dependences $t_a(h)$ and $\rho(h)$, the linear and integral absorption of radiowaves as well as the brightness temperatures of the SOA natural MCW radiation in various atmospheric layers for all satellite MCW radiometric channels are computed using the plane-layer model of natural MCW radiation of the system (Basharinov et al. 1974; Armand and Polyakov 2005); see also Chap. 2 of this book.

Because the radiometers SSM/I and AMSR-E are multichannel systems, their measurement data seems to be sufficient for determining the coefficients κ_t and κ_ρ required for retrieving the dependencies $t_a(h)$ and $\rho(h)$ over the ocean. The value of the discrepancy between simulated and measured estimates of the SOA brightness temperature is computed both with ascending and descending satellite orbits falling into cells $0.25° \times 0.25°$ centralized about the stations SMKF1 and 42019 for the following spectral and polarization channels of the radiometers SSM/I and AMSR-E: (a) 37 GHz (0.81 cm), 19 GHz (1.58 cm), vertical and horizontal polarizations; 22.235 GHz (1.35 cm), vertical polarization (radiometer SSM/I and b) 36.5 GHz (0.82 cm), 18.7 GHz (1.6 cm), 23.8 GHz (1.26 cm), vertical and horizontal polarization (radiometer AMSR-E).

This technique allows the computation of approximate values of the temperature and humidity of the atmosphere at various horizons for estimating its integral characteristics, such as the total water vapor content and enthalpy (heat content). It seems that mainly the atmosphere's integral characteristics will be informative in an analysis of the SOA dynamics in zones of activity of tropical cyclones, despite the fact that the real profiles of air temperature and humidity can be appreciably different from the exponential ones.

9.2.2   Some Results of Analysis of the Atmospheric Temperature and Humidity Dynamics at Various Horizons

We analyzed changes in the air temperature and humidity at various atmospheric horizons as a result of TC Katrina's impact in the period 21–31 August 2005. Figure 9.9 shows the height dependences of the air temperature and water vapor pressure at the point SMKF1 before TC Katrina's arrival (21 August) and after it
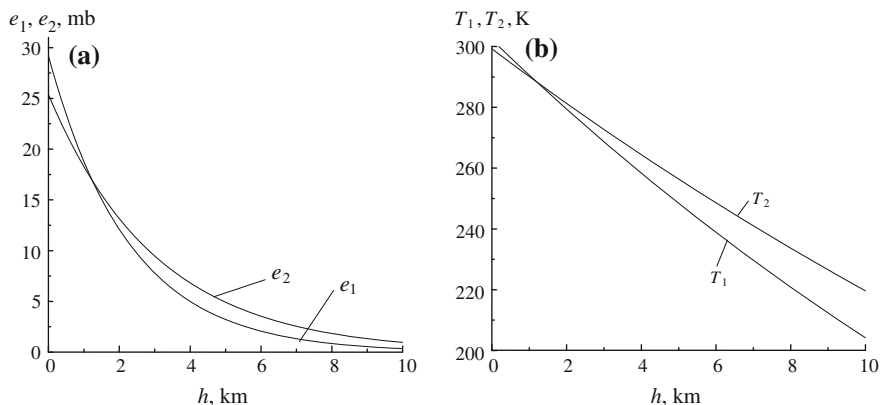
Fig. 9.9 Vertical distribution of the air humidity e (**a**) and temperature T (**b**) in the troposphere in the area of the SMKF1 station: e_1, T_1 (21 August); e_2, T_2 (28 August) 2005

left (28 August). It is important to take into account the periodicity (regularity) of observations of modern satellite MCW radiometric means, such as the DMSP SSM/I radiometer and EOS Aqua AMSR-E radiometer (see Appendix 2). One can see sharp contrasts of the atmospheric temperature and humidity at various levels h during passage of the cyclone through the point SMKF1: variations of parameter T are maximal at the upper boundary of the atmosphere (about 10 K), and variations of parameter e reach 2 mb at heights of 3–6 km.

Figure 9.10 shows estimates of the air humidity and temperature at various horizons of the atmosphere in the period 21–31 August 2005, as well as results of their approximation, which emphasize the behavior of parameters T and e over this time interval. Here, the program Origin—Polinomial was used for approximation of the smooth curves (Fig. 9.10b, e, f), and Sigmodial was used for approximation of the stick-slip plots (Fig. 9.10a, c, d).

The sharp (stick-slip) changes of the air temperature and humidity in the near-surface layer and at the upper boundary of the troposphere were observed at noon on 25 August when TC Katrina passed the point SMKF1. Variations of the air temperature and humidity at the upper boundary of the atmospheric boundary layer t_{1500} and humidity e_{1500} are monotonous (Fig. 9.10b, e).

9.2.3   Some Results of an Analysis of the Atmosphere's Integral Characteristics Dynamics

Based on the buoy data for air humidity in the near-surface layer and the computed estimates of this parameter in overlying atmosphere layers, the total water vapor content of the atmosphere Q in the layer 10–10,000 m was computed.
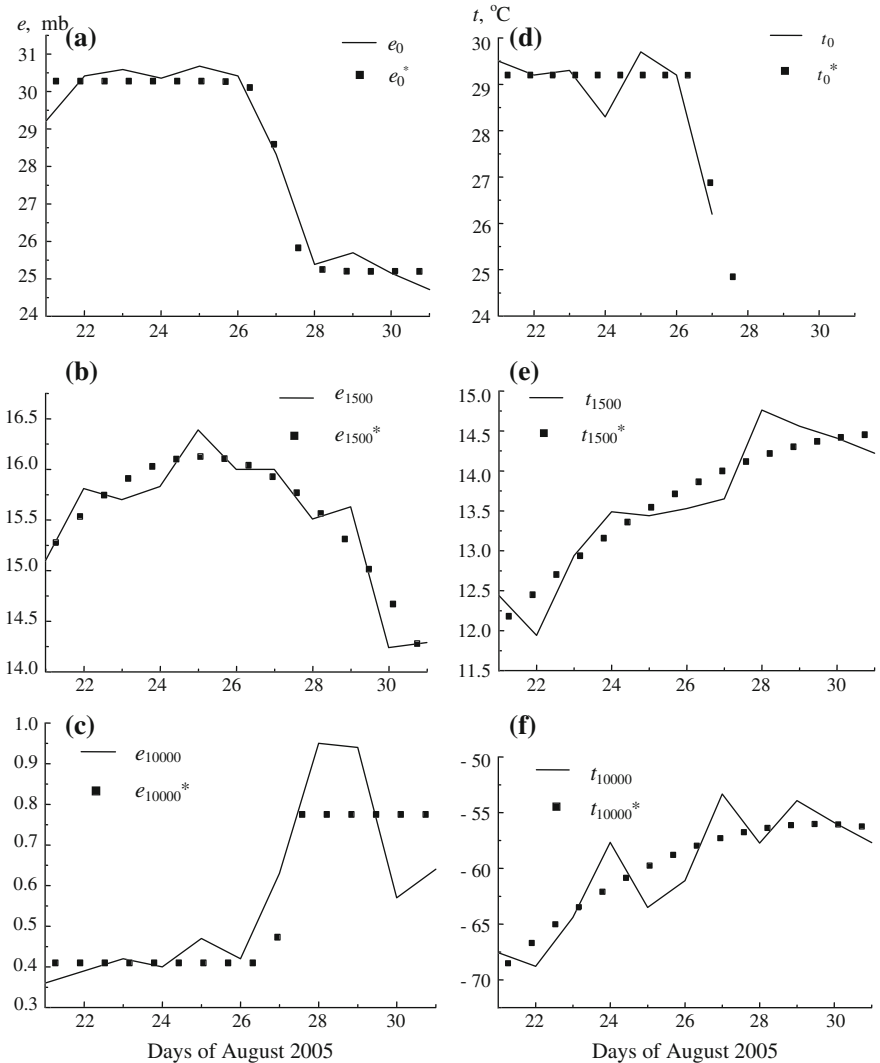
Fig. 9.10 Variations of the humidity and temperature of the atmospheric near-surface layer, boundary layer, and its upper layer for the period of 21–31 August at the levels of 10 m (**a**, **d**), 1500 m (**b**, **e**), and 10,000 m (**c**, **f**). *Solid lines* are the results of the applied algorithm applying; *dashed lines* indicate the results of their approximations

A comparison was made for the results of parameter Q with its satellite estimates derived with the radiometer SSM/I in area of the SMKF1 station and the AMSR-E radiometer in the area of the 42019 station. In addition, calculated estimates for atmospheric enthalpy in various layers were obtained for areas of activity of TCs Katrina and Humberto.
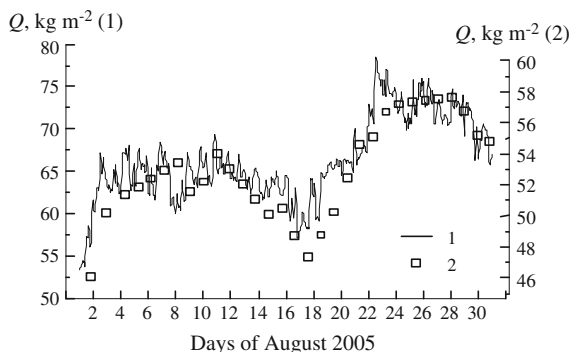
Fig. 9.11 Comparing estimates of the atmosphere's integral water vapor content Q in the area of the SMKF1 station: *1*—computed data for the layer 0–10,000 m; *2*—measurement data from the SSM/I radiometer

Dynamics of the atmospheric total water vapor near the SMKF1 station

Figure 9.11 compares the estimates of the total water vapor Q variations in the area of the SMKF1 station during the period August 1–30, 2005. These results were computed by a layer-wise integration of the air humidity at various heights with the satellite estimates of the parameter Q derived from measurement data from the SSM/I radiometer using a known technique (Alishouse et al. 1990). Appreciable variations of the parameter Q can be observed, which coincide with the passing of TC Katrina through the SMKF1 station, when a maximum for the near-surface heat fluxes was observed at noon on 25 August.

A difference between the absolute values of the computed and satellite estimates of the parameter Q can be explained by the fact that modeling of the SOA brightness temperature did not allow for an increase caused by the cloudiness and precipitation, which are registered by the satellite radiometer SSM/I. Irregularity of remote sensing in the area of the SMKF1 station and availability of noticeable gaps in the satellite measurements are also important considerations. However, good compliance is shown for the relative changes (variations) of both estimates; this is essential for validation of the developed technique for determining the air temperature and humidity and, especially, for their changeability at various horizons of the atmosphere during tropical hurricanes.

Dynamics of the atmospheric total water vapor in the area of the station 42019

We derived estimates of atmospheric total water vapor in the area of the station 42019 for the period of 6–15 September, including the stages of formation of TC Humberto. We compared satellite estimates of parameter Q with the measurement data from the radiometer AMSR-E (see Fig. 9.12). It can be seen that the formation of TC Humberto was accompanied by increases in the value of Q (at noon on 12 September). The maximum value of Q (at noon on 12 September) occurred together with the maximum fluxes of sensible and latent heat and wind speed (see Figs. 9.2
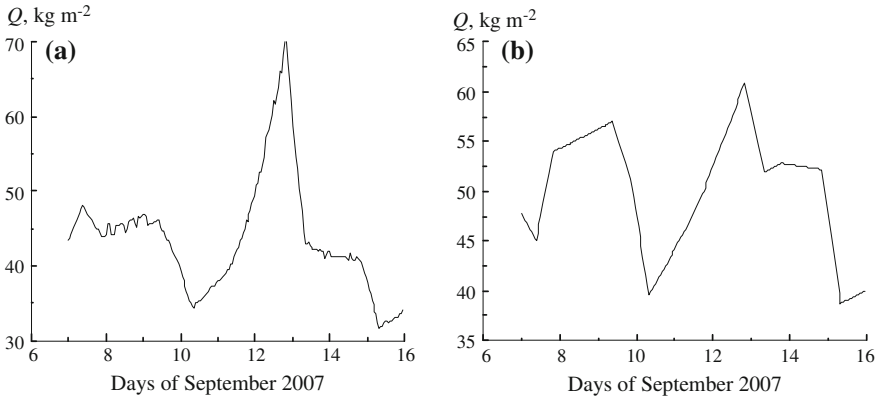
Fig. 9.12 Estimates of the atmospheric total water vapor content Q in the area of station 42019: **a** computed data for the atmosphere layer at 10,000 m; **b** measured data from the radiometer AMSR-E

and 9.5) and minimums of near-surface air temperature, humidity, and pressure (see Fig. 9.2). The peak values of Q on 12th September precede the time (7–9 September) of increased water vapor content in the atmosphere.

Figure 9.13 compares the satellite and computed estimates for the parameter Q after TC Humberto left the area of station 42019 for the time interval 13–20 September. It follows from the illustration that a reduction of atmospheric total water vapor occurred during this period in an oscillatory manner, similar to the case of near-surface fluxes of sensible and latent heat.

Fig. 9.13 Comparison of satellite (*1*) and computed (*2*) estimates of the atmospheric total water vapor content Q after the departure of TC Humberto in the area of station 42019
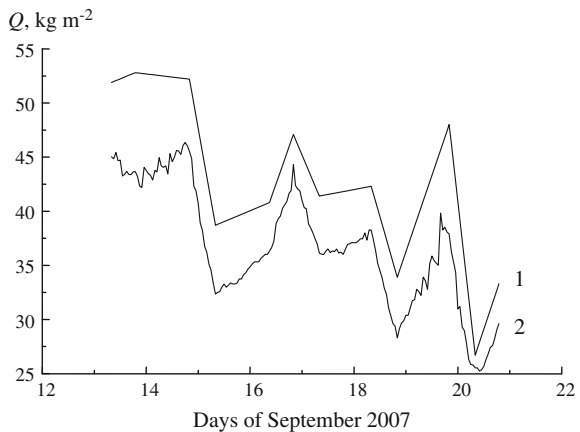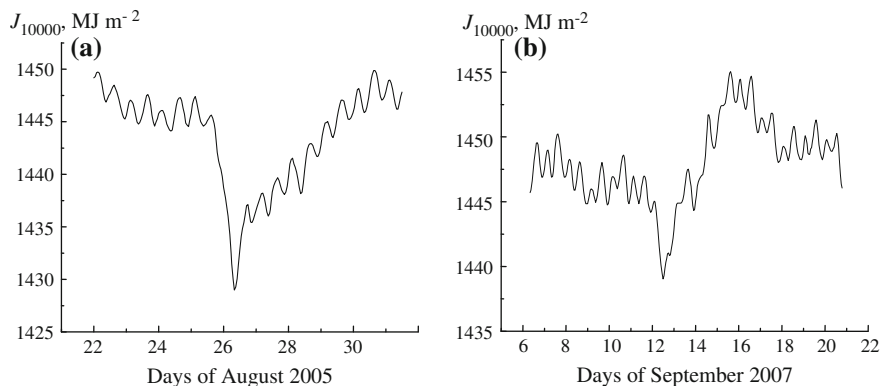
Fig. 9.14 Variations of the atmospheric enthalpy J_{10000} during **a** passing TC Katrina the station SMKF1 and **b** the formation of TC Humberto in area of the station 42019

Dynamics of atmospheric enthalpy in areas of the stations SMKF1 and 42019

Enthalpy (heat content) variations were computed for various atmospheric layers in areas of the stations SMKF1 and 42019 in periods of activity for TCs Katrina and Humberto. The estimates were obtained by a layer-wise integrating of the air temperature and humidity values calculated at various heights from adopted exponential model of the vertical distribution of the parameters t_a and ρ basing on the data of meteorological measurements at the stations SMKF1 and 42019 and simultaneous measurements from the F15 SSM/I and EOS Aqua AMSR-E radiometers.

Figure 9.14 demonstrates some results of computation of the enthalpy J for the atmospheric layer 10–10,000 m. The illustration shows that during passing Katrina the station SMKF1 and beginning TC Humberto in area of the station 42019 one can observe a sharp reduction of the $J_{10,000}$ values. This reduction is of the resonant type and accompanied by a strong increase in the vertical turbulent heat and moisture fluxes at the ocean-atmosphere boundary (see Figs. 9.4 and 9.5).

Thus, the tropical cyclones cause a reducing the atmosphere enthalpy in these areas. As shown in Grankov and Milshin (2010), just like this effect was observed in periods of the mid-latitude cyclones activity in the Newfoundland energy active zone of the North Atlantic in the experiment ATLANTEX-90.

9.3 Conclusion

The dynamics of different characteristics of the atmosphere in the periods of activity of the tropical cyclones Katrina (August 2005) and Humberto (September 2007) in the Gulf of Mexico was analyzed. This study is based on coupling the data of the buoy meteorological measurements with the data of simultaneous measurements

from the DMSP SSM/I radiometer (in area of the NOAA station SMKF1) and the EOS-Aqua AMSR-E radiometer (in area of the station 42019).

The technique of analysis of the air temperature and humidity at various horizons was developed that enable us to determine the atmosphere integral characteristics such as its total water vapor content and enthalpy during passing the TC Katrina through the station SMKF1 and formation of TC Humberto in area of the station 42019. It is shown, that in both cases the effect of taking off heat energy by the cyclones from the atmosphere and the ocean surface takes place. This effect results in strong disturbances of the temperature, humidity and pressure in the near-surface atmosphere and is accompanied by a sharp decrease of the atmosphere enthalpy and considerable increase of the vertical turbulent heat and moisture fluxes at the ocean surface.

The following features of the results of an analysis of the SOA parameters dynamics during the process of the formation of TC Humberto can be noted:

(a) Oscillatory nature of behavior of the sensible and latent heat fluxes as well as the atmosphere total water vapor after leaving by the formation location of the cyclone, that is at the stage of the SOA relaxation
(b) Availability of anomalies in behavior of the atmosphere total water vapor the 4–5 days before an appearance of TC Humberto. This leaves open to further research the question of what becomes of these anomalies as the tropical cyclones signs

This guess is required in further examination with observational data the processes of formation of other tropical cyclones in various oceanic areas in various years and seasons taking into account the effect of the atmospheric horizontal circulation.

Results of the researches confirm a role of the atmospheric total water vapor, which is ease accessible in studying with modern satellite MCW radiometric means at the stages proceeding to development of the storm situations in the ocean and atmosphere; this is an important and required condition for studying the problems of the tropical cyclone genesis (Grankov et al. 2012a, b; Sharkov et al. 2012; Ermakov et al. 2014).

The Relationship of Periodicity in Satellite and Station Measurements

The frequency (periodicity) of satellite MCW radiometric measurements is less than the frequency of buoy meteorological measurements. Therefore, the following question arises: Is this sufficient to describe high-speed processes in the SOA arising under the influence of a tropical cyclone? To answer to this question, we analyzed the regularity of measurements from the F-15 SSM/I radiometer in the

(a)

$T^b_{1.35}$, К

Days of August 2005

(b)

$T^b_{1.26}$, К

Days of September 2007
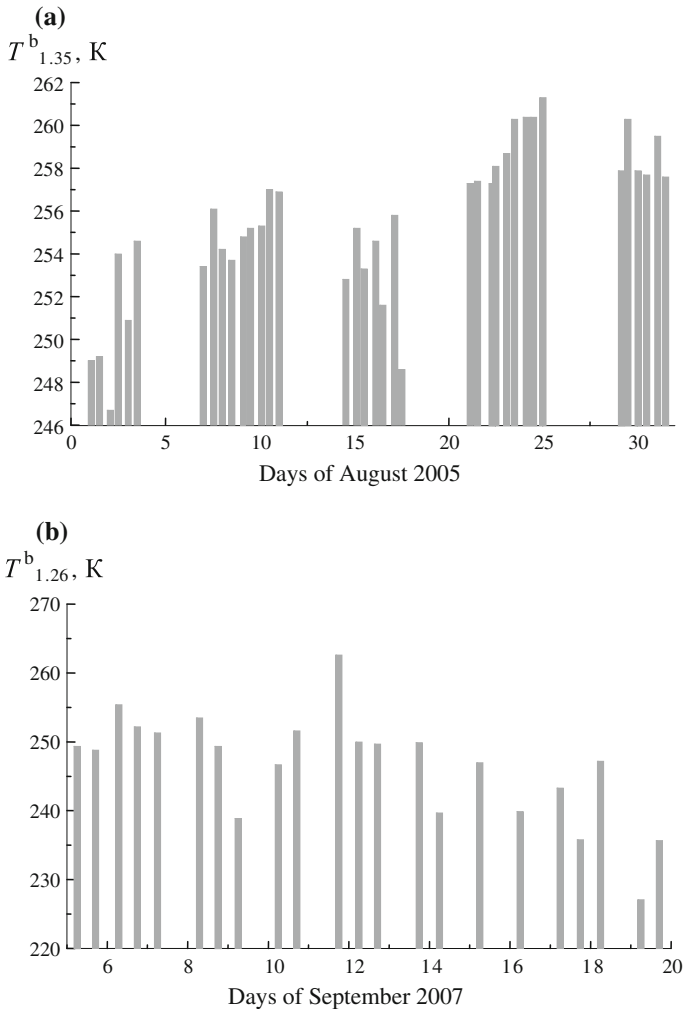
Fig. 9.15 Regularity of measurements from the DMSP F-15 satellite in areas of the station SMKF1 in August 2005 (**a**) and the EOS Aqua satellite in area of the station 42019 in September 2007 (**b**)

area of station SMKF1 and the EOS Aqua AMSR-E radiometer in the area of station 42019 during the various phases of activity for TCs Katrina and Humberto.

Figure 9.15 illustrates all samples of the brightness temperature measured by the SSM/I radiometer at the wavelength 1.35 cm (at vertical polarization) at the ascending and descending orbits of the F-15 satellite (a) and EOS Aqua AMSR-E radiometer at the wavelength of 1.26 cm at the same polarization (b) in the period of November 2009 to December 2010 when pointed above oceanic stations. The number and time position of samples for the other spectral and polarization

radiometric channels coincides exactly with those given in Fig. 9.15. Figure 9.15a shows that the number of samples for the SSM/I radiometer was 37 in August 2010. At that time, the number of buoy measurements was 744 in this period. Noticeable gaps in satellite measurements were observed in four regions with an overall duration of 80–90 h.

The periodicity of measurements aboard the EOS Aqua satellite was more favorable for conducting a joint analysis of the remote-sensed and direct data in area of station 42019: the number of satellite samples was 22, and the number of buoy measurements was 360 during the period from 5 to 19 September 2007 (Fig. 9.15b). In this case, there is a lack of evident gaps in measurement sets; the time interval between satellite samples does not exceed 22 h, which promotes the possibility of using the satellite-derived brightness temperatures in (quasi) continuous observations of the processes occurring in the SOA at the beginning of TC Katrina.

References

Alishouse JC, Snyder SA, Vongsatorn J, Ferrado RR (1990) Determination of oceanic total precipitate water from the SSM/I. J Geophys Res 5: 811–816

Armand NA, Polyakov VM (2005) Radio propagation and remote sensing of the environment. CRC Press LLC: Roca Raton

Basharinov AE, Gurvich AS, Egorov ST (1974) Radio emission of the planet Earth. Nauka, Moscow In Russian

Golitsyn GS (2008) Polar lows and tropical hurricanes: Their energy and sizes and a quantitative criterion for their generation. Izvestija, Atmosp Oceanic Phys 5: 579–590 In Russian

Ermakov DM, Sharkov EA, Chernushich AP (2014) The role of tropospheric advection of latent heat in the intensification of tropical cyclones. Remote Sensing Earth from Space 4: 3–15 In Russian

Grankov AG, Milshin AA (2010) Microwave radiation of the ocean-atmosphere: Boundary heat and dynamic interaction. Springer Dordrecht Heidelberg London New Jork

Grankov AG, Milshin AA, Novichichin EP (2012a) Analysis of behavior of the atmospheric characteristics in areas of activity of tropical cyclones Humberto and Katrina with the data of satellite microwave radiometric and direct measurements. Int J Rem Sens Applications, IJRSA Vol2 Iss. 2 pp.1–9 www.ijrsa.org ©World Academic Publishing

Grankov AG, Marechek SV, Milshin AA et al (2012b) Elaboration of technologies for diagnosis of tropical hurricanes beginning in oceans with remote sensing methods, Chapter in collective monograph "Hurricane Researches", InTech Publ. House

Hollinger PH, Peirce JL, Poe GA (1990) SSM instrument evaluation. IEEE Trans Geosci Rem Sensing 28: 781–790

Kawanishi T, Sezai T. Imaoka K et al. (2003) The Advanced Microwave Scanning Radiometer for the Earth Observing System (AMSR-E), NASDA's Contribution to the EOS for global energy and water cycle studies. IEEE Trans Geosci Rem Sensing 48: 173–183

Kharkevich AA (2007) Bases of the radioengineering (3-th edition). Moscow, Fizmatlit In Russian

Kunkee D, Boucher D, Poe G, Swadley S Evaluation of the Defense Meteorological Satellite Program (DMSP) Special Microwave Imager Sounder (SSMIS). In: Geoscience and Remote Sensing Symposium (IGARSS 2006) 7–12 July, Denver, Kolorado, 2006

Lappo SS, Gulev SK, Rozhdestvenskii AE (1990) Large-scale heat interaction in the ocean–atmosphere system and energy-active zones in the world ocean. Gidrometeoizdat, Leningrad In Russian

Sharkov EA, Shramkov JN, Pokrovskaya IV (2012) The integral water vapor in tropical zone as the necessary condition for atmospheric catastrophic genesis. Remote Sens. Earth from Space: 73–82 In Russian

Snopkov VG (1977) On correlation between the atmosphere water vapor and the near surface humidity seasonal variations of the water vapor content over the Atlantic. Meteorology and Hidrology 12:38–42 In Russian

Xrgian AX (1978) Physics of the atmosphere, vol. 1. Leningrad, Gidrometeoizdat In Russian

Chapter 10
Comparative Analysis of Prestorm Situations in the Florida Strait and Golubaya Bay in the Black Sea

10.1 Objectives of the Study

In this chapter we consider some specific characteristics of the behavior of atmospheric thermal and radiothermal (MCW) radiation during prestorm situations in water areas monitored directly and remotely. The results of this study were previously published by Grankov et al. (2014a, b).

The response of the ocean–atmosphere system was studied during the strong tropical cyclone (TC) Katrina in the Florida Strait in the region of buoy station SMKF1 in August 2005. (Based on NOAA classifications, tropical cyclones are considered to be ocean storms until they arrive at US coasts.) Synoptic variations of the following SOA characteristics were analyzed for the period 19–24 August 2005, which preceded arrival of TC Katrina:

(a) Air temperature and humidity in a 10-m surface layer near SMKF1, resulting from direct meteorological measurements from the station.
(b) Total water vapor content of the atmosphere obtained from processing MCW radiometric data and its enthalpy.
(c) Vertical turbulent fluxes of sensible and latent heat at the water–surface interface.
(d) Intensity of the SOA brightness temperature measured with the EOS Aqua AMSR-E radiometer in the water vapor radiation (absorption) band at the wavelength 1.26 cm (frequency of 23.8 GHz).

The US National Data Buoy Center (NDBC), part of the NOAA, provided the ground-based data for one part of the study. We also used routine measurements from the AMSR-E multichannel scanning radiometer from the US meteorological EOS Aqua satellite as a source of remote-sensed data. In the other part of the study on the coastal region of the Black Sea (Gelendzhik, the territory of the Southern Branch of the Shirshov Institute of Oceanology, Russian Academy of Sciences), meteorological

and microwave radiometric studies of atmospheric parameters were carried out simultaneously in a period that preceded a strong storm. The measurements were from September–October 2010 using meteorological sensors mounted at the end of a pier, a radiometer oriented upward and elevated, and azimuth scanning, which measured the intensity of MCW natural radiation of air at the wavelength of 1.35 cm. The MCW radiometric measurements were aimed at studying the variability of atmospheric parameters under different weather conditions (including prestorm conditions) and at using the technique for estimating the height distribution of atmospheric water vapor.

Simultaneously, researchers at the Institute of Space Research, Russian Academy of Sciences; Institute of Atmospheric Physics, Russian Academy of Sciences; and the Southern Branch of the Shirshov Institute of Oceanology, Russian Academy of Sciences studied parameters of the water surface and characteristics of surface air using optical, infrared (IR)-, millimeter-, and centimeter-range instruments.

Ground-based measurement data on the surface air temperature, humidity and the brightness temperature of the atmosphere were taken from the Black Sea experimental data for the period from September 21 to 31, which preceded the arrival of the storm. Later, these data series were added with measurement results of the AMSR-E radiometer of the EOS Aqua satellite at 1.26 cm (23.8 GHz) in the water area adjacent to the Golubaya Bay. It was impossible to use the satellite data for the water area of this bay because its size is several times smaller than the spatial resolution of this channel of the AMSR-E radiometer.

Using the previously listed instruments, we studied common and specific features in the behavior of surface air temperature and humidity, surface fluxes of sensible and latent heat, total moisture content and enthalpy of the atmosphere, and the MCW radiation characteristics of the SOA during time periods preceding the approach of TC Katrina to the SMKF1 region and the arrival of a sea storm in the region of Golubaya Bay.

10.2 Dynamics of the Near-Surface and Upper Atmosphere Layers Near the SMKF1 Station Before TC Katrina's Arrival

Surface Air Temperature and Humidity and Atmospheric Moisture Content

NDBC station SMLF1 (Sombrero Key) in the Florida Strait (24.38°N, 81.07°W) was used as a reference point for analysis of the effects of TC Katrina on atmospheric parameters. The shortest distance between TC Katrina's trajectory and this station was about 120 km on August 26, 2005 at 12.00 p.m. At this time, TC Katrina passed about 800 km from the point of origination in the Bahamas region. The volume of initial data obtained using SMKF1 sensors during the stage

Fig. 10.1 Variations in the surface air temperature t_a before the arrival of TC Katrina to the SMKF1 region in the Florida Strait. The *dashed curve* shows the approximation of the results by a degree of polynomial

$\Delta t_a, °C$

Days of August 2005
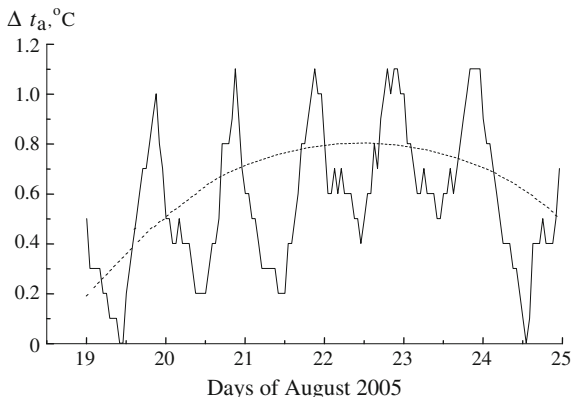
preceding the arrival of TC Katrina at the SMKF1 region included 144 hourly samples for the surface air temperature and humidity.

The effect of accumulating latent heat in the water vapor of the atmosphere was observed in this stage, which became apparent in the *stable* increase of the atmosphere's thermodynamic parameters—the near-surface air temperature and humidity as well as the SOA brightness temperature in the vicinity of the line of radiowave resonant absorption at 1.35 cm (22.235 GHz).

Figure 10.1 shows variations in the surface air temperature from August 19 to 24, 2005, recorded by SMKF1 sensors. Alternating peaks (maximum and minimum) of this parameter show its daily variations. It can be seen that the surface air temperature increased while TC Katrina approached SMKF1: the average (approximated) values of parameter t_a reached 0.5 $°C$ in the period from August 19 to 23, and the daily amplitude of its variations was 1 $°C$ (i.e., half as much).

Figure 10.2 shows the behavior of air parameters near SMKF1 for the week before the arrival of TC Katrina (August 18–27). Variations in the absolute humidity a of the surface air estimated from the results of wide-scale experimental research of a correlation between the water vapor pressure and the differences in the air and water temperatures (Snopkov 1980) in different parts of the World Ocean are shown in Fig. 10.2a (air humidity is not measured directly at NOAA buoy stations). Figure 10.2b, c shows variations in the total moisture content of the atmosphere Q, estimated from the EOS Aqua AMSR-E radiometer data according to a well-known technique (Alishouse et al. 1990. The brightness temperature T^b was measured in the region of resonance for atmospheric water vapor absorption of 1.26 cm.

As seen from Fig. 10.2a, the near-surface air humidity steadily increased by 3 g m^{-3}, the total moisture content of the atmosphere increased by 11 kg m^{-2}, and the SOA brightness temperature at a wavelength of 1.26 cm increased by 13 K during the time period preceding the arrival of TC Katrina in the region of SMKF1. The comparison between Fig. 10.2b, c confirms the correlation between SOA brightness temperature in the region of resonance for absorption of radiowaves by

Fig. 10.2 Variations in the
(a) absolute humidity of
surface air temperature *a*,
(b) total moisture content of
the atmosphere *Q*, and SOA
brightness temperature T^b
measured with the AMSR-E
radiometer at 1.26 cm
(vertical polarization) during
the approach of *TC* Katrina to
SMKF1. The *dashed curves*
show the approximation of
the results by a degree of
polynomial = 2
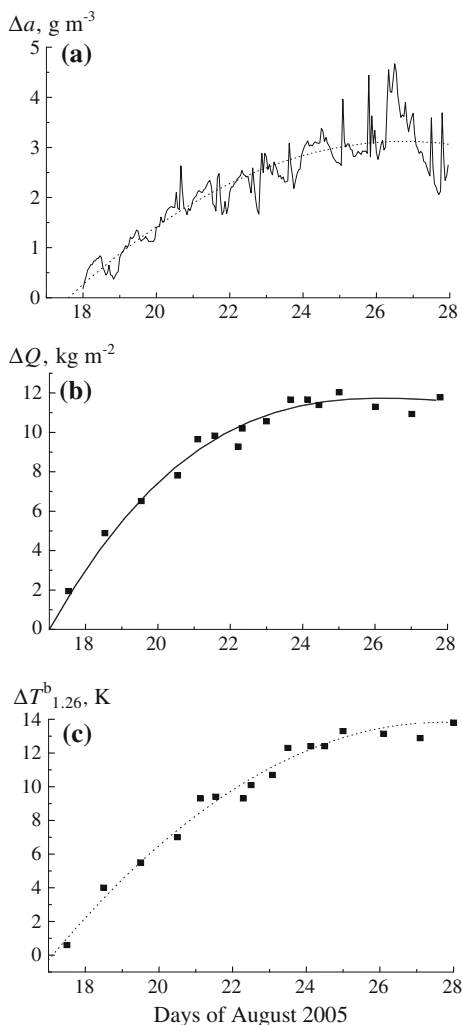
the atmospheric water vapor and the total moisture content of the atmosphere. The sensitivity of the SOA microwave natural radiation to variations in the total moisture content of the atmosphere $\Delta T^b_{1.26}/\Delta Q$ is close to its theoretical value, which is 1.1–1.2 K/(kg m^{-2}) at a wavelength of 1.35 cm (central line of resonance absorption of radiowaves by water vapor).

Fluxes of Sensible and Latent Heat Near the Ocean Surface

Using buoy measurement data on the ocean surface and surface air temperature, estimates of the air humidity, pressure and wind speed in the near-surface air layer, and vertical turbulent fluxes of sensible and latent heat have been calculated for SMKF1 at the water–air interface on the basis of bulk formulas (see also Chap. 1).
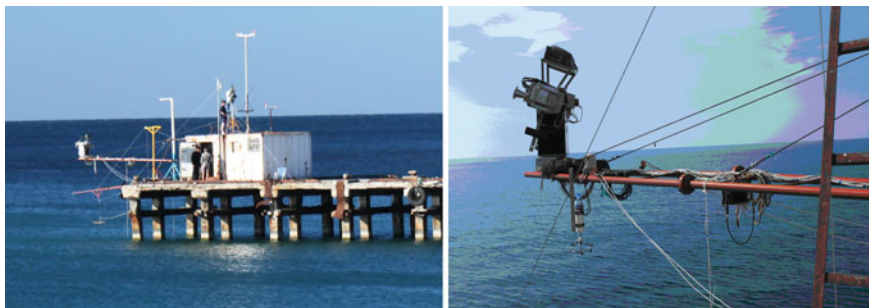
Fig. 10.3 Measuring complex (*left*) and scanning platform (*right*)

Figure 10.3 shows the calculated fluxes of sensible q_h and latent q_e heat (with 3-h smoothing); the average values of the heat fluxes decrease significantly due to the passage of TC Katrina through the SMKF1 region by about 20 W m^{-2} (from 30 to 10 W m^{-2}) for fluxes of sensible heat and by 150 W m^{-2} (from 350 to 200 W m^{-2}) for fluxes of latent heat, which is evidence of smoothing of the thermal contrasts between the ocean surface and surface air layer by the passing cyclone. The time of cyclone passage near SMKF1 (noon on August 26) is accompanied by positive surges of the parameters q_h and q_e, which reach 80 and 500 W m^{-2}, respectively.

It is interesting to note that the maximum value of fluxes of total (sensitive and latent) heat near SMKF1 (~ 600 W m^{-2}) is close to the estimate given by G.S. Golitsyn for tropical latitudes. This value is also comparable with fluxes of total heat in the Newfoundland energy active zone of the North Atlantic, which is often affected by strong midlatitude cyclones, reaching 800 W m^{-2} in March 1988 and April 1990, according to data from NEWFOUEX-88 and ATLANTEX-90 experiments.

Enthalpy of the Atmosphere

We have calculated the enthalpy (heat content) of the surface air layer in the period from August 21 to 31, 2005, based on buoy meteorological measurements. It has been ascertained that the enthalpy of water vapor accumulated in the surface air layer while TC Katrina approached the SMKF1 region in this period, with an increase in its specific value by 14.7 kJ m^{-2}.

An increment of the air heat content was calculated in the 0–10,000 m layer in the approximation of polytropic atmosphere with accounting for a vertical gradient of air temperature of -6.5 °C per km and the increment of total tropospheric water vapor content before the arrival of TC Katrina, which was about 5500 kJ/m^2 in August 21–31.

10.3   Dynamics of Characteristics of the Near-Surface and Upper Atmosphere Layers in Golubaya Bay Before Sea Storm Coming

Combined (simultaneous) measurements of meteorological and microwave radiation characteristics of the atmosphere were measured in Golubaya Bay near Gelendzhik in September 2010 in a prestorm period using experimental facilities of the Southern Branch of the Shirshov Institute of Oceanology. Measuring tools were mounted at the end of a pier (Fig. 10.3) and included the following:

1. Meteorological devices, mounted at the pier.
2. Radiometers operating in the infrared, millimeter, centimeter, and decimeter wavelength ranges, mounted at the scanning platform.
3. Devices for analysis of the water properties.

The pier is approximately 200 m long; the sea depth is 7 m. The scanning platform, on which the equipment was mounted (including a MCW radiometer operating at a 1.35 cm wavelength), was an important part of the measuring complex. This radiometer was designed and constructed by the Radio Engineering Corporation "VEGA" (Moscow). The platform was fixed to a 5-m-long metal truss. The top hemisphere was observed by scanning with a smooth variation in the angle from zenith to nadir and back for a series of fixed elevation directions for every $30°$.

Figure 10.4 shows the measured brightness temperature of the atmosphere at the wavelength of 1.35 cm for vertical scans in the period from September 23 to 30, which preceded a storm in Golubaya Bay (the sea storm's epicenter passed over the
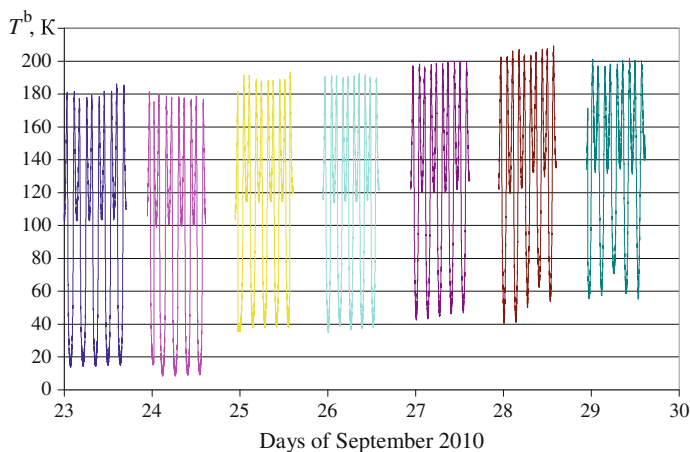
Fig. 10.4 Brightness temperature T^b of azimuth scans of the atmosphere's hemisphere at the wavelength of 1.26 cm for several days before the storm in Golubaya Bay

Fig. 10.5 Angular dependence of the brightness temperature of the atmosphere T^b at a wavelength of 1.35 cm in the prestorm period in Golubaya Bay in September. Curves 1–7 correspond to the dates ranging from September 23 to 30, 1990
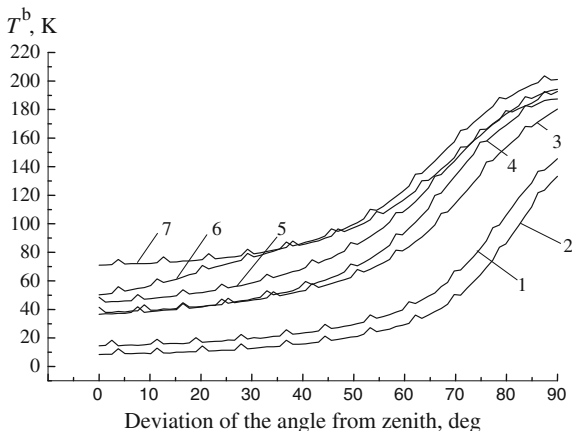
measuring complex on October 1, 2010). As can be seen from Fig. 10.4, an increase in the brightness temperature's maxima and minima was observed in this period, as recorded at rotating platform positions of 0 and 90°, respectively.

Figure 10.5 shows the brightness temperature of the atmosphere at 1.35 cm as a function of the angle deviation from zenith, which is tightly connected with the total moisture content of the atmosphere and clearly shows the effect of water vapor accumulation in the atmosphere during the prestorm period. The results shown in Figs. 10.4 and 10.5 are in a good agreement with classic ideas about angular dependences of the brightness temperature of the atmosphere.

Thermal Characteristics of Surface Air

Meteorological measurements from the pier show that the surface air temperature and humidity increased several days before the arrival of the storm to the region of Golubaya Bay. According to our calculations, the heat accumulated in the water vapor of the surface air layer; the specific heat content of the layer increased by about 61 kJ m^{-2}. Such a large increase in the heat content of water vapor of the surface air, as compared to the prestorm situation in the Florida Strait in August 2005 (14.7 kJ m^{-2}), is explained by the fact that variations in the surface air temperature and humidity in Goubaya Bay during the prestorm period were much higher than those in the SMKF1 region during the approach of TC Katrina.

The vertical fluxes of sensible, latent, and total heat were calculated using bulk formulas on the basis of direct measurement data on the water and air temperature and the surface wind speed. The results are shown in Fig. 10.6. It is seen that the flux of sensible heat decreased from 40 to −100 W m^{-2} and that of latent heat from 225 to 10 W m^{-2} upon nearing the storm. Thus, the water surface gave up heat to the surface air, and the characteristic of the heat exchange reversed about a day before the arrival of the storm to Golubaya Bay.

Fig. 10.6 Variations in the fluxes of sensitive q_h, latent q_e, and total heat q_{he} during the prestorm period in Golubaya Bay
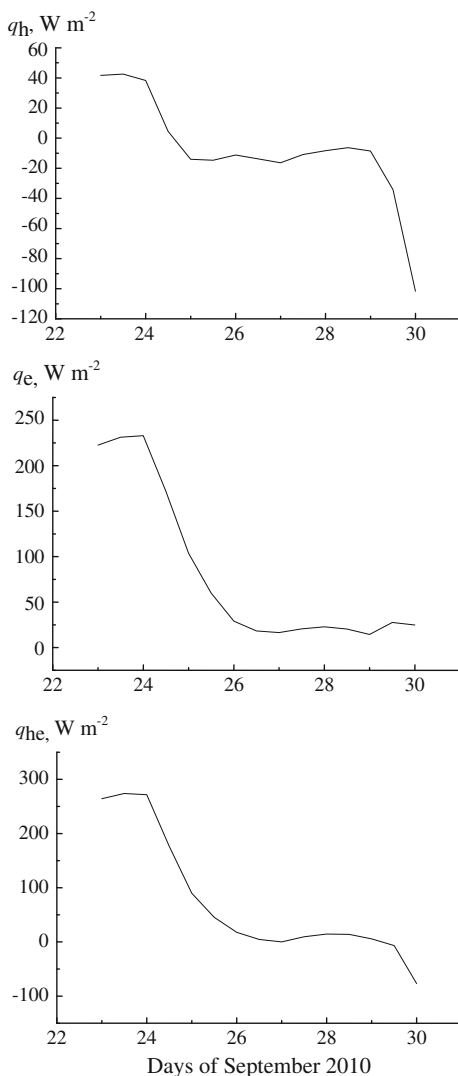
A comparison between Figs. 10.3 and 10.6 shows that the difference in the flux of sensitive heat was two times higher in Golubaya Bay during the prestorm period than that in the Florida Strait during the approach of TC Katrina to SMKF1, while the difference in the flux of latent heat is slightly lower.

Result of Combined Observations Near Golubaya Bay

The dynamics of surface air temperature and humidity measured by meteorological sensors at the pier were compared with the results of simultaneous measurements from the EOS Aqua AMSR-E radiometer at the wavelength 1.26 cm

Fig. 10.7 Variations in the thermal and radiothermal characteristics of the atmosphere in the prestorm period in Golubaya Bay: (**a**) surface air temperature (*1*) and humidity (*2*); (**b**) SOA brightness temperature at the wavelength 1.26 cm measured with the AMSR-E radiometer; and (**c**) SOA brightness temperature measured from the pier with the MCW radiometer at the wavelength 1.35 cm
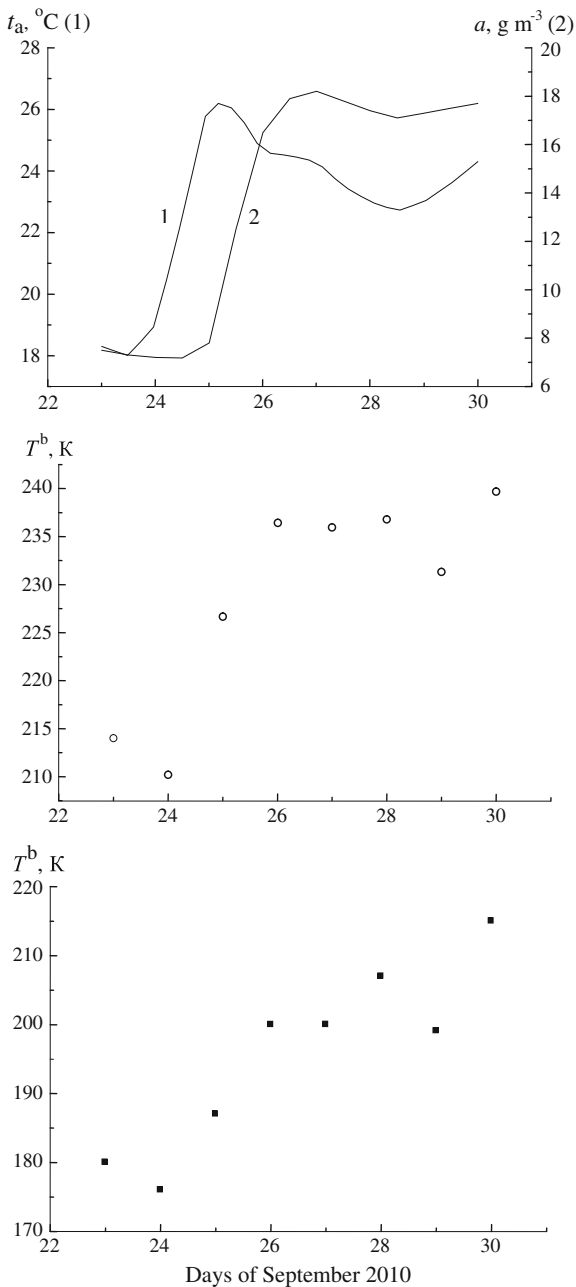
(23.8 GHz) in the sea region adjacent to Golubaya Bay. A comparison between satellite data on the SOA brightness temperature over Golubaya Bay is incorrect because the Golubaya Bay is several times smaller than the spatial resolution of the

1.26-cm channel of the AMSR-E radiometer. The size of the region selected corresponds to a satellite "spot"—the linear size of which is approximately 60 km at the wavelength of 1.26 cm, and the coordinates of the region center are 44°N, 38°E.

Figure 10.7 shows the comparison results for the surface air temperature and humidity, the SOA brightness temperature measured with the AMSR-E radiometer at the wavelength 1.26 cm, and the brightness temperature measured from the pier with the scanning MCW radiometer at a wavelength of 1.35 cm. In the last case, only samples corresponding to nadir measurements were used among all scans. Similar characteristics of the surface air temperature and humidity response at the pier and SOA brightness temperatures in the resonance region of radio wave absorption by water vapor in the atmosphere are seen from Fig. 10.7 independently of the method of satellite MCW radiometric measurements (upward or downward radiation fluxes).

10.4 Conclusion

In this chapter, we presented the results of a comparative analysis of the dynamics of surface air temperature and humidity, surface fluxes of sensitive and latent heat, total moisture content and enthalpy of the atmosphere, and MCW radiation characteristics of SOA during the time period preceding the approach of TC Katrina to the SMKF1 station in the Florida Strait (the end of August 2005) and the prestorm period in Golubaya Bay in the Black Sea (the end of September 2010) that allow us to make the following conclusions:

1. Similar features in the behavior of these SOA characteristics were observed, including a steady increase in the surface air temperature and humidity, total moisture content and enthalpy of the atmosphere, and the SOA brightness temperature, as well as a decrease in the intensity of heat and vapor exchange between the water surface and atmosphere.
2. MCW radiometric measurements in the region of radiowave resonance absorption in atmospheric water vapor obtained from satellites and ground-based devices during the Black Sea experiment agree well and can serve as a useful tool for controlling the variability of the total moisture content of the atmosphere in prestorm situations.
3. The results of our study confirm the role of the total water vapor content in the atmosphere (easily monitored with up-to-date satellite MCW radiometric instruments) during prestorm stages in seas and oceans. The latest studies (Sharkov et al. 2012) show that monitoring this parameter is an important and necessary condition for studying the problem of tropical cyclone genesis.

References

Alishouse JC, Snyder SA, Vongsatorn J, Ferrado RR (1990) Determination of oceanic total precipitate water from the SSM/I. J Geophys Res 5: 811 − 816.

Grankov AG, Marechek SV, Milhin AA et al. (2014a) Analysis of prestorm situations in the Florida Straight and Golubaya bay in the Black Sea. Izvestiya, Atmospheric and Oceanic Physics 1:85 − 91.

Grankov AG, Milshin AA, Novichikhin EA (2014b) Behavior of the brightness temperature of the ocean-atmosphere system under conditions of midlatitude and tropical cyclone activity. Radiophysics and Quantyum Electronics 10:639 − 650.

Sharkov EA, Shramkov JN, Pokrovskaya IV (2012) The integral water vapor in tropical zone as the necessary condition for atmospheric catastrophic genesis. Remote Sens Earth from Space 2: 73 − 82 In Russian.

Snopkov VG (1980), Computation of air humidity over the sea from the water–air temperature difference Meteorologija i Gidrologiya 2: 109–111 In Russian.

Chapter 11
Modern Satellite MCW Radiometric Means for Analyzing Ocean-Atmosphere Interactions

11.1 History and General Information

When studying the global ocean and its climatic forming factors, an arsenal of instrumentation in optical, infrared, and MCW electromagnetic ranges is used. In accordance with the requirements of the Global System of Climate Observations (Kondrat'ev et al. 1992) for remote sensing of characteristics from satellites, such as a spatial and temporal resolution, survey coverage, and its duration, polar space platforms are most suitable for accurate determination of geophysical parameters. Some types of current and prospective polar platforms, as well as their orbital parameters, are presented in Table 11.1; the low-latitude satellite TRRM is the exception in this series.

The idea of using MCW radiometric methods in climatic studies became a reality in 1978 after the launch of the Nimbus-7 multichannel scanning radiometer SMMR, which operated for about 9 years. Based on its measurements, an archive of antenna temperatures (the SMMR level 1A data set) at NASA's Goddard Space Flight Center (GSFC) was created. Later, these data were calibrated and processed in the form of brightness temperatures (the SMMR level 1B data set) at the Jet Propulsion Laboratory (JPL) during the Earth Observing System (EOS) Pathfinder program and archived at NASA's Marshall Space Flight Center Distributed Active Archive Center with 8-mm magnetic tapes—about 70 GB of information (Njoku et al. 1995).

Since 1987, the operative meteorological satellites DMSP with the radiometers SSM/I, SSM/T, and SSM/T-2 have been successfully functioning; the original measurement data and results of their processing are accumulated and stored in several USA scientific centers. Thus, due to efforts of specialists from NASA, NOAA, and the U.S. Department of Defense, there is a unique possibility to conduct climatic studies of the ocean using MCW radiometry data from a period of 35 years.

Table 11.1 Types of polar platforms, date of launch, and orbital parameters

Satellite	Data of launch	Inclination (°)	Height (km)	Period (min)	Local time of the equator crossing
TRMM	November 1997	35	400	92.5	–
DMSP F-15	December 1998	98.8	850	102.0	15:02, 03:02
Coriolis	January 2003	98.7	840	101.0	18:03, 06:03
DMSP F-16	October 2003	99	857	102.0	16:55, 04:55
DMSP F-17	November 2006	99	857	102.0	17:58, 05:58
Meteor-M, No. 1	September 2009	98.77	832	101.3	21:00, 09:00
DMSP F-18	October 2009	99	850	102.0	20:06, 08:06
GCOM-W1	May 2012	98.2	700	99	13:31, 01:31
Meteor-M, No. 2	July 2014	98.77	832	101.3	21:00, 09:00
DMSP F-19	April 2014	99	857	102.0	17:30, 05:30
Meteor-M, No. 2-1	2015	98.77	832	101.3	–
Meteor-M, No. 2-2	2016	98.77	832	101.3	–
DMSP F-20	2020	99	857	102.0	–

In our previous book (Grankov and Milshin 2004), we described briefly the following MCW radiometric systems: Nimbus 7 radiometer SMMR; DMSP radiometers SSM/I, SSM/T1, SSM/T2, TMI radiometer TMRR, Meteor-3M radiometer MTVZA, EOS Aqua radiometric complex including AMSR-E, AMSU-A, HSB, AIRS, MODIS, and CERES devices, ADEOS-II radiometric complex consisting of AMSR-E, GLI, AMSR-J, and SeaWinds measurement instrumentation, Sich-1M radiometer MTVZA-OK, NPOESS radiometers SMIS, CrIS, GPSOS, OMPS, SESS, VIIRS, and ATMS, Proteus L-radiometer MIRAS. In addition, the English version of this book (Grankov and Milshin 2010) describes the L-range-radiometer of the satellite MKA-FKI No. 1. In this chapter, we consider the characteristics of various MCW radiometers (scanners and sounders) presently operating in space.

11.2   Review of Recent MCW Radiometric Complexes

11.2.1   DMSP Radiometric Complex

Modern satellite MCW passive radiometers have been developed and used in the satellite meteorological program of the Defense Meteorological Satellite Program (DMSP). This program was designed to be a long-term monitoring program to obtain meteorological, oceanographic, and the solar activity information over the oceans (Hollinger et al. 1990; Defense Meteorological Satellite Program, DMSP 1997).

The DMSP satellites have an inclination of 98.8° and a height of 850 km with a periodicity of 102 min (14.2 revolutions per 24 h). Global coverage of the earth is accomplished after 3 days, with a partial one occurring every 24 h; the subsatellite tracks are repeated every 16 days. The main orbital parameters of the DMSP satellites are shown in Table 11.1. At present, six satellites of the DMSP series are functioning: F-12, F-13, F-14, F-15, F-16, and F-17. The first satellite in this series was satellite F-08, whose measurements (the places and dates of their conduction) coincided with the vessel measurements taken during the NEWFOUEXS-88 and ATLANTEX-90 experiments. The characteristics of MCW radiometric systems of the DMSP and other satellites are considered in detail in the following sections.

11.2.2   SSMIS—Special Sensor Microwave Imager/Sounder

At present, a new generation of the MCW radiometers is used on board the DMSP F-16 and F-17, which are designed for monitoring the ocean-atmosphere system and combine the functions of a scanner and sounder (SSMIS User Manual 2007). The channel parameters of this device are illustrated in Table 11.2.

The SSMIS collects MCW energy from Earth's surface and atmosphere with a rotating 61-cm parabolic reflector (see Fig. 11.1). This reflector focuses the energy on an assembly consisting of six feedhorns, which provide the initial frequency multiplexing for 24 channels. The reflector and the six feedhorns rotate with the entire sensor canister. Located at the top of the canister are a cold calibration reflector and a warm calibration source, which do not rotate with the canister. The feedhorns view a fixed cold calibration reflector and a fixed warm calibration source for each revolution of the sensor. These calibration data are used to convert the sensor output to absolute radiometric brightness temperatures. At the nominal orbital height of 833 km, SSMIS produces a swath width on the ground of 1707 km with 12.5 km scene spacing. The achieved swath width applies uniformly to all channels of the SSMIS. The 1.9-s interscan period provides along-track sample spacing (12.5 km) equivalent to the along-scan spacing.

Table 11.2 Characteristics of the scanner/sounder SSMIS

Center frequencies (GHz)	19.35, 22.235, 37, 50.3–59.4, 60.79–63.28, 91.655, 150, 183.31
Spatial resolution (km)	13.2 × 15.5–44.8 × 73.6
Swath (survey width) (km)	1700
Scanning method	Conical
Period of scanning (s)	1.88
Angle of sounding (°)	45
Incidence angle (°)	53.1
Mode of operation	Incessant
Output information flux (Kb s^{-1})	14.2
Mass (kg)	96
Power supply (W)	135
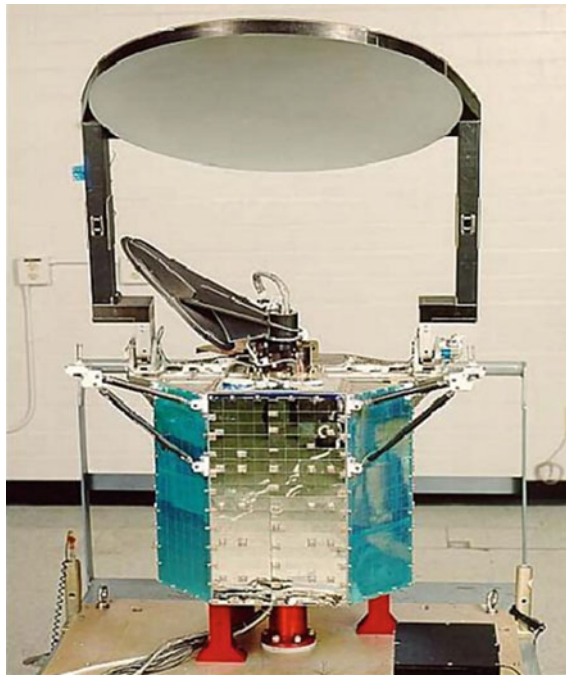
Fig. 11.1 MCW scanner/sounder of SSMIS

Table 11.3 Parameters of the TMI radiometer (TRMM Review Proposal 2007)

Frequency (GHz)	10.7	19.4	21.3	37	85.5
Polarization (V/H)	V, H	V, H	V	V, H	V, H
Sensitivity (K)	0.63	0.50	0.71	0.36	0.52
Pass band width (MGz)	100	500	200	2000	3000
Beam width (°)	3.68	1.90	1.70	1.0	0.42
Space resolution (km)	63 × 37	30 × 18	23 × 18	16 × 9	7 × 5
Antenna efficiency (%)	93	96	98	91	82
Swath (km)	760				
Angle of sounding (°)	45				
Incidence angle (°)	52.9				
Scanning method	Conical				
Period of scanning (s)	1.9				
Mode of operation	Incessant				

11.2.3   TRMM Radiometric Complex

The satellite Tropical Rainfall Measuring Mission (TRMM) developed in the framework of a joint America/Japan program was designed to capture regular synoptic information on tropical rainfalls as one of the appreciable weather and climate forming factors (Kondrat'ev et al. 1992; Remote Sensing 1998; TRMM Review Proposal 2007). This satellite launched in 1997; its main parameters are shown in Table 11.1.

The central task of the program was the extraction of information about the monthly mean estimates of precipitation and vertical profiles of latent heat in the atmosphere over periods of no less than 3 years. Remote-sensing devices were placed on board, including a MCW radiometer TMI (TRMM Microwave Imager), a meteorological radar (precipitation radar) with an electronic scanning at the frequency 13.8 GHz, a 5-channel scanning radiometer VIRS operating in the visible and IR-electromagnetic ranges (similar to the NOAA AVHRR-3 radiometer), an Lighting Imaging Sensor (LIS) for cloud brightness, and a CERES (radiation budget instrument) sensor for radiation balance characteristics. The TMI device is 5-channel scanning MCW radiometer operating at frequencies ranging from 10 to 91 GHz, with spatial resolution varying from 5 to 23 km in a swath of 520 km (see Table 11.3).

11.2.4   Coriolis Radiometric Complex

Instrumentation of a U.S. satellite launched in January 2003 allows one to determine wind speed and direction, as well as decide some other tasks as part of a weather forecast. The satellite's orbital parameters are presented in Table 11.1.

Table 11.4 Parameters of the WindSat radiometric complex (User's Manual 2006)

Frequency (GHz)	6.8	10.7	18.7	23.8	37.0
Polarization (V/H)	V, H	V, H	V, H	V, H	V, H
Sensitivity (K)	0.63	0.44	0.44	0.60	0.42
Pass bandwidth (MGz)	125	300	750	500	2,000
Beam width (°)	1.78	1.13	0.65	0.54	0.33
Spatial resolution (km)	39 × 71	25 × 38	16 × 27	20 × 30	8 × 13
Incidence angle (°)	53.8	50.1	55.6	53.2	53.2
Antenna efficiency (%)	96.8	97.7–98.8	97.3–98.3	96.2	96.9–98.8
Angle of sounding (°)	45				
Swath (km)	1400				
Scanning method	Conical				
Period of scanning (s)	1.899				
Mode of operation	Incessant				
Antenna diameter (m)	1.9				
Mass (kg)	306				
Power supply (W)	295				

The Coriolis satellite is equipped with two devices: WindSat and SMEI. The WindSat MCW radiometer is used for global research of the wind speed and direction over the ocean. The Solar Mass Ejection Imager (SMEI) sensor observes matter discharges from the sun's corona. WindSat is the first scanning radiometer-polarimeter operating in space (User's Manual 2006). The radiometer has 22 receiving channels at 5 frequencies (Table 11.4).
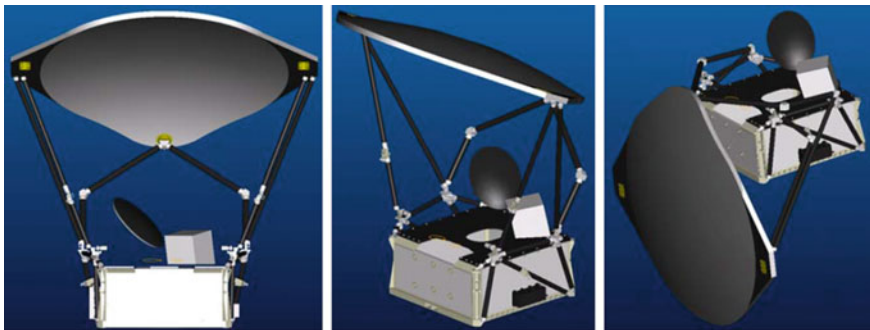
11.2.5 GCOM-W1 Radiometric Complex

GCOM-W1 is the first in the satellite series specified by the Global Change Observation Mission (GCOM) project (Global Change Observation Mission 2009). The project prolongs and extends the previous space programs EOS-Aqua (2002–2011) and ADEOS-II (2002–2003). The satellite's orbital parameters are shown in Table 11.1.

The main instrument of this satellite is AMSR-2 (Advanced Microwave Scanning Radiometer); its parameters are listed in Table 11.5. The radiometer retrieves the following geophysical parameters: total water vapor content in the atmosphere, liquid water content in the clouds, near-surface wind speed, ocean surface temperature, precipitations, ice concentration, snow thickness on land, and soil moisture. Figure 11.2 shows the radiometric complex AMSR-2 during the unwrap of its main reflector.

Table 11.5 Parameters of the radiometer AMSR-2 (User Manual 2013)

Frequency (GHz)	6.925 (7.3)	10.65	18.7	23.8	36.5	89
Polarization (V/H)	V, H	V, H	V, H	V, H	V, H	V, H
Sensitivity (K)	0.34 (0.43)	0.7	0.7	0.6	0.7	1.2
Pass band width (MHz)	350	100	200	400	1000	3000
Beam width (°)	1.8	1.2	0.65	0.75	0.35	0.15
Spatial resolution (km)	62 × 35	42 × 24	22 × 14	26 × 15	12 × 7	5 × 3
Swath (km)	1450					
Scanning method	Conical					
Period of scanning (s)	1.5					
Mode of operation	Incessant					
Angle of sounding (°)	47.5					
Incidence angle (°)	55					
Antenna diameter (m)	2					
Mass (kg)	405					

Fig. 11.2 AMSR-2 radiometric complex (User Manual 2013)

11.2.6   R MTVZA-GY Adiometric Complex of Russian Satellite Meteor-M No. 2

Spacecraft Meteor-M No. 2 launched in July 8, 2014; the first satellite of this series, Meteor-M No. 1, launched in September 2009 (see its orbital parameters in Table 11.1). Its multispectral optical and infrared devices are operating, commonly with the MTVZA-GY (Multichannel Air and Humidity Sounder) scanner/sounder designed for atmosphere profiling and ocean/land surface sounding (Boldyrev et al. 2008). The radiometer (see Fig. 11.3) is a modification of the Meteor-3M MTVZA

**Fig. 11.3** MTVZA-GY microwave scanner/sounder (Boldyrev et al. 2008)

Table 11.6 Characteristics of the MTVZA-GY scanner/sounder

Frequencies (GHz)	10.6, 18.7, 23.8, 31,5, 36.7, 42, 48, 52–57, 91, 183.31
Spatial resolution (km)	
In horizontal	198–16
In vertical	7–1.5
Swath (km)	1500
Scanning method	Conical
Period of scanning (s)	2.5
Mode of operation	Incessant
Angle of sounding (°)	53.3
Incidence angle (°)	65
Output information flux (Kb s^{-1})	35
Mass (kg)	94
Power supply (W)	80

Table 11.7 Parameters of the MTVZA-GY radiometric channels

Channel number	Central frequency (GHz)	Number of spectral bands	Frequency spectral bands (MHz)	Sensitivity of the radiometers (K)	Type of polarization (V or H)
1	10.6	1	100	0.06	V
2	10.6	1	100	0.06	H
3	18.7	1	200	0.05	V
4	18.7	1	200	0.05	H
5	23.8	1	400	0.04	V
6	23.8	1	400	0.04	H
7	31.5	1	1000	0.05	V
8	31.5	1	1000	0.05	H
9	36.7	1	1000	0.06	V
10	36.7	1	1000	0.06	H
11	42	1	1000	0.07	V
12	42	1	1000	0.07	H
13	48	1	1000	0.07	V
14	48	1	1000	0.07	H
15	52.80	1	400	0.08	V
16	53.30	1	400	0.08	V
17	53.80	1	400	0.08	V
18	54.64	1	400	0.08	V
19	55.63	1	400	0.08	V
20	$57.290344 \pm 0.3222 \pm 0.1$	4	50	0.12	H
21	$57.290344 \pm 0.3222 \pm 0.05$	4	20	0.2	H
22	$57.290344 \pm 0.3222 \pm 0.025$	4	10	0.3	H
23	$57.290344 \pm 0.3222 \pm 0.01$	4	5	0.45	H
24	$57.290344 \pm 0.3222 \pm 0.005$	4	3	0.5	H
25	91.655	2	2500	0.04	V
26	91.655	2	2500	0.04	H
27	183.31 ± 7.0	2	1500	0.08	V
28	183.31 ± 3.0	2	1000	0.1	V
29	183.31 ± 1.0	2	500	0.15	V

radiometer and Sich-1M MTVZA-OK radiometer. The main tactical and technical characteristics of the MTVZA-GY are listed in Table 11.6. Table 11.7 shows the parameters of its radiometric channels. Figure 11.4 demonstrates first result derived from the Meteor-M No. 2 MTVZA-GY.
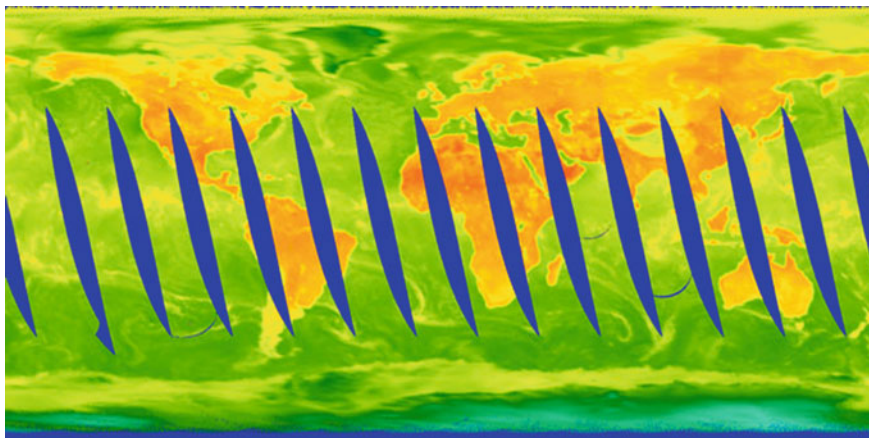
Fig. 11.4 Global spatial distribution in the Mercator projection of the brightness temperature at a frequency of 36.5 GHz (vertical polarization) on July 31, 2014 (site http://www.vniiem.ru/)

11.3 Informational Aspects in Studying the Characteristics of the Ocean–Atmosphere Heat and Dynamic Interaction with MCW Radiometric Methods

11.3.1 Processing Remotely Sensed Data in Centers for the Archiving and Dissemination of Information

In this section, we try to trace evolutional changes in information technologies since the publication of Grankov and Milshin (2004).

At present, the SSM/I, SSMIS, TMI, MTVZA, AMSU, MHS, WindSat, and AMSR-2 space radiometers let us obtain the global distribution of parameters of the atmosphere, ocean, cryosphere, and land. Table 11.8 provides the parameters retrieved from satellite MCW radiometric measurements and the accuracy of their determination, based on a review of Kondrat'ev et al. (1992), DMSP Program (2005), Navy Polarimetric Microwave Radiometer (2006), Jones et al. (2007), Global Change Observation Mission (2009), Grankov and Milshin (2010), and AMSR-2 User Manual (2013).

Retrieval of the parameters listed in Table 11.8 is carried out with a rate close to real time. A high productivity of processing is ensured with simple but effective algorithms. Usually, retrieved parameters are determined as linear combinations of the brightness temperatures measured by various radiometric channels with different weighting coefficients (Alishouse et al. 1990; Pulliainen et al. 1996; Comiso et al. 1997; Milshin et al. 1998). This situation was typical in the end of the 1980s and early 1990s. In the following years, algorithms for retrieving geophysical parameters (e.g., ocean surface temperature, near-surface wind speed, air

Table 11.8 Main characteristics of geophysical parameters retrieved by MCW radiometers averaged for a 0.25 by 0.25° square

	Parameter	Range	Resolution	Absolute error
1	Brightness temperature (K)	2.7–340	0.01	±(1–1.5)
2	Ocean surface temperature (°C)	0–35	0.15	±(0.5–1)
3	Wind speed (m s^{-1})	0–50	0.2	±(1–2)
4	Wind direction (°)	0–360	1.5	±(20–25)
5	Water content of the clouds (mm)	0.05–2.45	0.01	±0.05
6	Vapor content of the atmosphere (mm)	0–75	0.3	±(0.2–0.35)
7	Precipitation over the ocean (mm h^{-1})	0–0.25	0.1	±5
8	Atmosphere temperature profile (K)	180–335	–	1.0–2.5
9	Atmosphere humidity profile (g cm^{-3})	0–3	–	0.2
10	Soil moisture in the layer (0–2 cm) (g cm^{-3})	0–0.5	0.1	±0.1
11	Near-surface air temperature (K)	240–340	1	±(1–4)
12	Fluxes of total (sensible + latent) heat (W m^{-2})	0–1000	50	±100
13	Ice cower square (%)	0–100	5	±10
14	Ice thickness (cm)	0–100	1	±20
15	Classification of the surface types	13 types	–	–

temperature, humidity, vertical turbulent fluxes of sensible, latent heat and impulse, total water vapor content in the atmosphere, liquid water content in clouds) were constantly improved. Large sets of direct measurements for their testing and validation were used.

With later satellite MCW radiometric systems operating at frequencies of 11 and 7 GHz, the determination of ocean surface temperatures, soil moisture, and vegetation absorption factor (biomass) has become realistic. In addition, progress has been made in elaborating the methods for determining ocean surface temperature, near-surface air temperature, and humidity from satellite MCW radiometric measurements at millimeter and centimeter wavelengths. This has promoted the development of methods for retrieving near-surface surface vertical turbulent fluxes of sensible and latent heat.

U.S. scientific centers have accumulated large sets of MCW radiometric data, including the following:

- Current values of antenna and brightness temperature for the following radiometers: SMMR since 1978, SSM/I since 1987, SSM/T-1 since 1994, SSM/T-2 since 1993, TMI since 1997, AMSR-E, AMSU, and MHS since 2002, SSMIS since 2003, WindSat since 2003, and AMSRE-2 since 2012;
- Daily, three-day, and monthly mean values of near-surface wind speed, total content of the water vapor in the atmosphere, water content of the clouds, precipitation, precipitation intensity since 1987, ice characteristics
- Classified earth surface types since 1987

11.3.2   Peculiarities of Processing Satellite MCW
Radiometric Data for Studies of Heat
and Dynamic Processes in the SOA Interface

Attempts to use satellite MCW and IR data for the analysis of vertical turbulent fluxes of sensible and latent heat and impulse were undertaken long ago. However, real progress occurred after launching the DMSP satellite F-08 with the radiometer SSM/I in 1987.

In the following sections, we examine the role of satellite MCW radiometric methods in these studies, based upon the most significant projects of global flux mapping for many years. The important aim of these projects is creating archives that take into account the peculiarities of spatial and temporal variability of the SOA parameters. As a result, the necessity to assimilate vast and dissimilar arrays of satellite and earth-truth data is arising.

11.3.3   Global Archive OAFlux: Daily and Monthly Mean
Fluxes and Parameters of the Ocean and
Atmosphere

The archive Objectively Analyzed Air-sea Fluxes Project (OAFlux) was created by the Institute Woods Hole Oceanographic Institution (WHOI) under the financial support of the NOAA and NASA. The archive contains data collected since 1958 to the present day. Averaged daily and monthly (since 1958) global fields of the parameters are presented with spatial resolution 1 by 1° along latitude and longitude. Since 1987, the archival data have been based on satellite measurements.

The OAFlux archive describes the following parameters: the fluxes of sensible, latent, and total heat and impulse; evaporation; the wind speed scalar, zonal and meridional components at the 10 m height; the air specific humidity and temperature at the height of 2 m, and the ocean surface temperature. The archive was produced from the data of satellites DMSP F-08, F-10, F-11, F-13, F-14, and F-15 equipped by the radiometers SSMI, QuikSCAT with the scatterometer SeaWinds, EOS Aqua with the radiometer AMSR-E, and NOAA with radiometer AVHRR.

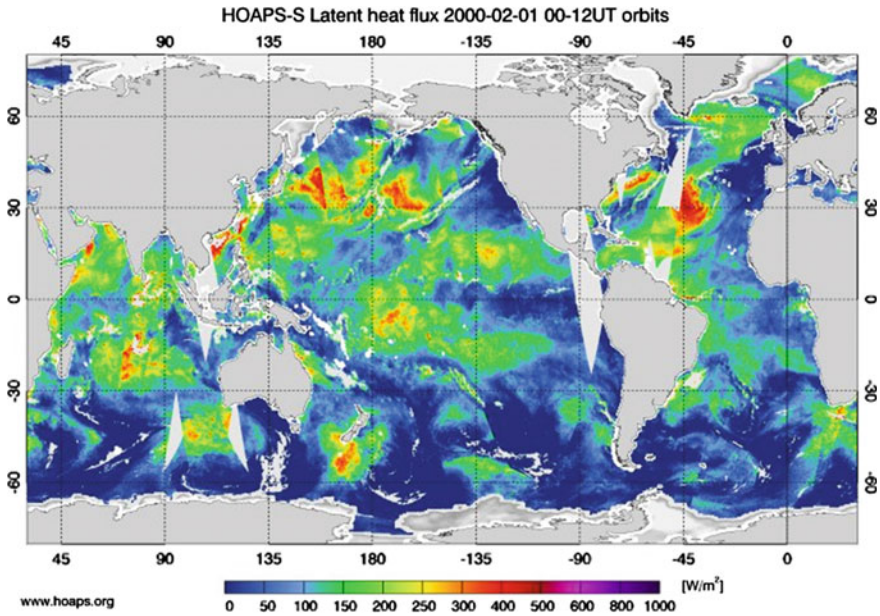One can see the global distributions of the monthly mean heat fluxes from the archive OAFlux at the site http://oaflux.whoi.edu/index.html.

Fig. 11.5 Global distribution of the latent heat flux with 12-h time resolution from the archive HOADS-3.2 (http://www.hoaps.org/)

11.3.4 Global Archive HOAPS: Monthly Mean Fluxes and Parameters of the Ocean and Atmosphere

Global archive HOAPS (Hamburg ocean-atmosphere parameters and fluxes from satellite data) was created by the M. Plank' Institute of the Meteorology and Hamburg University (Andersson et al. 2010). The HOAPS archive covers the area 80°N, 180°W, −80°S, 180°E with spatial resolution 0.5 by 0.5° and includes the following parameters: specific humidity of the near-surface air, total water vapor content in the atmosphere, near-surface wind speed, Dalton number, sensible heat flux, Earth radiation, evaporation rate, precipitation rate. We became acquainted with the version of the HOADS archive produced in 1987–1988 thanks to Dr. Joerg Schulz, who is one of the authors. Figure 11.5 illustrates the global distribution of the latent heat flux with 12-h resolution. The daily variations of latent heat exceed their annually averaged values by 2 times or more.

11.3.5   Global Archive J-OFURO: Monthly Mean Fluxes and Parameters of the Ocean and Atmosphere

The archive J-OFURO (the Japanese Ocean Flux Data sets (1998–2008 years) with Use of Remote Sensing Observations) was created and supported later on by the School of Marine Science and Technology, Tokai University (Kurihara et al. 2003). Daily and monthly averaged parameters are presented with a spatial resolution 1 by 1° along latitude and longitude. The archive contains the following parameters: the surface sensible, latent, and total heat fluxes, the zonal and meridional components of the impulse flux at the 10 m height, and the air humidity at the same level.

The J-OFURO archive was produced from the data of satellites DMSP F-08, F-10, F-11, F-13, F-14, and F-15 equipped by the radiometers SSMI, ERS-1,2 with the scatterometer AMI, QuikSCAT with the scatterometer SeaWinds, EOS Aqua with the radiometer AMSR-E, and NOAA with radiometer AVHRR. In addition, the air–sea temperature data from the NCEP/DOE reanalysis, the ocean surface temperature data from JMA MGDSST (Japan Meteorological Agency Merged satellite, and in situ data Global Daily SST) were used.

11.3.6   Archival Satellite MCW Data

In this section, we briefly describe archival satellite data that are presented used in our laboratory. 20 years ago we first started processing files with antenna temperatures measured from the DMSP F-08 radiometer SSM/I. These files were transmitted us by Dr. Petrenko; he obtained the data from the RSS firm (California) headed by Frank Wentz. In 1997, we received large sets of information from the NASA Marshall Space Flight Centre (MSFC).

At present, the main source of information is data from the DMSP SSM/I radiometers, TRRM TMI radiometer, and EOS Aqua AMSR-E radiometer. The primary data includes results of measurements during the period 1978–1996, conducted from the satallites Nimbus-7, DMSP F-08, F-10, F-11, F-13, and F-14 with 300 GBt capacity in the form of archivized files. Later (in 1996–2008), we obtained satellite data through the Internet and from the NASA centers as well as from the Russian Space Agency organizations. Later, this archive was increased due to the AMSR-E (2002–2011) and WindSat (2002–2010) data.

In 1990, satellite MCW radiometric data were accumulated in the form of the telemetric signals and the antenna temperatures. A suitable file had a large capacity and too complex of a structure to transform the initial satellite information into antenna or brightness temperatures measured with the geographical fixation of the pixels observed. After this, it was possible for secondary (or thematic) satellite processing.

For these aspects of the problems of ocean−atmosphere interaction, the following organizations have been engaged: Kotelnikov's Institute of Radioengineering and Electronics RAS (Dr. Alexander Grankov, Head of the laboratory), Shirhsov' Institute of the Oceanology RAS, (Dr. Sergey Gulev, Head of the laboratory), (Space Research Institute of RAS, department headed by Dr. Eugene Sharkov), Il'ichev Pacific Oceanographic Institute (Laboratory headed by Dr. Leonid Mitnik), Roscosmos' Department headed by Dr Igor Chernii, RosHydromet Center (Department headed by Jurii Resnyanskii), Institute of the Water Problems (Gennadii Panin as the laboratory Head).

11.4 Conclusion

Analysis of the characteristics of the MCW radiometers SSM/I, SSMIS, TMI, WindSat, AMSR-2, and MTVZA-GY in the satellites DMSP, TRMM, Coriolis, GCOM-W1, and Meteor-M show a tendency to use many frequency, polarization, and scanning satellite measurements during last 20–25 years. Now, we can see a clear convergence (similarity) of the various MCW radiometric systems (their frequencies, sensor sensitivity, swath/survey width, scanning method, spatial resolution).

Scanners, sounders, and scatterometers, such as SSMIS, MTVZA, and WindSAT, have appeared. The appearance of satellite MCW radiometers operating at frequencies of 7 and 11 GHz allow one to determine the ocean surface temperature and soil moisture from the satellites TMI, AMSR-2, and MTVZA-GY. The survey width (swath) has increased from 1400 to 1700 km in this time, and its full time is now 2–3 days. Expanding the functional possibilities of satellite MCW radiometers in tasks of the ocean-atmosphere heat interaction occurs from the use of radiometers operating at the millimeter wavelength range. Possibly, the most important finding in our research is the analysis of surface fluxes through the atmosphere from satellites at microwaves at its resonant lines.

Improvement of satellite MCW radiometer technologies resulted in their lifespan increasing to 14 years. Accumulated archives of satellite MCW radiometric data allow us to conduct climatic research of ocean-atmosphere heat interaction for a periods of 35 years. Certainly, however, the problems of using satellite MCW radiometric methods for analysis of synoptic processes at the ocean-atmosphere interface are real.

References

Alishouse JC, Snyder SA, Vongsatorn J, Ferrado RR (1990) Determination of oceanic total precipitated water from the SSM/I. J Geophys Res 5:811−816
Andersson K, Fennig K, C. Klepp C, et al. (2010) The Hamburg Ocean Atmosphere Parameters and Fluxes from Satellite Data – HOAPS-3. Earth Syst. Sci. Data 2:215–234

Boldyrev VV, Il`gasov PA, Pantsov VJu et al. (2008) Microwave scanner/sounder Meteor-M No.1 MTVZA-GY. Problems of electromechanics 107:22−25 In Russian

Comiso JC, Cavalieri D, Parkinson C, Gloerson P (1997) Passive microwave algorithms for sea ice concentrations. Remote Sens. of the Environment 3:357−384

Data Users' Manual for the Advanced Microwave Scanning Radiometer 2 (AMSR2) onboard the Global Change Observation Mission 1-st Water "SHIZUKU" (GCOM-W1). 2nd Edition (2013). Earth Observation Research Center, Japan Aerospace Exploration Agency

Defense Meteorological Satellite Program (DMSP) (1997) (Satellite Source/Platform Document). NOAA Satellite Active Archive

Defense Meteorological Satellite Program Special Sensor Microwave Imager Sounder (F16) Calibration/Validation Final Report, vol 1 (2005). Prepared by SSMIS Cal/Val Team

Global Change Observation Mission: Second Research Announcement SGLI on GCOM-C1. Algorithm development, fundamental data acquisition and validation preparation, and application study (2009). Earth Observation Research Center, Japan Aerospace Exploration Agency

Grankov AG, Milshin AA (2004) Relation between natural microwave radiation of the ocean-atmosphere system with the boundary heat and dynamic interaction. Nauka, Moscow In Russian

Grankov AG, Milshin AA (2010) Microwave radiation of the ocean-atmosphere: boundary heat and dynamic interaction. Springer Dordrecht Heidelberg London New Jork

Hollinger PH, Peirce JL, Poe GA (1990) SSM/I instrument evaluation. IEEE Trans. Geosci Rem Sensing 5:781−790

http://www.hoaps.org/

http://www.vniem.ru/

Jones LA, Kimball JC, McDonald KC et al. (2007) Satellite microwave remote sensing of boreal and arctic soil temperatures from AMSR-E. IEEE Trans Geosci Rem Sensing 7:2004−2018

Kondrat'ev KYa, Buznikov AA, Pokrovskii OM (1992) Global ecology: Remote sensing. Atmosphere, ocean, space –"Razrezy" program. VINITY, Moscow In Russian

Kurihara Y, Sakurai T, Kuragano T (2003) Global daily sea surface temperature analysis using data from satellite microwave radiometer, satellite infrared radiometer and in-situ observations. Weath Bulletin 73:1–18

Milshin AA, Grankov AG, Shelobanova NK (1998) Seasonal dynamics of sensible and latent heat fluxes under various levels of the forest fire danger at different geographical regions (Problems of Ecoinformatics). IRE RAN, IPE RAEN In Russian

Njoku EG, Rague B, Fleming K (1995) Nimbus-7 Scanning Multichannel Microwave Radiometer (SMMR): brightness temperature data (SMMR Level 1B Pathfinder). JPL Publication, Jet Propulsion Laboratory, Pasadena, CA

Pulliainen J, Grandell J, Hallikainen M (1996) SSM/I-based surface temperature retrieval methods for boreal forest zone. IGARSS'96, Burham Yates Conference Center, Lincoln, Nebraska, USA

Remote Sensing Applications. Putting NASA's Earth Science to Work (1998). Raytheon Systems Company, Mariland

Special Sensor Microwave Imager and Sounder (SSMIS) Antenna Brightness Temperature Data Record (TDR) Calibration and Validation (2007). User Manual. Center for Satellite Applications and Research NOAA/NESDIS

Tropical Rainfall Measuring Mission (TRMM) Senior Review Proposal (2007). NASA, GSFC

US navy polarimetric microwave radiometer. WindSat data products. Users manual. Version 3.0 (2006). D-29827. JPL, California Institute of Technology

Key Terms

Atmosphere boundary layer (*ABL*) The atmospheric turbulent layer with upper boundary of 1500 m (850 mb).

    Free atmosphere The atmospheric layer disposed above the ABL.

    Near-surface atmosphere The lower (10-m) air layer.

    Ocean boundary layer (*OBL*) The upper oceanic layer (tens of meters), which is immediately acting in the energy interchanges with an atmosphere.

    Seasonal variations The components with annual rhythm and its harmonics.

    Synoptic variations The components of atmospheric processes varied from some hours to some days.

    Mesometeorological variations The components of atmospheric varied from some minutes to some hours.

Abbreviations

MCW Microwave range of wavelengths

IR Infrared range of wavelengths

cm Centimeter wavelength range

mm Millimeter wavelength range

BT Brightness temperature

HP Horizontal polarization

VP Vertical polarization

SOA System ocean–atmosphere

EAZO Energy active zones of the ocean

R/V Research vessel

Index